DEVELOPEMENT OF HIGH-EFFICIENCY BORON DIFFUSED SILICON SOLAR CELLS

A Dissertation
Presented to
The Academic Faculty

By

Arnab Das

In Partial Fulfillment
of the Requirements for the Degree of
Doctor of Philosophy in the
School of Electrical and Computer Engineering

Georgia Institute of Technology

August 2012

DEVELOPEMENT OF HIGH-EFFICIENCY BORON DIFFUSED SILICON SOLAR CELLS

Approved by:

Dr. Ajeet Rohatgi, Advisor
School of Electrical and Computer Engineering
Georgia Institute of Technology

Dr. George Riley
School of Electrical and Computer Engineering
Georgia Institute of Technology

Dr. David Citrin
School of Electrical and Computer Engineering
Georgia Institute of Technology

Dr. Phillip First
School of Physics
Georgia Institute of Technology

Dr. Bernard Kippelen
School of Electrical and Computer Engineering
Georgia Institute of Technology

Date Approved: 04/23/2012

This work is dedicated to:

My parents
Suchita and Asoke Kumar Das
for their love and support at every step of the way

ACKNOWLEDGEMENTS

I am grateful first, to my advisor, Dr. Ajeet Rohatgi, for providing me with the opportunity and resources to pursue the research described in this thesis. I am particularly indebted to him for pushing me to develop a deeper understanding of solar cell physics and for providing me with the freedom to pursue a wide range of, sometimes far-etched, ideas and topics. His encouragement has led me to learn more than I otherwise would have. I am also deeply indebted to Dr. Dong Seop Kim, former assistant director at UCEP (currently at Samsung), for developing the foundations of the research that led to this thesis and for the time spent in guiding me in solar cell processing, characterization and theory. I would also like to thank Dr. David Citrin, Dr. Bernard Kippelen, Dr George Riley, and Dr. Phillip First for serving on my dissertation committee.

Special thanks (and commiserations) to Saptarishi Ramanathan for being a fellow passenger on the PhD boat, for many hours of banter especially the often hilarious (or soul-crushing depending on your point-of-view) discussions on football/soccer, and for interesting technical discussions and help with experimental work.

I also acknowledge the support of current and former members of UCEP, including Ajay Upadhyaya, Dr. Alan Ristow, Dr Abasifreke Ebong, Dr. Mohammed Hilali, Dr. Kenta Nakayashiki, Dr. Vijay Yelundur, Vijay Kumar Upadhyaya, Keith Tate, John Renshaw, Francesco Zimbardi, Attila Vamos, Dr. Young Woo Ok, Dr. Ian Cooper and Dr. Manav Sheoran. I am especially grateful to Kenneth Trotman, Ken Lamborn and Dean Sutter for their extensive assistance with equipment maintenance and to Carla East and Denise Taylor for their help with administrative issues. Special thanks go to Dr. Vichai Meemongkolkiat for his guidance during the early years of this thesis, to Jiun-Hong Lai for exposing me to issues on large-area, point-contacted cells, and to Brian Rounsaville for spending many hours assisting me with experimental work and for his

friendship. I also gratefully acknowledge the experimental help provided by Moon Hee Kang (Al_2O_3 depositions) and Kyung Sun Ryu (n-type studies).

I also wish to thank Robert Reedy at NREL for SIMS measurements, and Paul Ciszek and Dr. Keith Emery, also at NREL, for arranging I-V measurements and for helpful discussions on solar cell characterization. I am grateful to Dr. Ronald Sinton, of Sinton Consulting, for informative discussions on lifetime measurements.

The research in this thesis was supported by the U.S. Department of Energy and the Silicon Solar Consortium (SiSoC).

TABLE OF CONTENTS

LIST OF TABLES

LIST OF FIGURES

LIST OF SYMBOLS AND ABBREVIATIONS

PV	Photovoltaics
Si	Silicon
FZ	Float-zone
Cz	Czochralski
a-Si	Amorphous silicon
SRH	Shockley-Read-Hall
τ	Minority carrier Lifetime
τ_{EFF}	Effective minority carrier lifetime
τ_{BULK}	Bulk minority carrier lifetime
τ_{n0}	Electron lifetime
τ_{p0}	Hole lifetime
L	Carrier diffusion length
D	Carrier diffusivity
μ	Carrier mobility
N_A	Acceptor concentration
N_D	Donor concentration
q	Electron charge
v_T	Thermal velocity
σ_N	Electron capture cross-section
σ_P	Hole capture cross-section
N_T	Trap Density
S or SRV	Surface Recombination Velocity
FSRV	Front Surface Recombination Velocity
BSRV	Back Surface Recombination Velocity

BSR	Back Surface Reflector
R_B	Back Surface Reflectance
J_0	Saturation current density
J_{0E}	Saturation current density on emitter side of depletion region
J_{0B}	Saturation current density on base side of depletion region
J_{0B}'	Saturation current density on rear side of solar cell
J_{01}	Saturation current density of 1st diode in two diode model of a solar cell
J_{02}	Saturation current density of 2nd diode in two diode model of a solar cell
n_1	Ideality factor of 1st diode in two diode model of a solar cell
n_2	Ideality factor of 2nd diode in two diode model of a solar cell
I	Current
V	Voltage
J_{SC}	Short-circuit current density
V_{OC}	Open-circuit current density
FF	Fill Factor
R_S	Series resistance
R_{SHUNT}	Shunt resistance
n	Ideality factor in single-diode model
Q_F	Oxide charge density
IQE	Internal Quantum Efficiency
PECVD	Plasma Enhanced Chemical Vapor Deposition
SP	Screen Printed or Screen-Printing
PL	Photolithography
SEM	Scanning Electron Microscopy
SIMS	Secondary Ion Mass Spectroscopy

SUMMARY

Growing concern about the impact of fossil fuel use on the global climate has led to a recent surge of interest in alternate forms of energy generation with a focus on methods with lower emissions of carbon dioxide. Photovoltaics (PV) – the direct conversion of sunlight to electricity – is a promising alternative to fossil fuel technology as PV modules have zero emissions during operation and have a long 25 year+ lifespan. However, PV currently accounts for less than 0.1% of the total electricity generated in the United States. This is largely due to PV electricity being about two times more expensive than the retail price of electricity from the grid which is largely fed by fossil fuels. Cost calculations indicate that getting PV to grid-parity in the United States (~10 ¢/kWhr) without policy incentives will require ≥20% efficient cells manufactured at a cost of ~$1/W.

Crystalline silicon cells dominate the PV market today with ~90% market share. However, a majority of Si cells use the screen-printed, full Al-BSF structure which cannot achieve ≥ 20% efficiency using conventional screen-printing technology. This provided the motivation to produce ≥ 20% efficient Si solar cells in this thesis. The approach that was adopted in this research involved first fabricating and analyzing a high-efficiency, full Al-BSF cell, and then developing modifications to that cell that would lead to efficiencies ≥ 20%. Issues of commercial viability and throughput were also kept in mind during the development of the modified structure and process.

In the first phase of this thesis, a ~19% efficient, 300 μm thick, screen-printed Al-BSF cell (4 cm^2) was fabricated and analyzed to determine and quantify its major efficiency-limiting loss mechanisms. Through detailed experimental characterization and computer modeling, it was determined that this 'baseline' cell was primarily limited by back side losses, namely a high back surface recombination velocity (BSRV) of 600 cm/s and a low back surface reflectance (R_B) of ~70%. Further modeling showed that if the

BSRV and R_B could be improved to 200 cm/s and 95% (100% diffuse) respectively, while maintaining a high bulk lifetime of > 300 μs, 20% efficient cells could be achieved without making any changes to the front side processing. The simulations also revealed that this improved design could maintain efficiencies of ~20% even if the wafer thickness were to be cut in half to 150 μm. Developing cell designs that can maintain high efficiencies on thin substrates is important as the Si wafer alone accounts for ~60% of the cost of commercial cSi modules. Therefore, being able to reduce wafer usage with little to no loss in efficiency could lead to a significant cost reduction The remainder of the thesis research dealt with developing technologies for meeting the BSRV and R_B targets as well as developing cell fabrication processes that can integrate these technologies into a 20% efficient Si solar cell.

A review of the relevant literature indicated that the BSRV and BSR targets are not likely to be attained using the conventional Al-BSF structure. The cell concept that is instead pursued in this thesis is the boron back surface field (B-BSF) structure. For meeting the BSRV goal of 200 cm/s, a B-BSF is a technically attractive alternative to a conventional Al-BSF as: 1) a B-BSF can provide stronger field-effect passivation due to boron having higher solubility in Si than aluminum, and 2) the surface of a B-BSF can be more easily passivated with a dielectric. Furthermore, a B-BSF can be capped with a highly reflective material (or a dielectric/reflector stack) allowing the R_B target of ~95% to be achieved.

While several B-BSFs designs have been explored in the past, a literature survey showed that cell processes involving boron diffusion often use long processing times, high processing temperatures and frequently result in contamination of the Si substrate. In addition, all ≥ 20% efficient B-BSF cells that have been reported in the literature involved photolithography-based processing and prolonged thermal cycles at very high temperatures (> 1000°C). Such processing methods are too high-cost and low-throughput to be commercially viable. Therefore, another goal of this thesis is to develop a

fabrication process that can deliver a ≥ 20% efficient, full-area B-BSF cell while: 1) ensuring that the cycle time of each process step is no longer than the longest step used for the baseline full Al-BSF cell (90 minutes), and 2) using low-cost, screen-printing technology for contact formation.

The first step towards realizing a 20% B-BSF cell was to pick a boron diffusion source. In this thesis, dilute spin-on solutions of boric acid in de-ionized (DI) water were investigated as a novel, low-cost and non-toxic alternative to more conventional boron diffusion sources like boron tribromide (BBr_3) which are toxic and pyrophoric. It was found that boron emitters with a wide range sheet resistances (~20 – 200 Ω/sq.) could be achieved with very dilute boric acid sources (~0.5-2 wt.% boric acid in DI water) by controlling the diffusion time and temperature. This range of sheet resistances corresponds to surface concentrations in the range of ~$1x10^{19}$ to $1x10^{20}$ cm^{-3} and junction depths of ~0.2-1.5 μm. In addition, uniform diffusion was obtained on both planar and pyramid textured surfaces using these spin-on sources. These results demonstrate that spin-on boric acid solutions are promising boron diffusion sources for fabricating high-efficiency solar cells. Since the diffusion from many commercially-available, spin-on dopant sources are sensitive to age and ambient humidity and need refrigeration to maximize the shelf-life of the source, the stability of the spin-on boric acid sources were also tested. Experimentation showed that the boric acid sources are stable at room-temperature for at least 6 months. Diffusion from the sources *is* however sensitive to ambient conditions if boric acid-coated wafers are conventionally loaded in the diffusion boat, i.e. each slot in the diffusion boat has one boric acid-coated wafer. It was found that if *two* wafers are instead loaded back-to-back in *one* slot, reproducible doping can be obtained regardless of the ambient humidity (20-55%), ambient temperature (17-25 °C) and solution age (0-6 months). In addition, both wafers in a slot can be equally diffused even when only one of the two wafers is coated with boric acid. This reduces material consumption and the throughput per boat.

The next phase of the research involved selecting a diffusion condition/doping profile that can achieve the target BSRV of 200 cm/s and thereby deliver a 20% efficient B-BSF cell. The simplest B-BSF structure is one with full-area boron diffusion and full-area rear metallization because this structure requires just one additional step (boron diffusion) over the baseline Al-BSF process. However, modeling showed that achieving a BSRV of 200 cm/s with full-area metallization requires a ~3 μm deep, electrically 'opaque' B-BSF with a high surface concentration of ~$1x10^{20}$ cm^{-3}. A literature search revealed that even with very high processing temperatures of ~1100°C, fabricating such a heavily doped BSF requires a ~5.5 hr. deposition + drive-in process. So while an opaque B-BSF allows 20% efficiency to be achieved with a simple (and therefore commercially attractive) cell structure, the high-temperatures and long process times required to achieve an opaque B-BSF are commercially *un*attractive as it increases cost and reduces throughput. For example, the longest and highest-temperature step in the conventional full Al-BSF process is the $POCl_3$ (emitter) diffusion step which has a peak temperature of 860-870°C and lasts just ~90 minutes (this figure includes the time taken to ramp to/from the peak process temperature). Experimentation showed that maintaining the throughput of the Al-BSF process (i.e. limiting the boron diffusion cycle to 90 minutes) while using a relatively moderate peak temperature of 1000°C results in a 'transparent' ~1 μm deep B-BSF that *needs* to be passivated to achieve efficiency of 20%. Specifically, model calculations showed that a recombination velocity of ~40,000 cm/s at the p^+ surface (S_p^+) is required to achieve the target BSRV or $S_{p/p}^+$ of 200 cm/s. This means that if the throughput of the baseline Al-BSF process is to be maintained, increased process complexity in the form of an additional passivation step and local contacts is unavoidable. Therefore, finding a dielectric that: 1) provides high-quality passivation of a p^+ surface in a process that lasts ≤ 90 minutes, and 2) is stable through a high-temperature (700-800°C) screen-printed contact firing cycle, became the next focus of this thesis.

In the passivation studies, several different dielectrics – thermal SiO_2, low-frequency plasma-enhanced chemical vapor deposited (LF-PECVD) SiN_X, thermal SiO_2/PECVD SiN_X stacks, atomic layer deposited (ALD) Al_2O_3, a commercially available spin-on SiO_2, and a commercially available Al-doped spin-on glass (SOG) – were examined. From saturation current density (J_0) measurements on symmetrically boron diffused and passivated samples and Implied V_{OC} measurements on cell wafers, fired thermal SiO_2/SiN_X stacks and the Al-doped SOG were found to be the most promising dielectrics with both achieving S_p^+ of ~18,000 cm/s on planar (un-metallized) p^+ samples. However, only the fired thermal oxide/SiN_X stack was able to provide passivation of similar quality on textured p^+ samples. Area-average calculations then showed that achieving the cell-level S_p^+ of 40,000 cm/s with either dielectric requires a metal fraction of ≤ 2.5%. Since achieving such a low metal fraction with current screen-printing technology requires a point-contact pattern, the passivation studies also helped to determine the rear contact structure of the cells fabricated in this thesis.

In summary, the results of the passivation studies provided two options for achieving a 20% efficient, passivated B-BSF cell: 1) a point-contacted, transparent, *planar* B-BSF with either Al-doped SOG or thermal oxide/SiN_X passivation and 2) a point-contacted, transparent, *textured* B-BSF with thermal oxide/SiN_X stack passivation. Since planarizing one side of a wafer can add up to two steps to the cell fabrication process, the latter appeared to be the more commercially-friendly option. However, bulk lifetime studies showed that the thermal oxide/SiN_X passivation scheme resulted in severe degradation in the bulk lifetime due to Fe contamination of the wafer during oxidation. In contrast, the Al-doped SOG was found to both strongly getter Fe *and* passivate the B-BSF in the same thermal cycle. Since high lifetimes are required for achieving 20% efficient cells, these findings forced the use of the more complex rear-side structure – a *planar* B-BSF with Al-doped SOG passivation.

A surprising finding from the lifetime studies was that $POCl_3$ diffusion after the B-BSF diffusion was unable to effectively getter Fe and instead resulted in a net *increase* in the bulk Fe contamination. From experimental studies, this was attributed to Fe slowly leaking into the wafer bulk from the B-BSF during the $POCl_3$ cycle. The strong Fe gettering ability of the Al-doped SOG was attributed to its negative charge density, i.e. the gettering is driven by electrostatic attraction between negatively-charged complexes in the SOG and positively charge interstitial Fe.

The next phase of the thesis dealt with finding a back surface reflector (BSR) material that has R_B = 95% and diffusivity (β) = 100%. Since the passivation studies established that the rear contacts needed to be point contacts, the BSR also needs to be electrically conductive so that it can electrically interconnect the rear point contacts. Several materials were tested in this phase of the thesis – evaporated Ag, evaporated Al, a screen-printed Ag paste and a Ag colloid that is deposited with a brush. While none of these four materials met both the R_B and the β targets simultaneously, the Ag colloid came the closest, with the Al-doped SOG/Ag Colloid stack having $R_B \sim 98\%$ and $\beta \sim 70\%$. Electrical resistivity measurements also showed that after a short sintering step at 400°C, the resistivity of the Ag colloid is similar to that of screen-printed Ag pastes fired at ~700-800°C.

The final phase of the thesis involved integrating the results of the modeling, passivation, lifetime and BSR studies into a cell fabrication sequence. This was successfully completed and a confirmed efficiency of 20.2% was achieved on a $4cm^2$, passivated B-BSF cell on FZ Si. However, device modeling showed that if this cell structure and process were transferred to commercial p-type Cz Si material, the light-induced degradation (LID) effect that affects commercial p-type Cz material could reduce the efficiency to ~19%. Via both device modeling and device theory this large drop in cell efficiency due to LID was shown, to be linked to the well-passivated surfaces of the

B-BSF cell. Specifically, it was found that as the quality of surface passivation improves, the impact of LID on cell efficiency becomes larger. Since n-type substrates do not suffer from the same LID effect, the B-BSF cell process was applied to n-type FZ wafers. Since the Al-doped SOG used for rear passivation on the p-type B-BSF cells is not suitable for passivating a textured boron emitter, it was replaced with a thermal oxide/SiN_X stack. The p-type B-BSF and the n-type boron emitter cell processes were otherwise nearly identical. With this process, a confirmed efficiency of ~20.3% was achieved on a 4cm^2 front-emitter n-type Fz cell. The Fe contamination that results from using thermal oxide/SiN_X passivation did not limit the performance of the n-type cells as the minority carrier lifetime of n-type Si wafers is not as strongly affected by Fe impurities (compared to the effect of Fe on the lifetime of p-type Si wafers).

Thus, through a combination of modeling-driven device design, technology development and process integration, > 20% efficient, screen-printed cells (4 cm^2) were achieved on both p- and n-type substrates using a spin-on boron source. These achievements relied on technologies and processes developed in this thesis which resulted in high cell bulk lifetimes and well-passivated, boron-doped p^+-regions which served as the back surface field for p-base cells as the emitter for n-base cells.

CHAPTER 1

INTRODUCTION

1.1 The Promise of PV

Historically, our ever-increasing demand for energy has been satisfied mainly by expanding our use of fossil fuels [1]. Both globally and in the United States, fossil fuels currently account for ~85% of the energy mix (Figures 1.1 and 1.2). In contrast, the contribution of renewables such as PV to the energy mix has stayed comparatively stagnant over the past 50 years. Increased energy use has however been accompanied by an increase in mean global temperature (Figure 1.3) and increased emissions of greenhouse gases such as CO_2 due to burning of fossil fuels have been implicated as the cause [2]. Concern over rising temperatures has, in turn, led to increased demand for alternate sources of energy generation. The International Energy Agency (IEA) projects that limiting the global mean temperature increase to < 2.5°C by 2050 requires renewables to account for 17% of world energy generation [3].

Photovoltaics (PV) – the direct conversion of sunlight to electricity – is a promising renewable energy source as the annual global insolation of ~3.8×10^{24} J is ~10,000 times the global annual energy consumption (~5×10^{20} J) [1]. The promise of PV as an energy source is further enhanced by the fact that the global distribution of solar energy (Figure 1.4) matches up very well with current consumption and emission patterns. As shown in Figure 1.5, just five countries – the United States, China, India, Brazil and Australia – account for nearly half of both global energy use and global CO_2 emissions [4]. As each of them also happens to be rich in solar energy [5], PV has the potential to be a major player in both meeting global energy needs and in combating global CO_2 emissions.

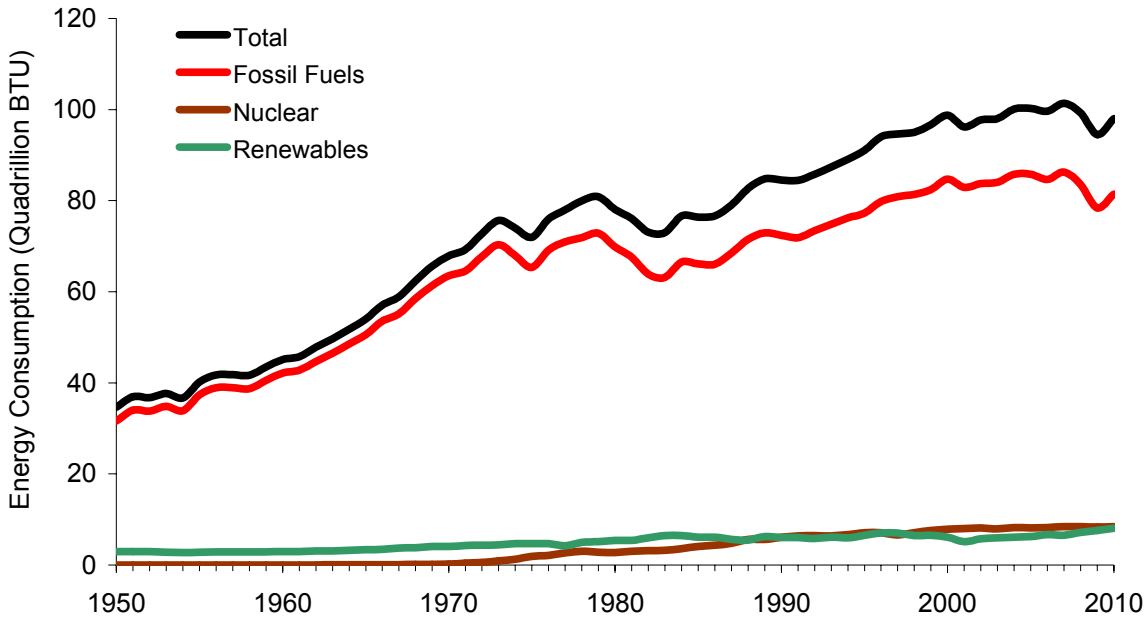

Figure 1.1 Energy consumption by source in the United States (1950-2010) [1].

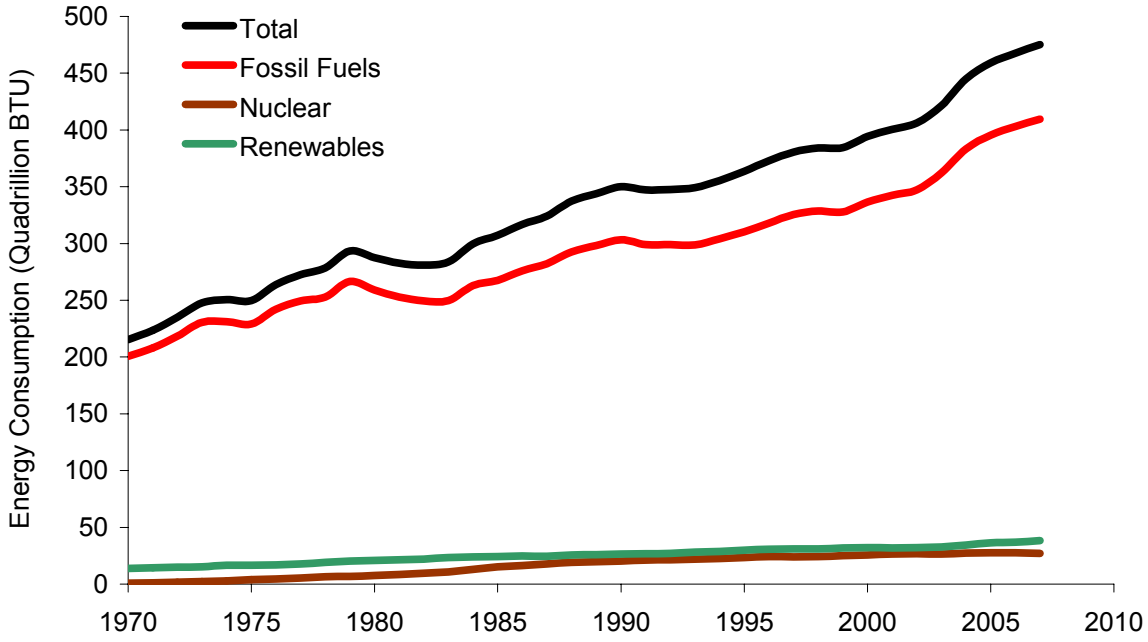

Figure 1.2 Global energy consumption by source (1970-2007) [1].

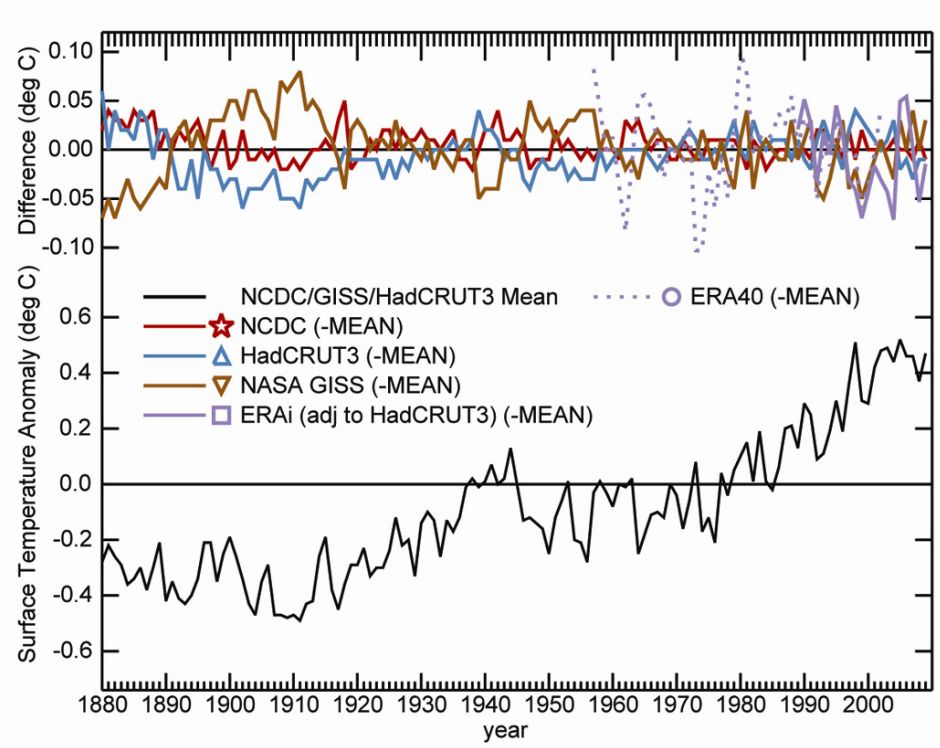

Figure 1.3 Global surface temperature anomalies with respect to the 1961 to 1990 average. Bottom: mean of the noted datasets and Top: difference between the noted data sets (Figure taken from Ref. 2).

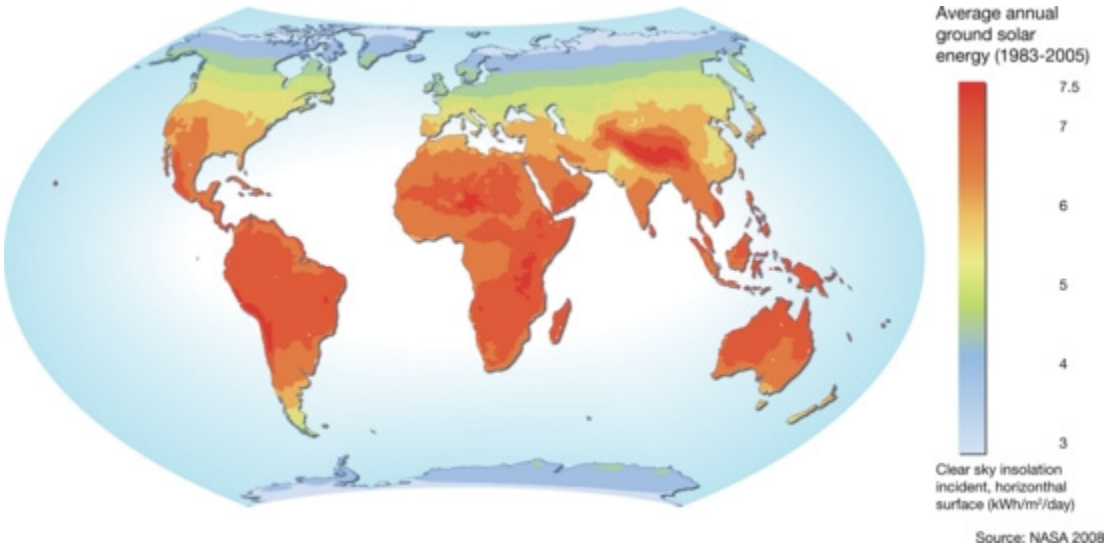

Figure 1.4 Global map of clear sky insolation incident on a horizontal surface (Figure taken from Ref. 5).

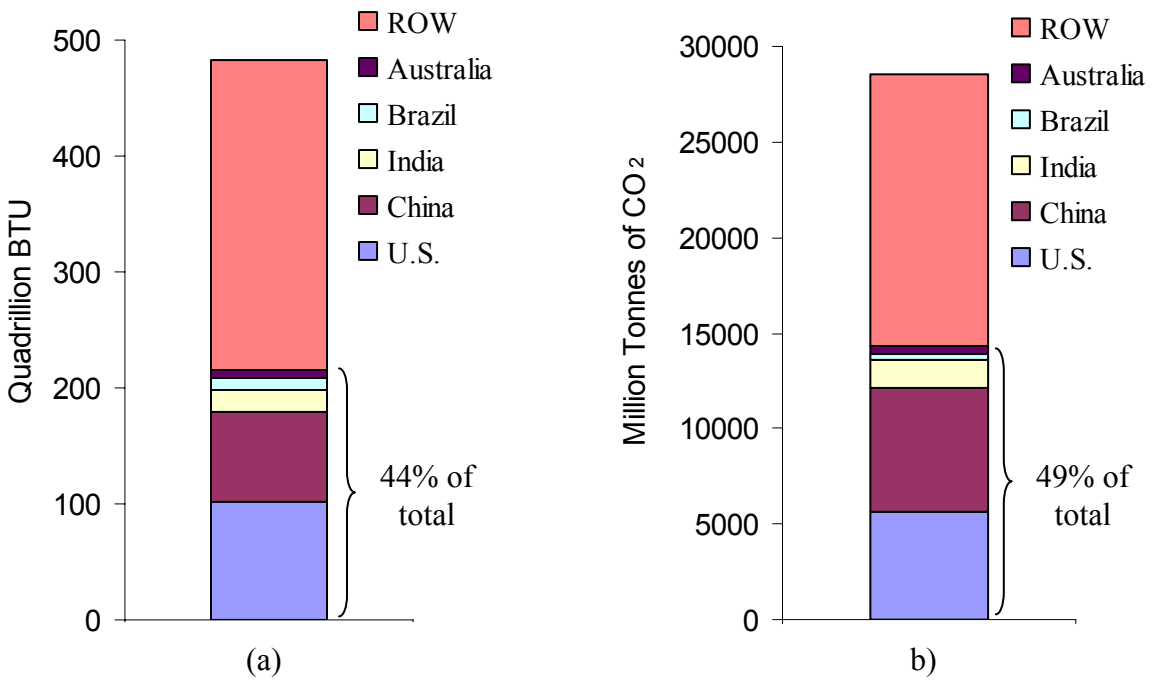

Figure 1.5 (a) Global energy consumption and (b) global CO_2 emissions [4].

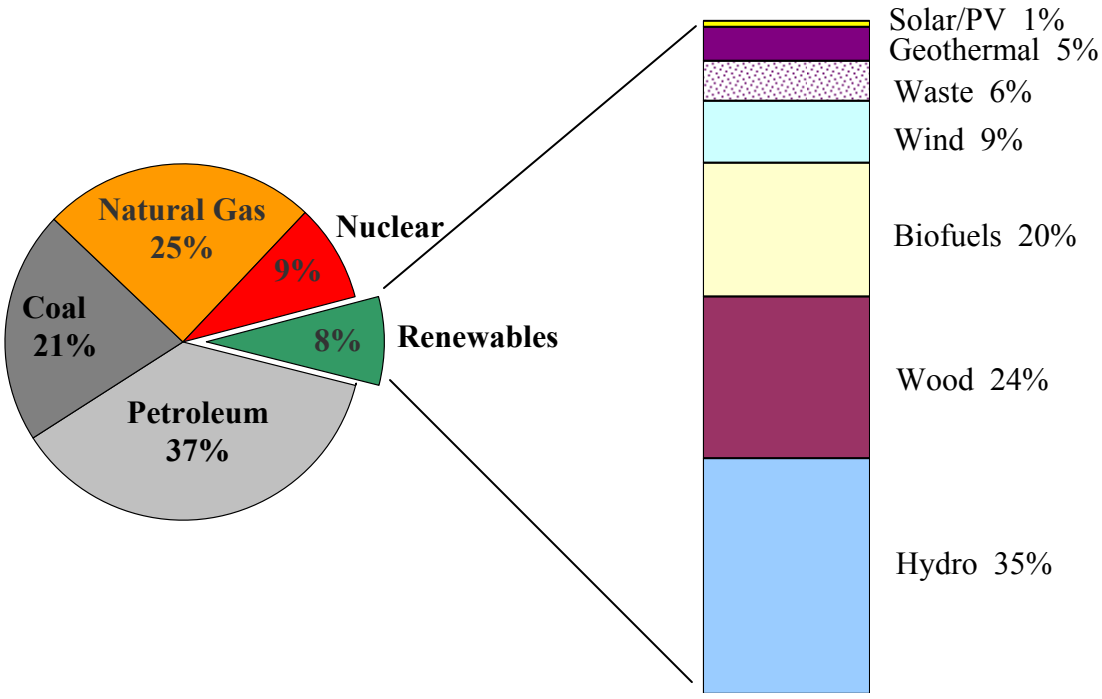

Figure 1.6 Energy mix by source in the United States (2009) [1].

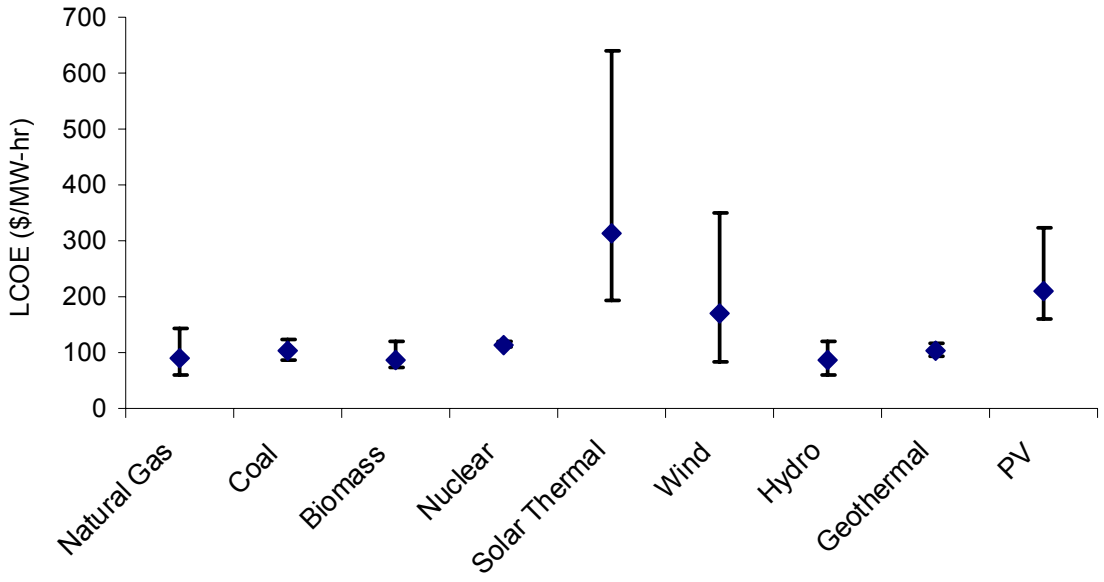

Figure 1.7 Costs of various electricity generation sources in the United States from plants under construction in 2011 [6].

However, PV accounted for < 0.1% of U.S. energy production in 2009 (Figure 1.6) mainly due to the cost of PV electricity generation being ~2x compared to that of fossil fuel and nuclear generation (Figure 1.7) [1], [6].

Higher efficiency solar cells (≥ 20%) on ~150 μm thick wafers have the potential to dramatically reduce the cost of PV generation if they can be produced at sufficiently low cost [7]. However, such high efficiencies have typically been achieved only in the laboratory using complicated and prolonged processing methods that make these cells much more expensive than their lower efficiency, industrially-produced counterparts. As the PV market is currently dominated by Si wafer based cells (Figure 1.8) driving down the cost of silicon solar cells is important for making PV economically competitive [8], [9]. The challenge of achieving high efficiency Si solar cells using low-cost, industrially feasible fabrication methods provides the impetus for this study.

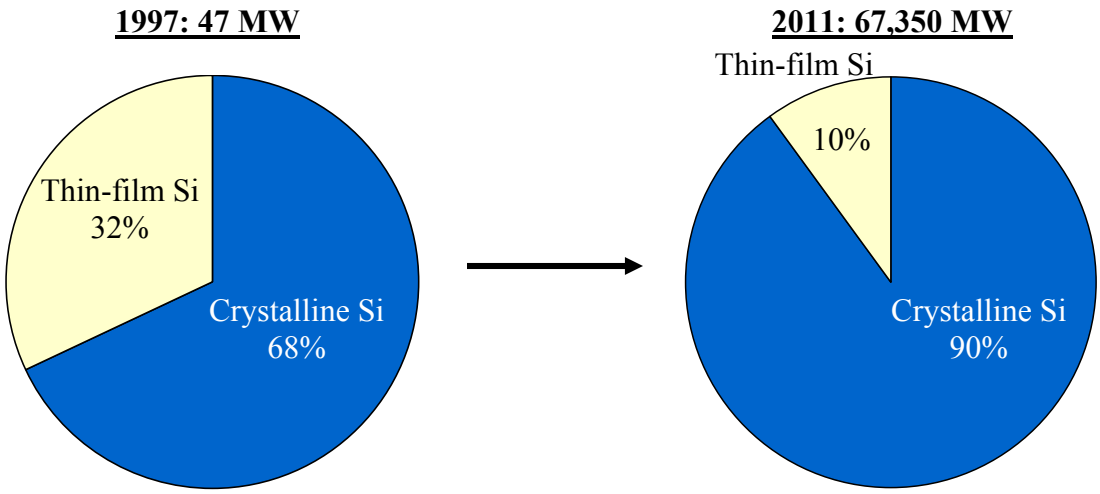

Figure 1.8 Global cumulative installed PV capacity and market share of crystalline silicon and thin-film technologies [8, 9].

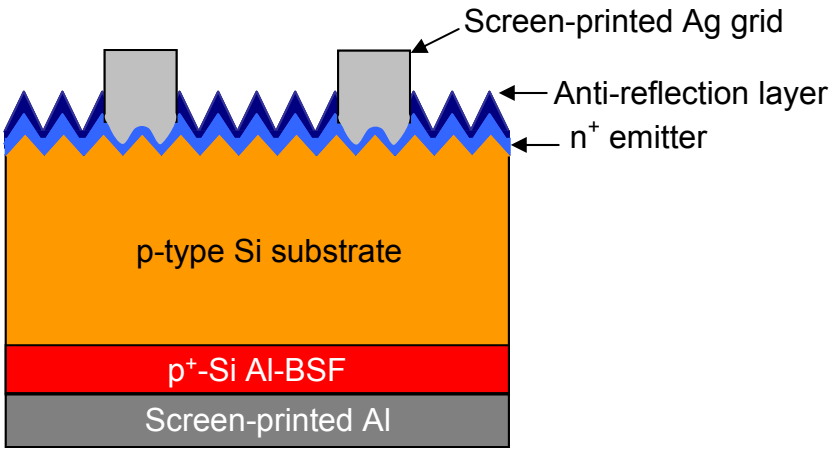

Figure 1.9 Schematic of the Al-BSF cell structure.

Currently, the Al-BSF structure shown in Figure 1.9 is the dominant industrial cell structure. In brief, the fabrication of this structure involves forming a p-n junction on the front of the device, depositing a silicon nitride (SiN) anti-reflection layer on the front, followed by screen-printing a layer of aluminum (Al) on the entire rear side of the wafer and a grid of silver (Ag) fingers on the front side. A short, high temperature firing process results in the screen-printed metals making electrical contact to the Si solar cell. During

this firing process, Al also dopes the silicon which results in the formation of a passivating p^+-Si layer called the aluminum back surface field (Al-BSF) [10]. The industrial popularity of the Al-BSF cell structure can be attributed to the low cost, high throughput nature of this simple fabrication process. However, this basic cell structure is insufficient for achieving the target of 20% efficiency on 150 μm thick wafers. The Al-BSF results in fairly high rear recombination losses and has a high degree of parasitic light absorption. As a result, the efficiency of commercial Al-BSF cells has plateaued at ~19% on ~1.3-3 Ω-cm ~180-300 μm thick wafers [7], [11]. Furthermore, a thermal coefficient mismatch between Al and Si often results in warping of wafers after Al-BSF formation with warping increasing as the wafer thickness drops [12]. Thinning down the wafer to ≤ 150 μm is an important commercial goal as the wafer alone constitutes ~50-60% of the cost of a cSi module (Figure 1.10) [13]. However, warping on thin wafers can lead to wafer breakage/cracking thereby reducing yields to unacceptably low levels.

These limitations point to a need for advanced cell structures that can achieve high efficiencies using industrially viable fabrication technologies while avoiding warping of thin wafers.

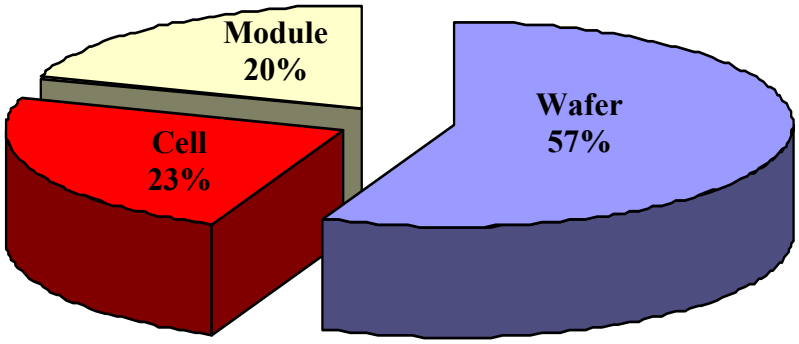

Figure 1.10 Cost breakdown of a crystalline Si PV module.

1.2 Thesis Outline and Specific Research Tasks

As noted in review above, the efficiency of the screen-printed Al-BSF cell is limited by high rear surface recombination losses and high parasitic absorption (i.e. low reflectance) at the rear surface. The aim of the research described here is to reduce both loss mechanisms by replacing the Al-BSF with a boron back surface field (B-BSF). The final goal is to demonstrate 20% efficient cells using a screen-printed B-BSF cell structure fabricated using low-cost, industrially relevant methods. The work done towards this goal is divided into 6 tasks as described below.

Though the Al-BSF structure is not the focus of this study, Task 1 involves the fabrication of a high efficiency (~19%) Al-BSF cell. After thorough experimental characterization, a detailed computer model of this 'baseline' cell is constructed. Simulations are then run on this model in order to identify a set of improved cell parameters – namely SRV, bulk lifetime and rear reflectance values – that can lead to 20% efficient cells. The remaining tasks will involve experimental realization of these improved cell parameters using a B-BSF cell structure. Task 2 involves the investigation of boric acid as a potential low-cost, non-toxic, spin-on boron diffusion source. The objectives of this task are to demonstrate that boric acid is a viable alternative to conventional boron diffusion sources and to identify boron diffusion processes that are capable of achieving 20% efficient cells. In Task 3, passivation studies are used to identify materials that can passivate a B-BSF well enough to meet the target BSRV value obtained in Task 1. Task 4 involves a systematic study of bulk lifetime degradation and iron contamination due to boron diffusion and the development of a cell fabrication sequence that limits the impact of iron on bulk lifetime. Task 5 is devoted to the study of back surface reflector materials with the aim of finding an electrically conductive and highly reflective, Lambertian reflector material that meets the reflectance targets obtained from the computer simulations in Task 1. In the final task, the results of all the previous tasks will be integrated to realize a 20% efficient screen-printed B-BSF solar cell.

1.2.1 Task 1: Identifying a Pathway to 20% Efficient Screen-printed Cells via Fabrication and Characterization of Screen-Printed Al-BSF Solar cells

The screen-printed (SP) Al-BSF cell structure is workhorse of the commercial PV industry due to the simplicity and high-throughput nature of the fabrication process. However, the high BSRV and a low R_B of this structure has limited its efficiency to ~19% on 180-300 μm thick cells using wafers in the ~1-3 Ω-cm resistivity range typically used in industry [7, 11]. With thinner wafers, manufacturing yield is a concern because firing of SP Al pastes results in wafer warping/bowing and increased breakage [12]; while 'low-bow' pastes can reduce the warping there is often a trade-off between wafer bow and passivation quality [14, 15]. A B-BSF structure is a promising alternative because it not only avoids the bowing problem and can also provide a lower BSRV because silicon can be doped more heavily with boron than with aluminum.

The first step towards attaining a 20% efficient B-BSF cell is to identify and quantify a set of cell parameters that is capable of achieving this efficiency target. To accomplish this goal, a ~19% efficient baseline Al-BSF cells is first fabricated. The process sequence used here to fabricate this cell is very similar to that used in industry – it features a $POCl_3$ diffused emitter with sheet resistance of 70-80 Ω/sq, front-side SiN passivation and single-printing of the front Ag gridlines (~120 μm wide) and rear-side, full-area Al. The electrical and optical characteristics of this cell are then determined from bulk lifetime, quantum efficiency, reflectance, light I-V and dark I-V measurements and used to build a computer model using PC1D [16]. Iterative simulations are then performed on this baseline model to determine the values for front and back surface recombination velocities (FSRV and BSRV), back surface reflectance (R_B) and bulk lifetime that are required for obtaining 20% efficient SP solar cells on ~150 μm thick Si wafers.

1.2.2 Task 2: Development of Boric Acid as a Spin-on Source for Boron Diffusion

Dilute solutions of boric acid in de-ionized water are investigated as a novel boron diffusion source for forming diffused layers for solar cells. While a review of the literature shows that there is a known chemical pathway that allows for the diffusion of boron into Si from boric acid, the applicability of this source to solar cell fabrication has not been previously demonstrated. The effect of source concentration, diffusion time and diffusion temperature on the sheet resistance and boron profiles is studied in this task. The stability of the source over time and the impact of processing methods and ambient conditions on reproducibility are also examined.

1.2.3 Task 3: Passivation of Heavily Boron Doped Silicon

In Task 1, the BSRV (i.e. the SRV at the p/p^+ interface or S_{p/p^+}) required for achieving 20% efficient cells was determined. In this task, the computer modeling from Task 1 is extended to identify 'opaque' and 'transparent' B-BSF profiles that can result in 20% efficient cells along with the passivation quality at the p^+ surface (S_{p^+}) required for both profiles. The trade-offs between the two profile types are examined and 'transparent' profiles are identified as being more suitable for industrial manufacturing. Based on this determination and the experimental work in Task 2, a boric acid diffusion recipe that can realize the simulated, transparent profile is chosen for cell fabrication. Finally, several dielectric materials are investigated with the goal of finding a passivation scheme that can provide the S_{p^+} value required for achieving a 20% cell with a transparent B-BSF. The impact of surface texturing on the passivation of the p^+-Si surface is also studied along with the stability of each passivating dielectric through a high-temperature, contact firing cycle and the stability over time.

1.2.4 Task 4: Study of Bulk Lifetime Degradation due to Boron Diffusions and Process-Induced Gettering of Iron

Though low post-diffusion bulk lifetimes have been reported for all boron sources, the physical cause of the low lifetimes has not been well investigated. In this task, the impact of boric acid diffusions on lifetime is experimentally studied with a focus on identifying process conditions and physical mechanisms that result in lifetime degradation. As iron (Fe) contamination is widely assumed to be cause of lifetime degradations, emphasis is placed on experimentally determining if Fe contamination can account for the low lifetimes reported in the literature for boron diffusion processes. The impact of processing conditions on Fe contamination and gettering is also examined and a novel, dielectric charge based mechanism for gettering Fe is discovered. The overall aim of this task is to meet or exceed the bulk lifetime target determined in Task 1.

1.2.5 Task 5: Characterization of Electrically Conductive, Back Surface Reflectors

Task 1 involved determining the values of BSRV and R_B that can lead to 20% efficient cells. While Tasks 2 and 3 are devoted to the meeting the BSRV requirements, this task focuses on finding a back surface reflector (BSR) material that can achieve the required R_B characteristics. Several materials are characterized in terms of their reflectance (R_B) and light scattering (β) ability. The electrical conductivity of these BSR materials is also studied in order to determine if they can serve as both the rear reflector and the back contact of a finished solar cell.

1.2.6 Task 6: Fabrication and Analysis of 20% Efficient B-BSF Solar Cells

This task involves bringing together the experimental work done on surface passivation, bulk lifetime and back surface reflectors in Tasks 2 through 5 in order to

achieve 20% efficient screen-printed solar cells on FZ Si. The electrical and optical parameters of the cell are analyzed in order to check how well the parameters of the experimentally realized cell match the values predicted by the computer modeling work done in Task 1. Since commercial solar cells are made on Cz Si wafers (which suffers from light-induced degradation or LID thanks to a high oxygen concentration in the material), the effect of LID on well-passivated, high-efficiency cell designs is examined through simulations and device theory. Since n-type substrates are not affected by the LID mechanism, a slightly tweaked version of the 20% p-type B-BSF cell process is applied to n-type substrates resulting in over 20% efficient n-type, front-junction screen-printed cells.

Chapter 2

BASICS OF SOLAR CELL PHYSICS

As the aim of this research is to reduce the recombination and the optical losses suffered by the Al-BSF cell structure, it is useful to first discuss the physical mechanisms behind these losses and identify the parameters used to quantify them. The focus of this section is on p-type devices where electrons are the minority carriers. N-type cells can be described in a similar fashion but with holes as the minority carriers.

2.1 Electronic Losses in a Solar Cell

In general, the operation of a p-type solar cell relies on two-steps: 1) transfer of energy from light to electrons via absorption, and 2) Transfer of the energized/photo-excited electrons to an external load. *Recombination* refers to any process that causes a photo-excited electron to lose its energy, thereby allowing it to be recaptured by the host semiconductor before step 2 is completed. In the language of semiconductor physics, absorption results in the *generation* of *electron-hole* pairs, where a *hole* is a conceptual particle representing the absence of an electron in the semiconductor lattice. The process of a photo-excited electron losing its energy and being recaptured by the lattice can therefore be thought of as an electron recombining with a hole. All electronic losses in a solar cell involve electron-hole pair recombination and it is the conceptual picture used in all the mathematical descriptions of recombination that follow.

In a typical Si solar cell, recombination occurs in various regions of the cell (Figure 2.1):

1. The base or bulk region
2. The front emitter
3. The front surface

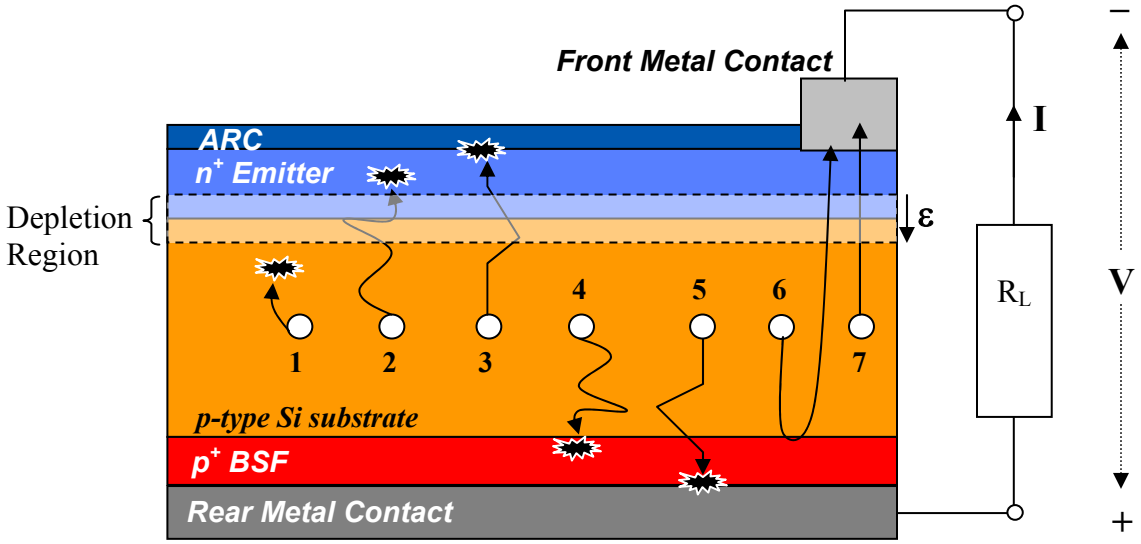

Figure 2.1 Schematic of a solar cell showing the common recombination regions in a Si solar cell (1-5), the direction of the electric field across the p-n junction and the preferred flow of minority carrier electrons (6-7).

4. The rear BSF (optional)
5. The rear surface

Recombination within the depletion region is relatively small in a well-made device and is not shown in Figure 2.1. Reducing recombination losses is an important goal of this thesis and in order to understand why, it is useful to examine basic solar cell operation.

2.1.1 Basic Solar Cell Operation

A solar cell is a device that is designed to generate an electrical current when it is illuminated. An electrical current is simply the flow of electrons and holes and these are generated in a semiconductor via absorption of light. However, when electron-hole pairs are photogenerated in a semiconductor slab, they move randomly through the lattice resulting in a net zero current flow. Creating a non-zero net current requires that the electrons/holes flow in a preferred direction and this achieved by forming a *p-n junction* or *diode* which is the most basic form of a solar cell.

The formation of the p-n junction results in an electric field, ε, being setup at the junction (Figure 2.1). Since electrons and holes are charged particles (negatively and positively charged respectively), they respond to this electric field with electrons being swept to the n-type region (as shown in Figure 2.1) and holes being swept to the p-type region (not shown). This flow of carriers across the p-n junction constitutes the *photocurrent* (I_L). The separation of charged carriers also creates a potential or voltage difference (V) across the solar cell diode called the *photovoltage*. This potential difference causes the photocurrent to flow through any external load connected to the cell, i.e. electrons flow out of the n-type side, through the external load and return to the hole-rich p-type side of the cell where it recombines with a hole.

The loss of photo-excited carriers via recombination hurts the process described above. Recombination in the base side of the depletion region (i.e. the wafer bulk, the BSF and the rear surface) results in carriers being lost before they cross the p-n junction thereby reducing the photocurrent. Recombination in the emitter side of the depletion region (i.e. the emitter bulk and the front surface) similarly results in minority carriers being lost before they can be separated and transferred to an external load.

Mathematically, the net current output of a solar cell, I, is given by

$$I = I_{Dark} - I_L = I_0(e^{\frac{qV}{nkT}} - 1) - I_L \tag{2.1}$$

where I_0 is called the *saturation current density* and n is the *ideality factor*. Note that the first term in Equation 2.1 (I_{Dark}) is simply the diode equation which describes the I-V relationship of a forward-biased diode. Physically, this dark current (I_{Dark}) is a *diffusion current* composed of electrons from the electron-rich n^+ emitter diffusing to the electron-poor p-type base. As the *drift current* of photogenerated carriers flows in the direction opposite to that of the dark diffusion current, it simply subtracts from the dark current according to the *superposition principle*. Graphically, the I-V curve of a solar cell is the diode I-V curve shifted down by the photocurrent, I_L (Figure 2.2). Note that the photo-

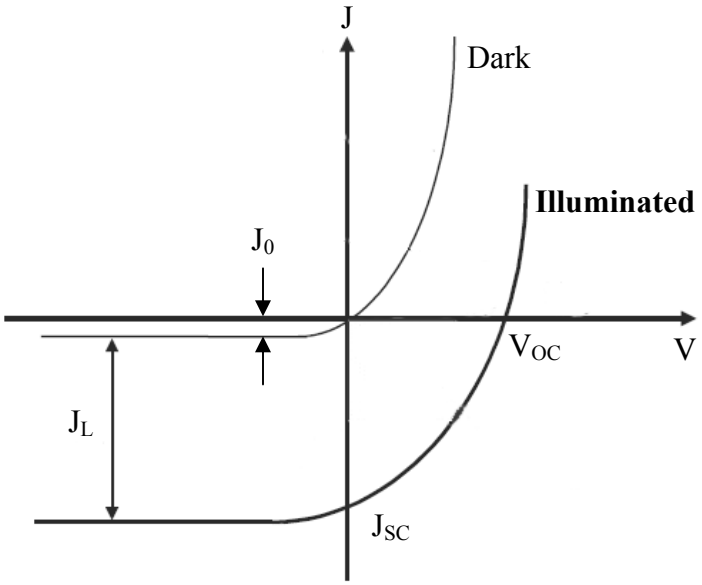

Figure 2.2 I-V characteristic of a solar cell in the dark and under illumination.

current is negative because the direction of current flow is, by definition, in the direction opposite to the flow of electrons. Conventionally however, the photocurrent in solar cells is written as a positive current and Equation 2.1 is also often written in terms of a current density, J (A/cm^2):

$$J = J_L - J_0(e^{\frac{qV}{nkT}} - 1) \tag{2.2}$$

The important operational modes of a solar cell are *open-circuit* – when there is no load connected to the cell – and *short-circuit* – when the two ends of the cell are short-circuited. Under short-circuit conditions, there is no potential drop/voltage difference across the device, i.e. V = 0 in Eq. 2.2. The second term in the equation therefore drops out and $J_{SC} \approx J_L$, is the maximum current output of the device.

Under open-circuit conditions, there is no external load and therefore no current flow, i.e. J = 0. Equation 2.2 can then be re-written as:

$$V_{OC} = \frac{nkT}{q} \ln(\frac{J_{SC}}{J_0} + 1) \tag{2.3}$$

Note that the discussion of the I-V characteristics has so far not included recombination. Physically, recombination of electron-hole pairs does not constitute a current. Mathematically however, recombination can be treated in the same way as the dark diffusion current, i.e. a *recombination current* that opposes the flow of the photocurrent. In the one-diode model of a solar cell given by Equations 2.1 and 2.2, both effects – the 'dark' diffusion current and recombination – are lumped into the single dark-current term

An increase in either the dark diffusion current or the recombination current increases J_0 and thus reduces both J_{SC} and V_{OC} (by equations 2.2 and 2.3). For an ideal diode, n = 1. In real devices, the ideality factor can be greater than 1. The ideal and non-ideal behaviors of real devices are often split up using the 2-diode model, with the I-V relationship being given by

$$J = J_L - J_{01}(e^{\frac{qV}{n_1 kT}} - 1) - J_{02}(e^{\frac{qV}{n_2 KT}} - 1) \tag{2.4}$$

where $n_1 = 1$ and J_{01} are the ideality factor and saturation current density of an ideal diode and J_{02} and n_2 represent the non-ideal diode. The 2nd diode is traditionally linked to recombination in the depletion region with $n_2 = 2$, but in real devices, n_2 is often greater than 2 due to various recombination phenomenon [17-19]. Three diode models have also been suggested for accurate modeling of lighted and dark I-V curves [19, 20].

It is clear from the discussion above that recombination results in a loss of both voltage and current and therefore reduces the efficiency, η, of a solar cell which is defined as

$$\eta = \frac{P_{out}}{P_{in}} = \frac{V_{OC}.J_{SC}.FF}{P_{in}} \tag{2.5}$$

where, P_{in} is the incident optical power (1000 W/m^2 for normalized AM1.5 illumination) and P_{out} is the electrical output power. Fill Factor (FF) is affected by V_{OC}, J_{SC} and electrical (series and shunt resistance) losses in the cell. An empirical mathematical model of how each affects the FF can be found in Ref. 21.

Experimentally, the *minority carrier lifetime*, τ, is used to quantify recombination losses within the silicon wafer. The lifetime is a statistical concept representing the amount of time an 'average' photo-excited electron survives before recombining and it is expressed in terms of a volume recombination rate (U) and the excess carrier concentration (Δn):

$$\tau \equiv \frac{\Delta n}{U} \tag{2.6}$$

where, typically, U is in units of cm^{-3}/s and Δn is in units of cm^{-3} and the lifetime is in units of seconds (s). There are three physical recombination mechanisms in a semiconductor:

1. Radiative Recombination
2. Auger Recombination
3. Recombination via defect states in the semiconductor band-gap (also called Shockley-Read-Hall or SRH recombination).

Surface recombination – which is caused by unsatisfied *dangling bonds* at the surface of a wafer – is treated as a special case of bulk SRH recombination applied to a two-dimensional surface. In practice, recombination occurs in all regions of a solar cell simultaneously. Experimental measurements therefore reflect an *effective recombination rate* and an *effective lifetime*, τ_{eff} (using equation 2.6):

$$U_{eff} = U_{bulk} + U_{emitter} + U_{front-surface} + U_{BSF} + U_{rear-surface} \tag{2.7}$$

$$\frac{1}{\tau_{eff}} = \frac{1}{\tau_{bulk}} + \frac{1}{\tau_{emitter}} + \frac{1}{\tau_{front-surface}} + \frac{1}{\tau_{BSF}} + \frac{1}{\tau_{rear-surface}} \tag{2.8}$$

Recombination in each region is effected by the radiative, Auger and SRH mechanisms and the following sections step through each of these.

2.1.2 Recombination Mechanisms

2.1.2.1 Radiative Recombination

Radiative recombination refers to the direct recombination of an electron and a hole as shown in Figure 2.3. It is the reverse of photogeneration process, with the energy of the electron being released as a photon.

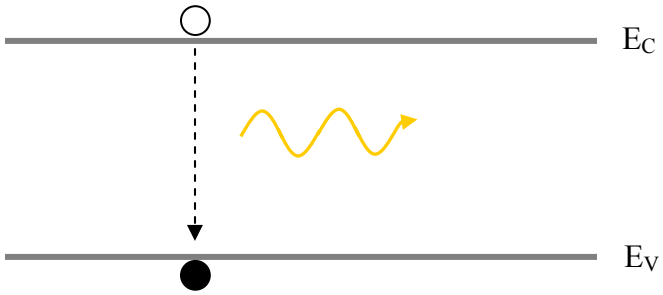

Figure 2.3 Energy band diagram illustrating radiative recombination.

The radiative recombination rate, U_{rad}, is given by:

$$U_{rad} = Bnp = B(n_0 + \Delta n)(p_0 + \Delta p) \tag{2.9}$$

where B is the radiative recombination coefficient and n and p are the electron and hole concentrations. n_0 and p_0 are the concentrations in the dark (due to doping) and Δn and Δp are the excess concentrations (generated by light in the case of a solar cell). Using Equations 2.6 and 2.9, the lifetime due to radiative recombination is:

$$\tau_{rad} = \frac{\Delta n}{B(n_0 + \Delta n)(p_0 + \Delta p)} \tag{2.10}$$

Under low level injection (LLI) conditions (where Δn, $\Delta p << n_0$, p_0) and high level injection (HLI) conditions (where Δn, $\Delta p >> n_0$, p_0), equation 2.10 simplifies to:

$$\tau_{rad,LLI} = \frac{1}{BN_{Doped}} \qquad \tau_{rad,HLI} = \frac{1}{B\Delta n} \tag{2.11}$$

where N_{Doped} is the electron/hole concentration due to doping, typically written as N_D and N_A for donor and acceptor dopants respectively.

Radiative recombination is not significant in silicon due to the fact that silicon is an indirect semiconductor, which means that the bottom of the conduction and valance bands do not line up in k-space (momentum). As recombination requires that both energy and momentum be conserved, radiative recombination in Si requires the participation of a phonon of the right momentum. This extra requirement reduces the probability of radiative recombination and is reflected in the low value of $B = 9.5 \times 10^{-15}$ cm^3/s measured for silicon [22].

2.1.2.2 Auger Recombination

Auger recombination is a phenomenon in which the energy lost by a recombining electron is transferred to a third electron or hole which gets kicked higher up in the conduction or valence band as shown in Figure 2.4.

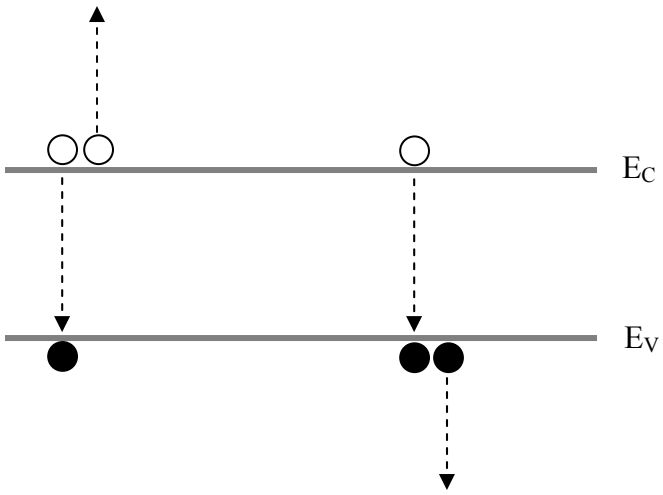

Figure 2.4 Energy band diagram illustrating the Auger recombination process.

The total Auger recombination rate is the sum of the recombination rates of the two-electron process and the two-hole process, U_{eeh} and U_{ehh}:

$$U_{Auger} = U_{eeh} + U_{ehh} = C_n n^2 p + C_p n p^2 \tag{2.12}$$

where C_n and C_p are the respective Auger coefficients. Using Equations 2.6 and 2.12, the Auger lifetimes under low- and high-level injection for n- and p-type silicon are

$$\tau_{Auger,LLI} = \frac{1}{C_n N_D{}^2} \qquad \tau_{Auger,HLI} = \frac{1}{(C_n + C_p)\Delta n^2} \qquad \textbf{(for n-type Si)} \tag{2.13}$$

$$\tau_{Auger,LLI} = \frac{1}{C_p N_A{}^2} \qquad \tau_{Auger,HLI} = \frac{1}{(C_n + C_p)\Delta p^2} \qquad \textbf{(for p-type Si)} \tag{2.14}$$

where the various symbols have their usual meanings. The most widely used Auger coefficients are those Dzeiwior and Schmid: $C_n = 2.8 \times 10^{-31}$ cm^6/s and $C_p = 9.9 \times 10^{-32}$ cm^6/s for silicon with dopant concentration greater than 5×10^{18} cm^{-3} [23]. These are also the values used by PC1D.

A comparison of Equations 2.11, 2.13 and 2.14 clearly shows that Auger recombination is much stronger in heavily doped silicon than radiative recombination – the Auger lifetime decreases as the square of the dopant concentration while the radiative lifetime decreases linearly with doping concentration. Auger recombination is therefore the dominant mechanism in solar cell emitters and back surface fields. It is also worth noting that values of the two Auger coefficients, C_n and C_p, show that Auger recombination in heavily doped n-type Si is roughly three times stronger than in p-type silicon. P-type cells, which have n-type emitters, are therefore more affected by Auger recombination.

Experimentally, the Auger recombination rate has been reported by several authors to be higher than that calculated by Dzeiwior and Schmid, which is thought to be a result of Coulombic interactions between the charged particles and other effects. The most recent results of Kerr and Cuevas [24] provide somewhat different expressions for the Auger

lifetime, but preserve the conclusions that the Auger recombination process is dominant over radiative recombination in heavily doped silicon and that it is three times more effective in heavily doped n-type silicon. These revised expressions are valid for dopant concentrations greater than $5x10^{15}$ cm^{-3}:

$$\tau_{Auger,LLI} = \frac{1}{1.8x10^{-24} N_D^{1.65}} \qquad \textbf{(for n-type Si)} \qquad (2.15)$$

$$\tau_{Auger,LLI} = \frac{1}{6x10^{-25} N_D^{1.65}} \qquad \textbf{(for p-type Si)} \qquad (2.16)$$

2.1.2.3 Shockley-Read-Hall (SRH) Recombination

The presence of defect states in the semiconductor bandgap can greatly enhance the probability of recombination by allowing an excited electron to lose energy in small increments (Figure 2.4) instead of in a single large step as in the case of radiative and Auger recombination. Such defect states are created by both impurities and crystal defects in a semiconductor lattice. Under 1-Sun illumination, SRH recombination is the dominant mechanism in the base or bulk region of solar cells fabricated on defective material (such as multicrystalline silicon) or material that is contaminated with impurities.

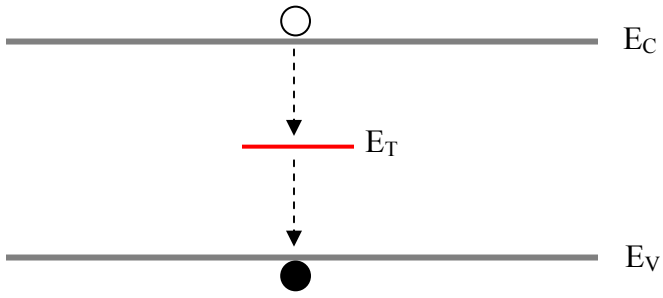

Figure 2.5 Energy band diagram illustrating recombination through a defect level in the bandgap.

These defects and impurities typically limit the SRH lifetime of commercially-used Czochralski (Cz) or multi-crystalline Si substrates to a few hundred microseconds or less. In contrast, the Auger-limited lifetime on typical wafer resistivities (≥ 0.6 Ω-cm) is over 1 ms using either the Dzeiwior and Schmid model or the Kerr model. SRH recombination often dominates in the bulk even for high quality material grown using the float-zone (FZ) method due to the introduction of defects and/or impurities during solar cell processing.

The recombination rate due to defect levels in the bandgap was first analyzed by Shockley and Read and Hall for a single defect level [25, 26]:

$$U_{SRH} = \frac{np - {n_i}^2}{\tau_{p0}(n + n_1) + \tau_{n0}(p + p_1)} \tag{2.17}$$

where τ_{n0} and τ_{p0} are the electron and hole lifetimes, which are related to the thermal velocity (v_{th}), the trap density (N_T), and the capture cross-section for electrons (σ_n) and holes (σ_p):

$$\tau_{n0} = \frac{1}{\sigma_n N_T v_{th}} \qquad \tau_{p0} = \frac{1}{\sigma_p N_T v_{th}} \tag{2.18}$$

The capture cross-sections are related to the probability of a defect state capturing an electron or a hole. n_1 and p_1 relate to the filling of the trap level with carriers, and are given by:

$$n_1 = n_i \exp(\frac{E_T - E_i}{kT}) \qquad p_1 = n_i \exp(\frac{E_i - E_T}{kT}) \tag{2.19}$$

where n_i and E_i are the intrinsic carrier concentration and the intrinsic energy level respectively, T is the temperature and k is the Boltzmann constant.

Using Equation 2.6, the SRH lifetime is then given by

$$\tau_{SRH} = \frac{\tau_{p0}(n + n_1) + \tau_{n0}(p + p_1)}{n_0 + p_0 + \Delta n} \tag{2.20}$$

where the symbols have their usual meanings. It can be seen from Equation 2.20 that the SRH lifetime depends on both the dopant level, the injection level and defect-specific properties like the capture cross-section and the defect energy level. The SRH lifetime under LLI and HLI conditions simplifies to

$$\tau_{SRH,LLI} = \tau_{p0} + \frac{\tau_{n0}(p_1 + \Delta n)}{N_D} \qquad \tau_{SRH,HLI} = \tau_{n0} + \tau_{p0} \quad \textbf{(for n-type Si)} \qquad (2.21)$$

$$\tau_{SRH,LLI} = \tau_{n0} + \frac{\tau_{p0}(n_1 + \Delta n)}{N_A} \qquad \tau_{SRH,HLI} = \tau_{n0} + \tau_{p0} \quad \textbf{(for p-type Si)} \qquad (2.22)$$

An important conclusion that follows from Equations 2.21 and 2.22 is that the SRH lifetime at LLI can be either approximately constant (the first term in the LLI equations) or increase with the injection level (the second term in the LLI equation) depending on the capture cross-section ratio and the energy level of the defect state. This relationship between the injection-level-dependent SRH lifetime and the properties of a defect can be used to identify the defect species in Si and is discussed in more detail in Chapter 8 for the case of Fe contamination of Si.

A second important conclusion is that defects close to the middle of the band (known as *recombination centers)* are the most effective recombination sites. For such deep defects, n_1 and p_1 become very small and the second term in the LLI equations drops out.

$$\tau_{SRH,LLI} = \tau_{p0} \quad \textbf{(for n-type Si)} \qquad (2.23)$$

$$\tau_{SRH,LLI} = \tau_{n0} \quad \textbf{(for p-type Si)} \qquad (2.24)$$

The HLI equations remain unchanged which means that the SRH lifetime also increases with injection level for deep defects.

2.1.2.4 Surface Recombination

Surface recombination can be treated as an extension of the bulk SRH mechanism applied to the two-dimensional surface, featuring a surface recombination rate, U_S in

Figure 2.6 Energy band diagram illustrating surface recombination through surface defect states in the bandgap.

units of cm^{-2}/s and a surface recombination velocity, S, in units of cm/s which is defined as:

$$S = \frac{U_S}{\Delta n_S} \tag{2.25}$$

where Δn_S is the excess carrier concentration at the surface. For a single surface state, the recombination rate is given by

$$U_S = \frac{n_s p_s - {n_i}^2}{\frac{n_s + n_1}{S_{p0}} + \frac{p_s + p_1}{S_{n0}}} \tag{2.26}$$

where n_s and p_S are the surface carrier concentrations and S_{p0} and S_{n0} are the characteristic surface recombination velocities for electrons and holes which are given by

$$S_{n0} = \sigma_n N_{ST} v_{th} \tag{2.27}$$

$$S_{p0} = \sigma_p N_{ST} v_{th} \tag{2.28}$$

N_{ST} is the density of surface states and the other symbols have their usual meanings from bulk SRH theory.

From the definition of surface recombination velocity (equation 2.25), we have:

$$S = \frac{n_o p_0 + \Delta n_S}{\frac{n_s + n_1}{S_{p0}} + \frac{p_s + p_1}{S_{n0}}} \tag{2.29}$$

for a single surface defect level. In practice, the wafer surface has a large number of surface states at various energy levels. The total surface recombination rate is calculated by integrating over the entire bandgap:

$$U_S = \int_{E_V}^{E_C} \frac{n_s p_s - {n_i}^2}{\frac{n_s + n_1(E)}{\sigma_p(E)} + \frac{p_s + p_1(E)}{\sigma_n(E)}} v_{th} D_{it}(E) dE \tag{2.30}$$

Where D_{it} is the surface trap density per unit energy (cm^{-2}/eV) and substitutes for N_{ST} used in the single defect level version for U_S.

It is clear from equation 2.29 and 2.30 that recombination at a surface requires the presence of all of the following – electrons, holes and the defect states which mediate the recombination process. Reduction in one or more of these three results in reduced surface recombination. In practice, this is achieved by *field effect passivation* and *interface passivation* (which is also called *chemical passivation*):

1. Field-effect passivation works by reducing the concentration of either electrons or holes at the surface by using an electric field that repels one or the other from the surface. This electric field can be set up either using a charged surface dielectric, and/or by doping the surface (Figure 2.7). The type of carrier – electron or hole – that is repelled depends on the dopant type and dielectric charge polarity. Field effect passivation of the rear surface of p-type cells is typically achieved with a p^+-doped surface layer called the back surface field (BSF) and/or a negatively charged dielectric; both of which repel minority carrier electrons from the rear surface. (Figure 2.6). Both heavier doping and a higher dielectric charge density result in a stronger surface electric field and steeper band-bending which enhances field effect passivation. While using a positively charged dielectric to

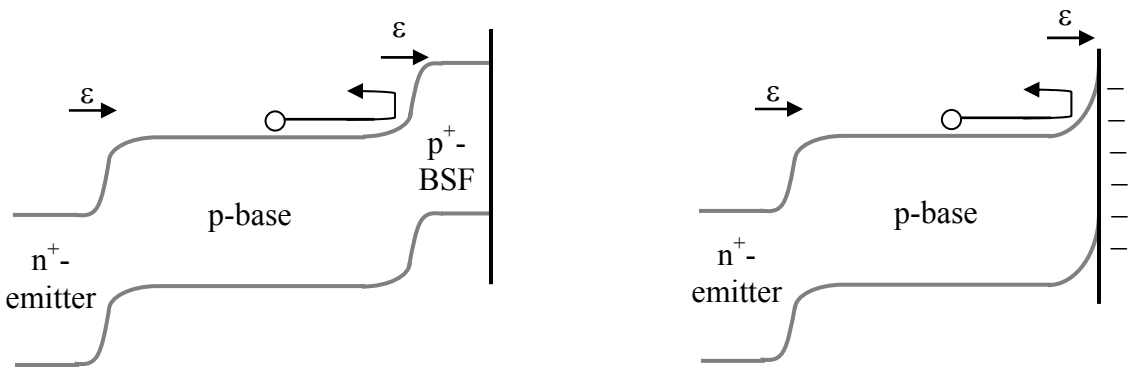

Figure 2.7 Band-diagrams illustrating the electric field and band-bending caused by (a) p^+-BSF doping and (b) a negatively charged dielectric and its effect on electron flow.

push holes away from the surface can have the same effect on S as a negatively charged surface dielectric, it increases the risk of *parasitic shunting* [19].

2. Interface passivation involves reducing the density (D_{it}) and/or capture cross-sections of surface defect states. In practice, this is achieved by depositing dielectrics that are can satisfy the dangling bonds at the wafer surface.

In real devices, both field-effect and interface passivation co-exist to varying extents depending on the structure used. Thermal oxide (SiO_2), for example, is commonly used to reduce the density of defect states (D_{it}) at the Si surface, but also has a positive charge density on the order of 10^{11} cm^{-2} [27]. High efficiency solar cells typically use both passivation methods. For example, the record-high efficiency of 25% was achieved with the PERL (passivated emitter rear locally contacted) structure which has both high quality rear SiO_2 passivation and localized B-BSF regions under rear point contacts [28].

2.1.3 Emitter Recombination

Before going through a discussion on emitter recombination, it is important to note that the term 'emitter recombination' is often used to denote recombination in any heavily doped region (i.e. $N_{emitter} >> N_{base}$), regardless if it is the heavily doped region of

a p-n junction (i.e. the emitter) or a BSF. In the following discussion, the term 'emitter' refers to both the emitter side of the p-n junction and to the BSF.

Emitter recombination is a complex phenomenon which is affected by multiple physical processes. It is therefore common to measure an *effective emitter recombination velocity* (S_{eff}) which includes the combined effects of all these processes including SRH and Auger recombination in the spatially non-uniform emitter, bandgap narrowing (BGN - which increases n_i within the emitter), as well as recombination at the emitter surface. For the BSF of a p-type cell, S_{eff} is defined at the p/p^+ interface (S_{p/p^+}) and for the emitter of a p-type cell, it is defined at the n^+/p interface ($S_{n^+/p}$) as shown in Figure 2.8. The effective recombination can also be characterized as a minority carrier recombination current, J_{rec} [29]

$$J_{rec} = J_{0E}\left(\frac{np}{n_{i^2}} - 1\right) \tag{2.31}$$

where n and p are the electron and hole concentrations at the interface. As any current density is simply the product of the electron charge and the electron recombination/generation rate, the emitter recombination current can also be written as

$$J_{rec} = qU_S \tag{2.32}$$

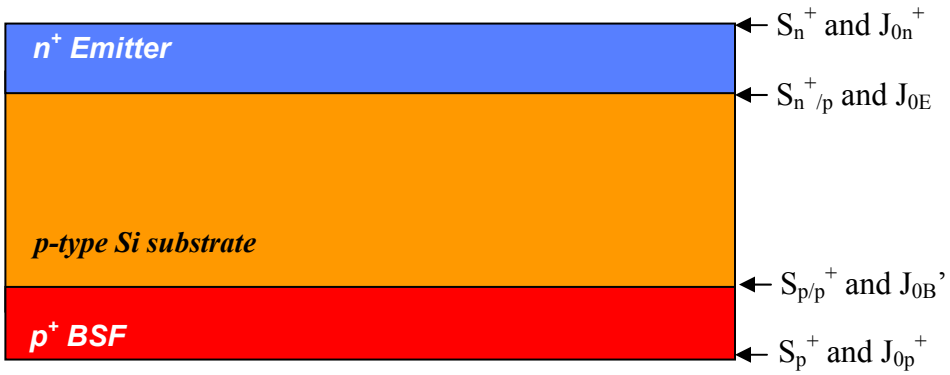

Figure 2.8 Schematic showing the interfaces at which effective recombination of heavily diffused surfaces is measured.

Using the definition of surface recombination rate (equation 2.25), and equations 2.31 and 2.32 we get

$$S_{eff} = \frac{U_S}{\Delta n} = \frac{J_{rec}}{q\Delta n} \tag{2.33}$$

For a p-type cell, this simplifies to

$$S_{eff} = \frac{J_{0E}(N_A + \Delta n)}{qn_i^2} \tag{2.34}$$

where N_A is the dopant density of the p-type base. Depending on whether the base is at high or low-level injection, either the N_A or the Δn term drop out. Note that, like S_{eff}, the value of J_{0E} is affected both by surface recombination and bulk emitter recombination.

J_{0E} can be experimentally measured using the transient photoconductive decay (transient PCD) method of Kane and Swanson [29]. If both J_{0E} and the emitter doping profile are known, the effect of recombination at the doped surface (S_n^+ or S_p^+) and recombination in the emitter bulk on J_{0E} can be separated using computer modeling. It should be noted that the value of S_n^+ or S_p^+ extracted from such computer modeling depends heavily on the physical models used to account for the Auger, SRH and BGN processes that affect emitter recombination. As discussed in Section 2.1.2.2, there are multiple physical models for Auger recombination. There are also multiple values for n_i and multiple BGN models [30-34]. In this thesis, PC1D and the models/values for Auger recombination, BGN and n_i implemented therein are used to calculate S at passivated emitter surfaces from J_{0E} measurements. Details on how PC1D is used for this purpose are given in Chapters 4 and 7 which discuss, respectively, passivation of phosphorous and boron emitters.

2.2 Optical Losses in a Semiconductor

The major optical losses in a typical silicon solar cell are summarized in Figure 2.9 showing:

1. Reflection at the front surface.
2. Parasitic absorption in anti-reflection coatings.
3. Parasitic free carrier absorption in heavily doped regions.
4. Parasitic absorption at the rear surface
5. Escape reflection from the cell interior.

Each of these mechanisms serves to reduce photogeneration and thus J_{SC} and V_{OC} (Equations 2.2 and 2.3). Reducing these losses is an important part of cell design and reduction of parasitic absorption at the rear surface is the focus of Chapter 9 of this thesis.

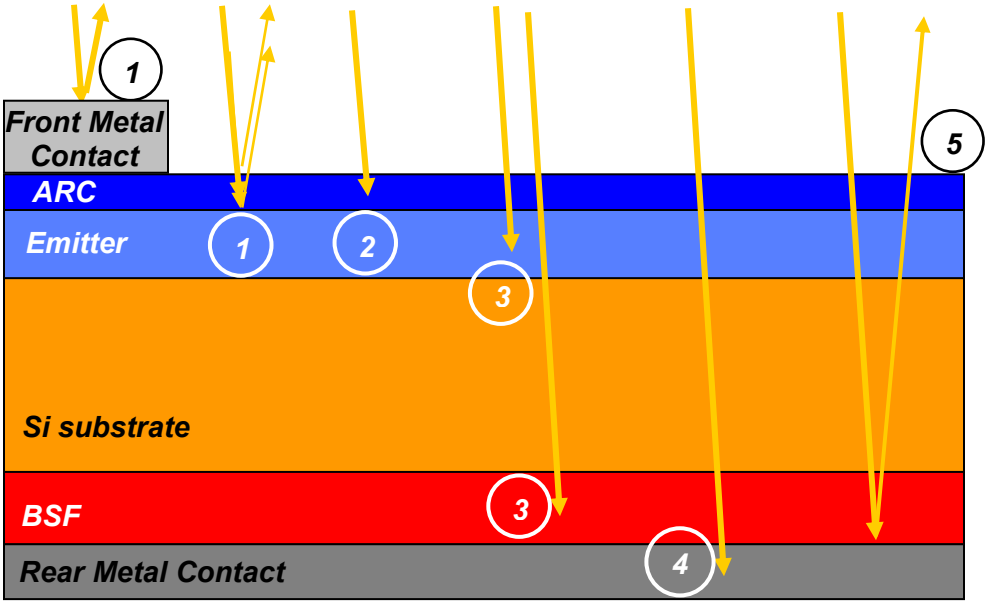

Figure 2.9 Schematic showing optical loss mechanisms in a silicon solar cell – 1) front surface reflection, 2) parasitic absorption in anti-reflection layer(s), 3) free carrier absorption in heavily doped regions, 4) absorption at the rear surface/rear contact and 5) escape reflectance. The arrows indicate light rays (refraction is ignored for simplicity).

2.2.1 Front Surface Reflection

The cumulative photocurrent density (J_L in A/cm^2) in a solar cell is given by

$$J_L = qG_L \tag{2.35}$$

where q is the electron charge and G_L is the cumulative generation rate in cm^{-2}.s^{-1}. Fewer photons entering the cell translate into reduced generation and thus a lower the photocurrent and (via Equation 2.3) a lower V_{OC}. Reduction of front surface reflection is therefore a very important element of solar cell design.

For a planar Si wafer in air, the reflectance at the Si surface for normally or near-normally incident light is given by the Fresnel equation [35]

$$R = \frac{(n_2 - n_1)^2 + k^2}{(n_2 + n_1)^2 + k^2} \tag{2.36}$$

where n_1 and n_2 are the refractive indices of air and Si respectively and k is the extinction co-efficient for Si. Due to the high index of Si (n > 3.5) over the wavelength range of interest (typically 300-1200 nm), the reflectance for bare silicon surface in air is very high (> 30%) as shown in Figure 2.10. This high surface reflectance can be reduced through the use of anti-reflection coatings (ARCs) and/or surface texturing.

For a planar wafer in air coated with a single, non-absorbing ARC (i.e. k = 0), the surface reflectance is given by [35]:

$$R = \frac{n_1^2 (n_1 - n_2)^2 Cos^2\theta + (n_0 n_2 - n_1^2)^2 Sin^2\theta}{n_1^2 (n_1 + n_2)^2 Cos^2\theta + (n_0 n_2 + n_1^2)^2 Sin^2\theta} \tag{2.37}$$

where n_0, n_1 and n_2 are the refractive indices of air, ARC and Si respectively and θ (the phase difference of the reflected rays) is given by

$$\theta = \frac{2\pi . n_1 d}{\lambda} \tag{2.38}$$

where d is the thickness of the ARC. If the thickness of the ARC is properly chosen, light reflected at the air/ARC interface and at the substrate/ARC interface (Figure 2.9) interfere destructively thereby reducing reflectance.

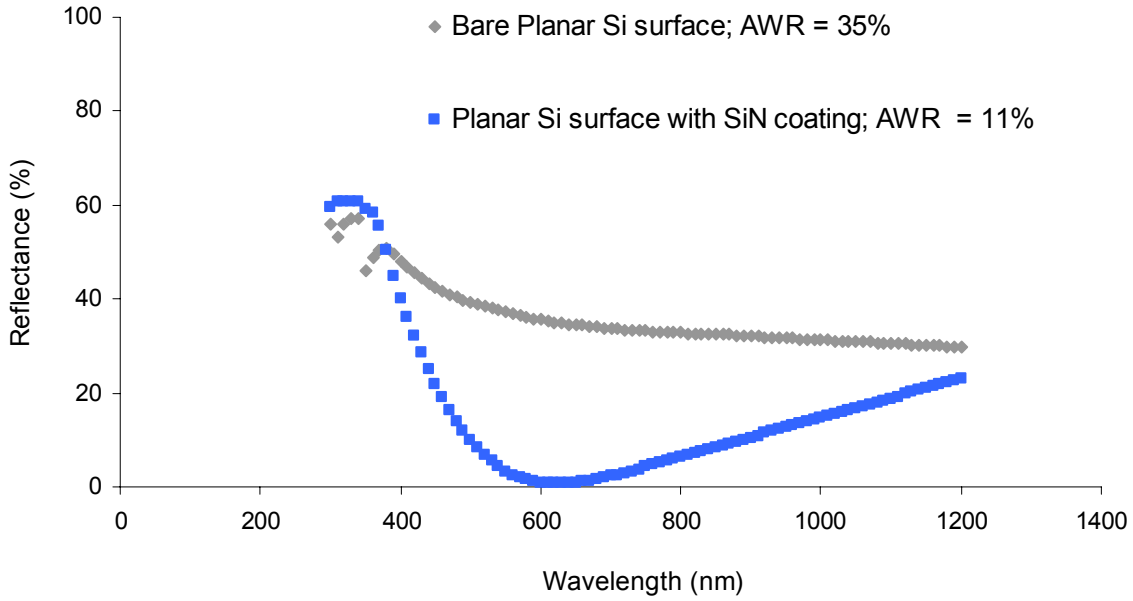

Figure 2.10 Reflectance of planar Si wafers in air with and without an anti-reflection SiN_X (n = 2.03 @ 600 nm) coating deposited at Georgia Tech. The long wavelength portion beyond 1000 nm is obtained via extrapolation.

For a given wavelength, λ, the reflectance becomes zero if the ARC meets the conditions

$$n_1 d = \frac{\lambda}{4} \tag{2.39}$$

$$n_1 = \sqrt{n_0 n_2} \tag{2.40}$$

ARCs that satisfy these conditions are sometimes referred to as *quarter wave* coatings. Generation in Si solar cells is maximized by minimizing the reflectance at 600 nm, which is close to the peak of the AM1.5 spectrum. For Si solar cells, thermal SiO_2 (n ~ 1.46 @ 600nm) and SiN_X (n ~ 2 @ 600 nm) are the most common ARC dielectrics due to their ability to passivate the silicon surface. As shown in Figure 2.10, a SiN_X layer (n = 2.03 at 600 nm) can reduce the average weighted reflectance (AWR) of a planar Si surface from ~ 35% to ~11%.

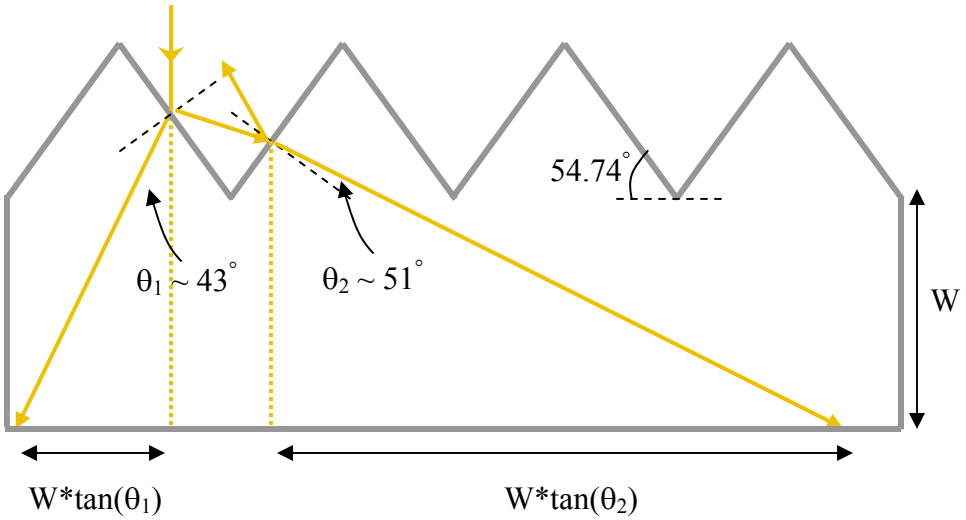

Figure 2.11 Ray diagram of normally incident light on a pyramid textured surface for λ ~ 600 nm. The gold dotted lines show the ray-paths without surface texturing (i.e. a planar surface). W is the wafer thickness.

Reflection can also be reduced by texturing the surface such that an incident ray strikes the surface at least twice (Figure 2.11). Random pyramid texturing is the most common industrial method for texturing the surface of a <100> single-crystal Si wafer and is the method used in this thesis. Even without an ARC, the double-strike reduces the average weighted reflectance down to ~11% (Figure 2.12). Using both pyramid texturing and a single layer SiN_X (n = 2.03 @ λ = 600 nm) ARC, the reflectance drops to ~4%.

A second benefit of surface texturing is that refraction at the front surface (Figure 2.11) increases the optical path length from W (the wafer thickness) to W/cos(θ) (~1.4 and ~1.6 times the wafer thickness for the first and second bounce rays respectively). This increased path length improves the absorption of long-wavelengths that are weakly absorbed in silicon. The enhancement in the path length can be further improved if the back surface is reflective as discussed in Sections 2.2.4 and 2.2.5.

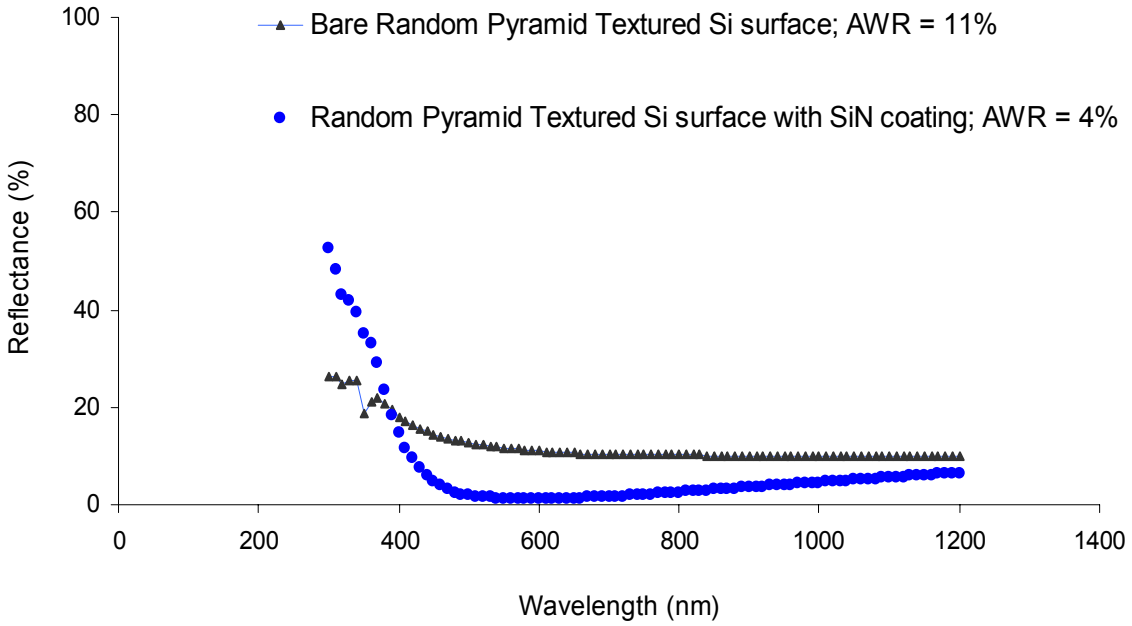

Figure 2.12 Reflectance of random pyramid textured Si wafers in air with and without an anti-reflection SiN_X (n = 2.03 @ 600 nm) coating deposited at Georgia Tech. The long wavelength portion beyond 1000 nm is obtained via extrapolation.

2.2.2 Parasitic Absorption in Anti-reflection Coatings

Absorption of light passing through a material is described by the Beer-Lambert law

$$I(x) = I_0 e^{-\alpha . x} \tag{2.41}$$

where I_0 is the intensity of incident light, I(x) is the intensity of light in the absorbing material at depth x, and α is the absorption coefficient which is a function of the imaginary part of the complex refractive index or *extinction coefficient*, k, of a material

$$\alpha = \frac{4\pi k}{\lambda} \tag{2.42}$$

The most common ARC materials used for Si solar cells, SiO_2 and SiN_X, have negligible to low absorption as their extinction coefficients are zero or nearly so over the 300-1200nm wavelength range [36]. Alternate AR coatings such as Indium Tin Oxide (ITO), ZnO and SiCN do however show appreciable absorption [37-40].

2.2.3 Free Carrier Absorption

Free carrier absorption (FCA) refers to an intraband process where carriers are excited to higher energy levels within the conduction or valance band, instead of being excited from the valence to the conduction band. As this does not cause any additional electron-hole pair generation, the FCA process does not contribute to the photocurrent and the absorbed energy is instead lost as heat.

The FCA process is significant only in heavily doped regions such as emitters and is observed as an enhanced absorption of long-wavelength light (compared to absorption in intrinsic or lightly doped silicon) [41]. In PC1D, this enhanced absorption is modeled as

$$\alpha_{FCA} = 2.6x10^{-27} n\lambda^3 + 2.7x10^{-24} p\lambda^2 \tag{2.43}$$

Where λ is wavelength in nm. Other values for the coefficients and wavelength exponents have also been reported [41]. Though FCA is a an undesirable process, PC1D simulations have previously been used to show that FCA in emitters has a much smaller impact on current loss than Auger recombination and BGN in emitters [42].

2.2.4 Rear Reflectance/Absorption

Figure 2.13 shows the absorption coefficients of Si as a function of wavelength. The weak absorption of Si wavelengths close to and beyond the optical band-edge of Si at ~1100 nm (1.12 eV) means that Si wafers need to be fairly thick to completely absorb, in a single pass, light in the 850-1200 nm range which holds nearly 25% of the optical energy in the AM 1.5 spectrum (Figures 2.14 and 2.15). But if the rear of a cell features a back surface reflector with 100% reflectance, the same amount of absorption can be achieved with half the wafer thickness as the back reflector will result in long-wavelength light making at least two passes through the cell as shown in Figure 2.9.

In practice, BSRs have reflectances < 100% due to parasitic absorption. In high-efficiency cells, parasitic absorption by the back surface reflector (BSR) is minimized by

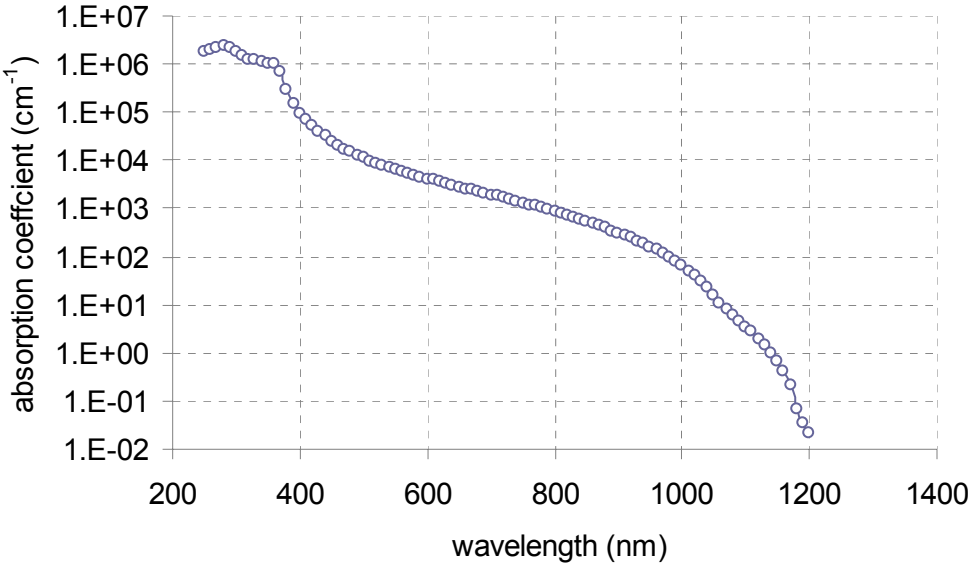

Figure 2.13 Absorption coefficient of silicon [44].

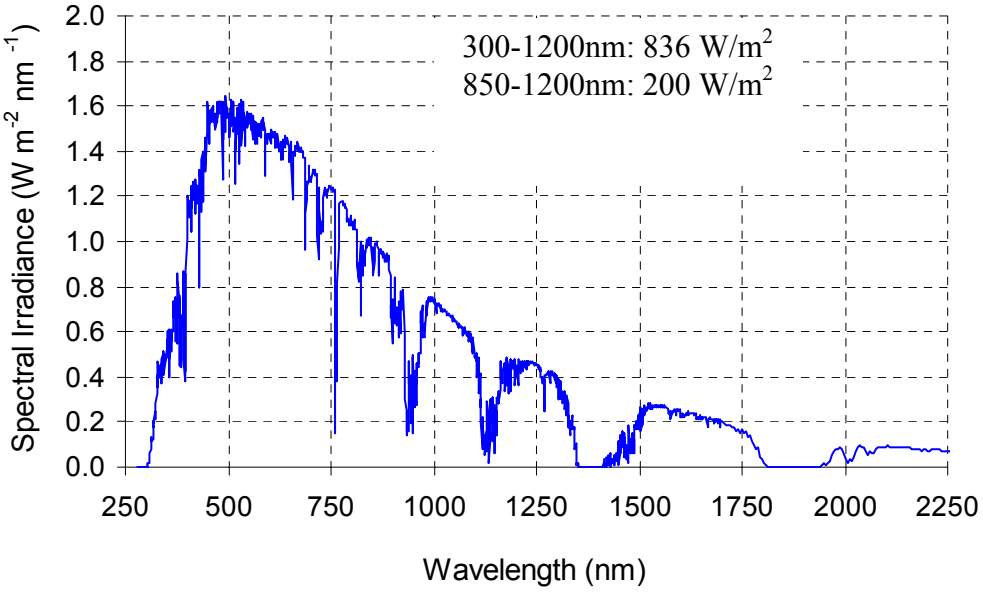

Figure 2.14 AM 1.5G (IEC 60904-3) spectrum [45]. The inset shows the cumulative power over selected wavelength ranges.

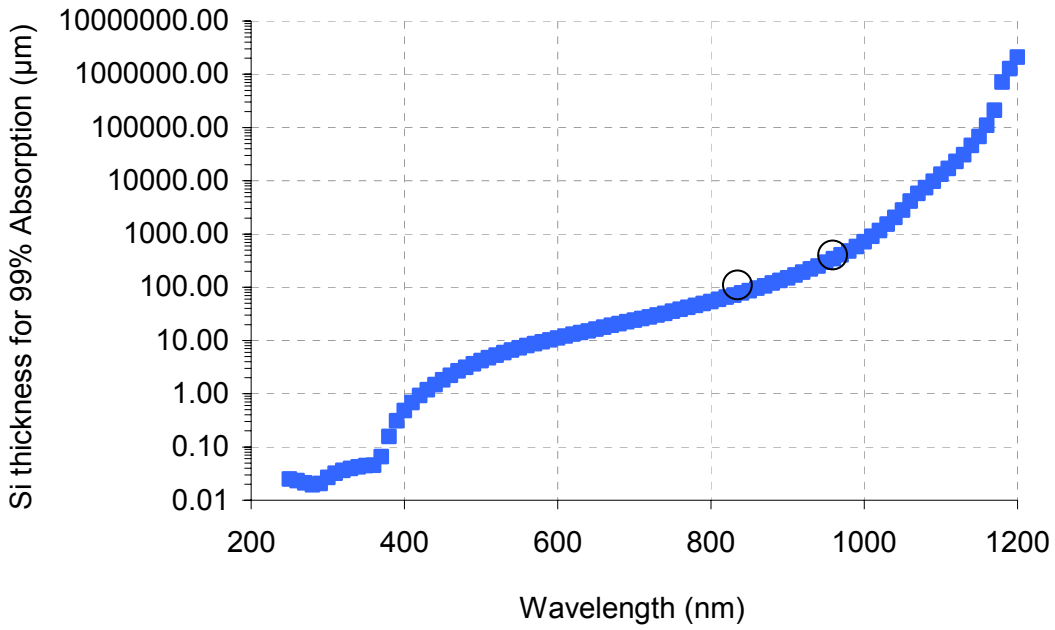

Figure 2.15 Thickness of Si wafer required to absorb 99% of light in a single pass as a function of wavelength. The circles show that a 50 µm thick and a 200 µm thick wafer will absorb 99% of light only up to wavelengths of 800 nm and 950 nm respectively [44].

using pure, evaporated metals such as silver and aluminum which have reflectances > 90% at such long-wavelength. For example, the record-high 25%-efficient PERL cell uses an evaporated Al layer as the BSR and as the rear contact [28]. Cheaper screen-printed pastes used in commercial silicon solar cells can have much greater parasitic absorption. This is discussed in detail in Chapter 9 of this thesis which compares several BSR materials and examines their effect on cell performance.

2.2.5 Light Trapping and Escape Reflectance

The effectiveness of a BSR depends not just on how reflective it is, but also on the angular distribution of the reflected light. For a device with a planar front surface, a BSR with specular or mirror-like reflectance will couple light out of the cell after just one

bounce (Figure 2.16), i.e. the *optical path length enhancement* due to a specular BSR is just ~2. The path length enhancement can be much greater if the rear reflectance (R_B) is diffuse as it promotes *light-trapping* via multiple total internal reflections of light within a cell as shown in Figure 2.16. Yablanovitch had shown that the limit to path length enhancement is achieved when the angular distribution of light inside a cell is completely randomized [48, 49]. At the limit of 100% diffuse rear reflectance, the number of passes a ray of light makes through a cell is $2n^2$ or ~ 25 for Si instead of just 2 as in the case of a specular BSR. Due to the longer path length of the oblique rays, the absorption enhancement is even greater at $4n^2$ or ~50 in Si for weakly absorbed light. Note that this enhancement limit takes into account the fact that even when light is reflected by a perfectly diffuse or *Lambertian* reflector, ~8% of it falls within a *loss cone* and is 'effectively specular' as it does not meet the critical angle (θ_c) required for total internal reflection (Figure 2.16) [50] .

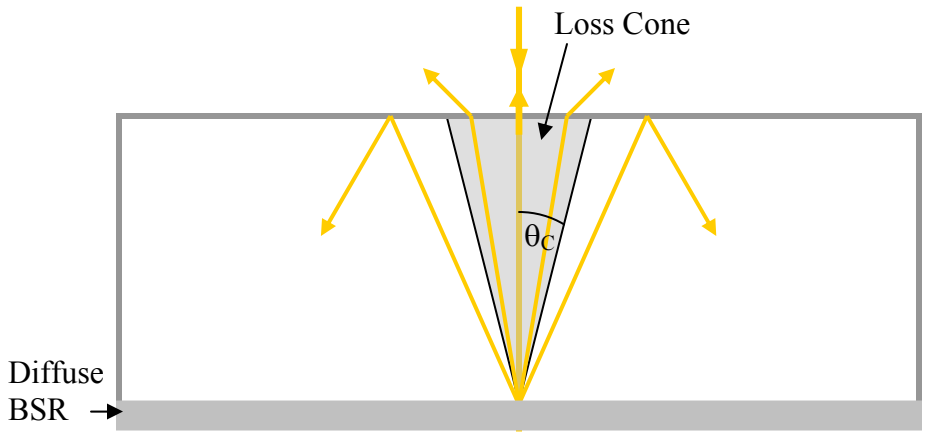

Figure 2.16 Ray diagram illustrating light-trapping and the loss-cone for diffuse rear reflectors.

2.3 Summary

In this chapter the principal electronic and optical loss mechanisms in solar cells have been discussed. In typical Si solar cells, the most prominent electronic loss mechanisms are bulk SRH recombination, emitter Auger recombination and surface recombination, while front reflectance and rear surface absorption are the major optical loss mechanisms. In the following chapter, a high-efficiency Al-BSF cell is fabricated and analyzed in order to quantify these loss mechanisms and their impact of cell efficiency.

Chapter 3

IDENTIFYING A PATHWAY TO 20% EFFICIENT SCREEN-PRINTED CELLS VIA FABRICATION AND CHARACTERIZATION OF SCREEN-PRINTED AL-BSF SOLAR CELLS

As discussed in Chapter 1, solar cells suffer from multiple losses which limit their efficiency. The first task in this thesis involved fabricating a high-efficiency screen-printed Al-BSF cell, quantifying the various loss parameters of the cell via computer modeling, and then identifying one or more sets of improved cell parameters that can lead to a 20% efficient screen-printed cell.

3.1 Experimental

All cells were made on 1.3 ohm-cm FZ wafers which were textured on one side. After cleaning, the wafers were $POCl_3$–diffused followed by an HF dip to remove the phosphosilicate glass and an oxidation at 900°C for 10 minutes followed by a 15 minute N_2 anneal at the same temperature. An anti-reflective SiN_X coating was then deposited on the front (textured) side using a LF-PECVD reactor followed by metallization via screen-printing. An Al paste (Ferro FX 53-038) was printed on the rear (planar) side and dried at 200°C followed by gridline printing of a silver paste (Heraeus 8969) on the front (textured) side and a second drying at 200°C after each print. The samples were then co-fired at a peak firing temperature of ~740°C. The front grid pattern defined 9 cells on each wafer and each cell was electrically isolated using a dicing saw followed by a forming gas anneal to reduce the series resistance of the cells.

The emitter was characterized using saturation current density (J_0) measurements on planar and textured $n^+/n/n^+$ samples fabricated on 500-700 ohm-cm FZ wafers. The measurements were performed using the transient PCD method of Kane and Swanson

[29]. The emitter doping profile was measured at NREL with secondary ion mass spectroscopy (SIMS) using a Cameca IMS-5F system. Though the SIMS method measures the total dopant concentration, the sheet resistance calculated from the profile using trapezoidal integration was within 5% of four-point-probe measurements of the emitter which indicates complete or near-complete ionization of the dopants. The surface recombination velocity, S_n^+, was then extracted using PC1D by importing the SIMS emitter profile into PC1D to create an n^+/p junction. The junction was forward-biased at 0.4 V, and the simulated minority carrier current density (J_p) at the depletion edge in the emitter was converted to a J_{0e} value using:

$$J_p = J_{0e} e^{\frac{qV}{kT}} \tag{3.1}$$

where V is the applied DC bias (0.4 V). The S_n^+ input in PC1D was then iteratively changed till the modeled J_{0e} at the depletion edge *in the emitter* matched the measured J_{0e}. Note that the calculated J_{0e} at the depletion edge *in the base* can also be used; the J_{0e} at both depletion edges is nearly identical as recombination within the depletion region is small. Therefore, the choice of junction edge for matching simulated and experimental J_{0e} values has a very small effect on the extracted S_n^+ values.

The bulk lifetime of completed cells was measured using the quasi-steady-state photoconductance (QSS-PC) method [51] after etching down the wafers to the bulk, followed by wafer cleaning and surface passivation with an iodine/methanol solution.

3.2 Results

3.2.1 Emitter Characterization

Figure 3.1 shows the SIMS profile of the phosphorous emitter which has a surface concentration of ~7.6×10^{19} cm^{-3} and a metallurgical junction depth of ~0.5 μm.

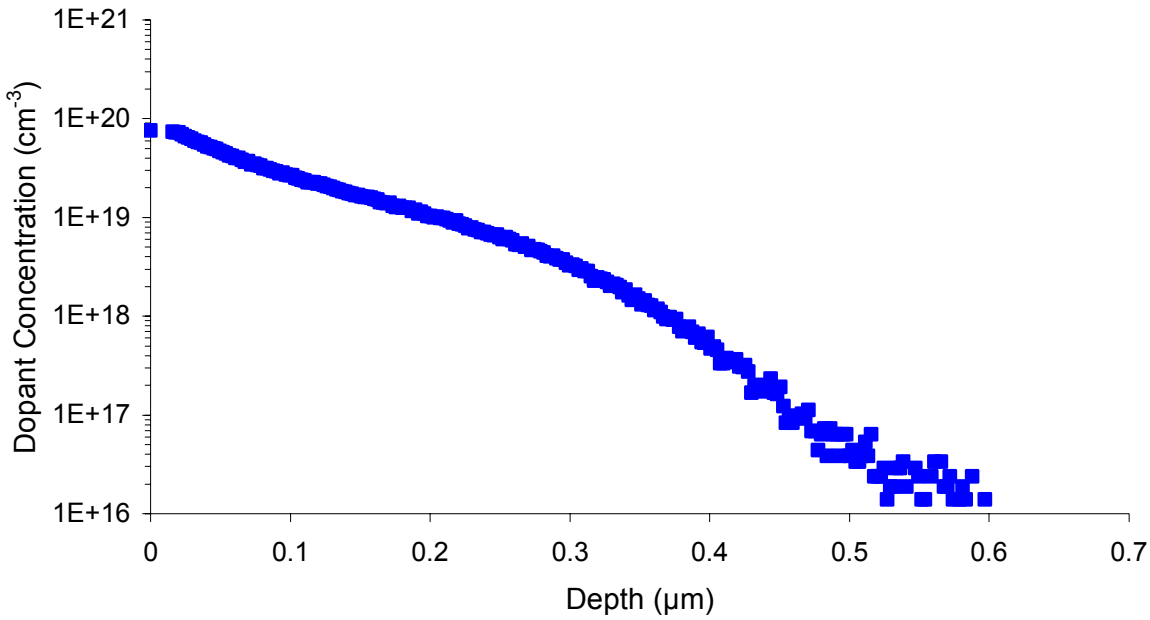

Figure 3.1 SIMS profile of the phosphorous emitter used in this work.

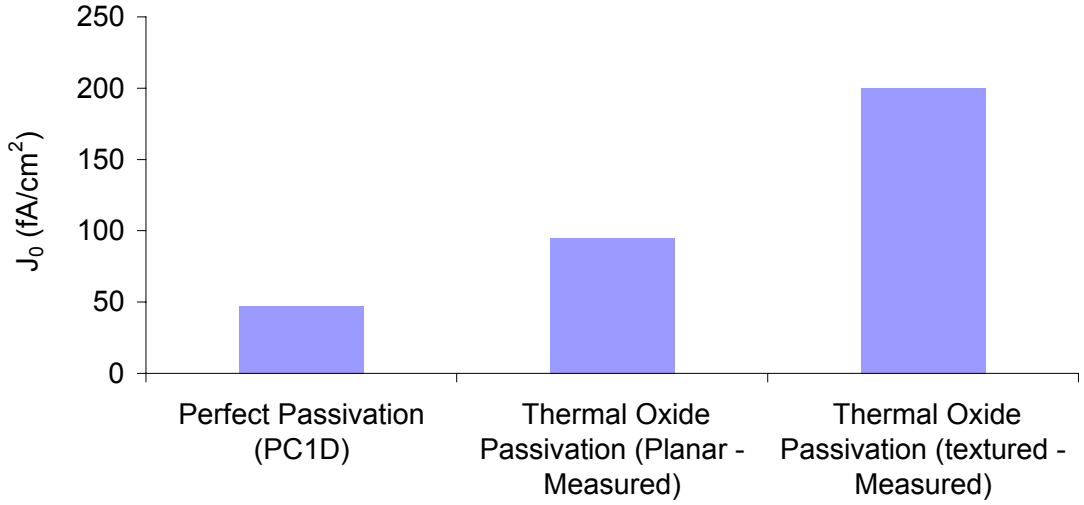

Figure 3.2 Saturation current density of the emitter in Figure 3.1 due to bulk emitter recombination only (perfect passivation, S = 0 cm/s), and due to bulk and surface recombination for thermal SiO_2-passivated planar and random pyramid textured surfaces.

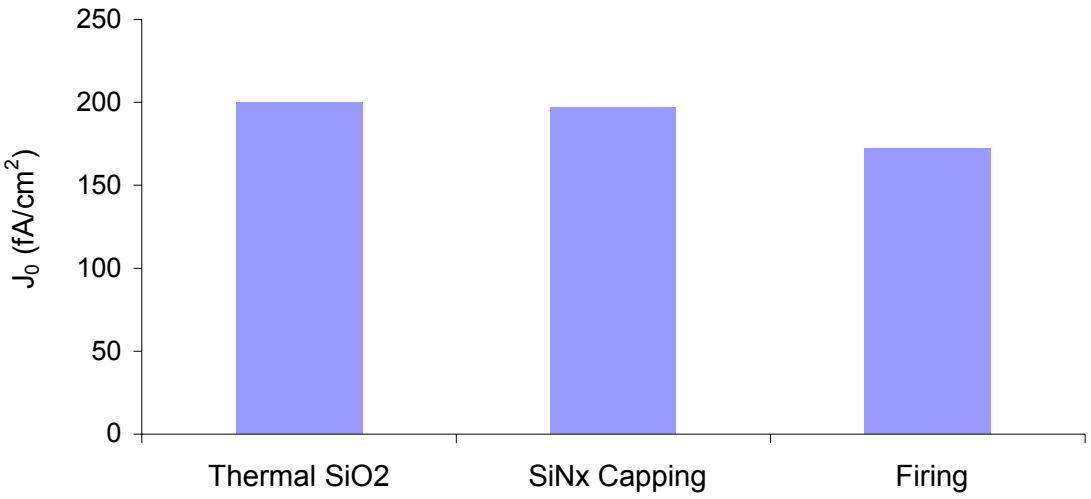

Figure 3.3 Measured saturation current densities, J_0, of thermal SiO_2-passivated, textured, phosphorous emitters at various steps of the cell fabrication sequence.

Assuming perfect passivation (S_n^+ = 0 cm/s), PC1D predicts that the bulk recombination within the emitter corresponds to J_0 of 47.4 fA/cm^2 (Figure 3.2). This sets a V_{OC} limit of nearly 710 mV which shows that the emitter is suitable for a high-efficiency cell. Due to imperfect surface passivation, the measured J_0 on oxide-passivated planar samples was twice as high at ~95 fA/cm^2. Texturing resulted in another doubling of the J_0 to ~200 fA/cm^2. The increase in J_0 due to texturing is in good agreement with the ~1.73x increase in surface area commonly assumed for random pyramid texturing and is consistent with the increase seen by other authors for passivated phosphorous emitters [52-54]. SiN capping and metal-free firing of the textured samples results in only a small reduction in J_0 to ~170 fA/cm^2 (Figure 3.3).

In order to see how the passivation quality of the oxide used here compares to previous reports, PC1D was used to extract an S_n^+ value for the oxide-passivated planar samples. As noted in Chapter 2, the value of S that is calculated from J_0 and dopant profile measurements depends heavily on the Auger model, BGN model, mobility model and n_i used. Figure 3.4 therefore compares the result obtained here only with those of

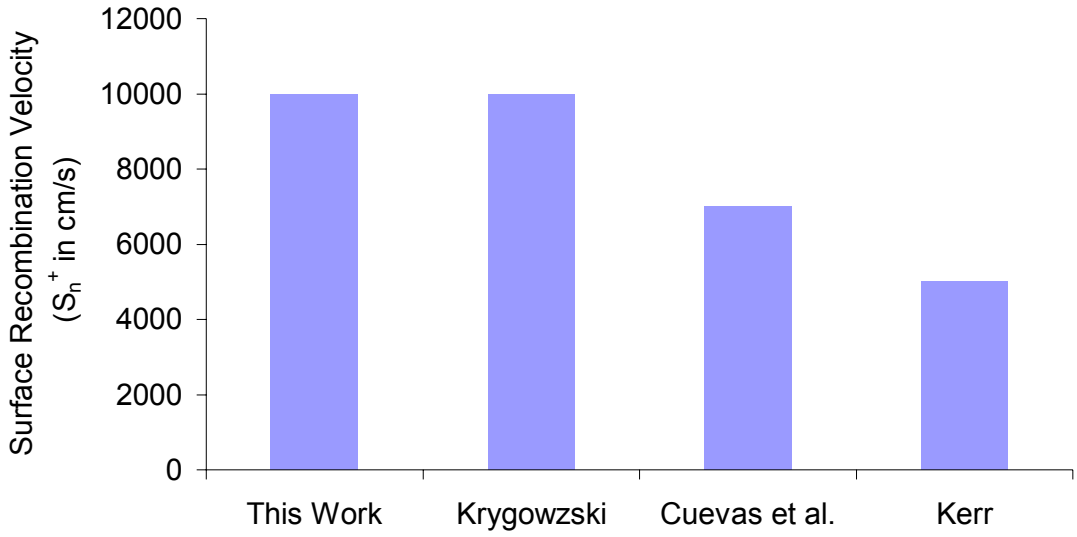

Figure 3.4 Extracted S_n^+ values for a thermal SiO_2 passivated phosphorous emitter ($N_{Surface}$ = $7x10^{19}$-$8x10^{19}$) as obtained for this work and as reported in Refs. 52, 54, and 55.

Cuevas, Krygowzki and Kerr who either used PC1D itself or used the models implemented in PC1D [52, 54, 55].

The results from this study and those of Krygowzki and Kerr are for SiO_2-passivated planar phosphorous emitters while that of Cuevas is for a forming gas annealed, SiO_2-passivated planar emitter. It should be noted that though Kerr used PC1D for their extraction of S_n^+ values, he modified PC1D's BGN model resulting in their extracted S_n^+ values being somewhat higher than the value that would have been obtained using PC1D's default BGN model. While the passivation quality for the ~14 nm thick oxide used here is similar to that of Krygowzski, it is higher than the result of Kerr by at least a factor of 2. That said, the passivation quality is still sufficient for a high-efficiency (20%) cell. The roughly 4x increase in J_0 (Figure 3.3) due to imperfect surface passivation and texturing lowers the V_{OC} ceiling from 710 mV to a still high value of 677 mV.

3.2.2 Fabrication and Analysis of Aluminum BSF Cell

Figure 3.5 shows the independently validated I-V characteristics of an 18.9% Al-BSF cell fabricated with the process sequence described in Section 3.1 The cell V_{OC} of 640 mV is considerably lower than the 677 mV ceiling set by the passivated textured emitter.

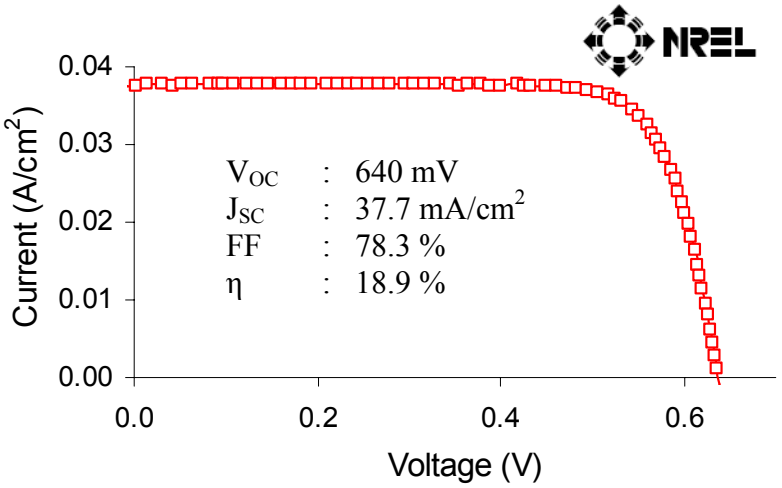

Figure 3.5 I-V characteristics of a high-efficiency, screen-printed Al-BSF solar cell.

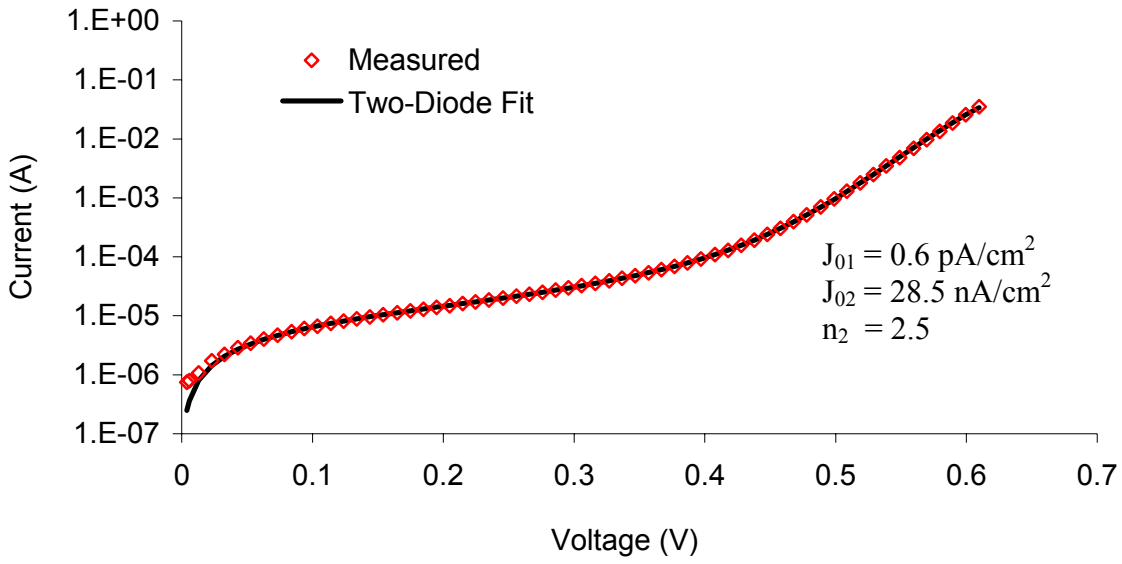

Figure 3.6 Two-diode fit to measured dark I-V curve for an Al-BSF cell.

In order to separate the various efficiency limiting mechanisms in the cell, the device was first thoroughly characterized via wafer thickness, wafer resistivity, light/dark I-V and bulk lifetime measurements. A 'best-fit' made to the dark I-V curve was used to extract the J_{01}, J_{02}, and n_2 values for the two-diode model of this cell (Figure 3.6).

$$J_{dark} = J_{01}(e^{\frac{q(V+JR_S)}{n_1 kT}} - 1) + J_{02}(e^{\frac{q(V+JR_S)}{n_2 KT}} - 1) + (\frac{V+JR_S}{R_{shunt}}) \qquad (3.2)$$

The series (R_S) and shunt (R_{shunt}) resistance values used for this fit were determined from light I-V measurements.

Apart from J_{01}, all of these experimentally determined cell characteristics and the SIMS emitter profile were fed into PC1D. The front surface reflectance was also experimentally determined and supplied as an input to PC1D. The FSRV, BSRV and R_B were then iteratively adjusted till a good match was obtained to the lighted I-V data and the measured internal quantum efficiency (IQE) and reflectance curves (Figure 3.7). The PC1D parameters for this fit are shown in Table 3-1. Figure 3.7 shows that the simulated performance of the modeled cell closely matches the experimental data. The fit reveals that the 18.9% Al-BSF cell has a front-surface recombination velocity (FSRV or S_n^+) of 21,000 cm/s, a high back-surface recombination velocity (BSRV) of 600 cm/s and a low internal back-surface reflectance (R_B) of 70% (diffuse).

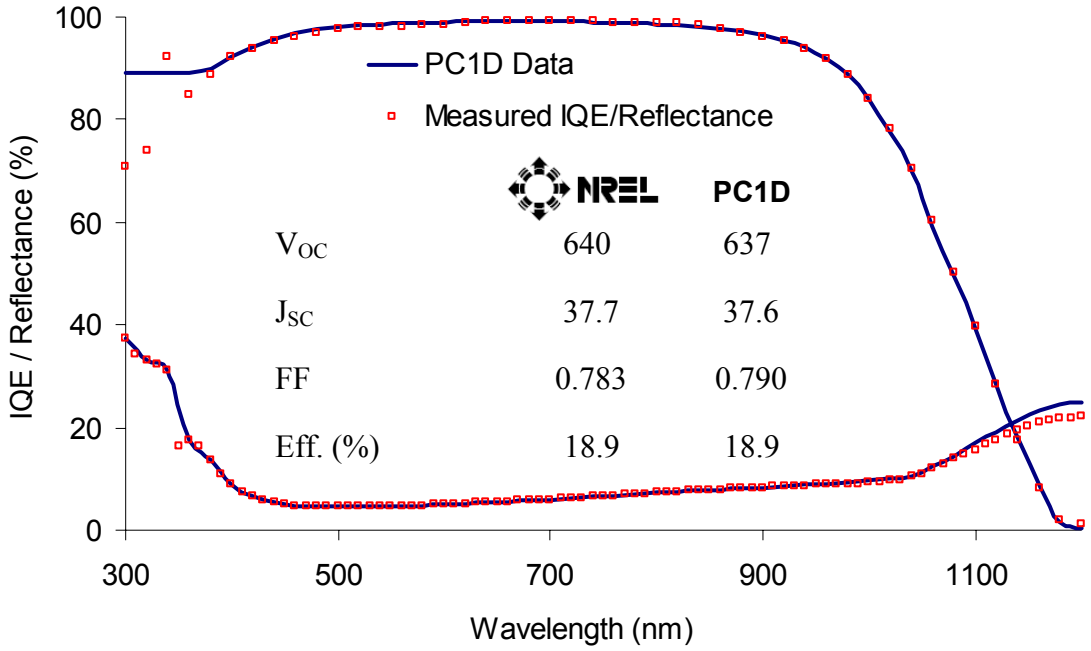

Figure 3.7 PC1D fit to the I-V, IQE and reflectance characteristics of the 18.9% efficient Al-BSF cell.

Table 3.1 PC1D cell parameters used for the 'best fit' to the 18.9% Al-BSF solar cell.

Cell Parameters	Textured FZ Cell
Wafer Thickness (μm)	300
Base Resistivity (Ω-cm)	1.3
R_S (Ω-cm^2)	0.77
R_{SH} (Ω-cm^2)	86000
2nd Diode Ideality Factor (n_2)	2.5
J_{o2}(nA/cm^2)	28.5
Emitter Sheet Resistance (Ω/sq)	70
Emitter Surface Conc. (cm^{-3})	8x10^{19} (from SIMS data)
Bulk Lifetime (μs)	450 (measured)
Front grid shading (%)	Measured Reflectance
BSRV (cm/s)	600
FSRV (cm/s)	21,000
R_B (%)	70
Texture angle (degrees)	54.7
Texture depth (μm)	3.5

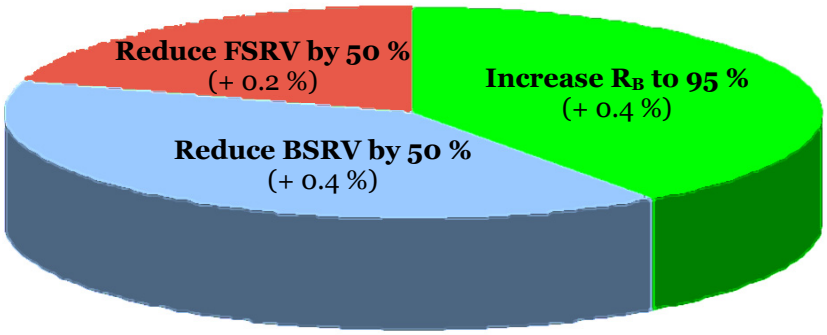

Figure 3.8 PC1D modeling showing the efficiency impact of improving the front and rear sides of an 18.9% Al-BSF cell.

3.2.3 Target Cell Parameters for a 20% Efficient Screen-Printed Solar Cell

Various parameters of the PC1D fit to the 18.9% Al-BSF cell were then adjusted in order to find a parameter set that would result in 20% efficient cells. The first round of such modeling (Figure 3.8) predicted that increasing R_B to 95% (diffuse) and reducing the BSRV and FSRV by 50% each, would increase the cell efficiency by 1% (abs.).

The results of Kerr (Figure 3.4) discussed in Section 3.3.2 indicate that a 50% improvement in FSRV is technologically feasible. However, the pie-chart in Figure 3.8 clearly shows that rear side improvements are the 'lower hanging fruit', i.e. improvements to the rear side will have a larger impact on cell efficiency. In the interest of simplifying the path to a 20% efficient cell, improvements to the front side were not pursued. This thesis will instead focus on rear side improvements only. With this choice made, a second round of PC1D simulations were run to establish the backside improvements which can result in 20% cells. It was found that 20% efficient cells can be achieved with the baseline emitter if BSRV and R_B can be improved to 200 cm/s and 95% (diffuse) respectively, with each contributing ~ 0.5% enhancement in efficiency.

A notable characteristic of this hypothetical 20% cell is that it is more tolerant of

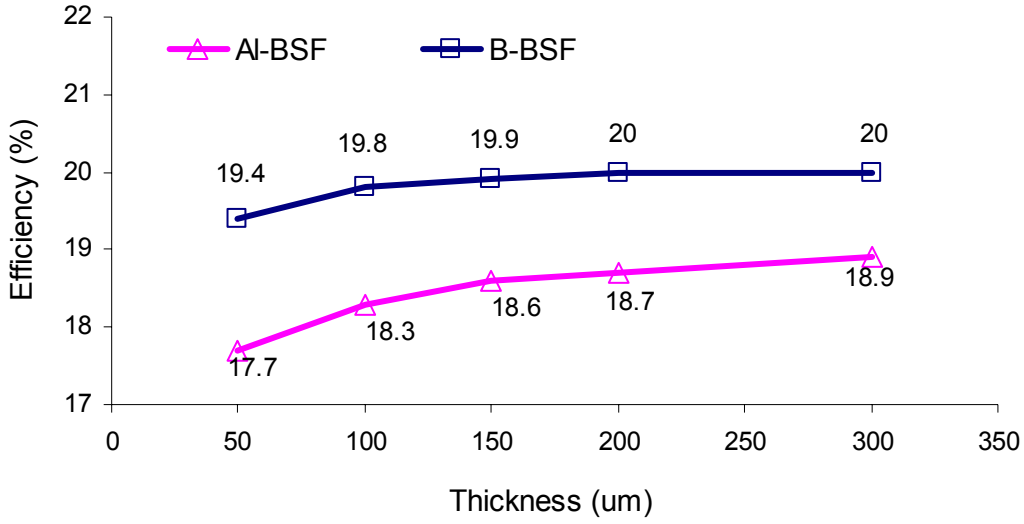

Figure 3.9 PC1D modeling of the relationship between cell efficiency and substrate thickness for an 18.9% Al-BSF cell and an analogous cell with improved BSRV (200 cm/s) and R_B (95%).

reductions in the wafer thickness (Figure 3.9). This is an important benefit of the proposed rear-side improvements because, as discussed in Chapter 1, the wafer alone accounts for ~60% of the cost of a PV module (Figure 1.10). Therefore, the ability to reduce cell thickness by 50% with no appreciable loss in cell performance could lead to significant cost reductions. PC1D simulations show the basic Al-BSF cell would lose 1.2% (abs.) efficiency when the substrate thickness is reduced from 300 μm to 50 μm while the improved 20% cell design loses just 0.6% (abs.).

3.2.4 Moving Away From the Al-BSF Structure

Conceptually, the simplest method of achieving the target BSRV and BSR values would be to optimize the paste composition and firing as this would require the least change to the process sequence. As seen in Figure 3.10, the Al solubility/doping density in Si increases with temperature up to ~1200°C [10]. Since the BSRV of 600 cm/s reported in the previous section was obtained with a relatively low firing temperature

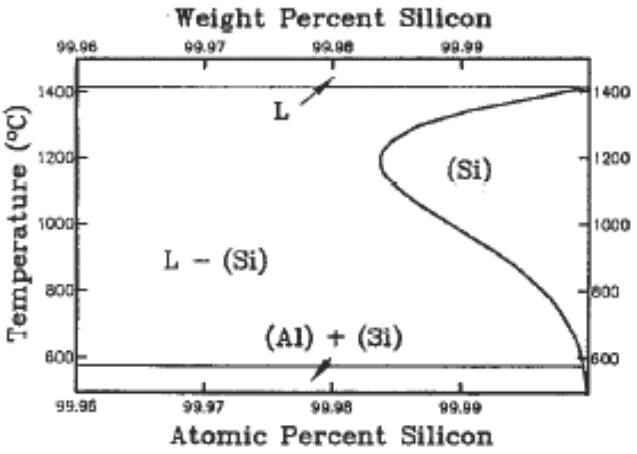

Figure 3.10 Solid solubility of Al in Si [10, 57].

reported in the previous section was obtained with a relatively low firing temperature of 740°C, further improvement in the BSRV can be obtained simply by increasing the firing temperature and using a silver paste on the front side that does not shunt the emitter at such high firing temperatures.

This strategy was previously employed successfully by Hilali, resulting in a 19% efficient 0.6 Ω-cm FZ Si cell fired at ~810°C [56]. This device was the highest efficiency screen-printed cell at the start of this thesis study and featured a BSRV of 600 cm/s (on 0.6 Ω-cm FZ Si) which corresponds to a BSRV of ~260 cm/s on the 1.3 Ω-cm material used in this work. Doping the Al paste with boron is another strategy to lower the BSRV because boron's higher solid solubility limit in Si results in heavier doping compared to a boron-free Al paste [58, 59]. Very recently, passivation quality similar to Hilali (~300 cm/s on 1.3 Ω-cm) has been obtained with such a paste using peak firing temperatures of ~860°C [59]. While such strategies get the simple Al-BSF structure closer to the target BSRV of 200 cm/s, the R_B values (as extracted via PC1D fitting) reported for several of the best SP Al-BSF cells have been in the 60%-70% range [56, 60-62]. This falls far short of the target R_B of 95%. In addition, the Al-Si alloying process leads to bowing of thin wafers and potentially lower manufacturing yields as discussed in Chapter 1 [12]. It is

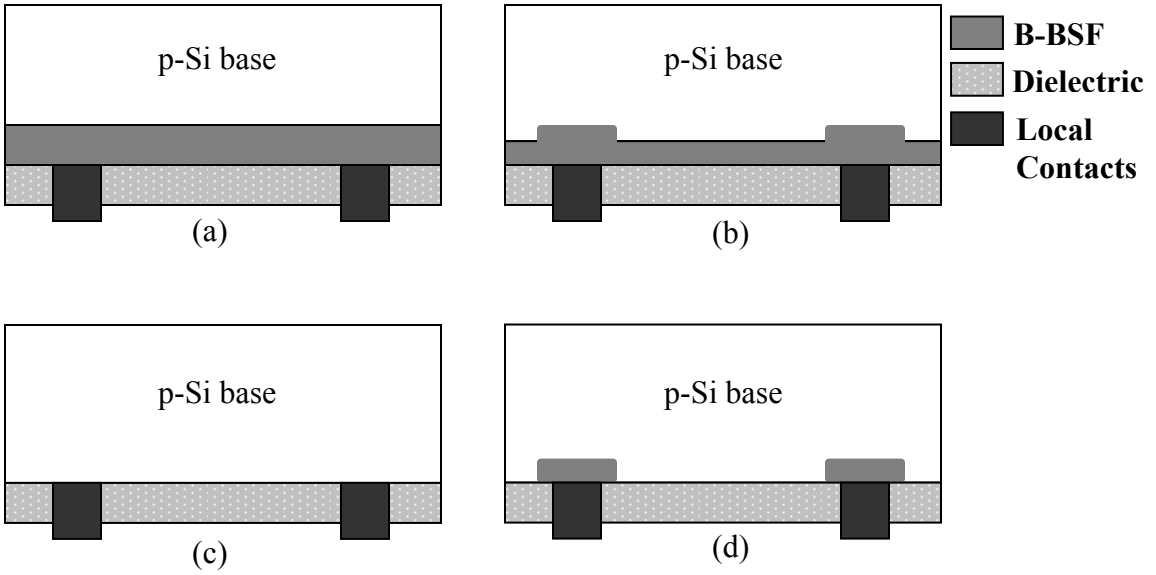

Figure 3.11 Schematics of advanced rear passivation concepts: (a) full-area B-BSF (PERT(s)), (b),Selective B-BSF (PERT), (c) Dielectric-only passivation (PERC) and (d) dielectric passivation with local B-BSF (PERL).

worth noting that according to the solid solubility diagram (Figure 3.10), higher Al doping and lower BSRVs (than those mentioned above) can be obtained by using even higher firing temperatures. In practice however, temperatures beyond ~900°C leads to agglomeration of liquid Al during the Al-Si alloying process, resulting in inhomogeneous BSF formation and higher BSRVs than those presented earlier [19, 63].

A number of alternative rear passivation concepts are capable of matching or exceeding the target BSRV and R_B numbers. Figure 3.11 illustrates these concepts – (a) a full-area B-BSF, (b) a selective B-BSF with heavier doping under the metal point contacts, (c) dielectric-only passivation and (d) dielectric passivation with local B-BSFs only under the metal point contacts. Efficiencies in excess of 20% have been achieved with each of these concepts at UNSW using complex, photolithography-based processing methods. These devices are commonly referred to by the acronyms PERT(s), PERT, PERC and PERL as noted in Figure 3.11 [28, 64-66]. Of the structures that feature a BSF,

Table 3.2 Cell efficiencies achieved with the PERL, PERT, PERT(s) and PERC structures at UNSW [28, 64-66]. Entries marked with a * were independently confirmed. The entry marked with a † was recently re-measured with the revised AM 1.5G spectrum (IEC 60904-3: Ed. 2) resulting in a higher confirmed efficiency.

Cell Type	Material	Efficiency
PERL	FZ (B)	24.7%* (25†)
PERT	MCZ (B)	24.5%*
PERT(s)	CZ (Ga)	20.9%*
PERC	FZ (B)	23.1%

the full-BSF concept is the simplest to achieve as additional process steps are typically required to obtain a spatially inhomogeneous BSF.

However, as Table 3.2 shows, significantly higher efficiencies have been achieved for the more complex PERL and PERT structures. From Ref. 65, it is not clear why the performance of the simpler PERT(s) structure lags behind its more complex brethren. However, the authors do note that on test samples, lifetimes over 1 ms were measured for the materials used to fabricate both the PERT(s) and PERT cells. In this work, an attempt is made to achieve an efficiency of 20% with the simplest full-area, passivated B-BSF/PERT(s) structure using only industrially compatible processing methods including screen-printing and relatively short thermal cycles. For simplicity, this structure will henceforth be referred to as simply the 'B-BSF' structure.

3.3 Summary

In this chapter, an 18.9% efficient, 4cm^2 screen-printed Al-BSF cell was successfully fabricated and modeled in PC1D. Using this 'baseline' model, simulations were performed in order to identify a combination of BSRV and R_B improvements that can

produce a cell efficiency of 20%. These simulations revealed that if no changes are made to the baseline emitter, a BSRV of 200 cm/s and a R_B of 95% (100% diffuse) are needed to achieve the efficiency target. Since the full-area, passivated B-BSF structure was chosen as the candidate structure for realizing this modeled 20% cell, the following chapter provides a review of the relevant literature.

Chapter 4

REVIEW OF PRIOR WORK ON BORON DIFFUSED SILICON SOLAR CELLS

In a typical process flow for fabricating an Al-BSF cell, three steps – rear surface passivation, rear contact formation and front contact formation – are combined into just one, short co-firing step. Due to the simplicity and high-throughput nature of this process, the Al-BSF structure has become the workhorse of the commercial solar cell industry. However, the relatively high BSRV and low R_B provided by an Al-BSF, coupled with stress-induced bowing on thin wafers, makes the structure unsuitable for next-generation, thin, high-efficiency solar cells [12, 56, 59-62].

From the technical standpoint, a B-BSF is a strong alternative to an Al-BSF because: 1) a B-BSF layer alone can provide stronger field effect passivation due to an order of

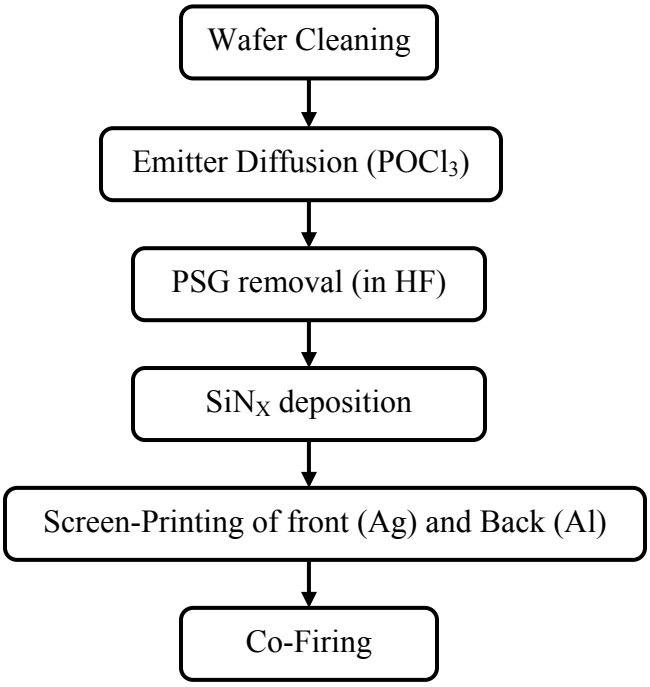

Figure 4.1 Process flow for a standard, screen-printed Al-BSF solar cell.

magnitude boron solid solubility in Si [10, 58, 59, 67, 68], and 2) a B-BSF can be easily capped with a passivating dielectric thus providing both improved field effect passivation and improved interface passivation compared to an Al-BSF. In fact, due to the higher solid solubility of boron in Si, a B-BSF can provide passivation superior to that provided by an Al-BSF even without dielectric passivation of the doped surface. This will be discussed further in Chapter 6. As a B-BSF is largely optically transparent, it can also be capped with a BSR material that is more reflective than fired, screen-printed Al paste.

The advantages of a B-BSF are exemplified by the fact that the cells with the highest, terrestrial conversion efficiencies – the PERL and PERT structures (see Figure 3.11 and Table 3.2) – both utilize B-BSFs. However, the fabrication sequence for both cells involve multiple, high temperature steps and photolithography which have prevented their commercial adoption. Outside of such complex processing schemes, B-BSF structures are currently not widely used in lab-scale fabrication and extremely rare in commercial manufacturing. Table 4.1 shows a list of the best B-BSF cells fabricated using various boron sources, substrate types and processing schemes [28, 64, 65, 69-74]. The entry from Solarworld Industries has been the only industrial attempt at manufacturing B-BSF solar cells, though production of this structure has since ceased [12].

It is apparent from Table 4.1 that the only B-BSF cells that exceed the efficiency of the best large-area, commercial SP Al-BSF cells [11] are those fabricated with processing methods – photolithography, prolonged high-temperature steps and evaporated metal contacts [64, 70, 71] – that are considerably more complex than commercial fabrication processes which typically feature lower thermal budgets (i.e. shorter processing time and/or lower temperature) and low-cost screen-printed contacts. All the other entries in Table 4.1 fall well below the ~19% peak efficiency obtained on basic, commercial Al-BSF cells [11]. The reason that the technical strengths of B-BSF passivation have not yet translated to commercially manufacturable, high-efficiency B-BSF cells is that most boron diffusion processes bring with them several challenges.

Table 4.1. List of the best boron back surface field solar cells fabricated using various processing techniques. All entries marked with a * were independently measured. The entry marked with a † was recently re-measured with the 2009 revision of the AM 1.5G spectrum (IEC 60904-3: Ed. 2).

Institute	Material	Boron Source	Cell Size	Efficiency	Selected Process Details
UNSW [28, 64, 70]	FZ	BBr_3	4 cm^2	24.7 % * (25 % †)	**PERL:** Local B-BSF (2hr. drive-in at 1070 °C); Selective emitter; 'Alnealed' SiO_2 passivated front/rear; evaporated contacts
ISFH [71]	FZ	BBr_3	4 cm^2	21.6 %	**PERL:** 15 ohm/sq local B-BSF (1hr. drive-in at 1050 °C); 150nm oxide passivated front/rear; evaporated contacts
Solarworld Industries [69]	CZ (B)	N/A	156 cm^2	18.8 % (18.4 % *)	2µm deep 7.5 ohm/sq B-BSF; Selective Emitter; Oxide passivated front/rear; SiN_X ARC; Bifacial SP contacts
Fraunhofer ISE [72]	FZ	Spin-on	N/A	14.6 %	RTP diffused B-BSF and emitter; RTO passivated front/rear; SiN/MgF_2 DL ARC; Evaporated contacts
TiM/Ferro [73]	CZ (B)	SP Paste	106 cm^2	13.7 %	Co-Diffused with boron and phosphorous pastes – 4mins at 950 °C; TiO_x ARC; Bifacial SP contacts
Uni. Konstanz [74]	mcSi	BBr_3	100 cm^2	15.7 %	60 ohm/sq B-BSF, $POCl_3$ Emitter; SiO_2/SiN_x on BSF; SiN_x on Emitter; Bifacial SP + plated contacts
	SoG Si		100 cm^2	16.1 %	

Legend: PL processed cells PL-free cells

First, boron diffusions often result in contamination of the Si substrate. Obtaining stable, high-quality passivation of a heavily boron doped silicon surface is a second challenge. The impact of poor surface passivation can be partially countered by relying on a deep, heavily doped, 'opaque' B-BSF which provides strong field effect passivation. But due to the relatively slow diffusivity of boron in Si, obtaining such a BSF requires the kind of long diffusion/drive-in step that industry prefers to avoid [71, 74]. In addition, prolonged high-temperature steps may increase the risk of wafer contamination. The literature data on these issues are reviewed in the following sections.

4.1 Common Features of Boron Diffusion in Silicon

Several sources of boron have been used by the PV community for high temperature thermal diffusion of boron into Si – liquid sources like boron tribromide (BBr_3) and boron trichloride (BCl_3), 'solid sources' such as boron nitride (BN) and doped atmospheric pressure chemical vapor deposited silicon dioxide (APCVD SiO_2), spin-on or spray-on dopants (SODs) and screen-printed paste sources [52, 64-85]. However, all of these methods share some common features which are discussed in this section.

4.1.1. Diffusion of Boron into Silicon

In general, diffusion of boron into silicon involves the deposition of boric oxide (B_2O_3) on the surface of a Si wafer. At high temperatures, B_2O_3 reacts with Si to form SiO_2 and B, the latter of which diffuses into silicon at high temperatures [68]:

$$2\ B_2O_3 + 3\ Si \rightarrow 3\ SiO_2 + 4\ B \qquad (4.1)$$

Typically, boron diffusion processes occur at temperatures ranging from 850-1150°C regardless of the boron source used [71-78]. Temperatures at the low end of that range (~850-950°C) are typically used only during the 'deposition' step of a diffusion process where a layer of B_2O_3 is deposited on the wafer surface. Due to the relatively slow diffusivity of boron in silicon, the 'drive-in' of boron to practical junction depths is

usually done at temperatures ≥ 950°C [70-73, 76]. The highest efficiency B-BSF cells in Table 4.1 used temperatures ≥ 1050 °C to form deep, heavily doped BSFs. Over this temperature range, the boron solid solubility in Si is ≥ $1x10^{20}$ cm^{-3} [67]. In contrast, at common firing temperatures of 700-900°C, the Al solid solubility limit is just ~$1\text{-}3x10^{18}$ cm^{-3} with a peak doping limit of ~$7x10^{18}$ at 1200°C (see Figure 2.10) [10].

At the high process temperatures, SiO_2 and B_2O_3 mix together forming a layer of borosilicate glass (BSG) on the silicon surface. In the cases where the source/diffusion process can saturate the wafer surface with boron atoms over the length of the diffusion process, an additional, dense layer of Si-B alloys can form at the interface between the BSG and the boron-doped silicon [81]. The composition of this 'boron rich layer' (BRL) has been studied by various authors and has been reported to be of the form SiB_x ($4 \leq x \leq 6$), and it can act as a source of boron in subsequent high temperature steps unless it is removed [75, 81, 82]. In addition to the SiB_x alloy, some oxidized silicon and boron may also be present in the BRL. It has been suggested by Arai *et al.*, that the BRL forms only when the rate of supply of boron to the silicon surface exceeds the diffusion rate of boron into silicon [81]. This conclusion is supported by the work of Negrini *et al.* who found that an increase in the BBr_3 partial pressure during diffusion (which would increase the supply of boron to the Si surface) resulted in an increase in BRL thickness [83]. The thickness has also been found to be inversely related to the amount of oxygen in the ambient [75, 81-83]. Diffusion processes using 'infinite sources' such as BBr_3 can easily keep the Si surface saturated with boron atoms as the liquid dopant can be continuously introduced into the ambient over the entire diffusion process. However, the saturation condition can also be met by limited dopant sources (SODs, solid sources and pastes) if the diffusion/drive-in process is short enough to allow the limited sources to keep the wafer surface saturated with boron. Regardless of what source and process conditions are used, the presence of a BRL after diffusion can be easily verified with a post-diffusion dip in hydrofluoric acid (HF). While HF is able to strip the BSG layer, it does not remove

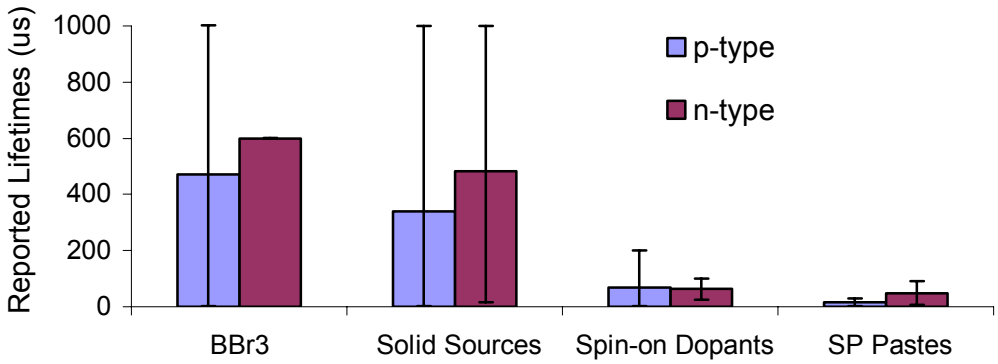

Figure 4.2 Bulk minority carrier lifetimes on p-type and n-type FZ Si wafers after boron diffusions using various sources as reported in Refs. 52, 71-73, 76, 78, 84-87.

the BRL under it. If no BRL exists, the wafer surface should become hydrophobic after the HF dip; if a BRL does exist, the surface remains hydrophilic. The BRL is usually removed by oxidizing it – this converts the BRL to a BSG layer – followed by an HF dip [75, 83, 84].

4.1.2 Lifetime Degradation of Si Substrates Due to Boron Diffusion

Degradation of the minority carrier lifetime in Si wafers is a second common feature of processes that involve boron diffusion (Figure 4.2). For every boron source commonly used for solar cell fabrication, low carrier lifetimes have been reported either immediately after the boron diffusion and/or after high-temperature processing steps that follow the boron diffusion [52, 71-73, 76, 78, 84-87]. This is especially true of the cheaper boron sources such as SODs and paste sources which are of industrial interest due to their lower cost (Figure 4.2) [52, 72, 73, 78].

Unfortunately, while lifetime losses are widely reported, the cause of the losses is often not investigated. Contamination of the wafer and generation of dislocations in the wafer are two mechanisms that have been identified as potential causes [85, 86]. Contamination is perhaps the most common assumption, with iron (Fe) being the most

widely suspected contaminant species [52, 72, 78, 84, 85, 87]. Generation of dislocations after boron diffusions has also been experimentally observed [86, 88-90]. These dislocations are generated due to relaxation of the mismatch stress caused by the large difference in the size of the boron and silicon atoms [90]. Though dislocations are initiated only at the surface of the boron diffused layer, it has been shown that subsequent high temperature processing can cause a network of dislocations to propagate deep into the bulk of the Si substrate resulting in a severe drop in the bulk lifetime [86]. It is worth noting however that dislocation generation has been reported to occur only under certain diffusion conditions. Higher diffusion temperatures and prolonged process times are more likely to generate dislocations as they result in higher dopant concentrations and therefore greater stress in the diffused Si layer. For example, Cousins and Cotter reported dislocations extending up to 200 μm into the wafer bulk for a 5hr+ diffusion process that resulted in a sheet resistance of 10 Ω/sq [86]. But for a shortened process at the same process temperatures (which resulted in a sheet resistance of 80 Ω/sq), little to no dislocations were observed. Using BBr_3 and BN solid sources, Gaisenau *et al.* identified process time/temperature combinations that can lead to the generation of diffusion-induced misfit dislocations [91]. Their results are reproduced in Figure 4.3. A recent work by Kessler *et al.* (using BBr_3) also reported an inverse relationship between the BRL thickness and bulk lifetimes – a thicker BRL was found to correlate with lower bulk lifetimes [92]. They proposed that stress at the BRL and Si interface results in dislocations which glide into the bulk.

Since a low minority carrier bulk lifetime results in incomplete collection of photogenerated carriers and thus lowers cell efficiency, finding methods to either avoid or reverse boron-diffusion-induced lifetime degradation is a major focus of this work and is covered in Chapter 8.

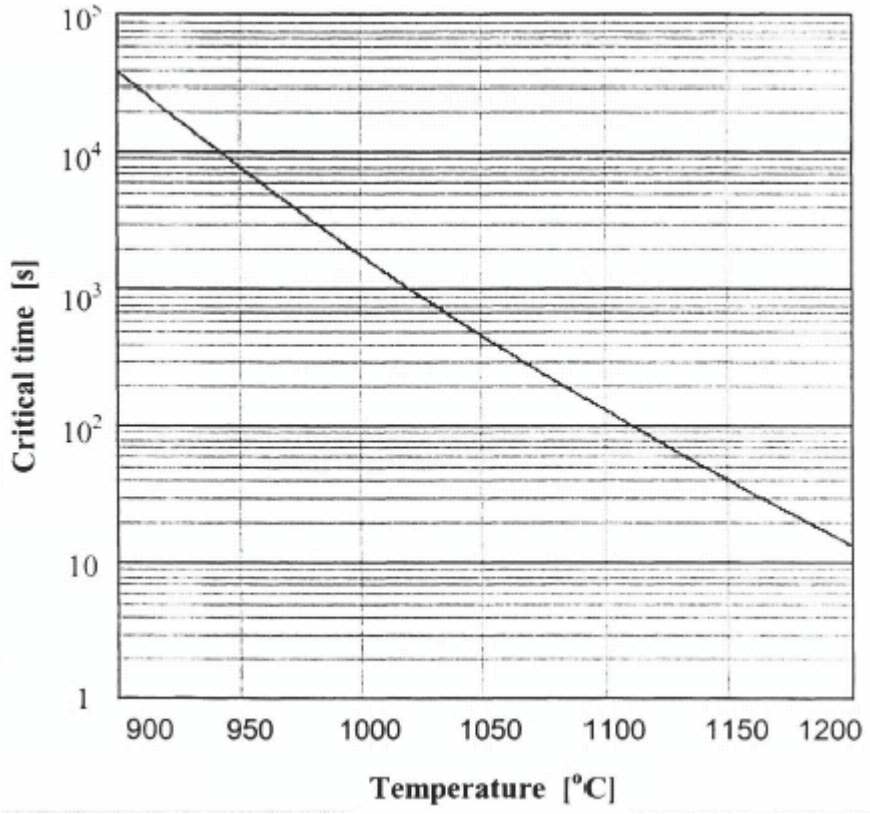

Figure 4.3 Critical boron diffusion time-temperature conditions that result in the generation of misfit dislocations (taken from Ref. 91).

4.2 Survey of Boron Sources Commonly Used in Solar Cell Fabrication

While the characteristics discussed in the previous section are common to most sources of boron, the following sub-sections will review characteristics that are specific to the boron sources that are most commonly used by the PV community.

4.2.1 Boron Tribromide and Boron Trichloride

Boron tribromide (BBr_3) and Boron Trichloride (BCl_3) diffusions are performed by introducing vapors of the dopant into the diffusion furnace by bubbling N_2 or Ar through a pressurized, temperature controlled bubbler containing liquid BBr_3/BCl_3. During the deposition step of the diffusion process, oxygen is also introduced into the furnace and BBr_3/BCl_3 and O_2 react according to the equations [93]:

$$4\ BBr_3 + 3\ O_2 \rightarrow 2\ B_2O_3 + 6\ BR_2 \quad (4.2)$$

$$4\ BCl_3 + 3\ O_2 \rightarrow 2\ B_2O_3 + 6\ Cl_2 \quad (4.3)$$

B_2O_3 then reacts with Si (according to Equation 4.1) releasing boron atoms which can diffuse into silicon. One advantage of these dopants is the generation of Br_2 and Cl_2 which can getter metal from the ambient and quartzware by forming the corresponding metal halides. This 'self-cleaning' ability of a BBr_3 process may be why it has been the most successfully used boron dopant source for fabricating PV devices (see Table 4.1 and Figure 4.2). Several groups have reported high lifetimes (500 μs-2 ms) after BBr_3 diffusion [70, 78, 94] and it has been used to fabricate several high efficiency cells, including the 25% efficient PERL cell which is the highest efficiency for single junction silicon solar cells to date [28, 64, 70]. However, severe degradation in lifetime (to values as low as 1-5 μs) on high quality float zone (FZ) silicon substrates have also been reported [52, 71, 84]. As mentioned previously, the cause of such large differences in lifetime is not clear since literature reports which mention lifetime degradation typically do not attempt to link the degradation to particular degradation mechanisms. Differences in processing equipment (which can be a source of contaminants) and process conditions (which can affect impurity diffusion, BRL formation and dislocation generation) are potential causes of the large spread in the lifetime data in the literature for BBr_3 diffusions (Figure 4.1) [87, 91].

The negatives associated with BBr_3 and BCl_3 derive largely from their toxic and pyrophoric nature [95-97]. While the evolution of Br_2 and Cl_2 during the process helps with gettering, they are both toxic and specialized scrubbing/venting systems are required to vent them safely. Additionally, BBr_3 and BCl_3 are themselves toxic and require careful handling and storage – BBr_3 reacts violently with water and reacts with moisture in the air or body to form hydrobromic acid. Similarly, BCl_3 boils at room temperature under normal atmospheric conditions and can react with moisture to form hydrochloric acid. The specialized systems required to handle and store these dopants can add to their cost.

In the context of industrial fabrication of B-BSF cells, one practical hurdle for gas phase dopants is that an additional masking/etch-back step is needed to prevent/remove diffusion on the emitter side of the device. In addition, depletion of the gas source from the front to the back side of a horizontal furnace can result in variation in sheet resistance depending on a wafer's position in the carrier boat.

4.2.2 APCVD Boron-Doped SiO_2 Solid Sources

SiO_2 based solid sources are usually Si or ceramic wafers on which a doped SiO_2 layer is deposited. Boron doped SiO_2 sources can be formed on sacrificial wafers by introducing a mix of diborane (B_2H_6), silane (SiH_4) and O_2 into an atmospheric pressure chemical vapor deposition (APCVD) system. Diborane and silane react with O_2 following the equations [93]:

$$B_2H_6 + 3\ O_2 \rightarrow B_2O_3 + 3\ H_2O \quad (4.4)$$

$$SiH_4 + O_2 \rightarrow SiO_2 + 2\ H_2 \quad (4.5)$$

The B_2O_3 concentration in the SiO_2 film can be controlled by varying the B_2H_6:SiH_4 ratio. During high-temperature diffusion, doping from the SiO_2 film follows Equation 4.1. APCVD sources are thought to be used by Sunpower Corp. for fabricating interdigitated back contact (IBC) cells and passivation studies have also utilized them as sources [33, 170].

A practical downside to using such sources is that deposition of the doped SiO_2 film is an additional high temperature step requiring a dedicated furnace. Furthermore, both B_2H_6 and SiH_4 which are used in the deposition of the source are toxic and can react explosively with air [98, 99]. An advantage that solid sources have over gaseous dopants like BBr_3 is that each wafer has its own source so there is relatively little variation in sheet resistance across the boat.

4.2.3 Boron Nitride

Boron nitride (BN) disks are a second type of solid sources. Boron diffusion from BN disks requires pre-activating them in an oxidizing ambient to form a surface layer of B_2O_3 [75, 100]:

$$4\ BN + 3\ O_2 \rightarrow 2\ B_2O_3 + 2\ N_2 \tag{4.6}$$

Once activated, the BN *source* wafers are typically interleaved with Si *target* wafers in a diffusion furnace and the doping reaction follows Equation 4.1. Two disadvantages with BN sources are that they require an additional activation step before diffusion and that they have also been linked to large drops in carrier lifetime post-diffusion [76, 84]. Using identical processing conditions and 70-80 Ω-cm n-type FZ Si wafers, Miyoshi *et al.* reported lifetimes > 300 μs for the BBr_3 source while the lifetime was just 15 μs for a BN source [84]. While the cause of such drops in bulk lifetime has not been conclusively identified, the low purity of BN sources has been mentioned as a possible cause [76, 84]. An additional concern with BN sources is the gradual loss of boron over multiple runs. This means that the sheet resistance on target wafers must be carefully monitored to determine when the sources need to be replaced. Repeatability from run to run can also be a concern if the wafers are not cleaned, stored and activated properly [100]. However, as with doped SiO_2 sources, variation in sheet resistance across the diffusion boat is reduced compared to gaseous dopants [100].

4.2.4 SOD and Paste Sources for Boron Diffusion

In recent years, spin-on or spray-on dopant (SOD) sources and screen- or ink-jet printable pastes have been investigated for use in solar cell fabrication by both academic research groups and in industry [52, 72, 73, 101]. The advantages of these sources are that they can be relatively low-cost and can be made of materials that are neither toxic nor pyrophoric. This allows them to be used in high-throughput, in-line diffusion systems, instead of being limited to batch processing in furnaces with specialized gas delivery and

exhaust systems. During diffusion, the dopants can be deposited directly on the Si device wafers or the device wafers can be interleaved with separate source wafers [52, 72, 101]. With both schemes, variation of sheet resistance across the boat is not a major concern. Simultaneous diffusion of boron and phosphorous has also been demonstrated with such sources which means emitter and BSF formation can be combined into a single high-temperature step [52, 73]. However, cross-diffusion around wafer edges is a possible complication that must be carefully checked for.

The major downside to SODs and paste sources is that they have consistently been associated with the lowest post-diffusion lifetimes and cell efficiencies as noted in Table 4.1 and Figure 4.2. As with other boron sources, the causes of such lifetime drops have not been investigated and transfer of contaminants from the SOD/paste sources is a common assumption [52, 73, 78]. This matter is investigated later in this thesis (Chapter 8).

4.3 Passivation of Boron Diffused Silicon Surfaces

While the higher solid solubility of boron in Si results means that a B-BSF can provide stronger field effect passivation compared to a SP Al-BSF, reducing recombination at the heavily boron doped Si surface requires passivating it with an appropriate dielectric. This section reviews literature results on materials that have been used to passivate boron diffused silicon surfaces.

4.3.1 Passivation of Boron Emitters by Thermally Grown SiO_2

Thermal oxidation is the most commonly studied method for passivating boron diffused silicon surfaces. Figure 4.4 summarizes published surface recombination velocities at the SiO_2/p^+-Si interface (S_{P^+}) for various boron doping densities as reported by various authors [33, 52, 94, 102]. All the data points are for planar <100> wafers.

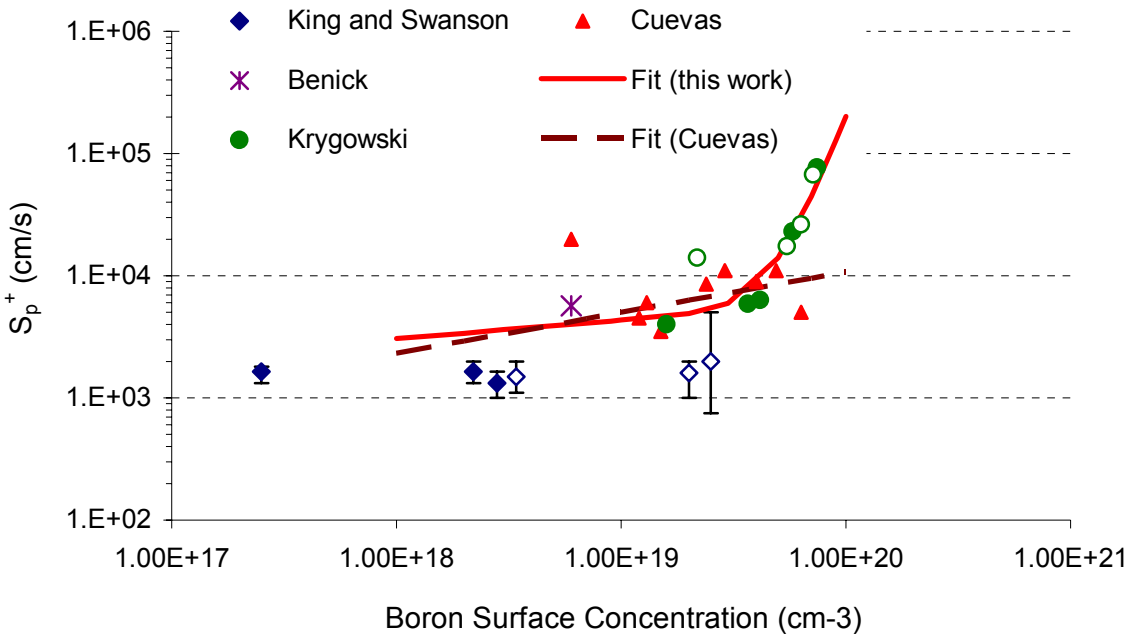

Figure 4.4 Surface recombination velocity (S_p^+) [33, 52, 94, 102] at boron diffused silicon surfaces passivated with thermal SiO_2 as a function of surface dopant concentration. Where reported, *ex-situ* oxidation and *in-situ* oxidation data from the same authors are noted with closed and open points respectively.

Note that S_p^+ is not the measured quantity; instead the J_0 values and dopant profiles for various oxide-passivated boron emitters were measured and S_p^+ was calculated from those measurements. Since the Auger model, BGN model and n_i value that is used for these calculations affect the extracted value of S_p^+, it is important to note that only the data of Benick *et al.* and Krygowski were extracted using PC1D. King and Swanson used a higher value of n_i (1.45×10^{10} cm^{-3} @ 300 K) than PC1D's (1×10^{10} cm^{-3} @ 300 K) and a somewhat different BGN model. Figure 4.5 plots the BGN-corrected intrinsic carrier concentration (n_{ie}) for the different BGN and n_i models/values using:

$$n_{ie}^2 = n_i^2 e^{\frac{\Delta E_G}{kT}} \tag{4.7}$$

The BGN model and n_i value used by King (Figure 4.5) results in a higher n_{ie} (by up to ~100%) compared to PC1D. This will result in lower calculated S_p^+ values than if PC1D

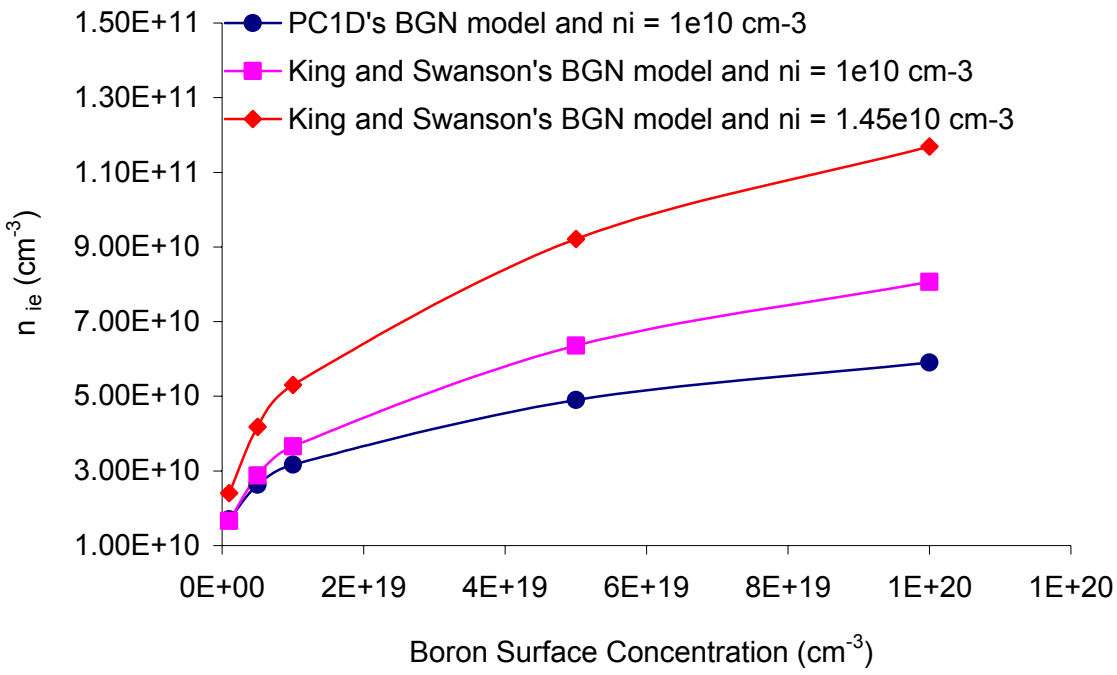

Figure 4.5 BGN corrected intrinsic carrier densities (n_{ie}) as a function of dopant concentration calculated using different values of n_i and the BGN models of PC1D and King and Swanson [16, 33].

had been used as observed in Figure 4.4. While Cuevas *et al.* used King and Swanson's BGN model, they used the same value of n_i (=1x10^{10} cm^{-3} @ 300K) as PC1D. This has a smaller impact on n_{ie} compared to PC1D which is perhaps why the values of Cuevas *et al.* in Figure 4.4 agree well with the values extracted using PC1D [94, 102].

There is noticeable scatter in the data points reported by the various groups, which may be due differences in the processing conditions used – forming gas anneal, oxidation temperature, oxide thickness, the presence or lack of TCA in the oxidizing ambient and *ex-situ* vs. *in-situ* oxidation (the two cases are separately marked with filled and open points in Figure 4.4 where possible). However, the scatter is similar to that seen on oxide passivated phosphorous emitters [34] and may lie within the bounds of experimental error (note the error bars on the data points of King and Swanson).

4.3.1.1 Development of a Parameterization for the Surface Recombination Velocity of Thermal Oxide-Passivated Boron Diffused Surfaces

Globally (Figure 4.4), S_p^+ appears to increase with surface concentration. This matches the trend seen on oxide-passivated phosphorous diffused Si surfaces and is also consistant with Snel's data which shows that the surface density of states increases with increasing dopant concentration for both boron and phosphorous doped Si surfaces [34, 103]. However, the increase in S_p^+ appears to be considerably slower for lower surface concentrations. Using only those S_p^+ values which were extracted using PC1D or an equivalent method, this behavior was approximated in this work by a fit which takes the form (solid line in Figure 4.4):

$$S_p^+ = S_{01}\left(\frac{N_A}{N_0}\right)^{\alpha_1} + S_{02}\left(\frac{N_A}{N_0}\right)^{\alpha_2} \tag{4.7}$$

where S_{01} = 4500 cm/s and S_{02} = 20 cm/s are the coefficients for the slow and fast rising regimes respectively and α_1 = 0.15 and α_2 = 4.5 are the respective slopes. $N_0 = 1.3\text{x}10^{19}$ cm^{-3} determines the 'knee' in the curve where the two regimes cross-over. The scatter in the relatively small number of data points and the lack of error bars on most data points creates some ambiguity as to the 'best' values to use for the variables in Equation 4.7. It is interesting to note however, that in for surface concentrations $\leq 5\text{x}10^{19}$ cm^{-3}, S_p^+ is almost constant. This matches the conclusion drawn by King and Swanson that the recombination velocity of oxide passivated boron diffused surfaces is constant [33]. Based on the larger data set shown in Figure 4.3, it seems that their conclusion may have been largely due to the surface doping range explored in that work. For comparison, the fit of Cuevas *et al.* to their own data points is also shown in the figure (dashed line).

Equation 4.3 also matches the form of the fit used by Altermatt *et al.* [34] to describe the S_n^+ vs. dopant concentration trend for oxide-passivated phosphorous emitters (Figure 4.6). Caution should be used when comparing values from the two curves in Figure 4.6 as Altermatt *et al.* employed Fermi-Dirac (F-D) statistics and quantum mechanically derived

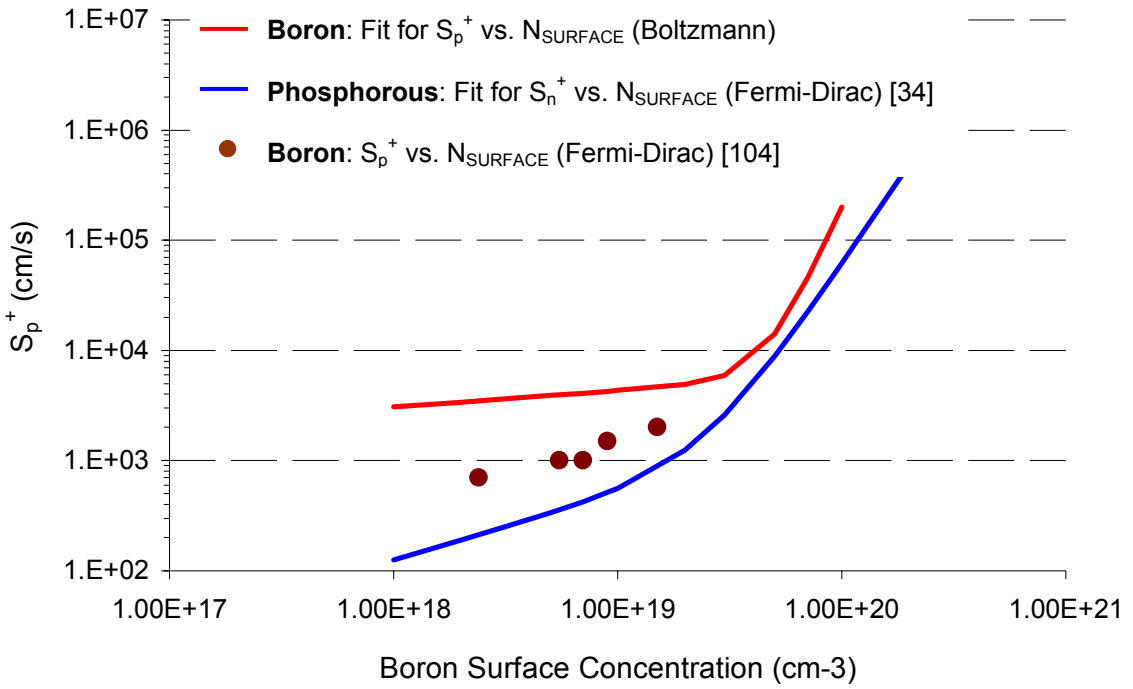

Figure 4.6 Comparison of surface recombination velocity vs. surface dopant concentration for boron (Figure 4.3) and phosphorous (Refs. 34 and 104).

BGN data for extracting S instead of Boltzmann statistics and apparent BGN data (as in PC1D) [34]. The differences between the two methods are however small enough [34] for the trends to be compared:

1. Both types of diffused emitters show two regimes (a slow rising and a fast rising regime) and the value for N_0 (which affects where the two regimes cross-over) is ~$1x10^{19}$ cm^{-3} for both phosphorous and boron emitters.
2. As described in Ref. 34, the largest impact of using the F-D statistics method instead of Boltzmann statistics (and apparent BGN) is that the latter method results in lower S-values at high dopant densities (approx. ≥ $1x10^{19}$ cm^{-3}), i.e. the blue curve in Figure 4.5 would shift downwards if it were based on Boltzmann statistics. Based on this, it seems reasonable to conclude that thermal oxides passivate a boron diffused Si surface more poorly than a phosphorous diffused one. In a separate work, Altermatt *et al.* drew the same conclusion from their

measurements on a relatively small range of surface dopant densities [104]. Their extracted S_p^+ data points, again using F-D statistics, are also shown in Figure 4.4 for comparison.

The poorer passivation quality on boron doped surfaces may be due to a combination of a larger capture-cross-section for minority electrons at the Si/SiO_2 interface [105] and the small positive charge in thermal oxides which can cause depletion at the diffused surface [27]. Unfortunately, this problem is compounded by two additional concerns:

1. The impact of texturing.
2. The stability of the passivation over time

4.3.1.2 Thermal SiO_2 Passivation of Textured Boron Doped Si Surfaces

The surface of both lab-scale and industrial Si cells are usually textured to enhance the absorption of light. Unfortunately, texturing has been reported to degrade surface passivation quality, especially for boron diffused surfaces. On planar p^+ layers diffused using a BBr_3 source (surface concentration of ~5e18cm^{-3}) Benick et al. reported an S_p^+ of 5700cm/s using *ex-situ* SiO_2 passivation [102]. Using the same diffusion and passivation processes on an inverted pyramid textured surface, their S_P^+ value increased by a factor of 11 to 63,000 cm/s. Though no S_p^+ values were reported, a similar increase in J_0 was observed by Krygowski (Figure 4.5) using spin-on boron sources [52]. For sheet resistances in the range of 50-200 Ω/□, random pyramid texturing was found to result in a 10-12x increase in J_0 when the boron emitter was passivated with an *ex-situ* SiO_2 layer (Figure 4.7). For the same sheet resistance range, using an *in-situ* oxide resulted in a smaller 5-6 times increase in J_0. Using a doped APCVD SiO_2 source, King et al. reported a similar factor of 5 increase in J_0 due to texturing for an oxide passivated ~150 Ω/sq. emitter with surface concentration similar to that of Benick [33, 106].

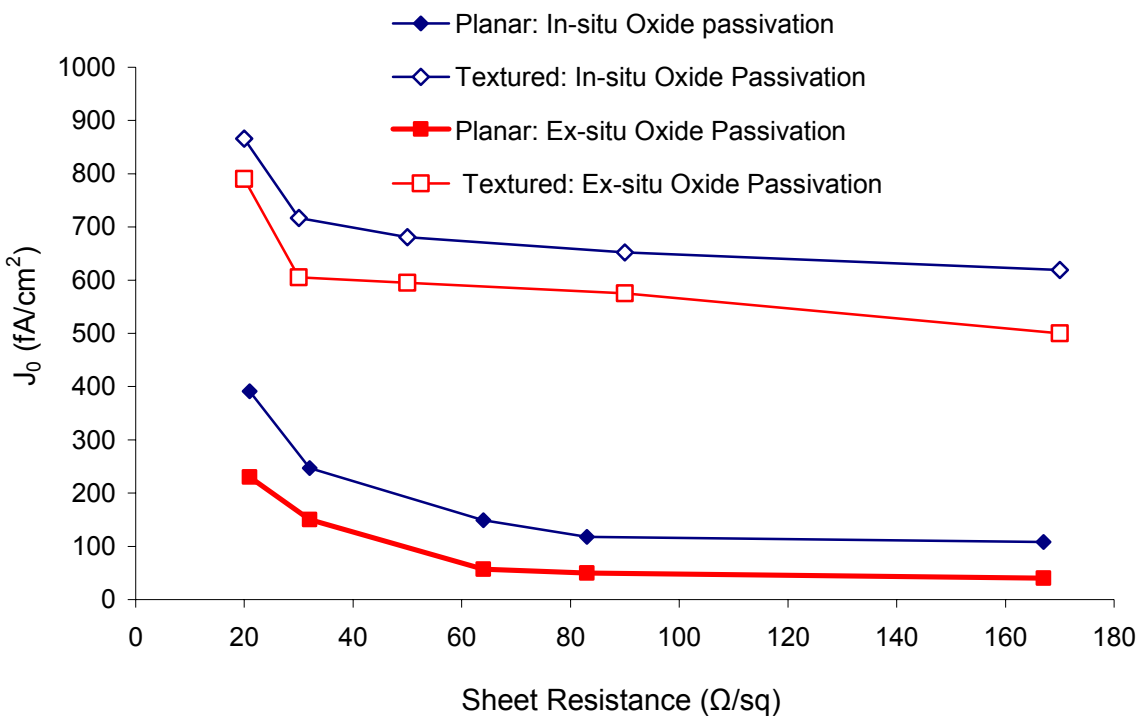

Figure 4.7 J_0 as a function of boron sheet resistance as reported by Krygowski on planar and textured surfaces using solid sources fabricated from spin-on dopants [52].

These results clearly indicate that texturing degrades the ability of thermal SiO_2 to passivate boron doped Si surfaces and that this degradation is independent of the dopant source used. Some increase in surface recombination after texturing a <100> planar surface is unavoidable due to the increase in surface area due to texturing (commonly assumed to be ~1.7x for random pyramid texturing) [34, 53] and due to the higher dangling bond density of the <111> textured surface. But it is worth noting that for a similar range of surface concentrations and sheet resistances, texturing increases the J_0 of oxide passivated *phosphorous* diffused surfaces by only a factor of 3 or less [53, 106].

In the context of B-BSF cells, the large negative impact of texturing suggests that the structure should be planar on the rear (B-BSF) side and textured only on the sunward-facing emitter side. However, single-side textured wafers are not favored in commercial

manufacturing because it requires at least one an additional step to either mask the rear side (before texturing) or etch back the rear side (after texturing). The trade-off between increased process complexity/cost (arising from using single-side textured wafers) and reduced B-BSF cell efficiency (arising from the texturing-induced passivation degradation) is explored in Chapters 6 and 7.

4.3.1.3 Temporal Stability of Thermal SiO_2 Passivation on Boron doped Si Surfaces

Commercial Si modules today have warranty periods of 20 years or greater. Therefore, stability of passivation over time is important. After a forming gas anneal, Altermatt *et al.* achieved some of the lowest J_0 values reported for thermal SiO_2 passivated boron emitters (Figure 4.6). Unfortunately, their excellent passivation degraded over a period two years of dark storage (Figure 4.8) [104]. Over the same period, the relationship between surface dopant concentration/sheet resistance and surface passivation quality also disappeared. When freshly passivated, J_0 and S_p^+ (extracted using Fermi-Dirac statistics) are lower for lower surface concentrations/higher sheet resistances (Figures 4.4). After the degradation however, Altermatt found that J_0 and S_p^+ were approximately constant for all doping densities (Figure 4.8). The degraded S_p^+ values were ~10,000-50,000 cm/s; an increase of more than an order of magnitude (see Figure 4.4). However, an FGA step was able to recover the passivation quality if TCA was used during oxidation. The recovery did not occur if TCA was omitted.

As both texturing and time appear to raise S_p^+ by about an order of magnitude, the worst-case scenario would appear to be a textured p^+ surface with unstable passivation. The results of Zhao *et al.* on n-type PERL cells with inverted pyramid textured, boron diffused emitters appears to confirm this fear – they reported a V_{OC} loss of up to 100 mV after 2-3 years of dark storage due to de-passivation of the textured, SiO_2-passivated boron emitter [107].

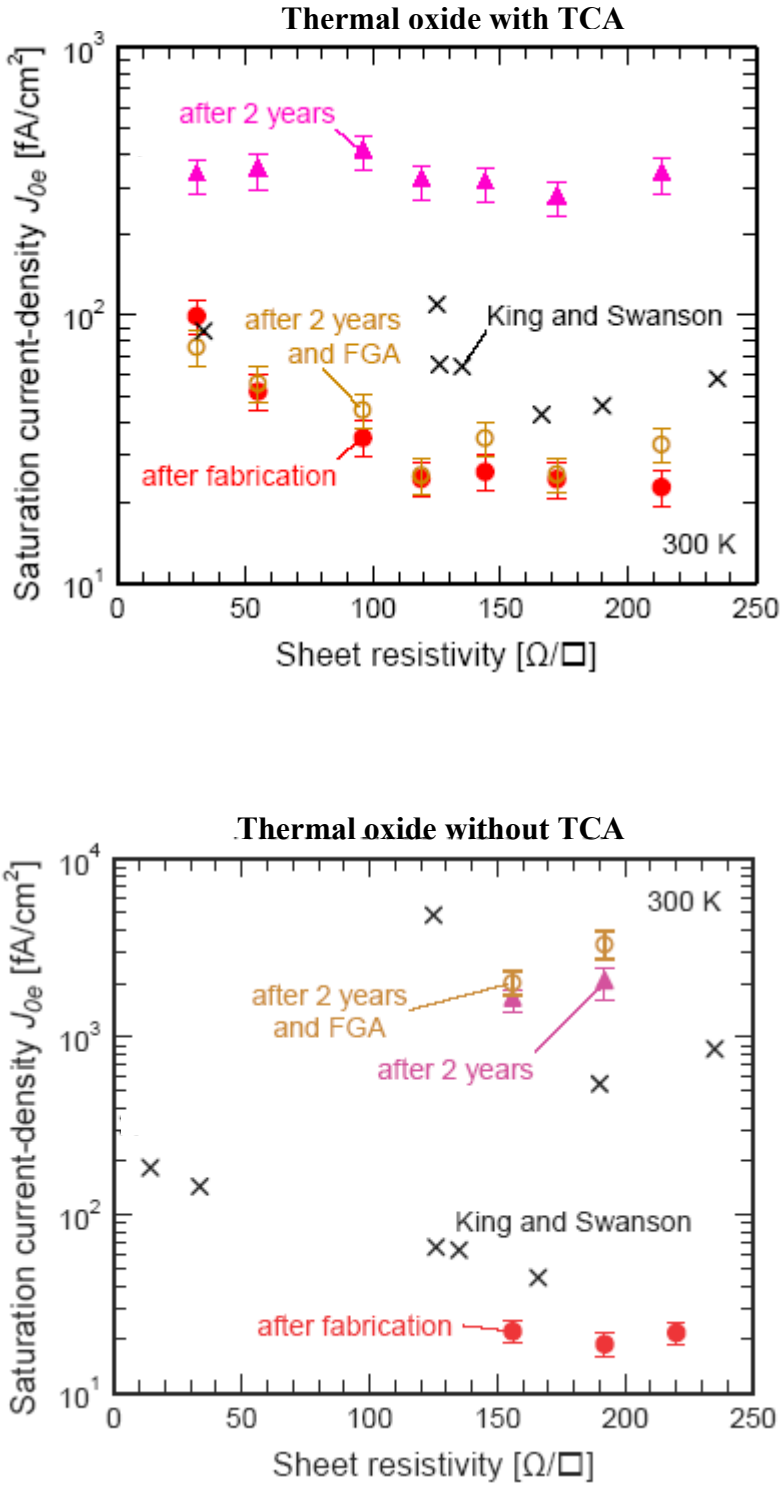

Figure 4.8 J_0 as a function of sheet resistance of forming gas annealed, thermal oxide-passivated, planar boron-diffused wafers [104].

4.3.2 PECVD Silicon Nitride Passivation of Boron Doped Emitters

Silicon nitride (SiN_X), usually grown using plasma enhanced chemical vapor deposition (PECVD), is perhaps the most widely used dielectric material in the PV industry. Due to a favorable index of refraction (~2.0) and excellent passivation of phosphorous diffused Si surfaces, it is widely used as the anti-reflection coating (ARC) and front passivating layer on p-type silicon solar cells [54, 69, 108]. However, PECVD SiN_X films provide exceptionally poor passivation on boron-doped p^+ surfaces, resulting in S_{P^+} values > 100,000 cm/s independent of the surface doping concentration (the corresponding J_0 values are ~1000 fA/cm^2) [104]. This is similar to the worst *post-degradation* passivation quality provided by thermal SiO_2 (Figure 4.8) [104]. While the high positive charge density of SiN_X has been speculated to be a cause of the poor passivation, the simulation work of Altermatt *et al.* indicates that poor interface quality is a more likely cause of the low quality passivation [104]. Chen *et al.* reported that annealing a SiN_X for 4 hours at 450 °C in a N_2 ambient resulted in much improved passivation [109]; however, such long anneal times may not be compatible with high-throughput industrial cell manufacturing.

4.3.3 SiO_2/SiN Stack Passivation of Boron Doped Emitters

On textured boron diffused surfaces, the passivation performance of as-deposited thermal SiO_2/SiN stacks is similar to or worse than that of SiO_2-only passivation [110, 111]. Veschetti *et al.* reported J_0 values of 700-1500 fA/cm^2 on textured 100-130 Ω/sq. boron emitters [111]. These values are comparable to those of Krygowski on textured surfaces (see Figure 4.5) using SiO_2-only passivation [52]. Notably however, a short firing cycle resulted in significant reduction of J_0 to ~90-150 fA/cm^2. These post-firing values on *textured* emitters are comparable to typical values for SiO_2-only passivation on *planar* boron emitters of similar sheet resistance [52, 94, 102, 104]. This suggests that hydrogenation of the p^+-Si/SiO_2 interface during firing can reverse the effect that

texturing has on SiO_2 passivation. Since it is not clear from the literature if firing a thermal SiO_2/SiN_X has a beneficial effect on planar boron emitters as well this topic is examined in Chapter 7.

Chemically grown oxide/SiN stack passivation has also been investigated and is currently thought be in production at Yingli [169]. It has been shown that firing a nitric acid SiO_2/SiN_X stack on a planar boron emitter results in a very large improvement in passivation [112]. Before firing, the passivation was comparable to SiN_X-only passivation. But post-firing, the J_0 was found to drop to just 23 fA/cm^2 which matches the best results obtained with Al_2O_3 passivation (see Section 4.3.4 below). This improvement was also attributed to hydrogenation of the Si/SiO_2 interface during firing.

4.3.4 Passivation of Boron Doped Emitters by Negatively Charged Dielectrics

Recently, negatively charged dielectrics have received significant attention because a high negative charge in the passivating dielectric provides field effect passivation in addition to interface passivation [102, 113-123]. Introduction of a negative charge density in thermal SiO_2 via corona charging was found to result in a large improvement of SiO_2 passivation quality on textured, boron doped surfaces [102]. As discussed in Sec. 2.5.1.2, Benick *et al.* reported a factor of 11 increase in S_P^+ when going from a planar (5700 cm/s) to a textured SiO_2-passivated p^+ surface (63,000 cm/s). However, addition of $3.2x10^{12}$ cm^{-2} charge density to the same SiO_2 layer (by corona charging) negated the effect of texturing, reducing S_p^+ on the textured surface to 4500 cm/s. On the cell level, this charge-induced improvement in the SiO_2 passivation resulted in a 2% (abs.) improvement in cell efficiency [102]. A similar beneficial effect was seen when corona charging was used to add a negative charge to unfired Si_3N_4/SiO_2 or $SiO_2/Si_3N_4/SiO_2$ stacks [113]. However, corona charging is not yet a commercial technique and data on the charge stability of these films over the 25-30 year life-span of a PV module is mixed [114, 115]. On relatively lightly boron-doped surfaces (boron concentration $\leq$ 1e16 cm^{-3}),

modeling work suggests that the charge density of a negatively corona charged $SiO_2/Si_3N_4/SiO_2$ stack will show only modest degradation over a period of 25 years, while Si_3N_4/SiO_2 stacks are considerably more unstable. UV-induced charge decay has also been reported, though the decay seems to be reduced under glass [115].

An alternate dielectric that has attracted recent interest is Al_2O_3 [116-123]. Although an extra annealing step is required to 'activate' Al_2O_3 passivation, excellent J_0 values of 6-70 fA/cm^2 have been reported on Al_2O_3-passivated, planar 30-150 Ω/□ boron diffused surfaces [116-121]. The excellent J_0 values provided by the annealed Al_2O_3 films are attributed to both field effect passivation from the high negative charge density (up to ~1e13 cm^{-3}) in the annealed films and also to high quality interface passivation from an interfacial SiO_x layer that either forms during the Al_2O_3 deposition or during the activation anneal [117, 118].

While these activation anneals are commonly performed for several minutes at 350-425°C, it has been shown that a short firing step is also able to activate the Al_2O_3 passivation. On a planar, industrial-type boron emitter (surface concentration ~8x10^{19} cm^{-3} and ~0.35 μm deep), J_0 values as low as ~60 fA/cm^2 and ~20 fA/cm2 were achieved using fired Al_2O_3 passivation and fired Al_2O_3/SiN_X stack passivation respectively [120-122]. The passivation provided by both was stable up to ~825°C. Critically, with the fired Al_2O_3/SiN_X stack passivation, texturing the emitter resulted in only a 2.5x increase in J_0. This is much lower than the ~5x-10x increase observed with thermal SiO_2 passivation (see Section 4.3.1 and Figure 4.7). While long-term stability of Al_2O_3 passivation has not yet been shown, accelerated testing under EVA/glass has shown that the passivation is UV-stable over a 2 year period [123].

4.3.4 Amorphous Silicon Passivation of Boron Doped Emitters

On boron emitters with sheet resistances in the range of ~20-200 Ω/sq., amorphous silicon/SiN_X stacks annealed at ~350°C provided J_0 values almost identical to those

obtained with forming-gas annealed thermal SiO_2 by Altermatt *et al.* (Fig. 4.6) [123] offering another good alternative for passivating boron doped surfaces. As with Al_2O_3, accelerated testing under EV/glass has shown that the aSi/SiN_X stack passivation is UV-stable [104].

4.4 Summary

Boron emitters/BSFs offer several advantages and disadvantages for next-generation solar cells. However, the challenge is to find a suitable low-cost boron diffusion source and passivating the resulting boron-doped surfaces. In this chapter, the literature on various boron diffusion sources were reviewed which shows that all sources have resulted in large degradations in bulk lifetime. BBr_3, which is toxic and pyrophoric, has been the most successful source with high post-diffusion bulk lifetimes being reported by a few research groups. Conversely, relatively safer spin-on/spray-on and printed sources have resulted in the lowest post-diffusion lifetimes. Therefore, an important task in this thesis is to develop a low-cost, non-toxic, spin-on source and a related process technology that provides high lifetimes and high cell efficiencies. Specifically, solutions of high purity boric acid and DI water will be examined in Chapter 5. The performance of common passivating dielectrics on heavily boron doped Si surfaces was also reviewed. Unlike phosphorous diffused surfaces, the most common dielectrics – thermal SiO_2 and SiN_X – have trouble providing high-quality, stable passivation on boron diffused Si surfaces. Relatively newer materials such as Al_2O_3 and a-Si appear to be more promising. Limited data suggests fired SiO_2/SiN_X stacks may also provide good passivation. Therefore, in Chapter 7, the passivation performance of fired thermal SiO_2/SiN_X will be examined along with that of various spin-on dielectrics.

Chapter 5

DEVELOPMENT OF BORIC ACID AS A SPIN-ON SOURCE FOR BORON DIFFUSION

As discussed in Chapter 4 (see Table 4.1 and Figure 4.2), the most successful boron diffusion source in terms of post-diffusion lifetime and cell efficiency has been BBr_3 which is pyrophoric and potentially toxic. Solid sources, spin-on dopants (SODs) and pastes are simpler and safer alternatives, but have thus far failed to match BBr_3 in terms of lifetime and cell efficiency. Therefore, this work examines if spin-on boric acid solutions can serve as an alternate spin-on source that combines low-cost, non-toxic characteristics with the high lifetimes achieved with the BBr_3 source. Since contaminants in SODs are thought to be the cause of their poor performance, boric acid was chosen for study as high purity boric acid is commercially available from several vendors [124, 125]. Additionally, boric acid is very safe – its median lethal dose (LD_{50} – a measure of toxicity) is similar to that of sodium chloride (table salt) and the boric acid solutions used in this work are only very weakly acidic [126, 127].

5.1 Chemistry of Boron Diffusion into Silicon using Boric Acid

First, the known chemistry of boron compounds was studied to see if a reaction pathway exists that will allow boric acid (H_3BO_3) to serve as a high temperature boron diffusion source [127, 128]. As discussed in Chapter 2, the first step in thermal diffusions of boron into silicon is the deposition of a layer of boric oxide (B_2O_3) onto the wafer surface. B_2O_3 then reacts with Si to liberate B atoms (Equation 4.1) which can diffuse into the wafer. The conversion of boric acid (H_3BO_3) into B_2O_3 proceeds as follows.

Boric acid (H_3BO_3) is a hydrate of boric oxide (B_2O_3) which exists in the crystalline phase [127].

$$B_2O_3 .3\ H_2O = 2\ H_3BO_3 \quad (5.1)$$

Diffusing boron from boric acid into silicon involves a two-step dehydration of boric acid. First, metaboric acid (HBO_2) is formed at temperatures beyond ~130°C [127, 128]. Metaboric acid is also a hydrate of B_2O_3 and its three phases co-exist as a mixture.

$$H_3BO_3 + \Delta \rightarrow HBO_2\text{-III} + H_2O \text{ (orthorhombic phase)} \quad (5.2)$$
$$\rightarrow HBO_2\text{-II} + H_2O \text{ (polyclinic phase)}$$
$$\rightarrow HBO_2\text{-I} + H_2O \text{ (cubic phase)}$$

Anhydrous boric oxide (B_2O_3) starts to form when this mixture is heated beyond 250°C. At 350°C, over 90 wt. % of the mixture is in the form of B_2O_3.

$$2\ HBO_2 + \Delta \rightarrow B_2O_3 + H_2O \quad (5.3)$$

B_2O_3 then reacts with silicon to liberate boron atoms which diffuse into silicon at high temperature.

$$2\ B_2O_3 + 3\ Si \rightarrow 3\ SiO_2 + 4\ B \quad (5.4)$$

Note that Equation 5.4 is identical to Equation 4.1 from Section 4. It has been repeated here for the reader's convenience.

5.2 Fabrication of Boric Acid based Spin-on Sources

To experimentally verify the feasibility of using boric acid as a diffusion source, spin-on dopant (SOD) sources were created by dissolving boric acid (> 99.999 %, Sigma Aldrich Corp.) in de-ionized (DI) water [124]. Boric acid exists as white, flaky crystals at room temperature so a liquid carrier is required if boric acid is to be used as a spin-on source. In this work, DI water was chosen as the carrier solvent for multiple reasons:

1. It is easily available in large quantities as is continuously created in-house in order to support wet processing steps.
2. DI water is also heavily used in industrial PV manufacturing. Therefore, a boric-acid/DI H_2O source can be easily created in an industrial setting.

3. Organic solvents (which are often used in commercial SODs) vaporize easily at room temperature which can change the dopant concentration in the SOD mixture over time. Low temperature and low humidity conditions are also required to slow down the decomposition of organosilicate materials such as TEOS which may be present in the SOD mixture [52, 129]. Maximizing the shelf life of common commercially available, spin-on sources therefore requires refrigerated storage and re-warming of the SOD before use. In contrast, the boric acid/DI water solutions used here are very stable at room temperature and across a wide range of humidity conditions as demonstrated later in this chapter.

As mentioned earlier, the boric acid/DI H_2O source is also very safe. No volatile, toxic or pyrophoric materials are created during the diffusion process either.

5.3 Diffusion from Boric Acid/DI Water Sources

Prior to depositing the boric acid solutions on to test Si wafers, the wafers were cleaned and a chemical oxide layer was grown in a 2:1:1 H_2O:H_2O_2:H_2SO_4 solution. This final step makes the surface hydrophilic and is essential for uniform spreading of the boric acid/DI H_2O source during spin-coating and for obtaining uniform sheet resistances after diffusion. On hydrophobic surfaces, the coated film was very non-uniform with visible streaks and large flakes of boric acid decorating the wafer surface after spin-coating. Uniform coating of a wafer does not, however, guarantee uniform and repeatable diffusion as discussed in the following sub-sections.

5.3.1 Single Slot Loading

In the first attempts at diffusion using spin-on boric acid sources, wafers were loaded into the carrier boat with one wafer per slot, with the boric acid coated sides facing each other. While diffusion did occur with this loading method, the sheet resistance across

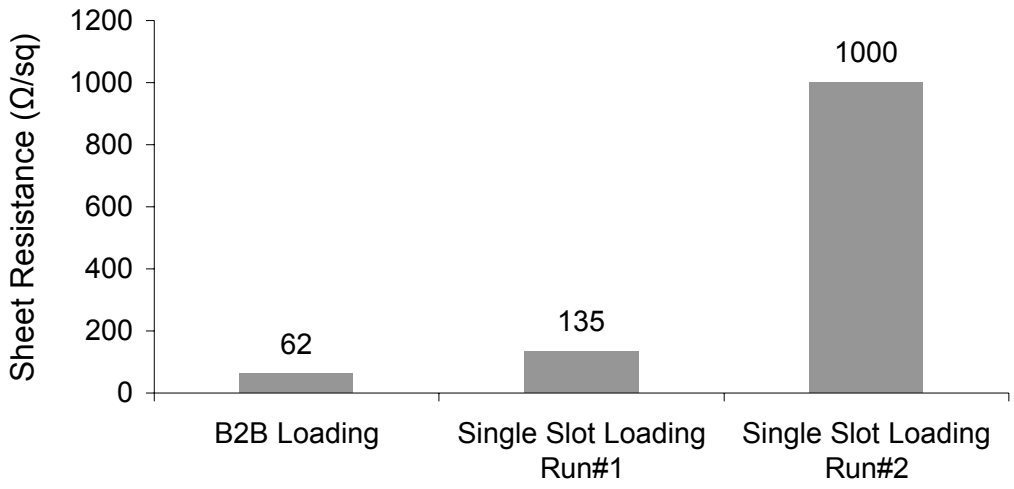

Figure 5.1 Sheet resistance measured on boric acid coated wafers using the B2B and single-slot loading methods after a 60 minute diffusion in N_2 at 950°C.

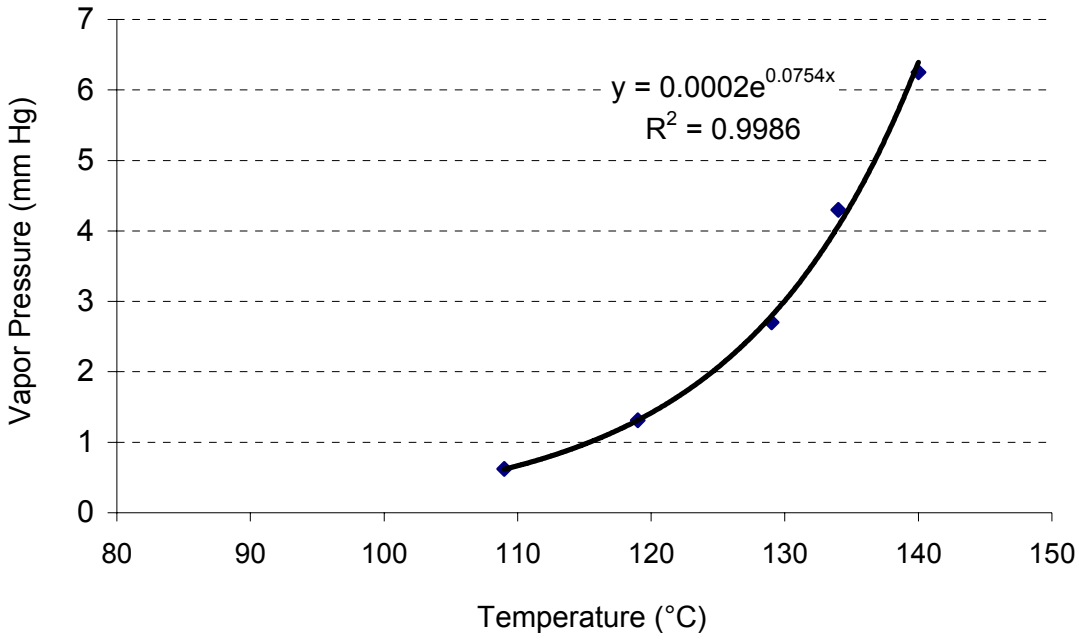

Figure 5.2 Vapor Pressure of boric acid (H_3BO_3) in the presence of steam (from Ref. 127). The solid line is a least-squares fit to the data.

runs was found to be very erratic (Figure 5.1). This variability is likely the result of the sensitivity of the vapor pressure of boric acid to temperature (Figure 5.2). While boric acid has a vapor pressure < 1 atm. at room temperature, it rises very quickly with temperature. At just ~120°C, the vapor pressure of boric acid is > 1 atm. resulting in vaporization of the source. Though the temperature of the boat during wafer loading was not directly measured, the furnace temperature during loading was always at ~800°C; it is therefore likely that a significant fraction of the boric acid source vaporized during the loading process. As atmospheric pressure can vary with the local weather, the single slot loading method is an unreliable method of performing diffusion using boric acid.

5.3.2 Back to Back Loading in One Slot

In order to combat vaporization during loading, wafers were loaded back to back (B2B) with two wafers in the same slot. In addition, only one wafer in each slot was coated with boric acid. It was found that this loading method produced the same sheet resistance on both wafers in each slot. As shown in Figure 5.1, the B2B loading method resulted in much lower sheet resistance than the single slot loading method. Furthermore, the results were reproducible as discussed later in this chapter.

5.3.3 Pre-Diffusion Treatment using Rapid Thermal Processing

An alternate method for getting around the vaporization problem was also developed in which boric acid coated wafers were loaded into a rapid thermal processing chamber and ramped to 850°C (1s hold time) at a rate of 80°C/s before loading into a diffusion tube furnace for further diffusion. This rapid thermal treatment ‘fixes’ the boric acid by converting it to B_2O_3 following Equations 5.1 through 5.3. Presumably, due to the rapid ramp rate, the reactions in Equation 5.1 through 5.3 occur faster than the loss of boric acid due to vaporization. With this ‘fixing’ pre-treatment, reproducible sheet resistances

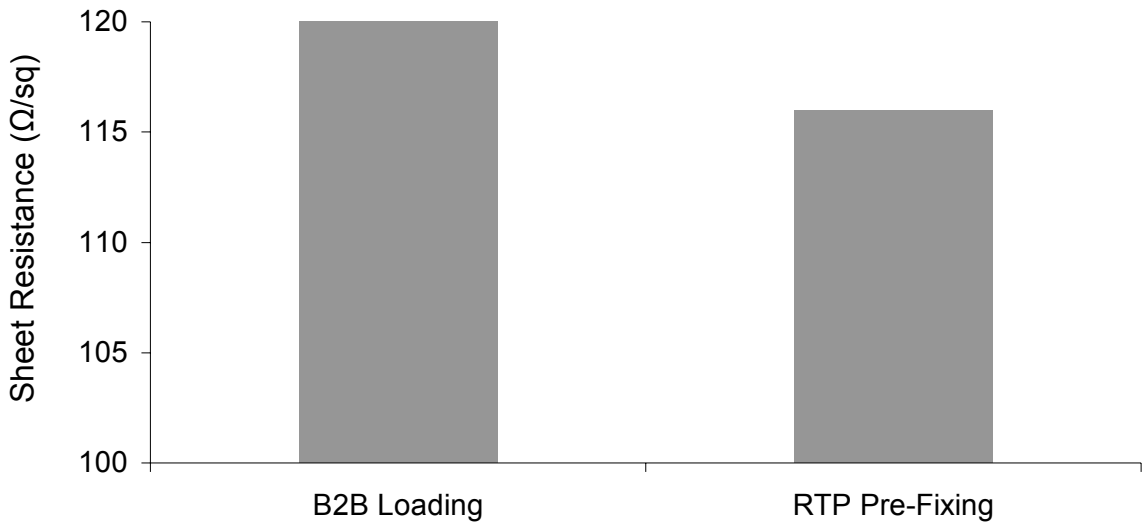

Figure 5.3 Sheet resistance measured on boric acid coated wafers using the B2B loading and RTP pre-fixing methods after a 60 minute diffusion at 925°C in N_2.

can be obtained using single-slot loading. However, this method involves one additional step and results in roughly the same sheet resistance as the B2B method (Figure 5.3).

As the B2B loading method is simpler, halves the use of boric acid and the spin-coating time (as only every other wafer in a pair needs to be coated), and doubles boat utilization (due to two wafers being in each slot), the RTP fixing method was not pursued further. For nearly all the work presented in this thesis, the B2B loading method was used.

5.3.4 Diffusion Results on Planar Wafers

The solubility limit of boric acid in water is ~5 wt.% at room temperature [127]. However, the solutions created in this work never approached the solubility limit. As Figures 5.4 to 5.7 show, by adjusting the boric acid concentration from 0.5 wt.% to just 2 wt.% and controlling the diffusion time and temperature, boric acid/DI H_2O sources can be used to form emitters with junction depth ranging from 0.2-1.6 μm and sheet resistance ranging from 20-200 Ω/sq.

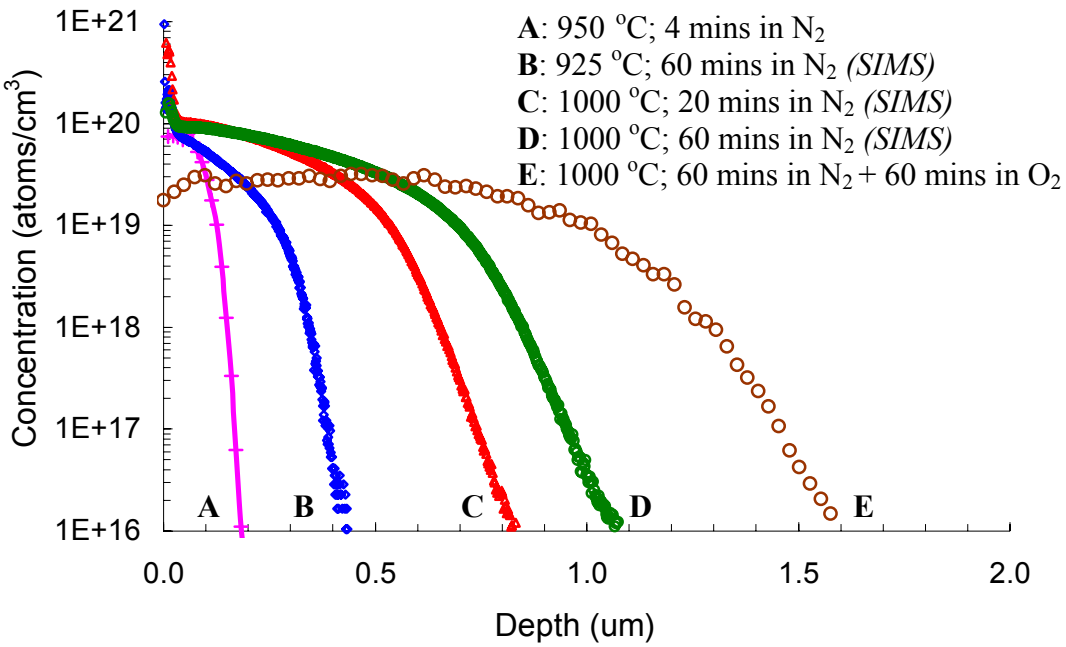

Figure 5.4 Boron profiles after diffusion at 925-1000 °C using 0.5-1 wt.% boric acid/DI H_2O sources as determined by SIMS (where indicated) or the spreading resistance method.

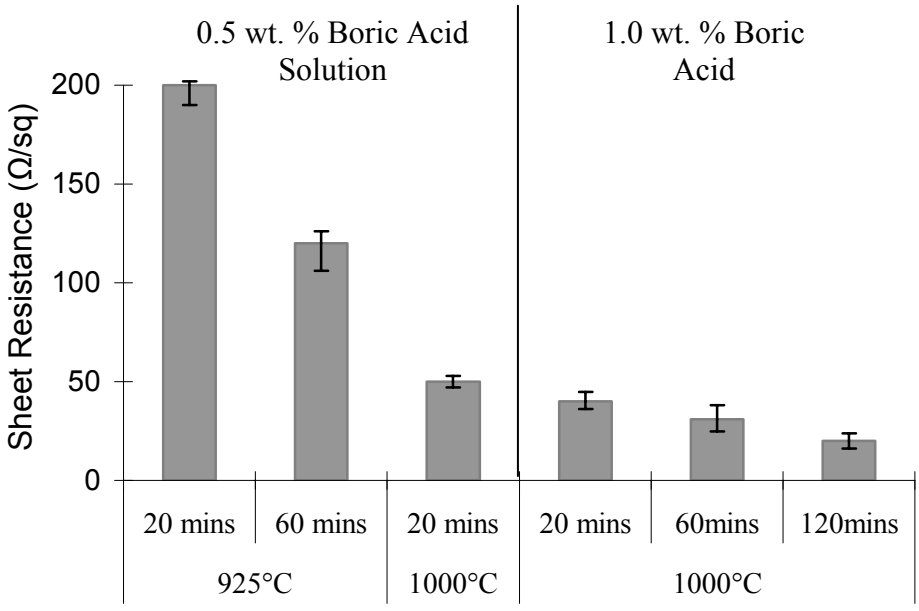

Figure 5.5 Sheet resistances achieved through diffusion with boric acid/DI water spin-on sources by controlling the source concentration and diffusion conditions.

Such flexibility is useful in solar cell design because different profiles have different uses – high surface concentrations make it easier to form ohmic contacts to diffused regions using SP pastes while low surface concentrations can improve passivation quality. Thin, lightly diffused regions are preferred for the sunward facing emitter layer (as this reduces parasitic absorption within the emitter) while deeper, more heavily doped layers are often used for BSFs (see Table 4.1) in order to maximize field effect passivation. The wide range of doping profiles and sheet resistances achieved demonstrates that boric acid is a viable boron source for a wide range of solar cell designs.

As discussed in Section 4, a boron rich layer or BRL forms at the Si surface if the boron source can keep the wafer surface saturated with boron atoms over the course of the diffusion process. For the diffusion temperatures shown in Figure 5.1, the solid solubility limit is $< 2x10^{20}$ cm^{-3} according to Ref. 67. The surface concentration for all the SIMS profiles in Figure 5.4 exceeds this limit which suggests the presence of a BRL. This indicates that for up to a ~60 minute diffusion at 1000°C, very dilute solutions of

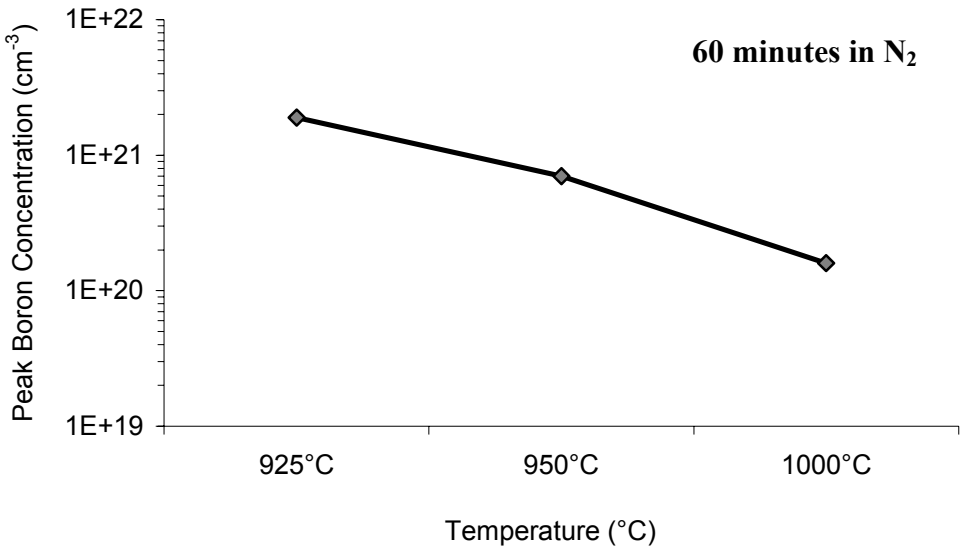

Figure 5.6 Peak boron concentrations after 60 minute diffusions in N_2 using a boric-acid/DI water source as measured using SIMS.

boric acid are 'quasi-infinite' sources in the sense that they can keep the Si surface saturated with boron atoms over the course of the diffusion process. The peak concentration of this BRL region does however drop with increased time and temperature. This may be due to diffusion of boron from the BRL as discussed in Chapter 4. An example of this drop in the peak boron concentration in the BRL is shown in Figure 5.6.

It can be inferred from Figure 5.7 that this 'quasi-infinite' characteristic holds for boric acid concentrations down to 0.5 wt. %. Using higher concentrations has a minimal impact on sheet resistance which indicates that the 0.5 wt. % solution does not get depleted over the course of the process. If a more easily depleted source is required for any application (such as a low surface concentration emitter layer), that role can also be served by boric acid/DI water solutions simply by reducing the boric acid concentration.

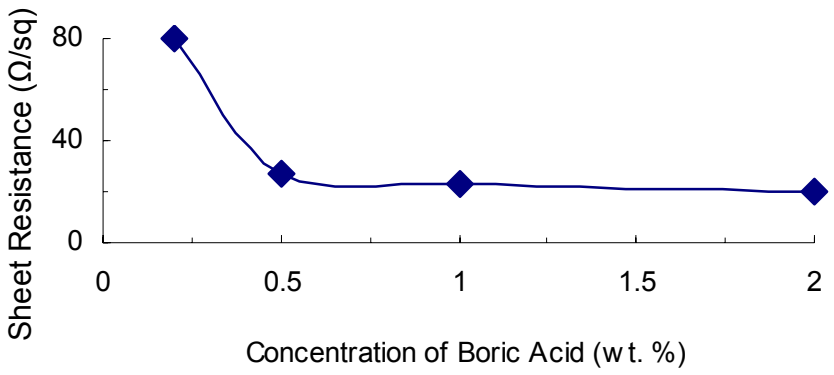

Figure 5.7 Sheet resistance of planar boron emitters diffused at 1000°C for 60 minutes using boric acid/DI water sources as a function of boric acid concentration.

5.3.5 Reproducibility of Boric Acid Diffusions

The reproducibility of diffusions with the boric acid spin-on solutions was tested since commercial SOD sources have been reported to be sensitive to age, storage temperatures and the ambient relative humidity and temperature during spin-coating [52, 129]. Figure 5.8 shows that the boric acid solutions are fairly insensitive to age, temperature and humidity. Over a ~ 1 year period, the standard deviation in sheet resista-

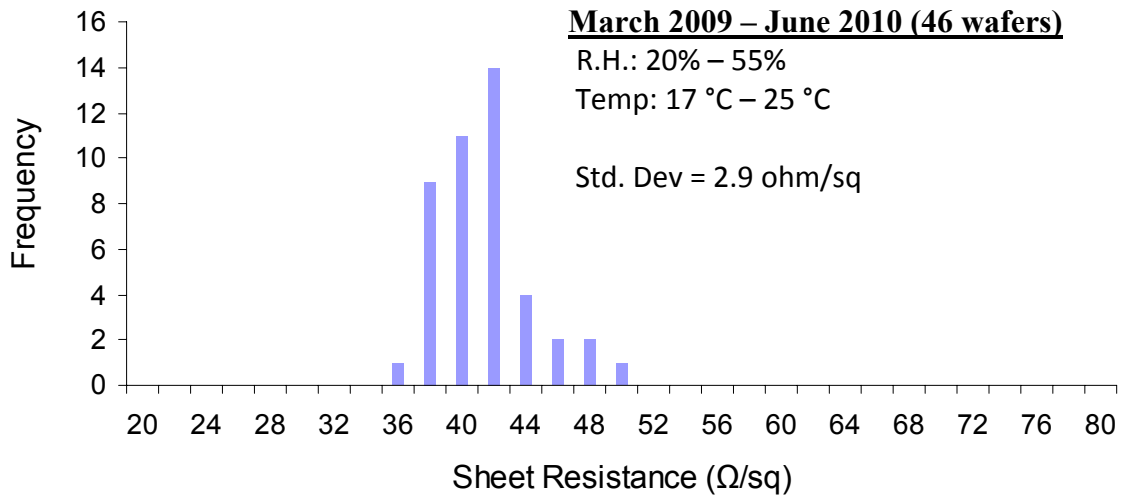

Figure 5.8 Histogram of sheet resistances obtained over time with the B2B loading method using the same diffusion process.

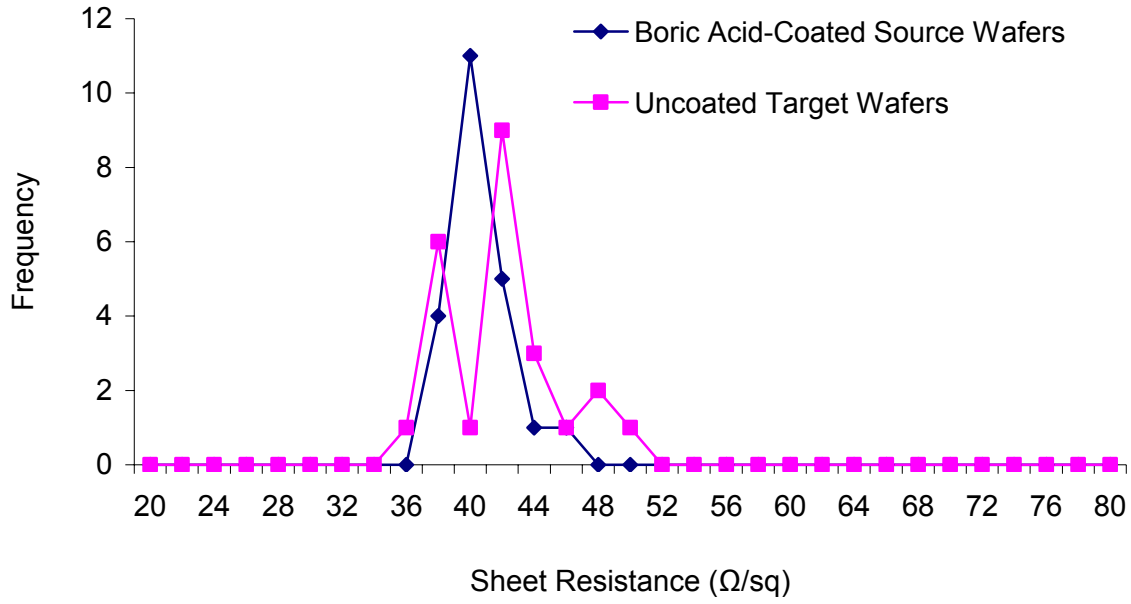

Figure 5.9 Histogram of sheet resistances over time achieved on source and target wafers with the B2B diffusion method. The data here is the same as in Figure 5.8.

nce was just 3 Ω/sq. despite large in ambient relative humidity (20% to 55%) and moderate temperature variations (17-25 °C). The shelf life of the boric acid solutions (i.e.

the period over which reproducible doping can be obtained) is at least 6 months. The upper limit of the shelf life has not been determined as the stocks of solutions prepared for this work ran out in 6 months or less.

The data in Figure 5.8 is re-plotted in Figure 5.9 by splitting the histogram into two – one for source wafers and the other for target wafers. As mentioned above, in the B2B loading method, only one wafer out of each pair is spin-coated with boric acid. Figure 5.9 demonstrates that with just one spin-coat, two wafers can be equally diffused.

5.3.6 Diffusion of Textured Wafers using Boric Acid/DI H_2O Spin-On Sources

With spin-on sources, non-uniform spreading of the source on rough, textured surfaces is a concern since discontinuities in diffused regions can affect cell performance. Therefore, the ability of spin-on boric acid/DI water sources to uniformly dope a random pyramid textured surface was checked using SEM imaging. Several samples up to ~6 cm long were imaged to allow reasonably large sections to be checked. Differences in doping concentration and dopant type show up in SEM images as a contrast difference [130] – the p^+ emitter formed using the spin-on boric acid source is clearly visible as a bright line in the SEM image in Figure 5.10.

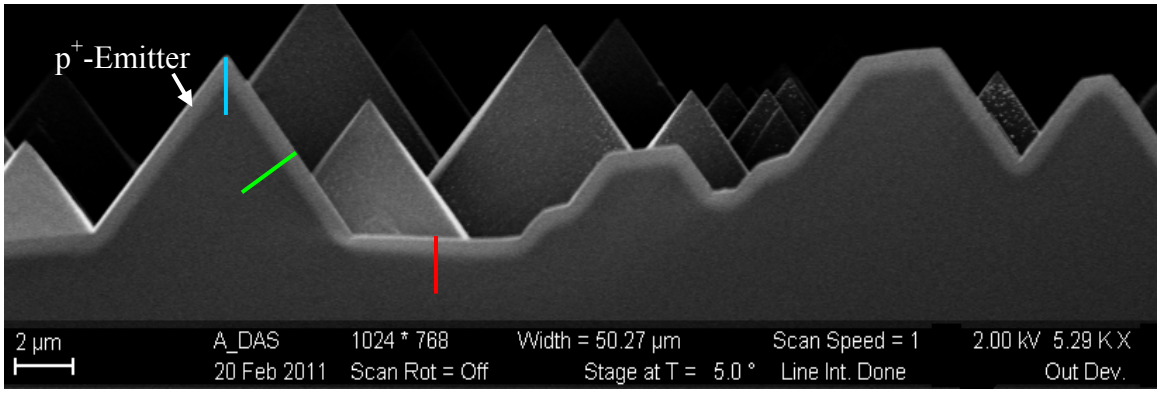

Figure 5.10 SEM image of a boron diffused layer formed on a textured surface using a boric acid/DI water spin-on source. Pixel intensity profiles of the marked regions are shown in Figure 5.11.

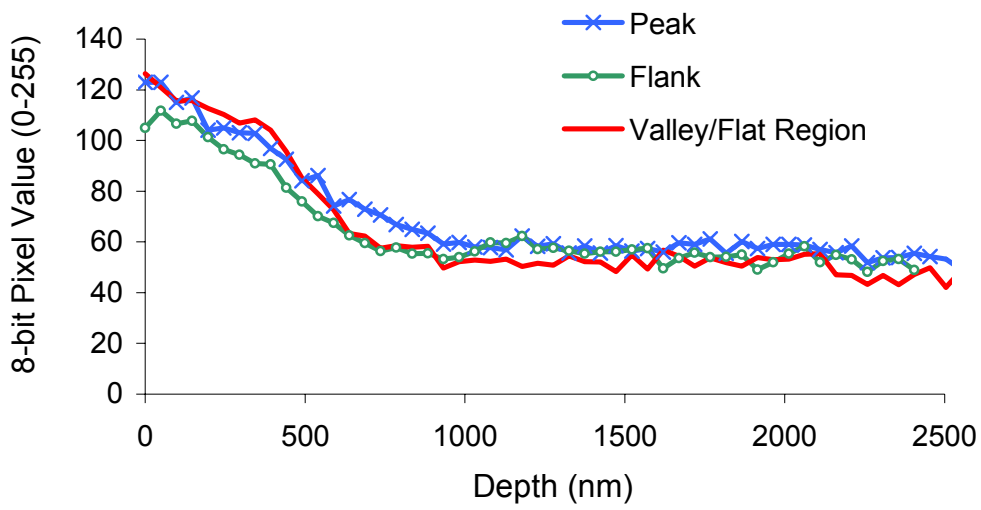

Figure 5.11 Pixel intensity profiles of the peak, flank and valley regions marked in Figure 5.10.

While no discontinuities in the diffused region were observed, it is difficult to determine from visual examination whether the junction depth varies across the rough surface. Elliot *et al*. have shown that the intensity/brightness of a doped region (stored as an 8-bit pixel value in the SEM images) is directly related to the ionized p^+ dopant concentration [130]. This provides a quantitative method of estimating junction depth from SEM images as variation in the pixel value across the p^+-n junction – referred to here as a 'pixel intensity profile' – can be extracted from the images. A few examples of such profiles are shown in Figure 5.11. From such measurements it was found that the depth of junctions formed using a spin-on boric acid solution is fairly uniform in the peaks, flanks and valleys of the textured surface. That said, the junction depth at the pyramid peaks does tend to be deeper than at the flanks/valleys. The opposite case – the junction depth being deeper at flanks/valleys – was never observed. However, the depth variation was small – the junction at peaks was deeper than the junction at neighboring valleys and flanks by only ~0.15 μm or less.

5.4 Summary

In this chapter, boron diffusion from spin-on boric acid/DI water solutions was experimentally demonstrated. Vaporization of the source during wafer loading is a concern that can be addressed by either loading two wafers in one slot in a source/target configuration or with a short, rapid thermal step to 'fix' the source onto the wafer. By controlling the boric acid concentration in the solutions, and the diffusion time and temperature, a wide range of sheet resistances and doping profiles compatible with high efficiency solar cells (see Chapter 6) can be achieved. The stability of boric acid/DI water sources and reproducibility of doping from these sources was also demonstrated. Finally, uniform diffusion on random pyramid textured surfaces was confirmed.

Chapter 6

MODELING AND DESIGN OF A 20% EFFICIENT B-BSF CELL STRUCTURE

In Chapter 3, modeling showed that obtaining a 20% efficient cell requires a BSRV or S_{p/p^+} (the S at the p/p^+ interface) of ~200 cm/s (subject to the constraint that the front-side processing of the cell is identical to that of the 18.9% Al-BSF baseline cell). Chapter 5 showed that boric acid/DI water solutions are viable sources for fabricating a B-BSF. The focus of this chapter is to establish, via PC1D modeling, a cell design and a boron diffusion process that can achieve the desired BSRV and efficiency targets.

While many cell designs/processes can hit the required BSRV and efficiency targets, having a commercially relevant structure/process is an important consideration of this thesis. Therefore, the modeling in this chapter was subjected to the following constraints:

1. No step in the B-BSF cell process should be longer than the longest step in the baseline Al-BSF process in order to maintain the same throughput, and
2. Minimize the number of process steps to minimize process cost.

As the longest step in the baseline Al-BSF process is a ~90 minute long $POCl_3$ diffusion, the goal is to find a B-BSF cell process that can achieve 20% while keeping the lengths of all the individual steps ≤ 90 minutes.

6.1 Choice of Cell Structure and B-BSF Profile

Figures 6.1 (a) and (b) show two candidate structures for a B-BSF solar cell. The structure with the fully metallized rear is clearly the simpler structure and would require the addition of just one step to the Al-BSF process, namely boron diffusion. The more complex local contact structure would require at least 3 additional steps – boron diffusion, rear dielectric surface passivation and a metal layer which would interconnect the rear

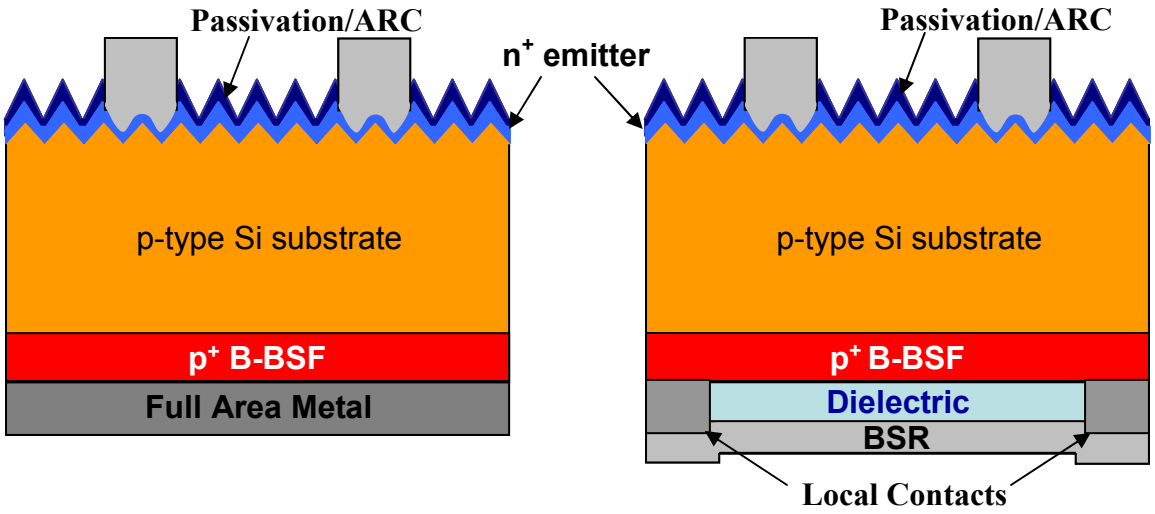

(a) (b)

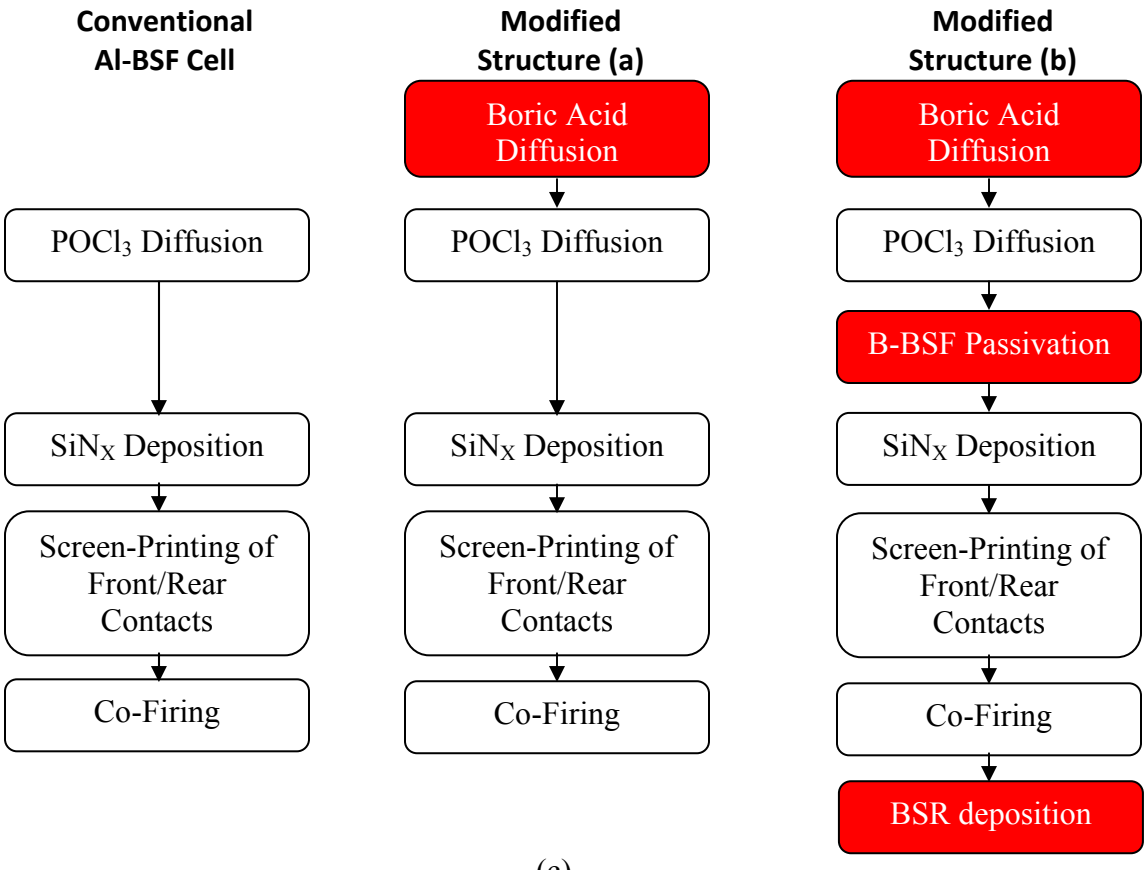

(c)

Figure 6.1 Structures and simplified process sequences for candidate B-BSF solar cells – (a) full-area metal contact B-BSF cell, (b) local-contact B-BSF cell and (c) comparison of their process sequence with that of a basic SP Al-BSF cell.

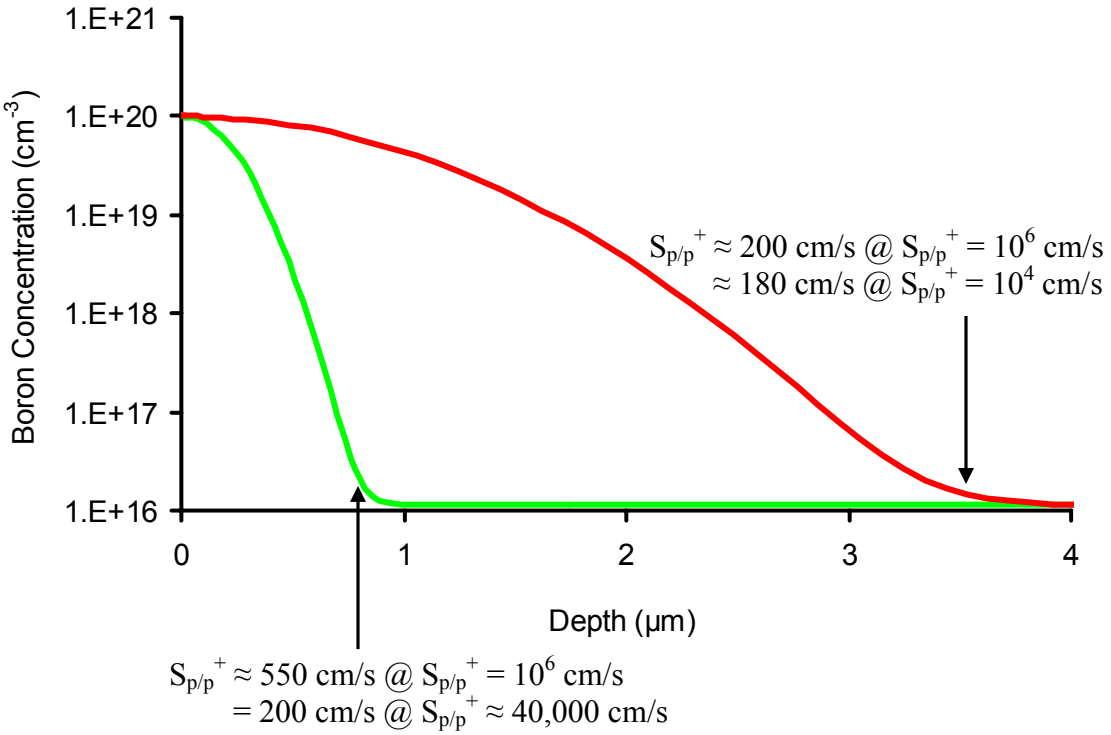

Figure 6.2 Candidate B-BSF profiles and surface recombination velocities for 20% efficient SP cells.

local contacts and also serve as the BSR.

In order to find an appropriate B-BSF profile that can achieve 20% efficiency with the simpler, fully-metallized structure, the 20% efficient PC1D model from Chapter 3 was extended to include a Gaussian p^+ profile on the rear side to model a B-BSF. Simulations run with this extended model showed that with no passivation of the B-BSF (i.e. full-area metallization), a ~3.5 μm deep B-BSF with surface concentration of $1x10^{20}$ cm^{-3} is required (red curve in Figure 6.2) to attain the target S_{p/p^+} value of 200 cm/s. Such a heavily doped BSF is considered to be electrically 'opaque' as the S_{p/p^+} value is *not* sensitive to the recombination velocity at the p^+-Si surface (referred to here as $S_{SURFACE}$ or S_{p^+}). As noted in Figure 6.2, the S_{p/p^+} value for such an opaque BSF is ~200 cm/s for $S_{SURFACE}$ ~$1x10^6$ cm/s (metallized p^+-Si surface) or 10,000 cm/s (well passivated p^+-Si surface). The down-side of this concept is that achieving such a deep boron BSF requires

high processing temperatures and long processing times. King and Swanson reported processing time > 5.5hrs and peak processing temperature of 1120°C for boron emitters of similar depth [33]. Such a prolonged diffusion step means that the simpler, fully-metallized B-BSF structure (Figure 6.1 (a)) does not meet the manufacturability criteria that all steps in the cell process sequence be ≤ 90 minutes long.

The experimental diffusion work done in Chapter 5 revealed that the most heavily doped emitter that could be achieved with a ~90 minute long process time (including temperature ramps) and a relatively reasonable peak temperature of 1000°C is only ~0.8 μm deep (see Figure 5.3 – curve C). In contrast to the opaque B-BSF process, this diffusion lasts < 30 minutes at 1000 °C; the resulting BSF has a sheet resistance of ~35 Ω/□. Unfortunately, such shallow BSFs are electrically 'transparent' so the S_{p/p^+} value is *very* sensitive to recombination at the p^+-Si surface. Using the Gaussian approximation of the experimental profile, when no passivation is applied (i.e. a fully metallized BSF with S_{p^+} of ~$1x10^6$ cm/s), the BSRV is ~550 cm/s; a value very similar to that of the baseline screen-printed Al-BSF cell (600 cm/s). In order to achieve the target S_{p/p^+} of 200 cm/s using this transparent B-BSF, S_{p^+} ~ 40,000 cm/s is required. This means that if the process throughput of the baseline Al-BSF cell is to be maintained, increased process complexity in the form of an additional passivation step and local contacts (Figure 6.1 (b)) is unavoidable.

6.2 Summary

The PC1D modeling work in this chapter showed that while fully metalizing the rear of the B-BSF cell minimizes the number of processing steps, achieving 20% efficiency with such a structure requires a very long and very high temperature boron diffusion step that is likely to be unattractive for commercial production. Therefore, based on model calculations, a more complex cell structure with a passivated, transparent B-BSF and rear

local contacts is proposed and selected in this thesis for achieving the goal of a 20% efficient, low-cost, screen-printed B-BSF solar cell.

One potential advantage of giving up process simplicity in exchange for a higher throughput and lower thermal-budget process is higher bulk minority carrier lifetime. As discussed in Chapter 4, reduced bulk lifetimes in processes utilizing boron diffusion have been reported for numerous boron sources — the loss in lifetime has been associated with the generation of gliding misfit dislocations and the introduction of contaminant species such as Fe [85, 86, 90]. Both misfit dislocation generation and Fe contamination are more likely to occur with prolonged, high-temperature processes [91, 131]. It is important to note that in the modeling done here, it was assumed that B-BSF cell processes will result in the same bulk lifetime (~450 μs) as the Al-BSF process. This assumption is relaxed in Chapter 8 which deals with process-induced lifetime degradation.

Chapter 7

DEVELOPMENT OF DIELECTRIC PASSIVATION FOR A 20% EFFICIENT, TRANSPARENT BORON BACK-SURFACE-FIELD SOLAR CELL

In the previous chapter of this thesis, a combination of experimental and modeling work was used to show that boron back surface fields (B-BSFs) that can be formed with a relatively short (≤ 90 minutes) diffusion cycle are electrically 'transparent' and need to be passivated in order to achieve high efficiencies. Modeling indicated that in order to achieve a 20% efficient SP B-BSF cell, an effective BSRV (S_{p/p^+}) of ~200 cm/s is required. In this chapter, several dielectrics are examined with the goal of identifying a material/process combination that can meet or exceed this passivation requirement in a relatively short (≤ 90 minutes) thermal cycle. The effect of negative charge in the passivating dielectric is also examined experimentally and through modeling.

7.1 Experimental

The passivation quality of various dielectric materials was quantified via saturation current density (J_0) and Implied V_{OC} measurements using the Transient-PCD and QSS-PC methods respectively [29, 51].

The J_0 samples are high resistivity (500-700 Ω-cm) n-type FZ wafers that were symmetrically boron diffused and passivated (Figure 7.1). Such high resistivity wafers were used as the Transient-PCD method requires that the base to be under high-level injection [29]. To extract the recombination velocity at the p^+ surface (S_{p^+}) from the J_0 measurements, the PC1D modeling program [16] was used. First, the SIMS profile of the BSF under study was imported into PC1D to create a p^+/n junction and S_{p^+} was fixed at a guessed initial value (the electron and hole recombination velocities were assumed to be

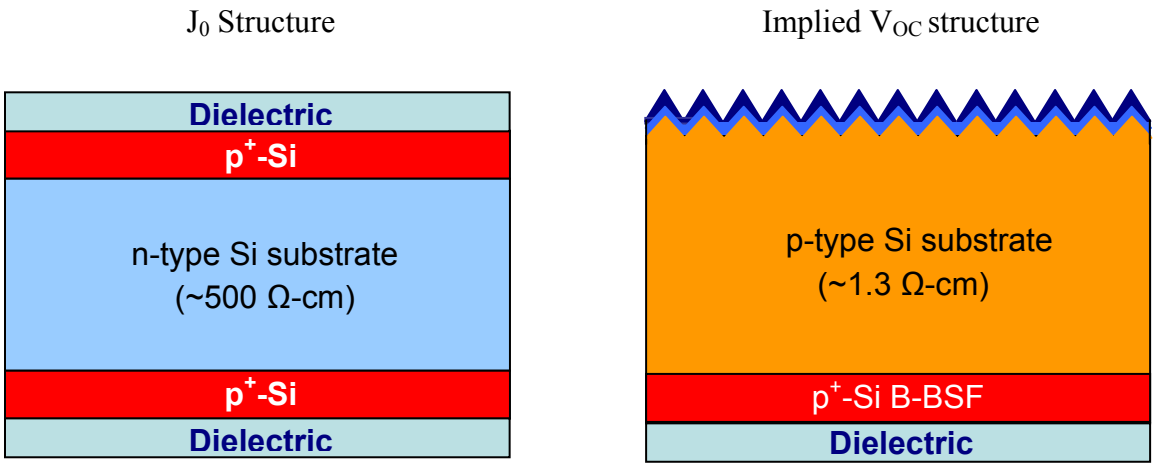

Figure 7.1 Schematics of test structures used for saturation current density (J_0) and implied open-circuit voltage (Implied V_{OC}) measurements.

equal). The p^+/n junction was then DC biased at 0.4V, and the simulated minority carrier current density (J_n) at the depletion edge in the emitter was converted to a J_0 value using:

$$J_n = J_0 e^{\frac{qV}{kT}} \tag{7.1}$$

where V is the applied DC bias (0.4 V). The S_p^+ value was then iteratively changed till the modeled J_0 at the depletion edge *in the emitter* matched the measured J_0. The calculated J_0 at the depletion edge *in the base* can also be used; the modeled J_0 at both depletion edges is nearly identical as recombination within the depletion region is small. Therefore, S_p^+ extraction is not strongly dependant on which depletion edge is used to match J_0. Note that the p^+/n junction can also be excited using an optical pulse (as is done in the experimental J_0 measurements); in PC1D, both methods were tried for a few cases and were found to be equivalent.

For the Implied V_{OC} measurements, 1.3 Ω-cm FZ Si wafers were diffused on the rear side with the same B-BSF used in the J_0 measurements and diffused on the front with the same $POCl_3$ emitter used for the baseline 18.9% Al-BSF cell (see Chapter 4). The B-BSF

was passivated with the same dielectrics used in the J_0 studies while the emitter was passivated with the same oxide/SiN_X stack used for the baseline Al-BSF cell.

7.2 Initial Passivation Studies

The B-BSF selected for cell fabrication (see Section 6.1) is ~0.8 µm deep and has a sheet resistance of ~35 Ω/sq. before passivation. However, the initial passivation studies in this thesis (which were performed before the ~35 Ω/sq. BSF was selected), used a more lightly doped ~80 Ω/sq. BSF. Figure 7.2 shows the profile of this BSF before and after passivation with a thermal oxidation step. The diffusion was performed at 925°C for 60 minutes followed by oxidation/drive-in at the same temperature. Note that this diffusion condition was not considered for cell fabrication as the total process time is longer than the 90 minute time limit imposed on all cell process steps in order to maintain the same throughput as the baseline Al-BSF process (see Chapter 6).

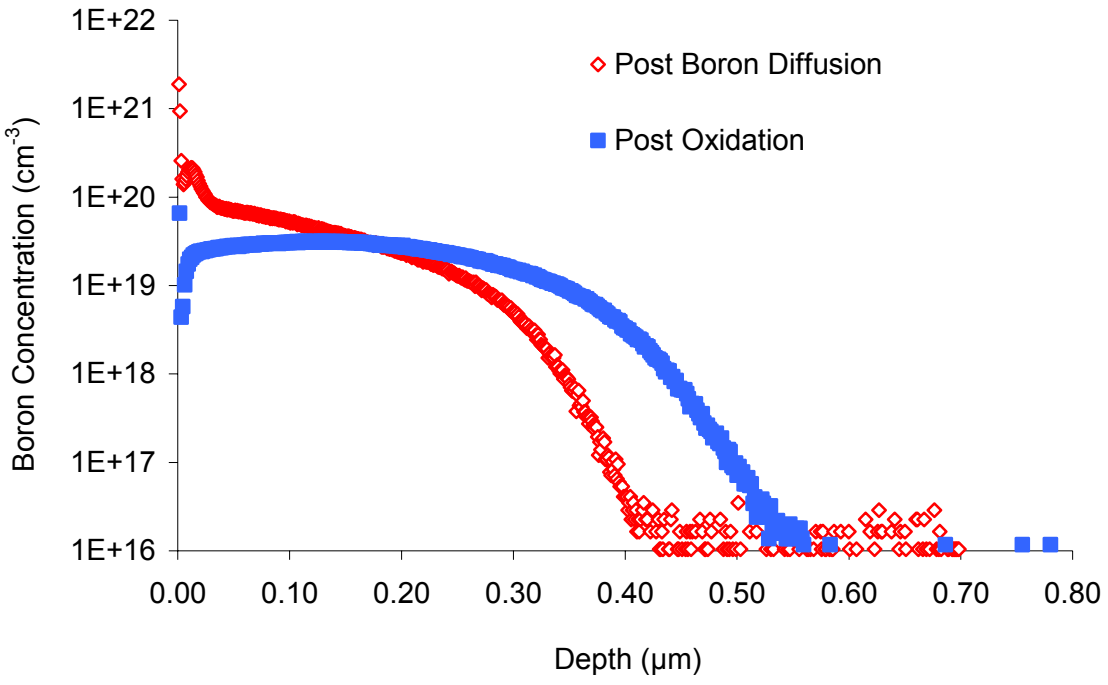

Figure 7.2 SIMS profiles of a B-BSF used for J_0 measurements before and after a thermal oxidation step.

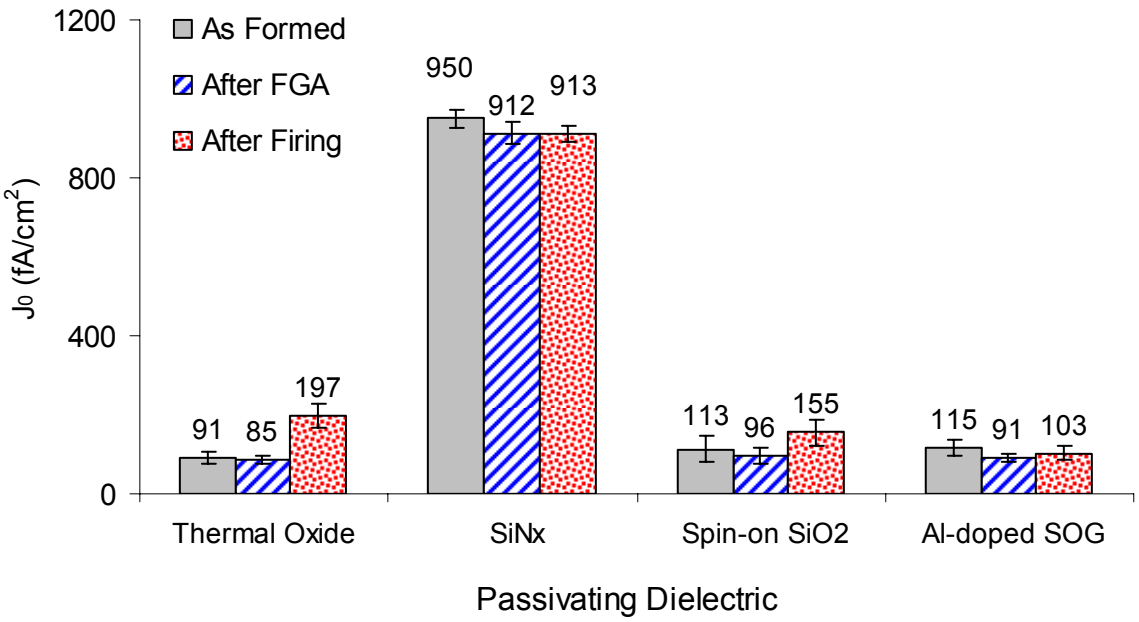

Figure 7.3 Saturation current density, J_0, of a ~110 Ω/sq. B-BSF (profile in Figure 7.2) passivated with various dielectric materials.

The passivation quality of four dielectric materials were examined – thermal SiO_2, PECVD SiN_X, and two SiO_2-based spin-on dielectrics from Filmtronics Inc. The two spin-on glasses (SOGs) were: 1) 20B – a solution with a silicate precursor which forms a pure SiO_2 layer upon curing and 2) Al 110 – an 'SiO_2-based' SOG which is doped with an aluminum compound [129]. The spin-on dielectrics were deposited onto both sides of the J_0 wafers via spin-coating and then cured in a tube furnace at the same conditions used to grow the thermal oxide. In all cases, the thermal oxidation step results in a significant depletion of boron at the Si surface (Figure 7.2) and the sheet resistance increases to ~110 Ω/sq. In order to allow for an 'apples-to-apples' comparison, the SiN_X passivated samples were also oxidized, but the oxide was stripped in a HF solution prior to SiN_X deposition.

Figure 7.3 shows the results of J_0 measurements after various processing steps: 1) immediately after passivation, 2) after a forming gas anneal (FGA) at ~400°C, and 3) after a short firing step (700-800°C) to simulate screen-printed (SP) contact firing. In

agreement with the literature record [104], SiN_X provided very poor passivation which did not significantly improve after FGA and firing. While the as-grown thermal oxide (~100 Å) provides high-quality passivation, it was found to be unstable through a high-temperature firing cycle. The degradation in the J_0 after firing is equivalent to a large 20mV drop in the V_{OC} ceiling. Since impurity diffusion to the Si/SiO_2 interface during firing was thought to be one possible cause of the degradation, it provided the impetus for examining SOGs as they provide thicker oxide layers (~1000 Å for the Al-doped SOG and ~2000 Å for the pure SiO_2 SOG) in the same process time. In the as-cured state, both provide marginally worse passivation than thermal SiO_2, but show better thermal stability through the firing cycle.

7.3 Cell-Specific Passivation Studies on Planar Surfaces

While the initial passivation studies used a ~110 Ω/sq B-BSF for J_0 measurements, later studies focused on the ~35 Ω/sq. boron profile that was determined via modeling (see Chapter 6) to be suitable for an industrial-type 20% efficient process. The remainder of this chapter examines the passivation characteristics of various dielectrics on only this B-BSF profile (Figure 7.4).

7.3.1. Al-Doped Spin-on Glass

As the Al-doped SOG showed the best firing stability in the initial passivation study, it was applied to the ~35 Ω/sq. transparent B-BSF. In order to mimic the cell fabrication process, the boron diffused J_0 samples also went through the thermal cycle of a $POCl_3$ diffusion step before being passivated. Both boron diffused surfaces were protected by a spin-on glass to prevent counter doping from the $POCl_3$ furnace itself. The profiles of the B-BSF before and after the $POCl_3$ and passivation steps are shown in Figure 7.4.

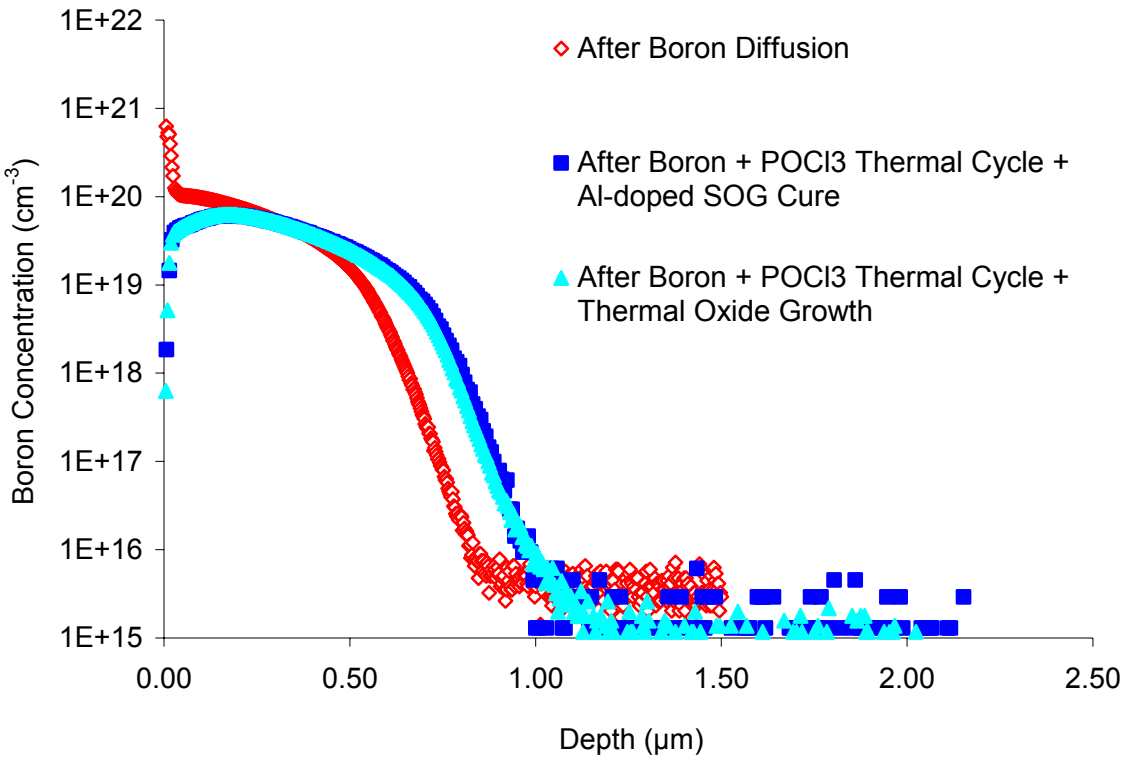

Figure 7.4 SIMS profiles of the B-BSF used for cell fabrication immediately after boron diffusion and after the subsequent thermal steps in the cell fabrication process.

The final B-BSF profile is very similar regardless of whether the BSF is passivated by a thermal SiO_2 layer or by the Al-doped SOG (which is cured using the same oxidation process). The passivation step reduces the surface boron concentration and the sheet resistance of the B-BSF increases from ~35 Ω/sq to ~40-45 Ω/sq. As J_0 measurements were performed only after passivation, the post-passivation profile was used in PC1D for S_p^+ extraction. The oxidation/SOG cure was performed for 10 minutes at 900°C followed by a 15 minute N_2 anneal – the same process is used to passivate the emitter of the 18.9% Al-BSF cell that is the 'baseline' cell for this thesis.

The PC1D modeling in Chapter 6 had predicted that passivation of the transparent B-BSF is required for achieving high cell efficiencies. The measured J_0 results (Figure 7.5) provide experimental confirmation of this. Immediately after boron diffusion, the B-BSF

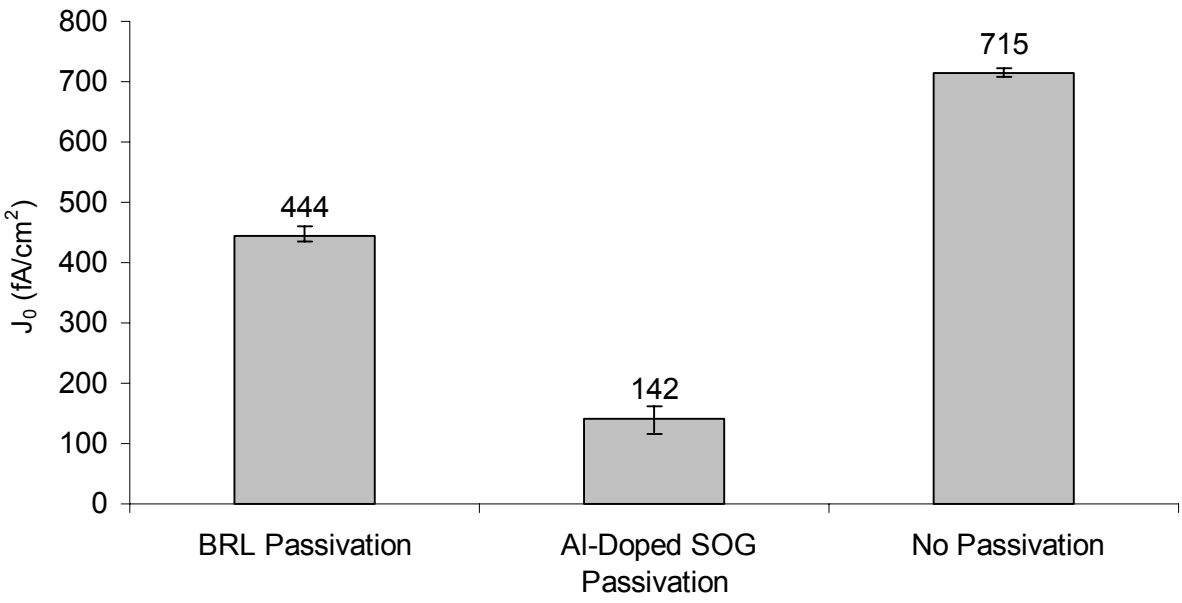

Figure 7.5 Saturation current densities, J_0, of the cell B-BSF.

is poorly 'passivated' by the boron-rich layer (BRL) resulting in J_0 values over 400 fA/cm^2 which corresponds to a V_{OC} limit of just ~650 mV. But after passivation with the Al-doped SOG, J_0 drops to values as low as 116 fA/cm^2 (~140 fA/cm^2 avg.) which corresponds to a V_{OC} limit of about ~685 mV.

On one sample, the SOG passivation was etched off in a HF solution and J_0 was re-measured. Removal of the surface passivation resulted in J_0 ~715 fA/cm^2 (an increase of ~600 fA/cm^2) which reduces the V_{OC} limit by more than 40 mV. This experimentally confirms the modeled prediction (see Chapter 6) that the shallow BSF chosen for cell fabrication is electrically transparent. The need to passivate the transparent B-BSF is the reason that the emitter of the baseline 18.9% Al-BSF cell (see Chapter 3) was passivated with a SiO_2/SiN_X stack instead of just SiN_X (since the emitter gets passivated with a thin thermal oxide layer in the same step used to cure the SOG). The oxidation/curing recipe used for these passivation studies were chosen because it:

1. Satisfies the requirement that all steps in the B-BSF cell fabrication process last no longer than the 90 minutes (the length of thermal cycle of the $POCl_3$ step)

2. Provides good passivation of both the B-BSF and the phosphorous emitter (see Chapter 3 for the results on the phosphorous emitter), and
3. Results in only a thin (~150 Å) SiO_2 layer on the emitter which, after capping with a SiN_X layer, shows similar reflection to a ~750 Å SiN_X-only ARC.

The J_0 values from Figure 7.5 were converted to $S_{p/p}^+$ values (Figure 7.6) for a 1.3 Ω-cm substrate calculated using:

$$J_0 = \frac{qn_i^2 S_{p/p^+}}{N_A} \tag{7.2}$$

The value used for N_A was 1.14×10^{16} cm^{-3}. For n_i at 25°C, 8.6×10^9 cm^{-3} was used which is equivalent to 1×10^{10} cm^{-3} @ 300K [30]. The results (Figure 7.6) show that with no passivation or with BRL passivation, $S_{p/p}^+$ exceeds the target value of 200 cm/s required for 20% cells as well as the $S_{p/p}^+$ value of 600 cm/s of the baseline Al-BSF cell.

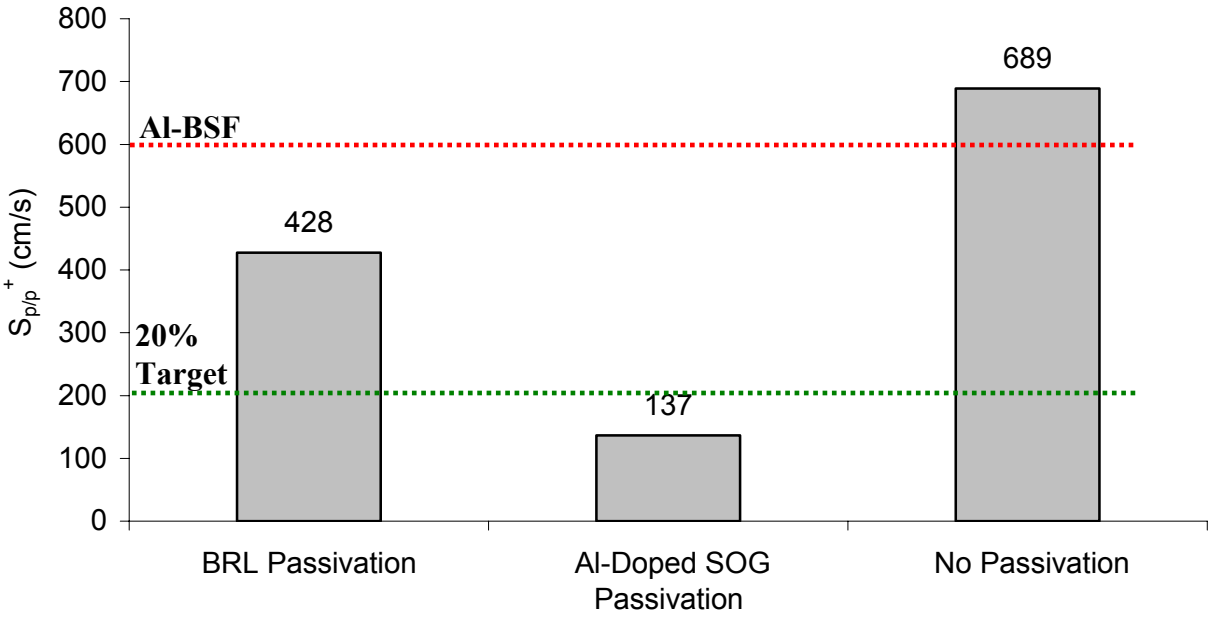

Figure 7.6 $S_{p/p}^+$ or effective BSRV values for the cell B-BSF. The dashed lines show the target BSRV value (200 cm/s) for achieving a 20% cell with this B-BSF as well as the BSRV of a baseline 18.9% Al-BSF cell.

With the Al-doped SOG passivation however, S_{p/p^+} is lower than the target value which leaves some headroom to accommodate the degradation in passivation that will occur after metallization. This issue is examined further in Section 7.5.

In the literature review of Chapter 4, it was noted that the passivation provided by thermal SiO_2 passivation on boron diffused surfaces was reported to degrade over time (see Section 4.3.1.3) resulting in large increases in J_0 (see Figure 7.7) and losses in V_{OC} exceeding 100 mV [107]. Therefore, the stability of the Al-doped SOG passivation used in this work was examined using both J_0 measurements and Implied V_{OC} measurements on un-metallized cell wafers.

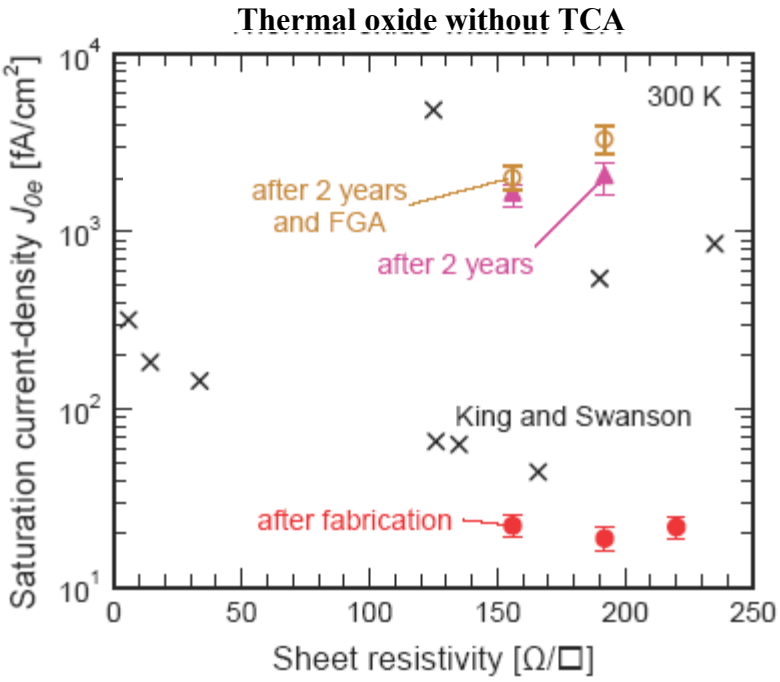

Figure 7.7 J_0 as a function of sheet resistance of forming gas annealed thermal SiO_2-passivated, planar boron-diffused wafers as reported by Altermatt *et al.* [104].

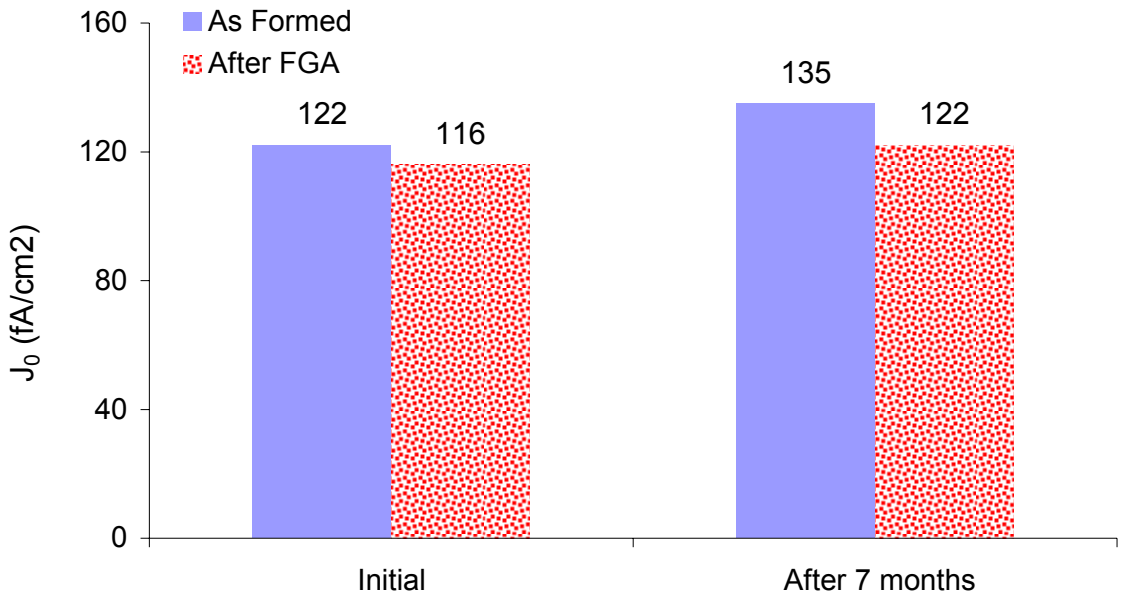

Figure 7.8 Temporal stability of Al-doped SOG passivation on a ~45 Ω/sq B-BSF.

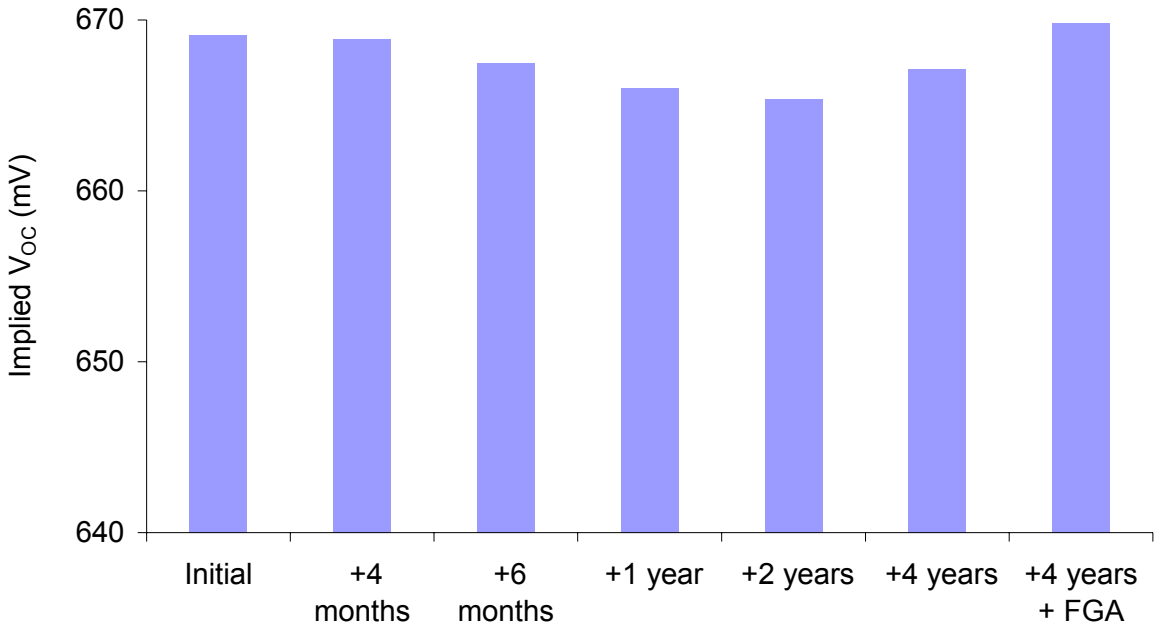

Figure 7.9 Implied V_{OC} of an un-metallized B-BSF cell over time.

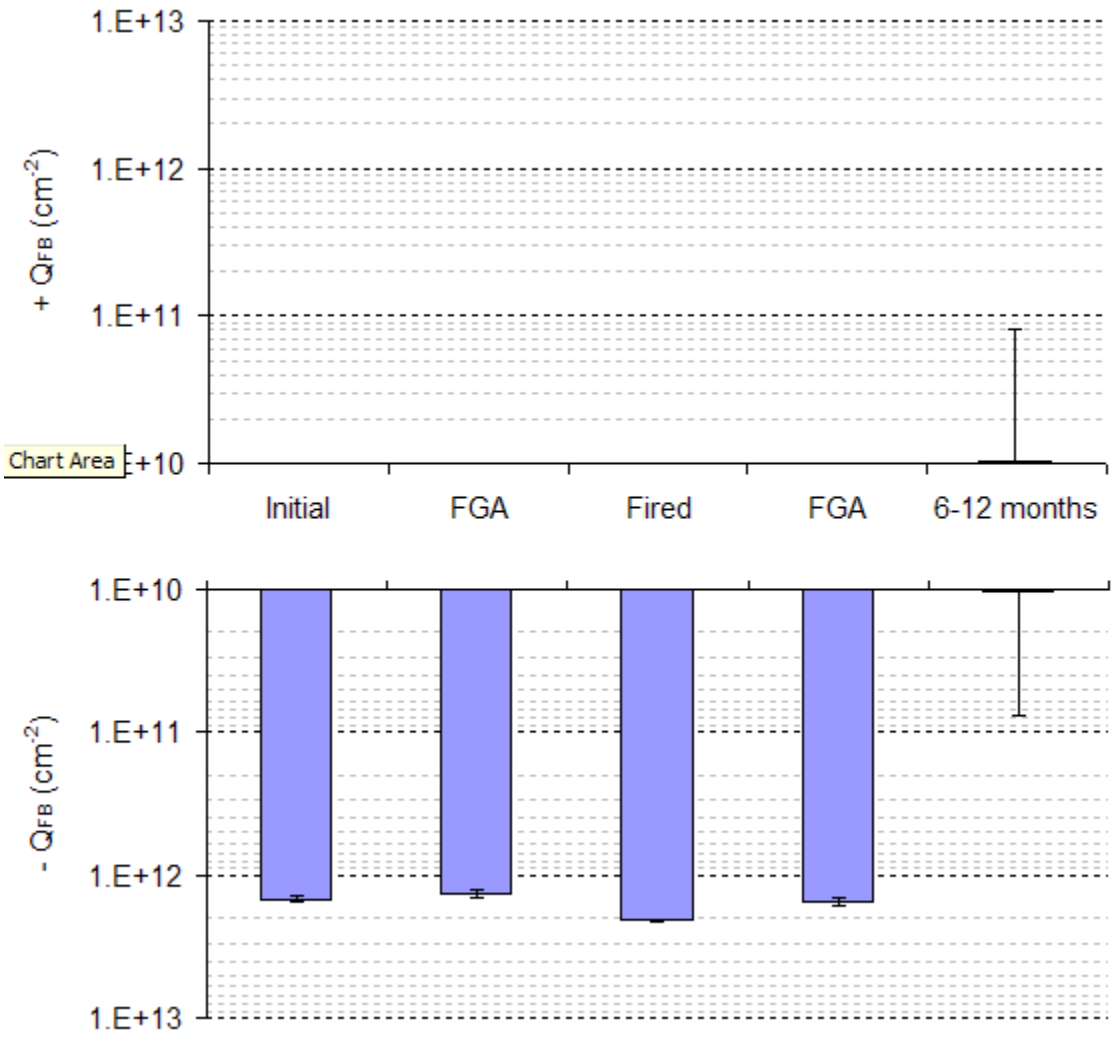

Figure 7.10 Charge in the Al-doped SOG at various process steps and over time. The data is from Ref. 19.

Over a period of 7 months of dark storage in air, only a slight increase in J_0 was found to occur which could be completely reversed with an FGA step (Figure 7.8). Similar behavior was observed on the Implied V_{OC} samples (Figure 7.9) which were passivated on the rear with the Al-doped SOG and on the front with a thermal SiO_2/SiN_X stack. V_{OC} gradually stabilized after a period of 1 year and the small drop of ~3mV was completely reversible with a FGA step. The slight instability in the passivation provided by the Al-doped SOG may be related to its charge. It was previously shown that the as-cured Al-

doped SOG is negatively charged, and that the negative charge dissipates over a period of 6-12 months (Figure 7.10) [19]. Since the presence of a negative charge in a passivating dielectric can significantly improve passivation of a p^+ layer [102], [113-123], the effect that the dissipation of charge in the Al-doped SOG has on passivation quality was investigated through modeling.

7.3.1.1 The Effect of Dielectric Charge and the Boron Profile on Passivation

Work by other authors on boron emitters with relatively low surface concentration ($N_s \sim 5x10^{18}$ cm^{-3}) showed that the application of a negative charge density of ~$4x10^{12}$ cm^{-2} to SiO_2 and SiO_2/Si_3N_4 stacks significantly improved passivation, with a ~6x reduction in J_0 and ~40 mV boost in the V_{OC} [102], [113]. Since loss of negative charge in the Al-doped SOG resulted in a much smaller degradation in J_0 and V_{OC} for the more heavily-doped (~40-45 Ω/sq) B-BSF used in this work, modeling was used to examine how emitter passivation is affected by: 1) the magnitude of the dielectric charge and 2) the surface/peak doping concentration of emitter being passivated. To explore the relationship between the two, the 20% efficient PC1D model built in Chapter 6 was modified to include a charge density at the rear surface. This charge was varied and its impact on passivation was examined by using the change in the simulated cell V_{OC} as an indication of change in passivation quality. The effect of surface concentration was examined by repeating this for a variety of B-BSF profiles – the SIMS profile of the B-BSF used here (Figure 7.4) and four Gaussian profiles with surface concentrations ranging from $6x10^{18}$ cm^{-3} to $1x10^{20}$ cm^{-3} (Figure 7.11). S_p^+ was not varied with surface concentration in order to isolate the effect of surface charge from surface recombination. Instead, the S_p^+ for all the profiles was fixed at 40,000 cm/s which is the target S_p^+ for the B-BSF used in this work (see Chapter 6). The results are summarized in Table 7.1.

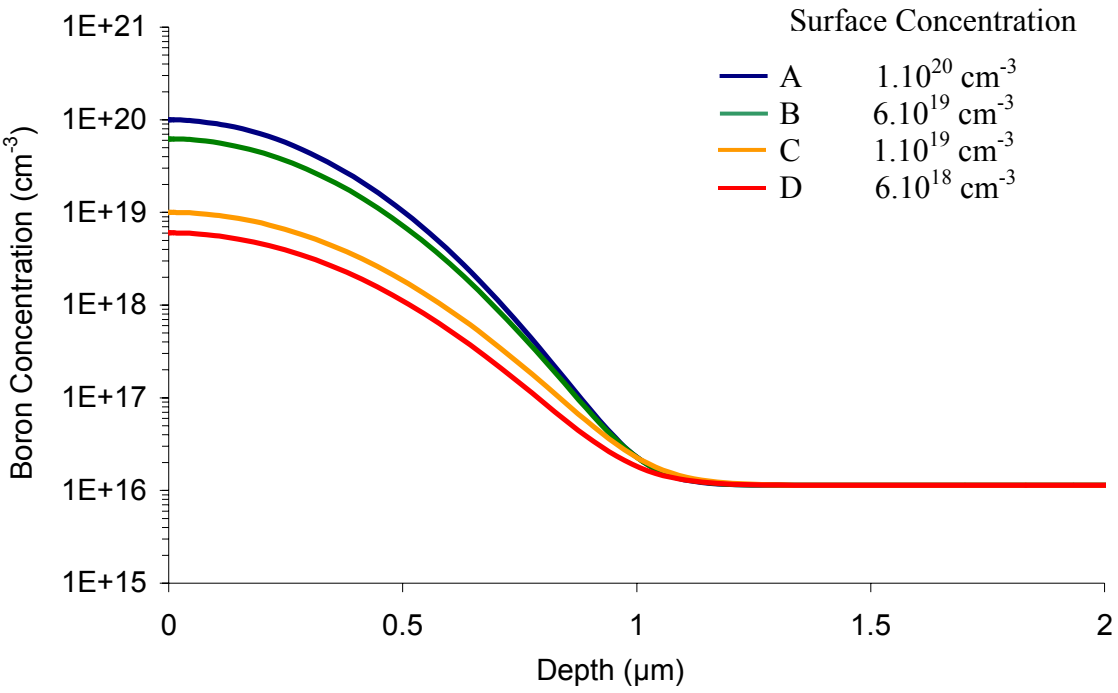

Figure 7.11 Gaussian boron profiles used to model of the effect of charge and surface doping concentration on passivation.

Table 7.1. PC1D modeling showing that the effect of rear dielectric charge depends on the BSF doping profile. Profiles A-D are from Figure 7.11 and the SIMS profile is from Figure 7.4.

B-BSF Profile	Initial Cell V_{OC} (mV)	ΔV_{OC} due to dielectric charge density		Initial Cell Efficiency (%)	Efficiency after applying dielectric charge density	
		$Q_{Dielectric} = -10^{12}$ cm^{-2}	$Q_{Dielectric} = -10^{13}$ cm^{-2}		$Q_{Dielectric} = -10^{12}$ cm^{-2}	$Q_{Dielectric} = -10^{13}$ cm^{-2}
A	649	+ 1 mV	+ 4 mV	20.1	20.1 %	20.3 %
SIMS	648	+ 2 mV	+ 6 mV	20	20.1 %	20.4 %
B	649	+ 2 mV	+ 7 mV	20.1	20.2 %	20.5 %
C	644	+ 6 mV	+ 16 mV	19.8	20.2 %	20.7 %
D	641	+ 8 mV	+ 19 mV	19.7	20.1 %	20.7 %

For both the SIMS boron profile and its Gaussian approximation (Curve B), a negative charge of -1x10^{12} cm^{-2} increases the simulated V_{OC} by just 2 mV. This is in good agreement with the ~3 mV loss in V_{OC} over time that was experimentally observed with the Al-doped SOG passivation (which has similar charge – Figure 7.10) and provides support for the theory that the instability is due to the SOG losing its charge over time.

The simulations also show that the effect of a negative surface charge is higher for lower surface concentrations, which explains why the effect of charge on V_{OC} observed in this work is smaller than that reported previously for more lightly doped boron emitters. A charge density of -1x10^{13} cm^{-2} also has a much larger effect than a charge density of -1x10^{12} cm^{-3}. It is interesting to note that cells with a lower surface concentration BSF (Profiles C and D) start off with lower V_{OC} and efficiency, but with a surface charge density of -1x10^{13} cm^{-2}, these cells outperform the high-surface-concentration BSF cells. Since similarly high charge densities have been reported for Al_2O_3 films [117, 118], efficiencies beyond 20% appear to be possible if Al_2O_3 is used for passivating the B-BSF in this work. While lowering the surface concentration could lead to even higher efficiencies, this was not pursued in order to avoid difficulties associated with forming screen-printed ohmic contacts to Si with low doping concentrations. The sheet resistances for profiles C and D (Figure 7.11) are 200 Ω/sq. and 270 Ω/sq. respectively.

7.3.2 ALD Al_2O_3

As the modeling in the previous section indicated that a dielectric with a high negative charge density could improve passivation, the passivation quality of Al_2O_3 was also evaluated using J_0 measurements. In order to facilitate comparison, these samples were processed identically to the Al-doped SOG passivated J_0 samples. The SOG was then etched-off in a buffered HF solution, followed by deposition of ~200 Å of Al_2O_3 via

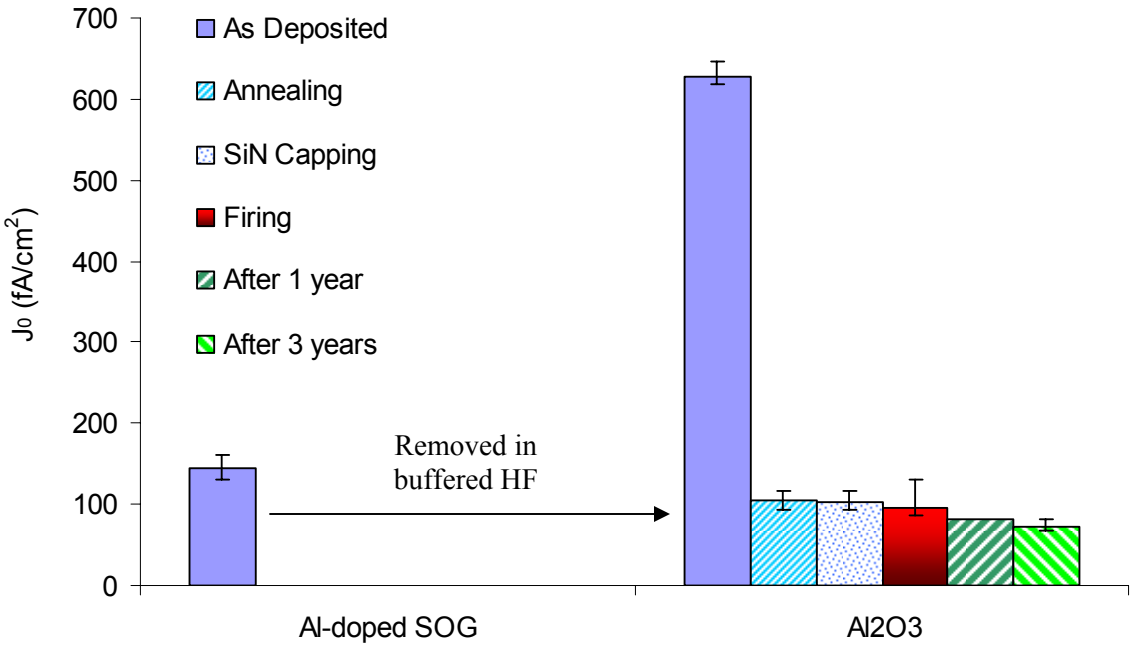

Figure 7.12 Saturation current density of the cell B-BSF after passivation with the Al-doped SOG and with Al_2O_3 at various processing steps.

atomic layer deposition (ALD). The samples were measured with the Al-doped SOG passivation, after Al_2O_3 deposition and after subsequent processing steps (Figure 7.12).

In the as-deposited state, Al_2O_3 provides extremely poor passivation in agreement with literature reports on ALD Al_2O_3 [116, 133]. A short N_2 anneal at 425°C significantly improves the passivation quality, resulting in J_0 values that are lower than those achieved with the Al-doped SOG. The passivation quality is also thermally and temporally stable, even showing small improvements after SiN_X capping and firing. To track stability over time, the samples were stored in the dark in air; under these conditions, the passivation shows no degradation over a 3 year period. Using Equation 7.2, the $S_{p/p}{}^+$ of the Al_2O_3 passivated B-BSF works out to be ~70-100 cm/s, which is better than the ~140 cm/s achieved with the Al-doped SOG and significantly below the target of 200 cm/s.

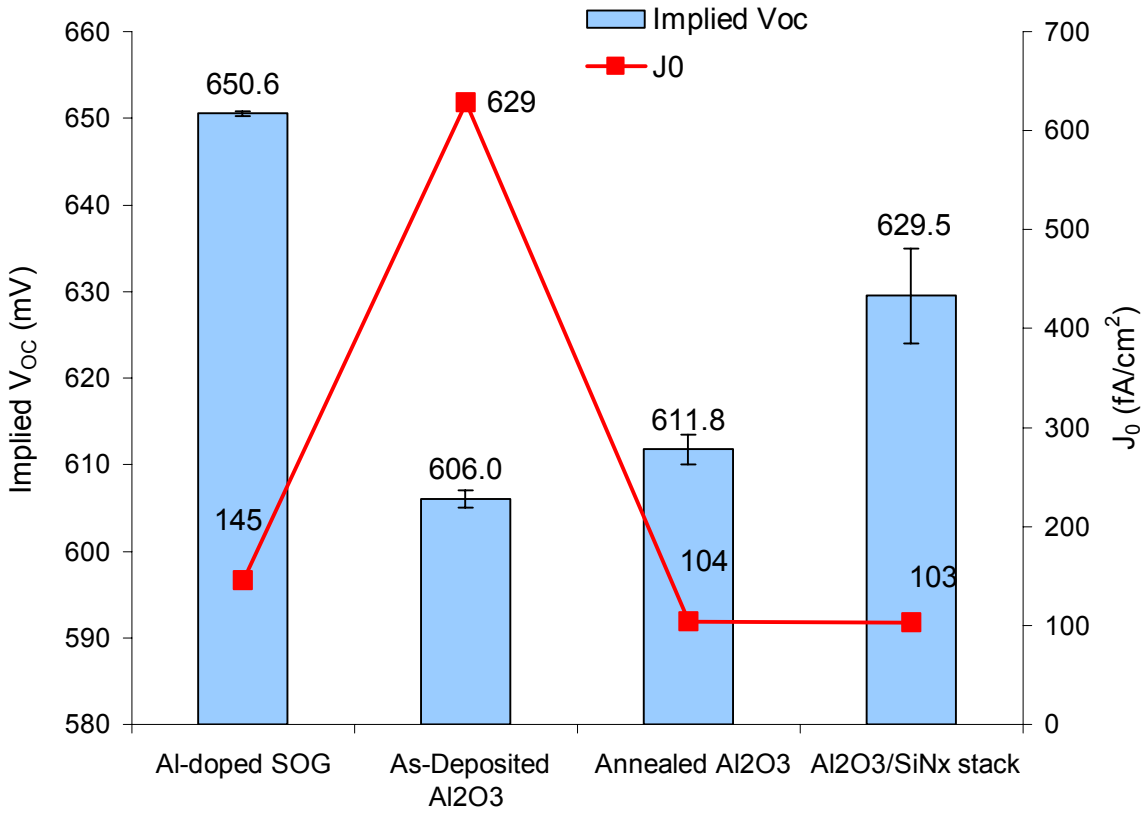

Figure 7.13 Implied V_{OC} of B-BSF cell wafers passivated with Al-doped SOG and with ALD Al_2O_3 at various process steps, and J_0 of the passivated B-BSF used in the cell wafers. The J_0 data is taken from Figure 7.12.

However, Implied V_{OC} measurements (Figure 7.13) on un-metallized cell wafers did not to agree with the J_0 measurements. Improvements in J_0 ought to correspond to higher Implied V_{OC} values; however, the Al_2O_3-passivated cell samples failed to show much improvement in after annealing and SiN_X capping showing Implied V_{OC}s ~20mV lower than Al-doped SOG passivated samples fabricated in the same run. The reason for the discrepancy between the two measurements is not known. The Al_2O_3-passivated J_0 samples were fabricated in the same run as the cell samples, so run-to-run variability does not explain the discrepancy.

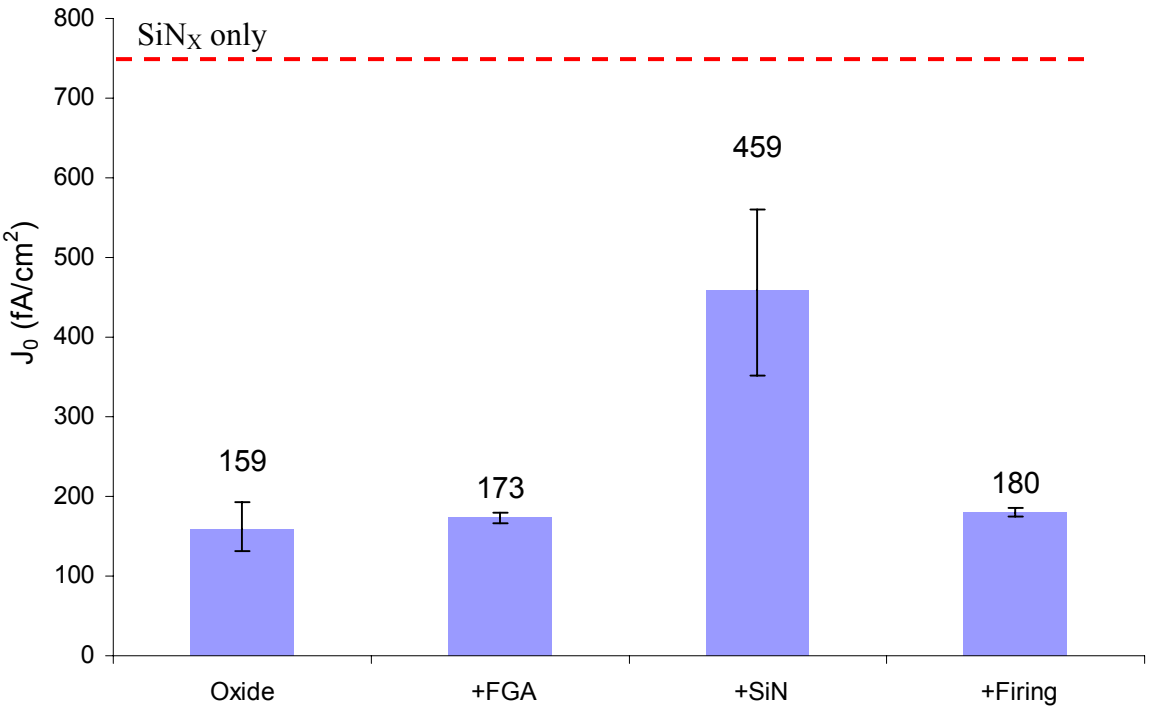

Figure 7.14 Saturation current densities, J_0, of the cell B-BSF with thermal SiO_2, SiN_X and SiO_2/SiN_X stack passivation.

7.3.2 Thermal SiO_2/SiN_X Stacks

In the initial passivation studies, both thermal oxide (SiO_2) and PECVD silicon nitride (SiN_X) were considered and discarded – thermal SiO_2 passivation was found to be unstable through a firing cycle while SiN_X passivation resulted in extremely high J_0 values (Figure 7.2). However, a SiO_2/SiN_X stack behaved differently from either dielectric alone (Figure 7.14).

While capping the thin (~140 Å) oxide layer with SiN_X results in a large increase in J_0, the passivation quality is still significantly better than SiN_X passivation alone. As both the stack and the SiN_X alone have approximately the same charge density (~$1x10^{12}$ cm^{-2}), this suggests that a low quality Si/SiN_X interface is responsible for the high J_0 values measured on SiN_X-passivated p^+-Si surfaces. For the SiO_2/SiN_X stack, damage to the Si/SiO_2 interface during the PECVD process may be responsible for the increase in J_0

after SiN_X-capping. This issue is explored further in Section 7.4.2. Firing the oxide/SiN_X stack results in almost complete recovery of the passivation quality – the J_0 after firing is only ~1.1x higher than that achieved with thermal SiO_2 passivation alone. As the positive charge density of the fired stack (~$1x10^{12}$ cm^{-2}) is about an order to magnitude higher than that of the SiO_2 (~$1x10^{11}$ cm^{-2}), the post-firing recovery suggests that the positive charge only has a small impact on the passivation quality of the B-BSF used here. This further re-enforces the view that the poor passivation quality of SiN_X on heavily boron-doped surfaces is due to a low-quality interface, and not due to the high positive charge density. This experimental determination also agrees with the simulation results of Altermatt *et al.* which reached the same conclusion [104].

Using Equation 7.2, the J_0 of the fired stack converts to an S_{p/p^+} value of ~170 cm/s which is only slightly better than the cell-level target of 200 cm/s. This sets a very tight limit on the allowable area coverage of the rear metal contacts as discussed in Section 7.5.

7.4 Cell-Specific Passivation Studies on Textured Surfaces

As noted in Chapter 4, several authors have reported that the recombination velocity at the textured p^+-Si/thermal SiO_2 interface is 5-10x higher than on a planar p^+ surface with J_0 values showing similar degradation after texturing [52, 106, 102]. This suggests that achieving a 20% efficient cell with a BSRV of 200 cm/s requires that the B-BSF surface be planar. However, achieving single-side texturing of a wafer typically adds one or more steps to the fabrication sequence thereby increasing processing cost. Single-side texturing usually involves either: 1) masking of one side of the wafer before texturing followed by removal of the mask layer or 2) double-side texturing, followed by one-side masking and etch back of the un-masked textured side of the wafer. Since avoiding these steps would simplify the fabrication process, the passivation quality of the Al-doped SOG and the oxide/SiN_X stack were also examined on textured J_0 samples. Other than being

textured on both sides, these samples were processed identically to the planar J_0 samples discussed in the previous section.

7.4.1 Al-doped SOG

With Al-doped SOG passivation, the J_0 values for the textured samples are 5–6x higher than on the counterpart planar wafers, with values as high as 900 fA/cm^2 being recorded. The degraded passivation is also reflected in Implied V_{OC} measurements, with double-side textured, precursor cell wafers having Implied V_{OC}s of around 640 mV; approximately 20 mV lower than the Implied V_{OC}s on planar B-BSF wafers that were processed simultaneously. The fact that these *un-metallized*, double-side textured B-BSF samples exhibited V_{OC}s similar to that of *metallized* Al-BSF cells suggests that if the Al-doped SOG is to be used as the rear passivating dielectric of a 20% B-BSF cell, the rear surface must be planar. Note that non-uniformity in the B-BSF is not a likely cause if the high J_0 values as the spin-on boric acid source was found to result in a fairly uniform boron doped layer that follows the contours of the pyramid texture (See Chapter 4).

7.4.2 Thermal SiO_2/SiN_X Stacks

The J_0 data shown in Figure 7.15 compares the response of textured and planar boron diffused surfaces at various process steps (the planar data is the same as that in Figure 7.14). With thermal-SiO_2 passivation alone, the J_0 of the textured p^+ surface is four to five times higher than on the counterpart planar surface. As noted at the start of this section, such a large increase in J_0 is in good agreement with previous literature reports and is also similar to the increase observed with Al-doped SOG passivation. The most striking difference between the planar and textured cases is in their response to a PECVD SiN_X deposition step – on planar p^+ surfaces, SiN_X-capping increases J_0 but reduces it on identically processed textured p^+ surfaces. The behavior of the two surfaces after a short FGA step offers a clue as to why this difference exists.

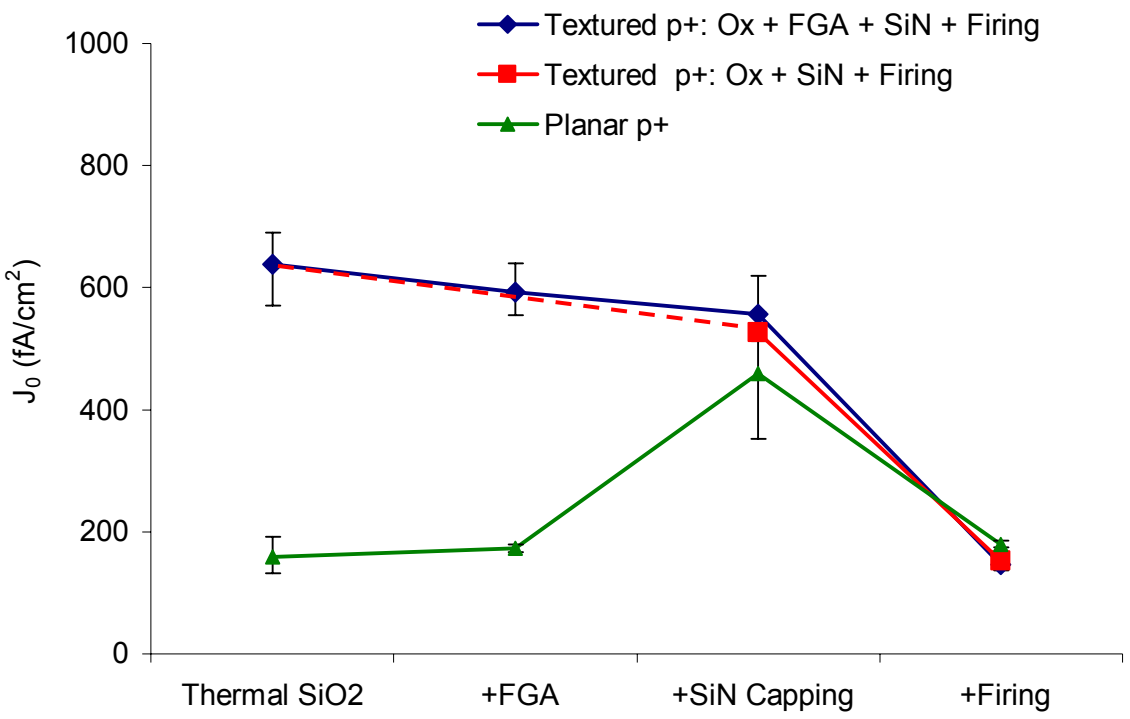

Figure 7.15 Saturation current density, J_0, of textured boron diffused surfaces at various process steps.

On the planar surfaces, hydrogenation from the ~400°C FGA has nearly no effect on J_0 which suggests that the as-grown p^+-Si/SiO_2 interface has relatively few dangling bonds (or other sites) available for passivation by H-atoms. Therefore, hydrogenation during a ~400°C PECVD SiN_X deposition is also unlikely to improve the J_0 of the thermal SiO_2-passivated planar p^+ samples; instead the negative effect of plasma-induced damage can be expected to dominate. The observed increase in J_0 after SiN_X capping matches the expected behavior. While the higher positive charge density in the SiO_2/SiN_X stack (compared to thermal SiO_2) can also increase J_0, the full recovery of the planar J_0 after firing (which does not change the dielectric charge) suggests that the increase in dielectric charge is not responsible the large increase in J_0 observed after SiN_X deposition.

Unlike the planar case, the textured SiO_2-passivated samples show a small reduction in J_0 after the FGA step. The increased sensitivity to hydrogenation exhibited by the

textured samples can be explained by assuming that (unlike the planar case) the SiO_2-passivated, *textured* p^+ surface has a significant density of unsatisfied dangling bonds which can be H-terminated. This is a plausible explanation as {111} oriented textured surfaces have a larger dangling bond density than the {100} surface of the planar wafers. A similar increase in sensitivity to hydrogenation is also observed when n^+-Si surfaces are textured [53]. This excess availability of un-satisfied dangling bonds offers a possible explanation for why SiN_X deposition reduces the J_0 of the textured p^+ surface, i.e. the increase in surface defect density due to plasma-damage is outweighed by the competing reduction in surface defects by *in-situ* hydrogenation of dangling bonds at the textured p^+-Si/SiO_2 interface. It is worth stressing however that the experimental results plotted in Figure 7.15 simply show the *net* effect of all the processes that occur simultaneously during a PECVD step and more work is needed to conclusively separate out the impact of the competing hydrogenation and plasma-damage processes.

A short firing step results in large improvements in surface passivation on both the planar and textured surfaces. The textured samples show a fourfold reduction in J_0, while the planar samples experience a smaller factor of 2.5 improvement in J_0. Potential explanations for the improvement include the release of hydrogen from the SiN_X layer and thermal annealing of surface defects – both have been shown to occur during firing [134, 135]. On the planar samples, this hydrogenation/annealing effect appears to fully heal the plasma-induced damage caused by the PECVD step. The magnified effect of firing on textured surfaces is perhaps due to the excess dangling bonds on the textured surface not being completely satisfied by PECVD hydrogenation. As a large amount of hydrogen is released from SiN_X during firing, these remaining dangling bonds can be H-passivated by the firing step in addition to the healing of plasma-induced damage. After firing, both the planar and textured SiO_2/SiN_X passivated samples have nearly identical J_0 values of ~150 fA/cm^2. Furthermore, the fired SiO_2/SiN_X stack provides nearly identical passivation on the textured B-BSF and textured phosphorous emitter used for the cells

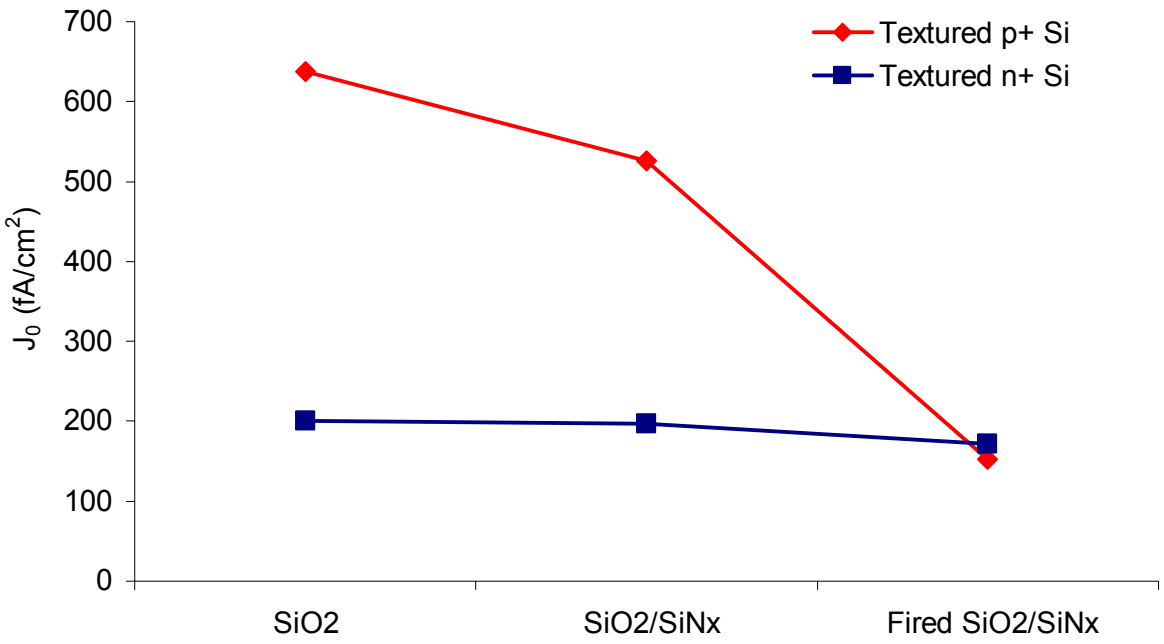

Figure 7.16 Comparison of the J_0 of textured boron and phosphorous diffused surfaces at various process steps.

cells fabricated in this work (Figure 7.16). As noted earlier in Figures 3.1 and 7.4, both the emitter and BSF have similar surface concentrations of ~$7x10^{19}$ cm^{-3} and ~$5x10^{19}$ cm^{-3} respectively.

Although the ~1.7x increase in surface area due to texturing might be expected to result in $J_{0,textured}$ being at least 1.7x higher than $J_{0,planar}$, this effect is suppressed for well passivated, heavily doped emitters as recombination within the emitter starts to dominate J_0. This effect holds for both p^+ and n^+ emitters and similar results (i.e., $J_{0,textured} \approx J_{0,planar}$) have been reported for SiO_2-passivated n^+-Si emitters with surface concentrations similar to our samples [53], [136]. The stability of the fired stack was also tracked over time and found to be stable on both planar and textured surfaces (Figure 7.17). These results suggest that fired thermal SiO_2/SiN_X stack passivation may allow for 20% efficient,

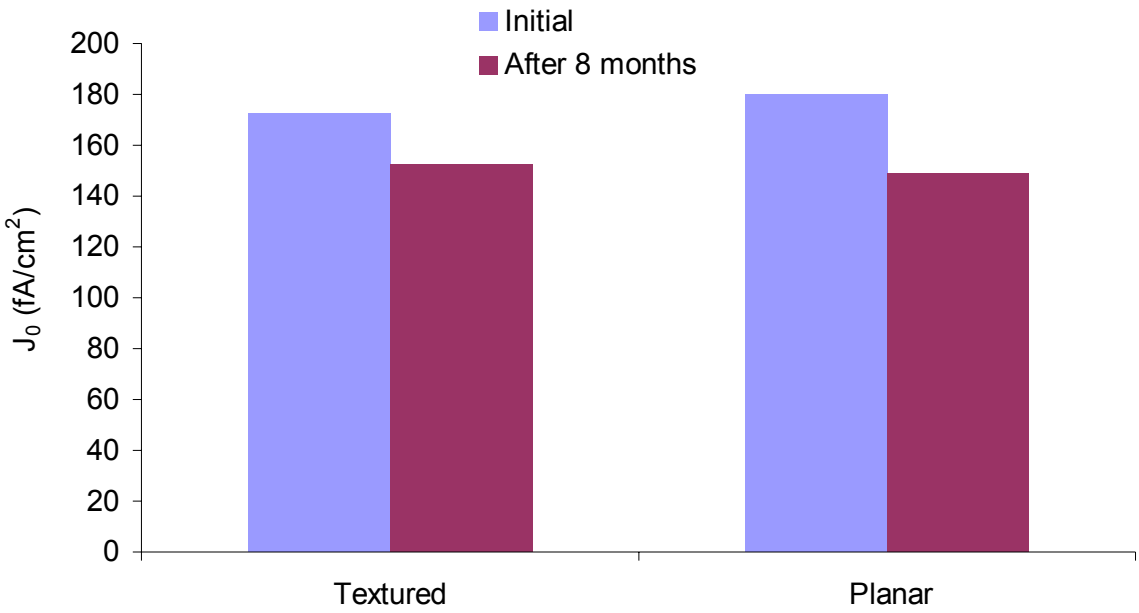

Figure 7.17 Stability of fired thermal SiO_2/SiN_X stacks over time.

B-BSF cells to be achieved even if the rear surface is textured. However, it will be shown in Chapter 8 that this passivation process can lead to contamination and lifetime degradation of the Si substrate, which led to the use of the Al-doped SOG on a planar B-BSF for cell fabrication.

7.5 Effect of Passivation Quality on the Rear Contact Pattern

The discussion in the previous sections show that the Al-doped SOG, ALD Al_2O_3 and fired thermal SiO_2/SiN_X stacks all beat the $S_{p/p}^+$ of 200 cm/s targeted for a 20% efficient SP B-BSF cell. However, the 200 cm/s value is the target that needs to be met *after* metallization. Since the passivation quality before metallization is now known, it is possible to estimate the maximum allowable rear metal fraction using

$$S_p^+ = f_{metal} * S_{metal} + f_{dielectric} * S_{dielectric} \quad (6.1)$$

where f_{metal} and $f_{dielectric}$ are the area fractions of the metal contacts and dielectric passivated regions respectively and S_{metal} and $S_{dielectric}$ refer to S_p^+ under the metallized and passivated regions respectively. Using PC1D and the measured SIMS profile of the B-BSF chosen for cell fabrication (Figure 7.4), it was found that the $S_{p/p}^+$ of 200 cm/s corresponds to an S_p^+ of ~40,000 cm/s. The S_p^+ values achieved with the various dielectrics was similarly extracted and plugged into Equation 6.1, assuming S_{Metal} of $1x10^6$ cm/s.

Table 7.2 Recombination velocity, S_p^+, at the dielectric/p^+ interface and the maximum allowable metal fraction for achieving an effective $S_{p/p}^+$ of 200 cm/s.

	S_p^+ or $S_{Dielectric}$ (cm/s)	Max. Allowable Rear Metal Fraction (%)	Surface Type
Al-doped SOG	17,000	2.5	Planar
Thermal SiO_2	22,000	2.0	Planar
Thermal SiO_2/SiN_X	18900	2.5	Planar/Textured
ALD Al_2O_3	6800	3.5	Planar

The results, summarized in Table 7.2, show that even with the best passivation achieved in this work (Al_2O_3), the rear metal fraction needs to be ≤ 4%. Such a low limit to the maximum allowable metal fraction implies that the rear SP contacts should be point contacts instead of grid-line contacts. Therefore, the B-BSF cells fabricated in this thesis will use point contacts to the B-BSF.

7.6 Summary

In this chapter, the passivation quality of four dielectric materials – an Al-doped spin-on glass, atomic layer deposited Al_2O_3, thermal SiO_2 and thermal SiO_2/SiN_X stacks – were examined. Figure 7.18 summarizes the J_0 achieved with each on the ~45 Ω/sq B-BSF that will be used for cell fabrication. Of particular note are the results obtained with Al_2O_3 and fired SiO_2/SiN_X stacks. On planar surfaces, Al_2O_3 offers the best passivation by a fair margin; however, implied V_{OC} measurements showed lower V_{OC}s than those achieved with the Al-doped SOG. The fired SiO_2/SiN_X stack is also attractive as it provides good passivation on textured surfaces, which suggests that it may be possible to achieve a 20% efficient B-BSF cell even if the rear surface is textured. Compared to passivation with thermal SiO_2 alone or the Al-doped SOG which perform poorly on textured surfaces, SiO_2/SiN_X passivation would simplify fabrication by allowing double-side textured wafers to be used, thereby lowering cost. It should be noted however, that

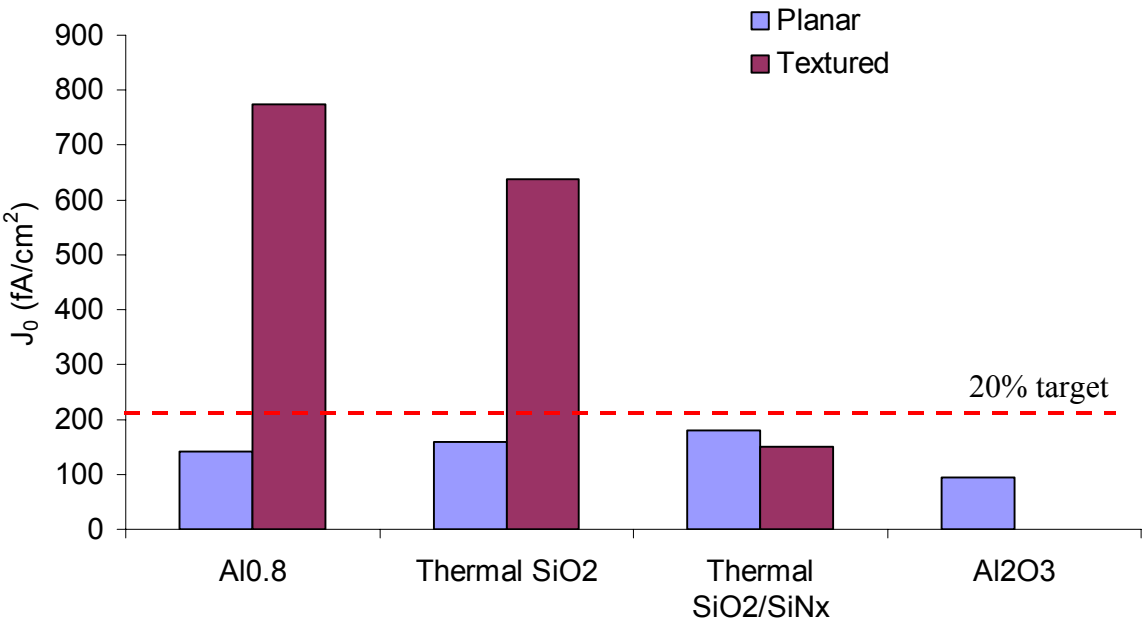

Figure 7.18 Summary of passivation results on the cell B-BSF. While the thermal SiO_2 passivation is thermally unstable, the as-grown results are shown for completeness.

the passivation method that is used must be able to maintain bulk lifetimes high enough to achieve 20% efficient cells. It is shown in Chapter 8 that the SiO_2/SiN_X passivation method can severely degrade the bulk lifetime. This led to the use of the Al-doped SOG on a planar B-BSF for fabricating 20% efficient cells.

Chapter 8

BULK LIFETIME DEGRADATION DUE TO BORON DIFFUSION AND DEVELOPMENT OF PROCESS-INDUCED GETTERING SOLUTIONS

In Chapter 6, computer modeling highlighted BSRV improvements as a way of going beyond the efficiency of a baseline Al-BSF cell. However, that modeling assumed that a B-BSF cell would have the same bulk lifetime (~ 450 μs) as an Al-BSF cell. As discussed previously in the literature review of Chapter 4, this is not a safe assumption for processes that involve boron diffusion. As seen in Figure 8.1, very low lifetimes have been reported in the past for every type of boron diffusion source.

For improvements in BSRV to have a large impact on cell efficiency, the bulk minority carrier lifetime has to be high enough for the photogenerated carriers to 'see' the rear surface. If bulk lifetimes are too low then, regardless of the BSRV, photogenerated carriers near the rear surface of the cell will recombine in the bulk before they can reach the front junction and therefore fail to benefit from improved rear passivation.

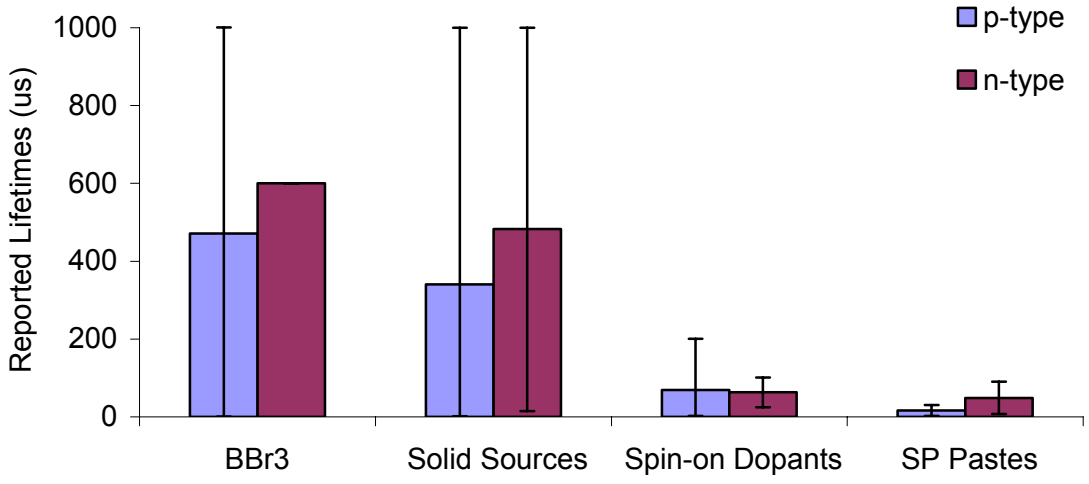

Figure 8.1 Bulk minority carrier lifetimes on p-type and n-type FZ Si wafers after boron diffusions using various sources as reported in Refs. 52, 71-73, 76, 78, 84-87.

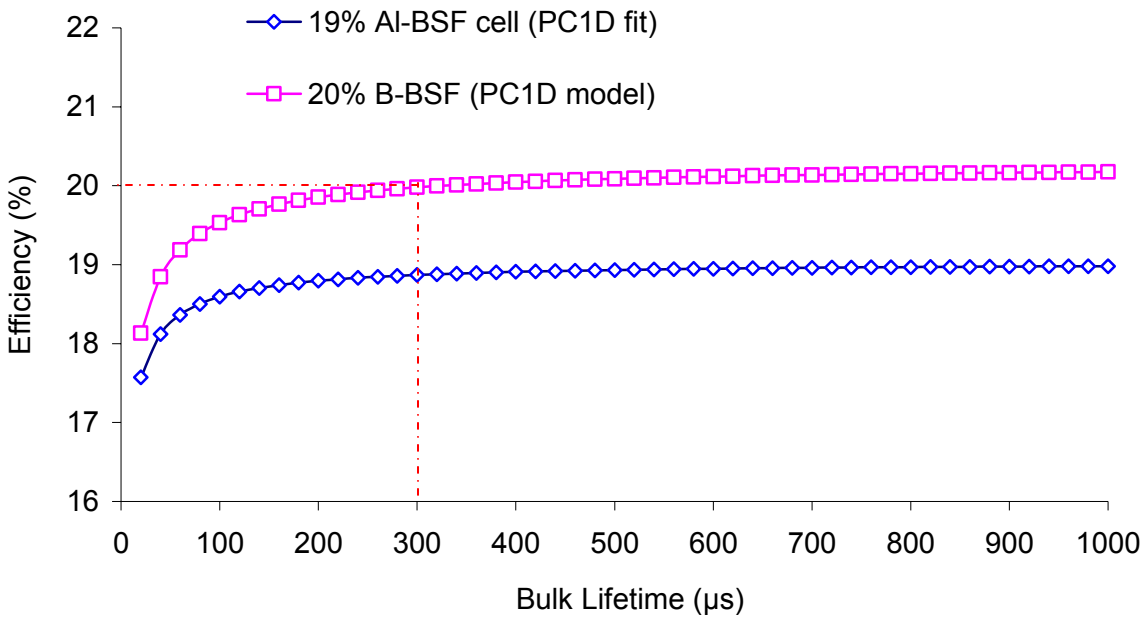

Figure 8.2 Modeled impact of bulk lifetime on the efficiency of the baseline 18.9% Al-BSF cell and a hypothetical 20% cell, both on 300 µm thick Si substrates. The dash-dot line shows the lifetime threshold for achieving 20% efficiency.

This effect was quantified by varying (in PC1D) the bulk lifetime of a conventional full Al-BSF cell (18.9%) and of a 20% efficient cell which features improved BSRV and BSR (the details of both models were presented earlier in Chapter 3). Both devices are 300 µm thick. The results, plotted in Figure 8.2, show that while bulk lifetime affects the efficiency of both devices, the higher efficiency cell is considerably more sensitive to lifetime degradation. When the bulk lifetime is swept from 1 ms to 20 µs, the modeled efficiency of the 20% cell drops by 2% (abs.), while the Al-BSF cell loses just 1% (abs.). The modeling also shows that efficiency of the well-passivated cell drops below 20% for lifetimes under 300 µs. At a lifetime 50 µs, its efficiency becomes lower than that of the baseline full Al-BSF cell presented in Chapter 3 which has a bulk lifetime of ~450 µs. This is a realistic prospect, especially for cheaper sources like spin-on dopants which have historically resulted in very low lifetimes (Figure 8.1). In Chapter 5, the spin-on boric acid/DI water sources that were developed as part of this research were shown to be

versatile candidates for low-cost boron diffusion. In this chapter, the impact of this source on bulk lifetime is examined.

8.1 Experimental Method for Tracking Bulk Lifetime and Identifying the Cause of Degradations in Bulk Lifetime

While bulk lifetime degradations in processes involving boron diffusion have been widely reported, the cause of the degradations is not fully understood. When a given process is found to cause lifetime degradation, it is important to identify the mechanism behind that degradation so that a cure for it can be developed. This chapter investigates the cause of bulk lifetime degradations associated with spin-on boric acid diffusions, by tracking bulk lifetime through various process steps while simultaneously looking for the lifetime signatures the most common suspects – Fe contamination and dislocation generation during boron diffusion.

Float-zone (FZ) Si wafers of 0.6-1.4 Ω-cm resistivity were used for this study. The lifetime of the wafers was measured after every step of the cell process – boron BSF diffusion, $POCl_3$ emitter diffusion and surface passivation. The lifetime measurements were performed using the QSS-PC method after etching away all surface layers plus ~5-10 μm of each wafer surface [51]. The etched wafers were then cleaned and passivated with an I_2/Methanol solution prior to QSS-PC measurement [139]. From measurements on cleaned but otherwise unprocessed FZ wafers, it was determined that the I_2/Methanol passivation provides surface recombination velocities < 10 cm/s using

$$\frac{1}{\tau_{eff}} = \frac{1}{\tau_{bulk}} + \frac{2S}{L} \tag{8.1}$$

where τ_{eff} is the measured lifetime and τ_{bulk} was taken to be the Auger-limited lifetime reported by Kerr [54]. As the surface recombination velocities are very low, the effective

Table 8.1 Summary of recombination characteristics for interstitial iron (Fe_i) and the iron-boron complex (FeB). The trap-level and capture-cross-section for Fe_i are taken from Ref. 142 and those for FeB from Ref. 143. n_1 and p_1 are calculated using $n_i = 8.6 \times 10^9$ (25°C) based on $n_i = 1 \times 10^{10}$ cm^{-3} (300K) [30].

Fe State	Trap Level (E_T in eV)	σ_n (cm^{-2})	σ_p (cm^{-2})	n_1 (cm^{-3})	p_1 (cm^{-3})
Fe_i	$E_v + 0.38$	4×10^{-14}	6.95×10^{-17}	9.6×10^6	1.3×10^{13}
FeB	$E_c - 0.23$	3×10^{-14}	2×10^{-15}	3.4×10^{15}	3.4×10^4

lifetime of samples with I_2/Methanol passivation can be regarded as the true 'bulk lifetime', i.e. $\tau_{eff} \sim \tau_{bulk}$. The QSS-PC method was also used to detect the presence of Fe and/or dislocations as outlined below [86, 140, 141].

8.1.1 Detection of Iron in Boron Doped Silicon using QSS-PC Lifetime Measurements

The concept behind the detection of Fe from injection-level dependant (ILD) lifetime measurements was developed by Zoth and Bergholz for the surface photovoltage method, which was then adapted for the QSS-PC method by Macdonald *et al.* [140, 141]. Both methods rely on the fact that Fe in boron-doped Si can be cycled between two states. In the dark, Fe exists as a FeB complex. But energy from heat or illumination (such as the flash illumination used during QSS-PC lifetime measurements) can dissociate the FeB pairs leaving Fe in its interstitial form (Fe_i). The two states have very different trap levels and capture cross-sections (Table 8.1) which results in markedly different ILD lifetime curves being measured before and after FeB dissociation.

As previously discussed in Chapter 2, the carrier lifetime in Si due to a recombination center can be described by SRH statistics. For p-type silicon with a dopant concentration of N_A, the SRH lifetime is given by

$$\tau_{SRH} = \frac{\tau_{p0}(\Delta n + n_1) + \tau_{n0}(N_A + \Delta n + p_1)}{N_A + \Delta n} \tag{8.2}$$

where the symbols have their usual definitions (see Chapter 2). Under low-level injection conditions, Equation 8.2 can be simplified to

$$\tau_{SRH,LLI} = \tau_{n0} + \frac{\tau_{p0}(n_1 + \Delta n)}{N_A}. \tag{8.3}$$

As Fe_i is a deep trap (Table 8.1), n_1 « Δn for the range of injection levels under consideration with the QSS-PC method ($\Delta n > 1x10^{13}$ cm^{-3}). In addition, the large electron/hole capture cross-section asymmetry means that τ_{n0} « τ_{p0}. Therefore, for Fe_i, equation 8.3 further simplifies to

$$\tau_{Fe_i,LLI} = \frac{\tau_{p0}\Delta n}{N_A}. \tag{8.4}$$

The strong dependence of the Fe_i-dominated lifetime on the injection level (Δn) is apparent in Equation 8.4. For FeB, which is a shallower trap with a much smaller capture cross-section asymmetry, the same simplifications cannot be made and Equation 8.3 must be used to calculate the FeB-limited lifetime.

For a Fe concentration of $5x10^{11}$ cm^{-3} and wafer resistivity of 0.6 Ω-cm (N_A ~ $2.6x10^{16}$ cm^{-3}), the FeB and Fe_i lifetime curves are plotted in Figure 8.3 using the simplified equations 8.3 and 8.4, along with the curves obtained using the full SRH equation (Equation 8.2). The signature of Fe contamination of boron-doped Si is immediately apparent, namely the appearance of strong injection-level dependence after dissociation of the FeB pair ***and*** a cross-over point. The position of this cross-over point can be used to distinguish Fe contamination from other impurities which may also undergo a state transition due to light-soaking.

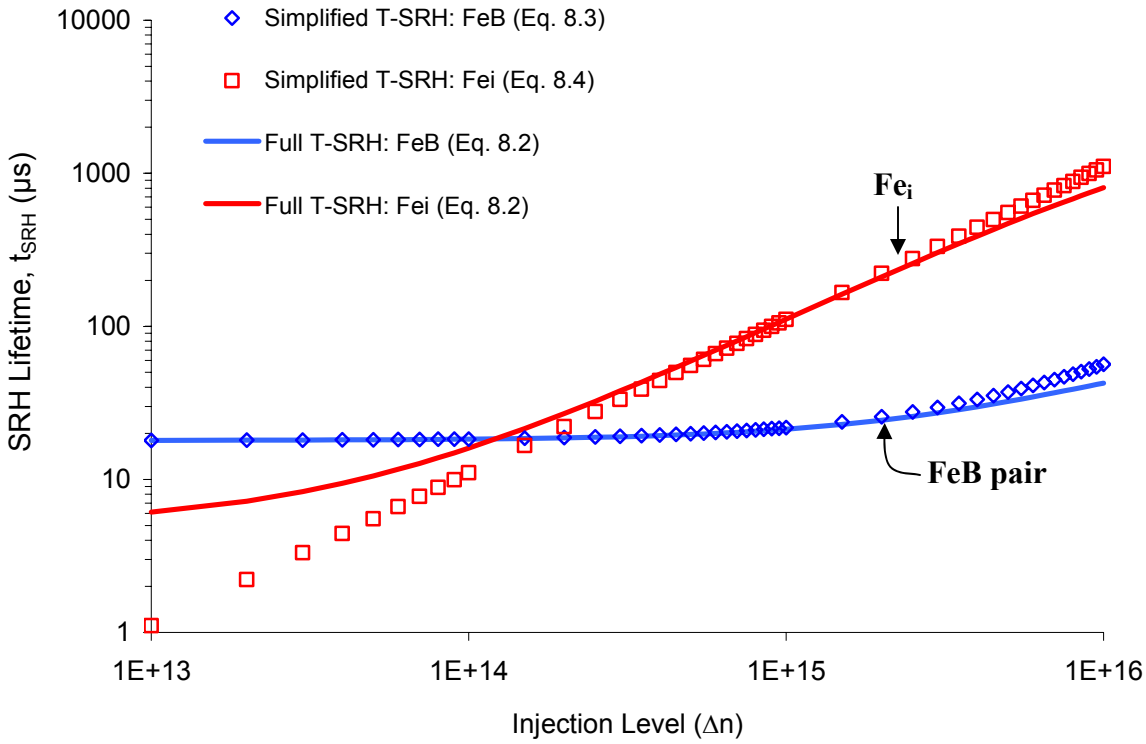

Figure 8.3 Calculated FeB-limited and Fe_i-limited lifetime curves for 0.6 Ω-cm Si with Fe concentration level of $5x10^{11}$ cm^{-3}.

Experimentally, dissociation of FeB pairs in this work was achieved by repeatedly flashing the QSS-PC tester's lamp till the measured lifetime was saturated (each flash dissociates a fraction of the total FeB concentration). At this point, complete dissociation was assumed. Once the 'dark' FeB-dominated and the 'light-soaked' Fe_i-dominated curves are obtained experimentally, the Fe concentration, [Fe], can be extracted from the lifetimes at a chosen injection level using

$$[Fe] = C\left(\frac{1}{\tau_{Fe_i}} - \frac{1}{\tau_{FeB}}\right) \tag{8.5}$$

Values for the pre-factor C for a range of injection levels were obtained by Macdonald [141]. Figure 8.4 shows the experimentally obtained FeB and Fe_i curves for one boric acid diffused sample exhibiting both signatures of Fe contamination which suggests that

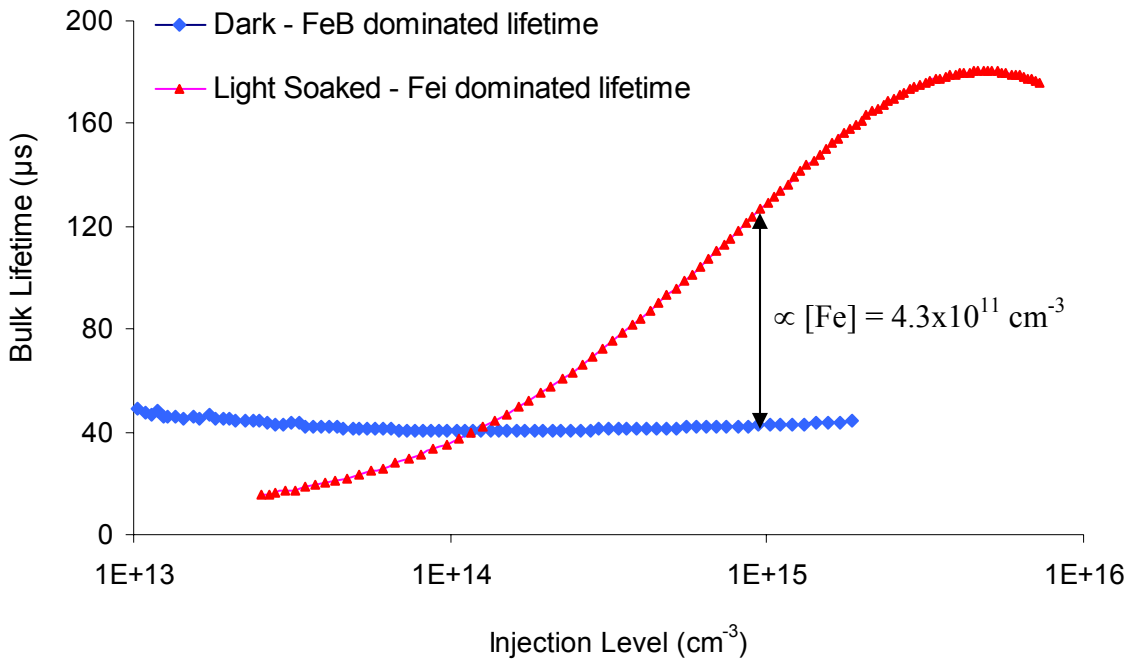

Figure 8.4 ILD lifetime curves of a boric acid-diffused sample before and after light-soaking. The inset shows the Fe concentration calculated for this sample.

diffusion using the boric acid/DI H_2O spin-source does result in iron contamination. For the 0.6-1.4 Ω-cm wafers used in this work, the cross-over point for Fe-contaminated Si has been found by various authors to lie in the range of $1x10^{14}$ cm^{-3} to $4x10^{14}$ cm^{-3} [143, 145-147]. In this work, the cross-over points lie in the range of $1.2x10^{14}$ cm^{-3} to $3x10^{14}$ cm^{-3} indicating that Fe is the most likely contaminant in our samples. The detection limit of this method is ~ $1x10^{10}$ atoms/cm^{-3}.

8.1.2 Suitability of Iodine/Methanol Passivation for Fe Detection

The lifetime that is measured on passivated samples is an effective lifetime which includes all recombination pathways in the sample.

$$\frac{1}{\tau_{eff}} = \frac{1}{\tau_{FeB}} + \frac{1}{\tau_{Fei}} + \frac{1}{\tau_{Auger}} + \frac{1}{\tau_X} + \frac{2S}{L} \qquad (8.6)$$

The 2S/L term comes from surface recombination of the symmetrically passivated sample and the $1/\tau_X$ term is due to all other SRH recombination pathways which may be present in addition to recombination due to Fe. Therefore, the method of extracting the Fe concentration in Si from the difference of the inverse effective lifetimes (Equation 8.5) is valid only when recombination due to Fe is the only recombination pathway that changes due to light- soaking (or the contribution of the other pathways is comparatively small). Past studies using the lifetime method of Fe detection have used SiN passivation which is thought to be stable over time [143, 145-147]. In contrast, this work uses I_2/Methanol solutions for passivation. While preparing these solutions is more convenient and less-time consuming that doing a double-side SiN deposition, I_2/Methanol passivation is known to be unstable over time [139]. This raises the concern that changes in S during light-soaking will affect the extraction of [Fe]. This concern was tested (Figure 8.5) using a relatively lightly contaminated sample which has a high bulk lifetime and is therefore

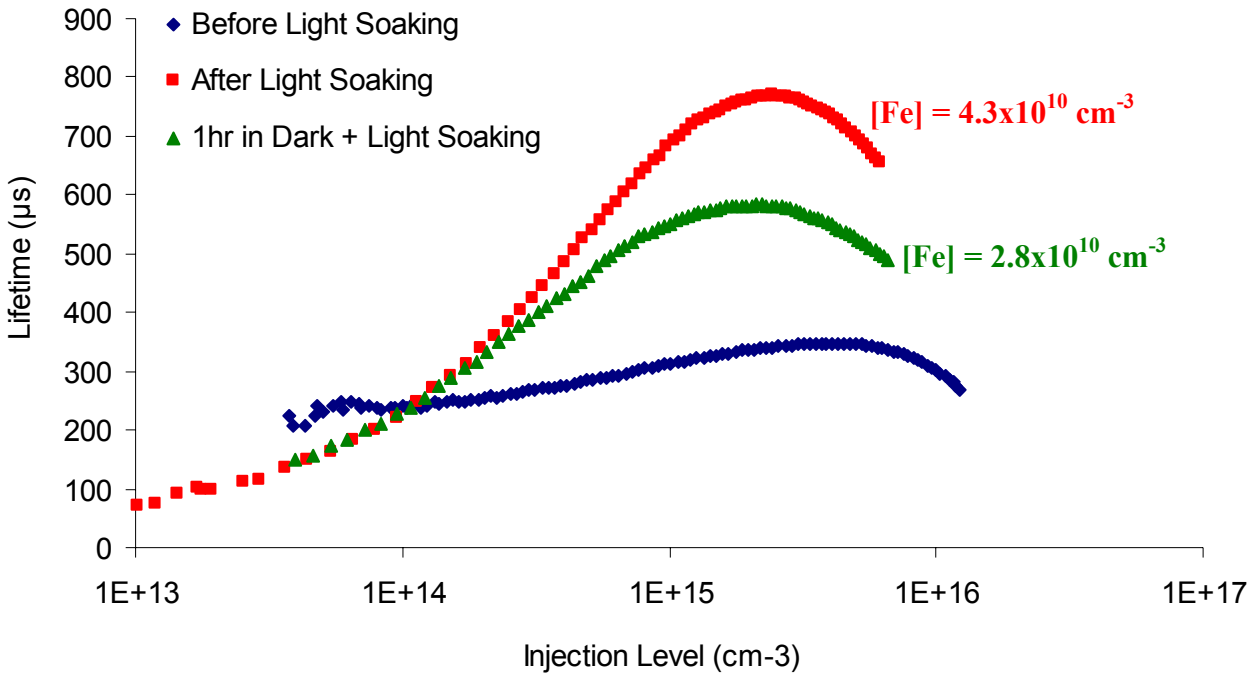

Figure 8.5 Impact of the degradation of I_2/Methanol passivation over time on the extraction of Fe concentration from QSS-PC effective lifetime measurements.

sensitive to changes in the surface passivation quality. The sample was passivated with I_2/Methanol and measured before and after light-soaking. This sample was then allowed to sit in the dark for 1 hr. (during which Fe and B re-pair) after which the light-soaking and lifetime measurements were repeated. Figure 8.5 shows the resulting curves and the corresponding Fe concentrations that were extracted. While the passivation quality does degrade over time, its impact on the computed Fe concentration is fairly small even for such low levels of Fe contamination. On more heavily contaminated samples ([Fe]~$4x10^{11}$ cm^{-3}), a longer 3 hr. delay resulted in only a 25% error in the extracted Fe concentration. Since the typical light-soaking time in the measurements here was ~10 minutes, the change in I_2/Methanol's passivation quality over time has a negligible impact on the results.

8.1.3 Detection of Dislocations in Silicon using QSS-PC Lifetime Measurements

Interestingly, the ILD lifetime signature for the dislocation networks that form for heavy boron diffusions is the same as that for Fe_i, i.e. a strong injection level dependence in the lifetime curve [86]. However, if dislocations are the cause of lifetime degradation, the ILD in the lifetime curve should exist without any need for light-soaking. None of the boric acid diffused samples studied here showed strong ILD in their 'dark' lifetime curves which suggests that dislocation generation was minimal or insignificant. This conclusion is bolstered by the report of Gaisenau *et al.* who found a threshold range of time-temperature conditions below which dislocations did not form (Figure 8.6) [91]. As the boron diffusion condition chosen for cell fabrication here (the dot in Figure 8.6) falls below this range of threshold conditions, dislocations are not expected to be present which explains the lack of the dislocation signature in ILD lifetime curves.

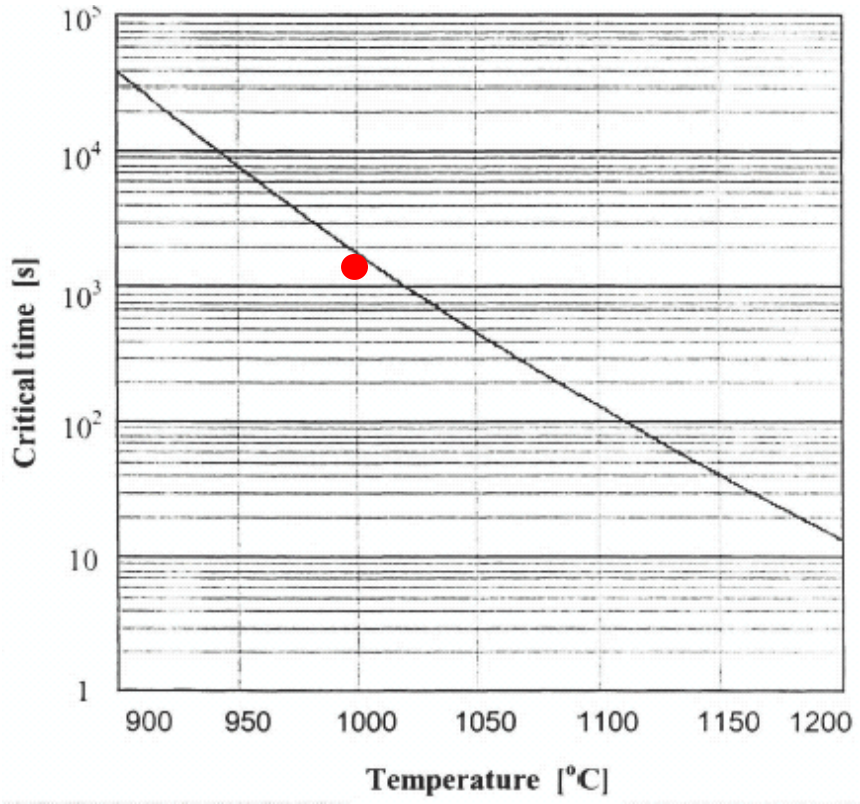

Figure 8.6 The solid line shows the combinations of boron diffusion time and temperature beyond which the generation of misfit dislocations occurs (figure taken from Ref. 91). The dot shows the time/temperature combination for the boron diffusion process used in this work for cell fabrication (see Chapter 6).

8.2 Tracking and Understanding of Process-Induced Iron Contamination and Gettering

The discussion in the prior section clearly shows that the boric-acid/DI H_2O source used in this work can result in Fe contamination of Si wafers. In this section, the change in Fe contamination levels during various cell processing steps is tracked. The process sequence involves boric acid diffusion in N_2 ambient at 1000°C for ~20 minutes, followed by $POCl_3$ diffusion+drive-in at ~870°C for ~40 minutes and finally an oxidation/passivation step at 900°C for 25 minutes (10 min. oxidation followed by a 15 min. N_2 anneal). The boron diffused side was protected with a spin-on diffusion mask

during $POCl_3$ diffusion and the BSG//PSG were etched in buffered HF before the final oxidation.

Figure 8.7 shows that immediately after boron diffusion, the average lifetime of the Fz Si wafers used in this study is ~500 µs which is more than sufficient for achieving high efficiencies on the 300 µm thick substrates used here (see Figure 8.2). While this average lifetime value is perhaps the highest reported for a spin-on boron source and comparable to lifetimes reported for BBr_3 diffusions (Figure 8.1), there is a very wide spread (~50 µs - 800 µs) in the bulk lifetime. This corresponds to a more than one order of magnitude variation in the Fe concentration as also shown in Figure 8.7. As noted in Figure 8.2, at the low-end of this lifetime distribution, the well-passivated 20%-capable cell that is the goal of this work will achieve efficiencies below the 18.9% baseline Al-BSF cell.

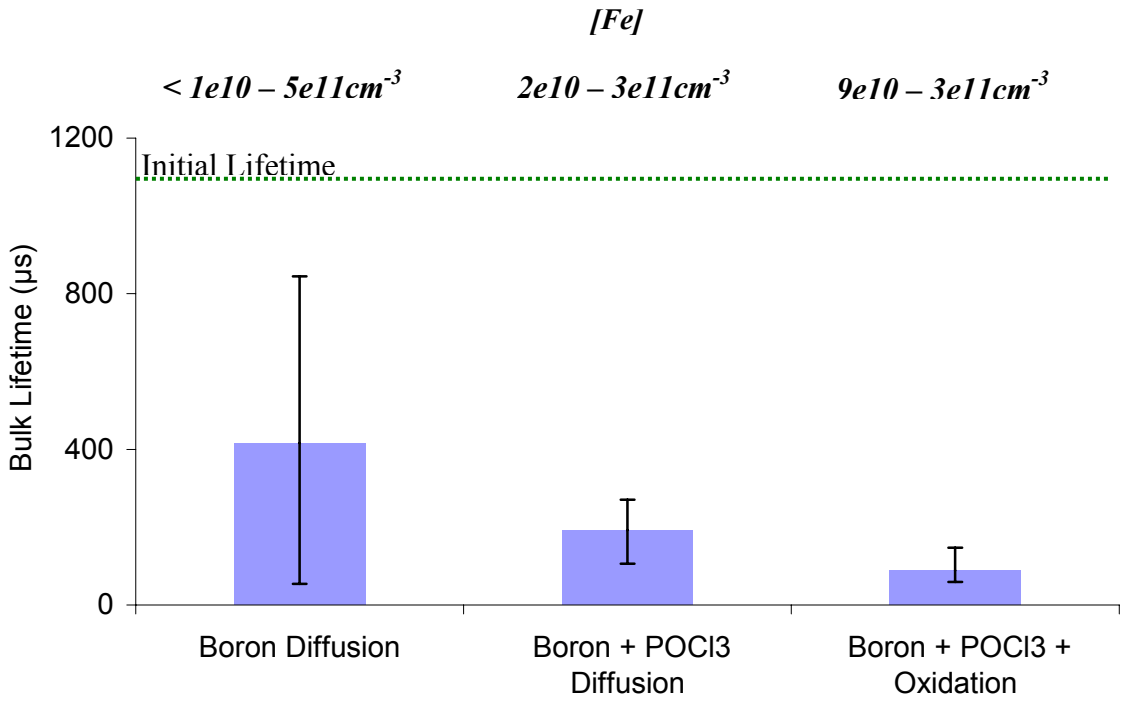

Figure 8.7 Minority carrier bulk lifetimes on FZ Si substrates after various cell processing steps. The dashed line shows the average starting lifetime of cleaned, unprocessed wafers. The data in bolded italics is the Fe concentrations extracted from lifetime measurements at each step.

$POCl_3$ diffusion is well known to be very effective at gettering Fe from the Si bulk [87, 148] and was therefore expected to help recover the loss in lifetime experienced due to the boron diffusion step. However, the results here indicate that the gettering effect is more complex. $POCl_3$-diffusion improved lifetimes only for those samples that had very low lifetimes (and therefore, the highest bulk Fe concentrations) after the boron diffusion. This can be seen in Figure 8.6 by comparing the low end of the lifetime error bars. But on average, lifetimes dropped after $POCl_3$ diffusion. The lifetime situation becomes even worse after the thermal oxidation/surface passivation step with lifetimes below 100 μs and [Fe] > $1x10^{11}$ cm^{-3}.

One explanation for this trend is that each subsequent high-temperature step exposes the samples to more and more Fe from the furnaces; however, this theory would not explain the degradation in lifetime after $POCl_3$ diffusion as the 'self-gettering' nature of the process should prevent additional Fe from being introduced to the samples.

An alternate explanation is that the wafers are originally contaminated with Fe during the boron diffusion step, but that most of this Fe is trapped in/gettered into the boron diffused layer only to be injected into the bulk during the subsequent high-temperature steps. This is plausible, as boron diffusion is known to getter Fe from pre-contaminated wafers [149, 150]. The question then arises – if Fe is being injected into the bulk, why is $POCl_3$-gettering unable to remove it? There are two potential explanations for this effect:

1. The injection of Fe into the bulk during the $POCl_3$ diffusion is a slow, gradual process resulting in the gettered bulk Fe being continually replenished by Fe leaking from the p^+ layer. A similar theory has previously been proposed for multicrystalline Si, with the grain-boundaries serving as the constant source of Fe during a $POCl_3$ diffusion process [151]. The theory that the p^+ layer is not emptied of Fe during the short, industrial-type $POCl_3$ process that is used here is supported by the fact that the oxidation step after $POCl_3$ diffusion releases, on average, even more Fe into the bulk.

2. An alternate explanation is that the presence of the boron diffused layer somehow interferes with gettering by the n^+ layer on the other side of the wafer.

If the first theory is correct, then injecting Fe from the p^+ layer to the bulk *before* $POCl_3$ diffusion should result in strong gettering. Experimentally, this is exactly what was observed. By performing an oxidation step immediately after the boron diffusion, Fe can be strongly driven out of the p^+ layer and into the wafer bulk as shown in Figure 8.8. Once the Fe is in the wafer bulk, $POCl_3$ gettering is able to completely remove Fe from the sample and bulk lifetime rises back to above 1 ms. This data supports the first theory and also shows that the presence of the p^+ layer does not hinder $POCl_3$-gettering. Note that the oxidation step for injecting Fe into the wafer can be performed either *in-situ* or *ex-situ*.

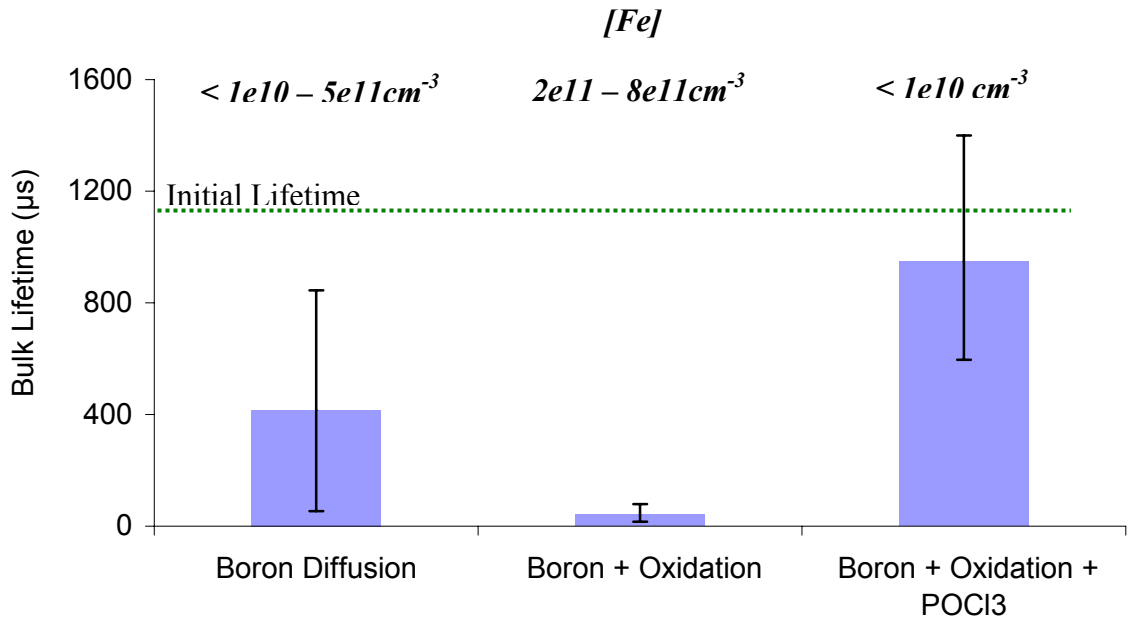

Figure 8.8 Minority carrier bulk lifetimes showing the effect of a pre-$POCl_3$ oxidation on the Fe gettering ability of $POCl_3$-diffusion. The dashed line shows the average starting lifetime of the wafers. The data in bolded italics is the Fe concentrations extracted from lifetime measurements at each step.

It remains unclear why the injection is much stronger during oxidation than during $POCl_3$ diffusion. The lower temperature of the $POCl_3$ diffusion (870°C vs. 900 °C for the oxidation) is unlikely to be the cause. Over the 40 minute diffusion/drive-in step, the diffusivity (D) of Fe_i at 850°C (~$9x10^{-7}$ cm^2/s) corresponds in an average diffusion length ($L = \sqrt{4D\tau}$) for Fe of ~900 μm or three times the thickness of the 300 μm wafers used for this study [87, 131]. One possibility is that the amount of oxygen in the ambient determines the effectiveness of the Fe injection process. Using BN solid sources, Ohe et al. had also reported that anneals after a boron diffusion degraded bulk lifetimes with anneals in N_2 resulting in much smaller lifetime degradation than O_2 anneals [85]. The relatively small amount of oxygen in the ambient of a typical $POCl_3$ process may slow the injection of Fe into the bulk during a $POCl_3$ diffusion step. The $POCl_3$ process used here had just ~5% (vol.) O_2 in the ambient. Though the work of Ohe *et al.* made no attempts to detect Fe, the authors did speculate that Fe is gettered/segregated into the p^+ layer during boron diffusion and then re-injected into the bulk during subsequent high temperature anneals. The simultaneous tracking of lifetime and Fe in this study provides experimental confirmation of their speculation. Lifetime degradations due to oxidation performed after a BBr_3 diffusion step have also been reported which suggests that the Fe-injection phenomenon is not limited to a specific boron source [71, 148].

8.2.1 Dielectric-based Gettering of Fe

Since performing an oxidation before $POCl_3$ diffusion allows $POCl_3$ gettering to remove Fe from the wafers, any surface passivation process can be used without running the risk of injecting more Fe from the p^+ layer. However, the need to have an additional high-temperature Fe-injection step lengthens the cell process sequence. It would be advantageous if process-induced Fe gettering could instead to be rolled into the passivation step. Therefore, the gettering characteristics of the two passivating spin-on glasses (SOGs) studied in Chapter 7 (a pure-SiO_2 SOG and an Al-doped SOG) were

examined. As in the passivation study, both dielectrics were annealed at the same condition used for growing the thermal oxide.

Figure 8.9 shows that after passivating the B-BSF with the spin-on SiO_2, the bulk lifetime and the corresponding bulk Fe concentration are almost identical to the values obtained with thermal SiO_2 passivation indicating that neither the thermal nor the spin-on SiO_2 layer performs any Fe gettering. However, after passivation with the Al-doped SOG, no Fe was detected in the bulk and the bulk lifetime showed complete recovery. For the process-flow used in Figure 8.9 (i.e. boron diffusion, followed by $POCl_3$ diffusion and then oxidation), *some* of the Fe in the wafer is likely being gettered by the $POCl_3$-diffusion step. To see the Al-doped SOG alone could getter the Fe introduced by the boron diffusion step, test wafers were boron diffused and oxidized (*ex-situ*) to inject Fe into the wafer bulk.

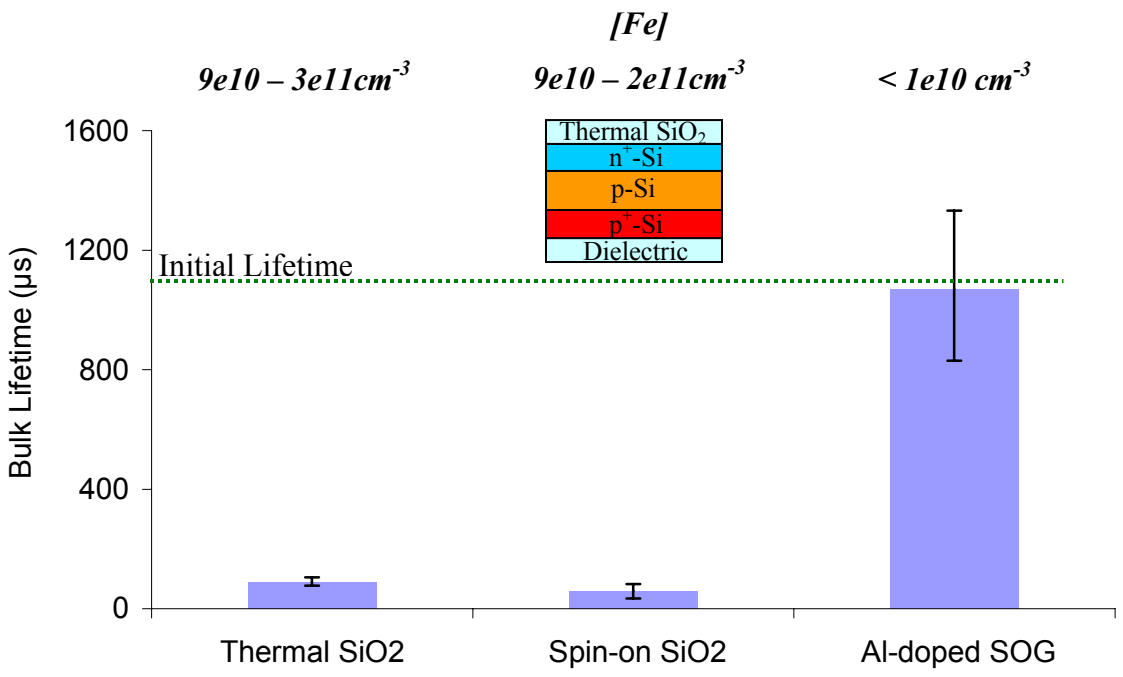

Figure 8.9 Minority carrier bulk lifetimes of $n^+/p/p^+$ silicon wafers after passivation of the B-BSF with various dielectrics. The inset shows the structure being passivated/gettered. In all cases, the front n^+ side gets oxide passivated in the same step as the rear passivation.

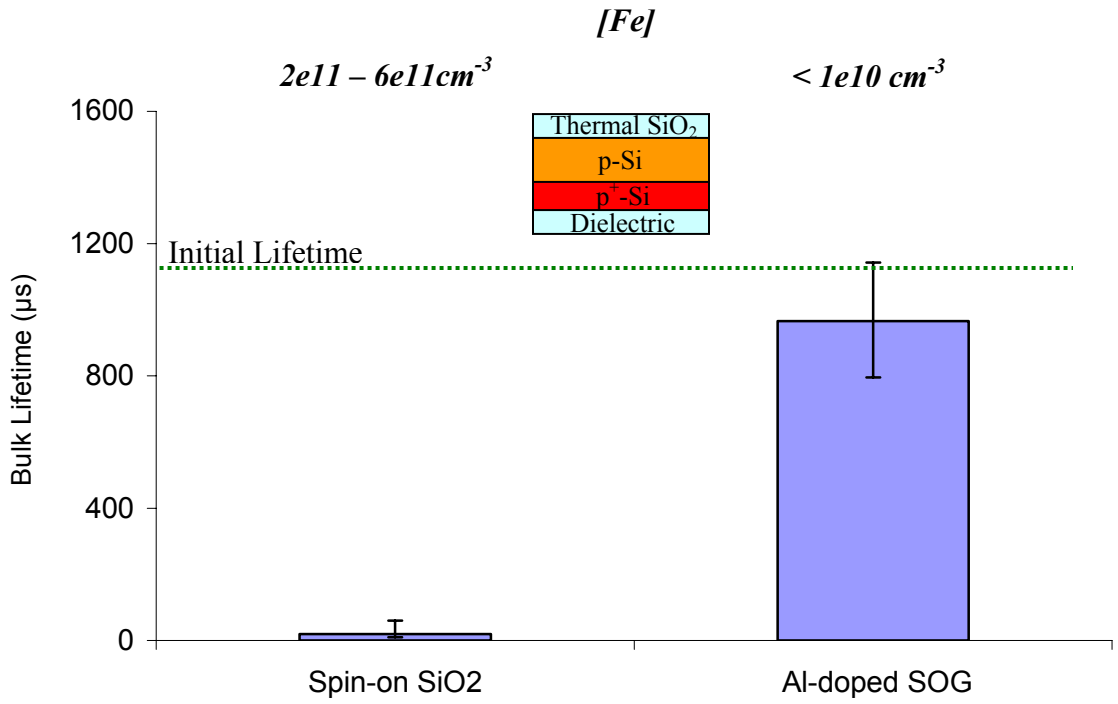

Figure 8.10 Minority carrier bulk lifetimes of Fe-contaminated p/p$^+$ silicon wafers after passivation of the B-BSF with various dielectrics. The inset shows the structure being passivated/gettered. In both cases, the front side gets oxide passivated in the same step as the rear passivation.

At this step, the average bulk lifetime and Fe concentration was ~30 µs and 4.2x10^{11} cm^{-3} respectively (measured on sacrificial wafers). The oxide layer was then stripped in HF and the boron-diffused surface was re-passivated with either the spin-on SiO_2 or the Al-doped SOG. The results in Figure 8.10 clearly show that the gettering by the Al-doped SOG alone is strong enough to reduce the bulk Fe concentration to below the detection limit (~1x10^{10} cm^{-3}) of the QSS-PC method.

Note that all of the samples used for the passivation/gettering experiments thus far have had a pre-existing boron diffused layer. Gettering of bulk Fe to pre-existing boron diffused layers has previously been shown by Joge *et al.* and Terakawa *et al.* using 600°C anneals [149, 150]. Complete lifetime recovery was reported after a 2.25 hr [149] long anneal. However, the fact that neither the thermal oxide layer nor the spin-on SOG

manages to remove Fe from the bulk suggests that gettering to the pre-existing p^+ layer is ineffective during the short, higher temperature anneal that is used here to cure the Al-doped SOG (~25 minutes at 900°C with the full process cycle lasting ~60 minutes). This, in turn, suggests that the lifetime recovery observed with the Al-doped SOG (Figure 8.10) can be entirely attributed to gettering by the Al-doped SOG.

In order to further examine if Fe is being *co-gettered* by the pre-existing p^+-Si layer and the Al-doped SOG, additional samples were created. As before, the samples were boron diffused and oxidized to inject Fe into the bulk which resulted in bulk Fe concentration was ~$6x10^{11}$ cm^{-3} (measured on a sacrificial wafer). But before attempting to getter the Fe from these samples, the boron diffused layer was removed by etching away ~5 μm from each surface. These etched wafers were then passivated with: 1) a re-grown thermal oxide, or 2) the spin-on SiO_2 or 3) the Al-doped SOG. The spin-on dielectrics were applied to the same side that was boron diffused. The final structure of these samples is shown in Figure 8.11. Some control samples in the same run were gettered using the Al-doped SOG *without* etching off the p^+ layer (i.e. the structure in Figure 8.10). The results (Figure 8.11) show that gettering by the Al-doped SOG is able to remove > 98% of the bulk Fe even when no boron-diffused Si layer exists underneath it. However, unlike the control samples (which had the p^+ layer intact during the passivation/gettering step), a small amount (≤ 2x10 cm^{-3}) *was* detected in the bulk which suggests that some gettering to the pre-existing p^+-Si surface does occur in the short, 900°C oxidation cycle. However, this gettering is far too weak to have a significant effect on the wafer lifetime.

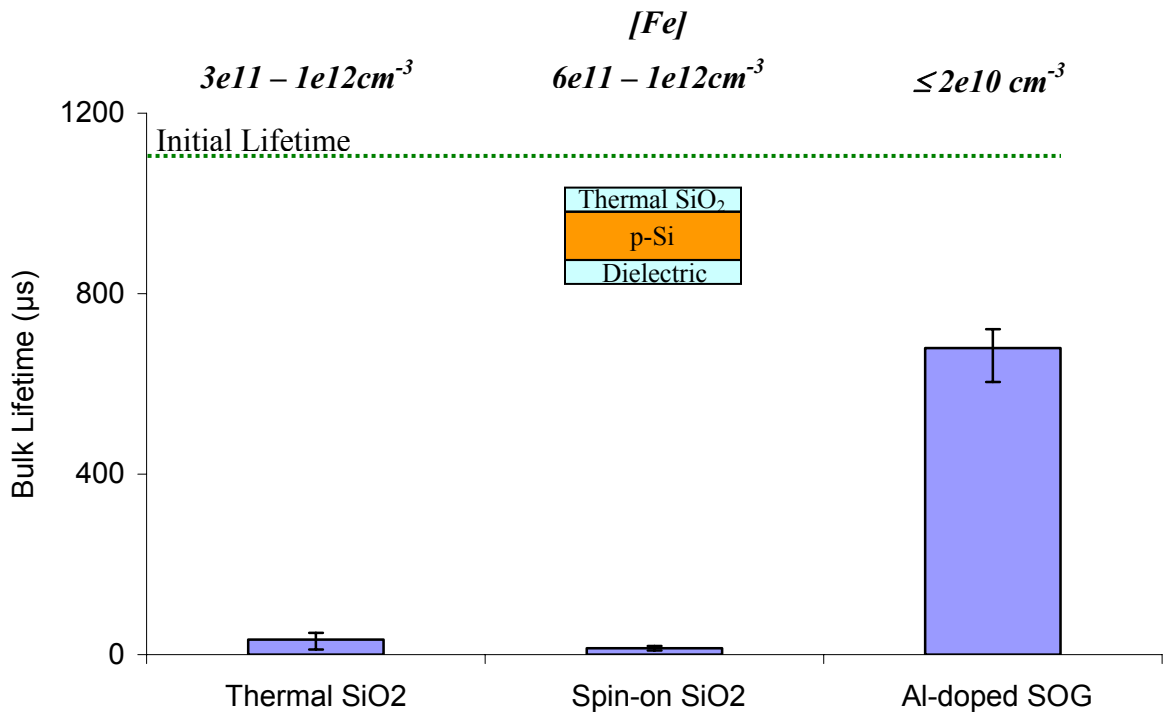

Figure 8.11 Minority carrier bulk lifetimes of Fe-contaminated p-type silicon wafers after passivation of one side with various dielectrics. The inset shows the structure being passivated/gettered. In all cases, the other side of the wafer gets oxide passivated in the same step.

8.2.2 Mechanism for Fe gettering by Al-doped SOG

As Al-BSF formation is known to getter Fe from the bulk [87], the Al-doped SOG was spun onto undiffused FZ wafers and annealed. No change was observed in the sheet resistance of the wafers which indicates that there is little to no Al-BSF formation to explain the gettering effect. The lack of Al-Si alloying is further supported by surface secondary ion mass spectroscopy (Surface SIMS) data of an Al-doped SOG passivated Si wafer (note that the SOG was removed in HF before the measurement). The results in Figure 8.12 show that the surface Al concentration of ~1x10^{17} cm^{-3} after passivation with the Al-doped SOG is: 1) similar to the background Al contamination in our processing environment (as measured on control samples which were cleaned but otherwise not

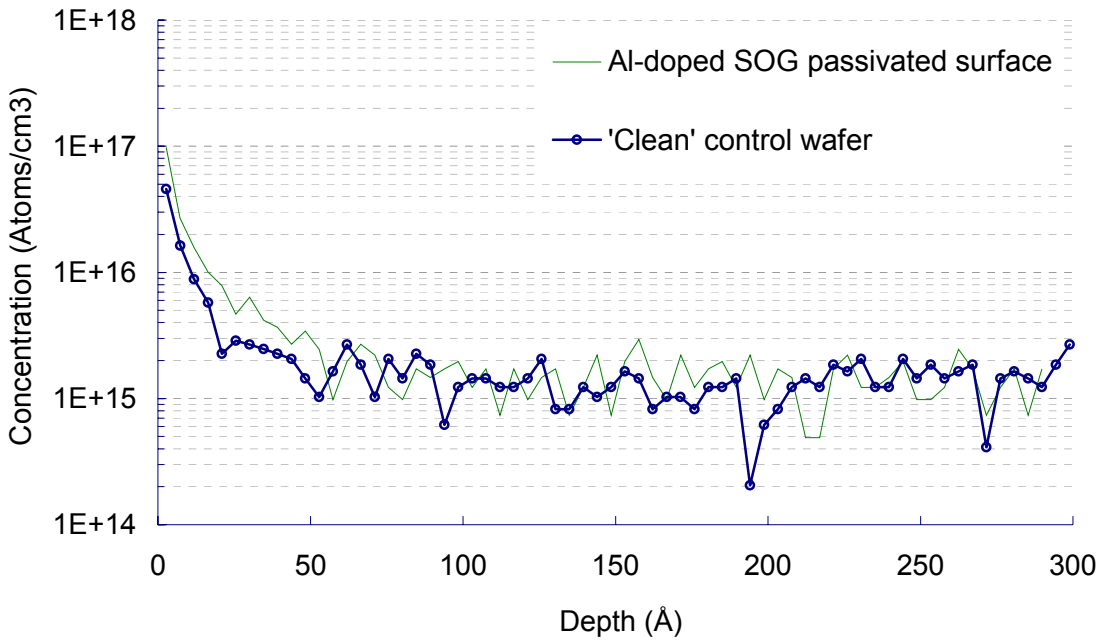

Figure 8.12. Surface SIMS measurement of Al at the surface of a wafer passivated with the Al-doped SOG and at the surface of a 'clean' control wafer.

not processed), and 2) an order of magnitude lower than the ~$4x10^{18}$ cm^{-3} solubility of Al in Si at 900°C [10]. Therefore, both the sheet resistance and SIMS measurements suggest that Fe gettering exhibited by the Al-doped SOG cannot be explained by Al-BSF formation. An alternate explanation lies in the dielectric charge. As noted in Chapter 7, the cured Al-doped SiO_2 exhibits a negative charge density of ~$1x10^{12}$ cm^{-2} while both the thermal and the spin-on SiO_2 exhibit a small positive charge. Shimizu *et al.* have previously shown that treating the surface of Si wafers with $Al(NO_3)_3$ prior to growing a thermal oxide results in the formation of an oxide layer with a negative charge [152, 153]. They argued that Al replaces some Si atoms in the SiO_2 network resulting in the formation of an $(AlOSi)^-$ complex. Similarly, the bonding of Al with oxygen at the interfacial SiO_2 layer that is formed during deposition of Al_2O_3 is thought to be the source of the high negative charge density of Al_2O_3 [154]. It is therefore plausible that a

similar negatively charged complex forms during the oxygen annealing of the Al-doped SiO_2-based SOG. Further, the correlation between the charge polarity of the passivating dielectric and its Fe gettering ability suggests that electrostatic attraction between a negatively charged complex in the Al-doped SOG and the positively charged interstitial Fe may be responsible for the observed gettering effect of the Al-doped SiO_2. Note that electrostatic attraction is also the driving force for the pairing of Fe_i with negatively charged boron ions in p-type Si [87].

8.2.3 The Source of Fe Contamination

In order to determine where the Fe detected in this study comes from, the background contamination from cleaning, handling and the furnaces was measured by sending FZ wafers through the entire process sequence but without depositing any dopants or dielectrics on the wafers. Note that none of these 'dummy' wafers were put into the $POCl_3$ furnace to avoid 'auto-doping' and gettering by the furnace. From this, the background Fe contamination was found to be $\leq$ 2e10 cm^{-3} after the boron diffusion thermal cycle, which rises to $\leq$ 5.5e10 cm^{-3} after both the boron and oxidation thermal cycles – both are about an order of magnitude lower than the Fe contamination levels detected on the boron diffused and oxidized samples. While this demonstrates that Fe does exist in the processing environment, the boric acid source used in this work may also be a source of Fe since it is only certified to be ~99.999% pure on a metals basis by the manufacturers [124, 125]. It is difficult to establish if the much-higher-than-background levels of Fe detected in the wafers after boron diffusion and oxidation is primarily due to contamination from the boric acid source or due to the boron layer strongly 'gettering' the background Fe (i.e. removing Fe from the ambient and accumulating it in the wafer).

The level of Fe contamination on boron diffused and oxidized was also fairly consistent (~$2x10^{11}$ – $8x10^{11}$ cm^{-3}) during the ~3 year period of this study. The larger

variation in bulk Fe concentrations observed directly after boron diffusions and after a subsequent $POCl_3$ diffusion (see Figure 8.7) is possibly due to variability in the fraction of the trapped Fe that is injected into the bulk. The reason for this variation is currently not known. The boric acid solution used in this work is not a likely source of the variation, as similar variation was seen even when the same batch of solution was used. Additionally, all the solutions were agitated for 3 minutes prior to use which would have homogenized any Fe in the solution. All tweezers and pipettes used for handling the wafers and dispensing the solution were also cleaned in a 2:1:1 DI $H_2O/H_2O_2/HCl$ solution immediately before use to remove trace metals.

8.2.4 The Sink for Fe

While the lifetime measurements clearly show that the Al-doped SOG provides strong gettering of bulk Fe, it is unclear if the gettered Fe remains in Si at the Si/Al-doped SOG interface or if it leaves the Si substrate. To try and answer this question, Surface SIMS measurements (detection limit ~ $5x10^{15}$ cm^{-3}) were performed on samples which were boron diffused to introduce Fe into the wafer and then oxidized to drive the Fe into the bulk. After this oxidation step, the bulk Fe concentration was ~$1x10^{12}$ cm^{-3} as measured on sacrificial wafers. The remaining wafers were deglazed in HF and then gettered with the Al-doped SOG. The Al-doped SOG was then stripped in HF before the SIMS measurement.

The results (Figure 8.13) showed that the surface Fe level on an Al-doped SOG gettered wafer is very similar to the background surface-Fe contamination as measured on a control wafer. The control wafers were simply cleaned and went through no further processing. Immediately before packaging and shipping, both the control and gettered wafers were simultaneously subjected to an HF dip and DI water rinse and were handled using the same materials (beakers, chemicals, tweezers and carriers). This was done so that the final environmental exposure of the control and gettered samples was as similar

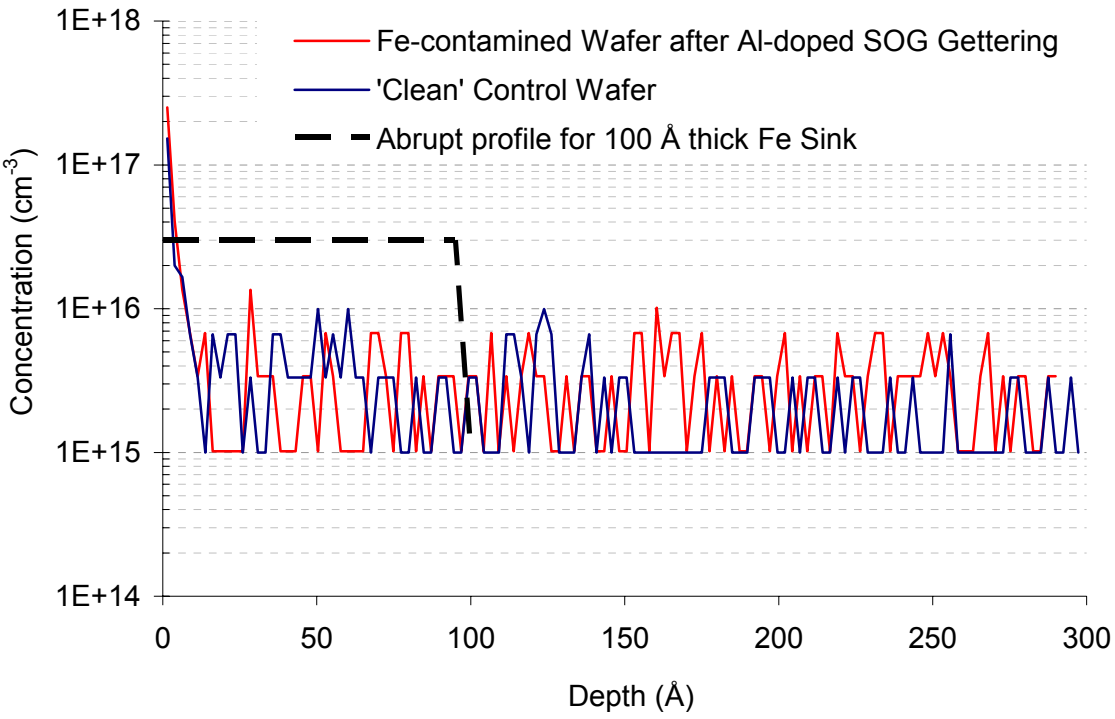

Figure 8.13 Surface SIMS measurement of Fe on a Fe-contaminated wafer after gettering with the Al-doped SOG and on a 'clean' control wafer.

as possible (note that the same procedure was used for the Al Surface SIMS measurements shown in Figure 8.12). The measurements were repeated twice on samples prepared over 1 year apart and similar results were obtained on both occasions.

Due to the significant background contamination, it is unclear if: 1) the gettered Fe remains in Si at concentrations below the background contamination level or 2) it leaves the Si substrate and goes into the dielectric. Note that if all the bulk Fe (~$1x10^{12}$ cm-) in the 300 µm thick wafer was gettered to a 100 Å thick surface layer, it would result in an average surface Fe concentration of ~$3x10^{16}$ cm^{-3} (as shown with the dotted lines in Figure 8.13) which is about three time higher than the background contamination. This suggests that if the gettered Fe remains in Si, the gettering site is > 100 Å thick. This, however, is not a definitive conclusion and further work is required to narrow down the

final location of the gettered Fe, i.e. is it in a > 100 Å thick Si surface layer or does it escape into the Al-doped SOG?

8.3 Conclusions

The spin-on boric acid/DI H_2O source developed in this work provides the highest average post-diffusion lifetime reported for spin-on sources. However, the large spread in the post-diffusion lifetime distribution prompted an experimental study into the lifetime degradation mechanism. The results show that Fe introduced during boron diffusion can get trapped in the boron diffused layer and released into the substrate during subsequent high-temperature steps. We have also shown that $POCl_3$ gettering of the trapped Fe is in-effective unless the Fe is first injected into the bulk from the boron doped layer via an oxidation step. The search for methods to reverse the boron diffusion-induced lifetime loss also led to the discovery of an Al-doped spin-on glass that can simultaneously getter Fe and passivate a p^+-Si surface in a short oxygen anneal step (Chapter 7). A comparison study of various SiO_2/SiO_2-based materials found a correlation between the charge polarity in the passivating dielectric and its gettering ability – only the negatively charged Al-doped SOG exhibited a gettering effect. This suggests that the gettering occurs due to electrostatic interaction between the negatively-charged dielectric and positively charged Fe_i^+ ions though further studies are required to confirm this and to identify where the gettered Fe ends up.

Since the passivation studies of Chapter 7 and the Fe studies presented in this chapter show that the Al-doped SOG provides sufficiently high-quality passivation and gettering on a planar p^+ surface to obtain a 20% efficient B-BSF cell, an Al-doped SOG passivated, planar B-BSF structure will be used for cell fabrication (Chapter 10).

Chapter 9

CHARACTERIZATION OF ELECTRICALLY CONDUCTIVE BACK SURFACE REFLECTORS

In Chapters 5-8, various pieces of the targeted 20% efficient B-BSF cell (Figure 9.1) were successfully developed – the boron diffusion profile/diffusion condition (Chapters 5 and 6), the cell structure and passivation scheme (planar, passivated B-BSF with point contacts – Chapter 7), and a cell process sequence that achieves high bulk lifetimes (Chapter 8). This chapter deals with the last remaining piece – finding a back surface reflector (BSR) material that meets the optical requirements for a 20% efficient cell (95% reflectance and 100% diffusivity) and is also conductive enough to serve as the electrical interconnect for the rear point contacts.

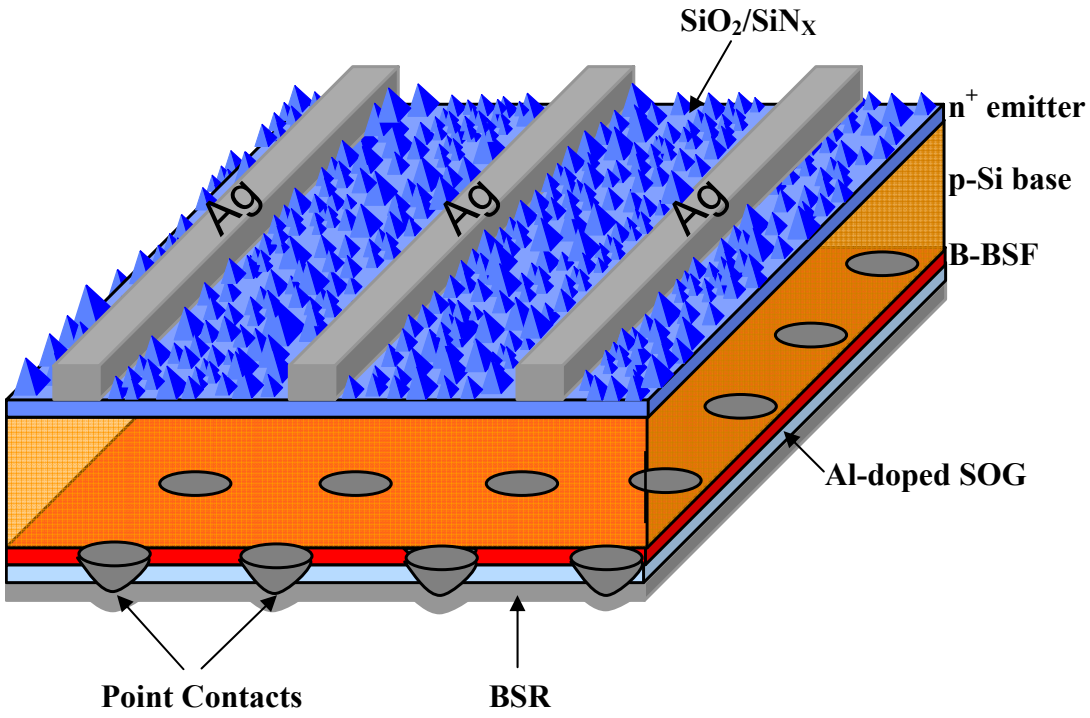

Figure 9.1 Cross-section of B-BSF cell fabricated in this work.

9.1 The Role of Back Surface Reflectors in Solar Cells

As discussed in Chapter 2, BSRs are commonly used in Si solar cells because they result in light making at least two passes through the cell. This enhances absorption in the long-wavelength portion of the AM1.5 spectrum where Si absorbs poorly (see Figure 2.13) [43]. Diffuse BSRs are especially advantageous as they promote light-trapping via total internal reflections of light within the cell. For Lambertian reflectors, these effects result in a path length enhancement of $4n^2$, where n is the index of refraction of the absorbing substrate. For Si cells (n = 3.52), the path length enhancement due to a Lambertian reflector is ~50 [49]. This enhancement limit takes into account the fact that even when light is reflected by a perfectly diffuse reflector, ~8% of it falls within a *loss cone* and is 'effectively specular' since it does not meet the critical angle (θ_c) required for total internal reflection (Figure 9.2) [50].

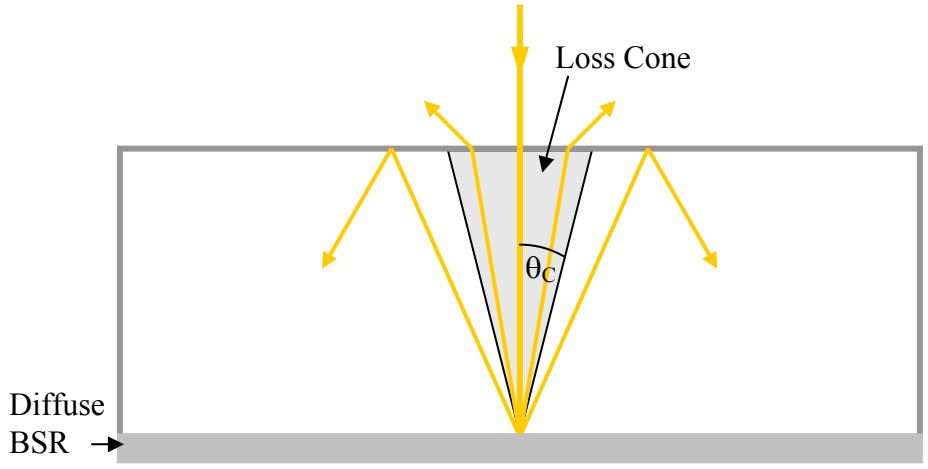

Figure 9.2 Ray diagram illustrating light-trapping by diffuse rear reflector and escape of light within the loss-cone.

The impact of a BSR is greater for thinner cells as they absorb less light in a single pass. Since reducing the wafer thickness is important for cost reduction (see Figure 1.10), a highly reflective BSR is an important part of a high-efficiency cell design. While thick

wafer-based cells are the focus of this thesis, BSRs are also an important component of high-efficiency thin-film solar cells [155]. On such devices, various reflector schemes – textured dielectric layers, metal or dielectric/metal reflector stacks, ordered gratings, reflective pigment-loaded dielectrics and even commercially available white paint – have been researched [156-160]. The use of textured conductive oxides (TCOs) as the BSR is advantageous because a single layer can serve as the rear passivation layer, the rear electrical contact, and the BSR. However, the surface roughness of textured TCO layers has been associated with losses in V_{OC} and FF [161, 162, 163]. Additionally, these layers are a source of absorption losses, require index matching for optimal coupling of light into the cell and their light scattering ability decreases for longer wavelengths [157]. The diffuse reflectance of ordered grating structures is similarly wavelength dependent [158]. Pigmented diffuse reflectors such as white paint and pigment loaded dielectric layers have superior diffuse reflectance characteristics, but provide neither passivation nor conductivity [159, 160]. This work examines a third scheme where diffuse reflectance and electrical conductivity are combined in a single layer, leaving rear surface passivation to a dedicated passivating layer.

9.2 Experimental

Five BSR materials – evaporated Al, evaporated Ag, SP Al Paste, a SP fritless Ag paste and a brushed-on Ag colloid – were evaluated. The optical characteristics of each material were evaluated by depositing them on to one side of FZ Si wafers. In order to minimize light absorption by the wafers and light scattering at the wafer surfaces, the wafers were 'shiny-etched' down to a thickness of ~200 μm using a HNO_3:CH_3COOH:HF solution and coated on one side with the various BSR materials. The total hemispherical reflectance of the samples was then measured from the bare (uncoated) side. This simulates the operation of a solar cell where light will impinge on the BSR only after it has passed through the substrate. The total hemispherical reflectance of these samples

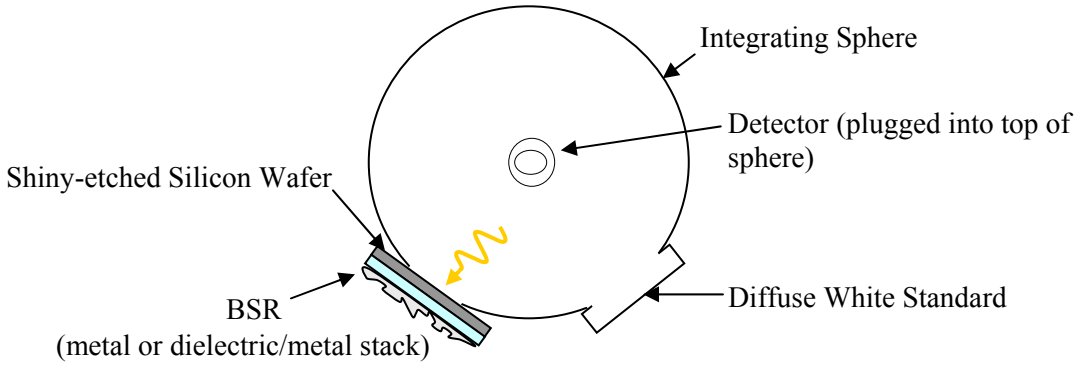

Figure 9.3 Top-down view of the integrating sphere setup used for characterizing the reflectance characteristics of various BSR materials.

was measured using an Optronic Laboratories OL 750 spectroradiometric measurement system with an integrating sphere. This setup is illustrated in Figure 9.3.

In order to separate out the specular reflectance and diffuse reflectance of a sample, two measurements were performed on each sample – a total reflectance measurement and a diffuse reflectance measurement. For the latter, a specular 'light trap' was installed in the integrating sphere. Since this light trap absorbs nearly all light that falls within the loss cone, when the light trap is installed, only light that is diffusely reflected by the sample is measured. From these measurements – the reflectance (R_B) and the scattering fraction (β – i.e. the fraction of incident light that is scattered by the sample instead of being reflected specularly) of each material were calculated. Only wavelengths greater than 800 nm were examined in this study as shorter wavelengths (which are strongly absorbed by Si) will be almost completely absorbed by the substrate before reaching the BSR [44]. Both R_B and β were calculated at a wavelength of 1300 nm. This wavelength was chosen to minimize the effect of absorption by the Si substrate. β was calculated by simply taking the ratio of the diffuse and total reflectances at 1300 nm. For diffuse reflectors, R_B can be extracted from total reflectance measurements using [164, 165]

$$R_B = \frac{R_T - R_{fe}}{(1 - R_{fe})(1 - R_{fi}) + (R_T - R_{fe})R_{fi}} \tag{9.1}$$

where R_T is the measured total reflectance, R_{fe} is the reflectance of silicon (~34 %) and R_{fi} (the internal reflectance at the planar front Si surface assuming a Lambertian rear surface) is 92% [50]. For specular BSRs ($\beta \approx 0$), $R_B \approx R_T$ for long-wavelengths since nearly all light reflected by the BSR falls within the loss cone and thus escapes from the front surface after just once bounce [164].

Since the B-BSF cells in this work are passivated with a spin-on dielectric (the Al-doped SOG – see chapters 7 and 8 for details), the BSR for the cell is a dielectric/metal stack. Therefore, the reflectance measurements and R_B/β calculations were repeated with one side of the test wafers being coated with the Al-doped SOG and the metals being deposited on top of the SOG.

9.3 BSR Characterization

Figures 9.4 and 9.5 show the measured total reflectance (dashed line) and diffuse reflectance (points) curves for samples with evaporated Ag and the Ag colloid as the BSR. The Ag colloid BSR was sintered for 5 minutes at 400°C for reasons that will be discussed later in this section. The total *escape* reflectance (solid line in Figures 9.4 and 9.5) is the measured total reflectance curve (which is the sum of diffuse and specular reflections from both the front and rear surface of the test wafer) shifted down by ~34% (the reflectance of the bare front Si surface). The resulting curve is the (diffuse + specular) reflectance of only the rear, BSR coated surface. Since the shiny-etched front side of the samples has nearly zero diffuse reflectance (Figures 9.4), only scattering by the BSR contributes to the measured diffuse reflectance. Figure 9.4 clearly shows that the evaporated Ag BSR has nearly zero diffuse reflectance, which indicates that it is a specular/mirror-like reflector. In contrast, Figure 9.5 shows that reflection by the Ag

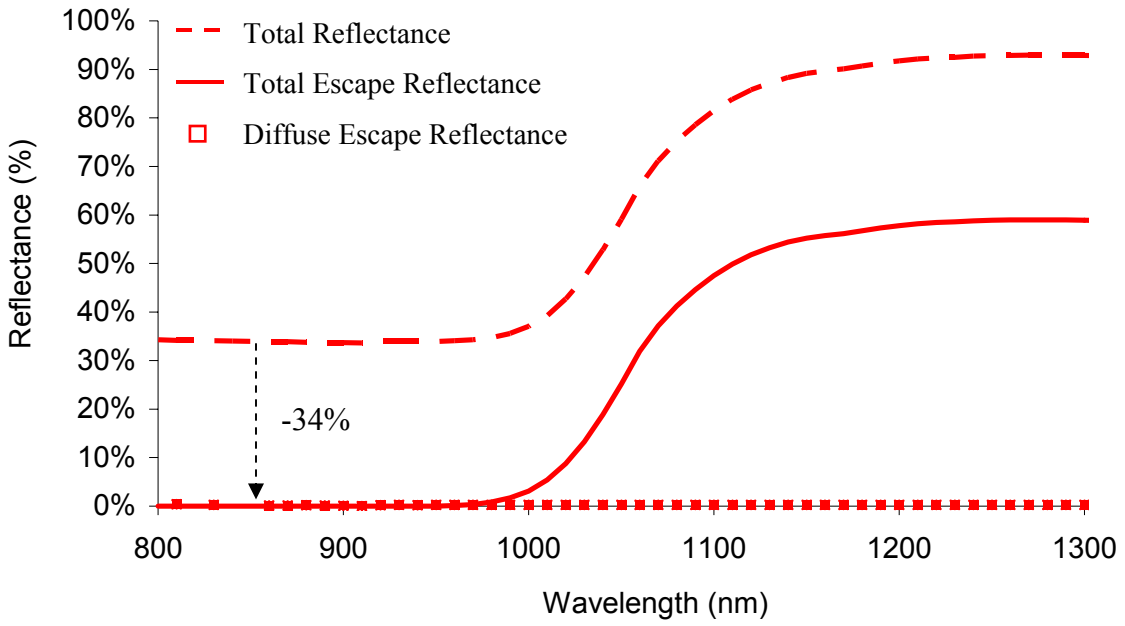

Figure 9.4 Reflectance curves of shiny-etched Si wafers with an evaporated silver reflector on the rear side.

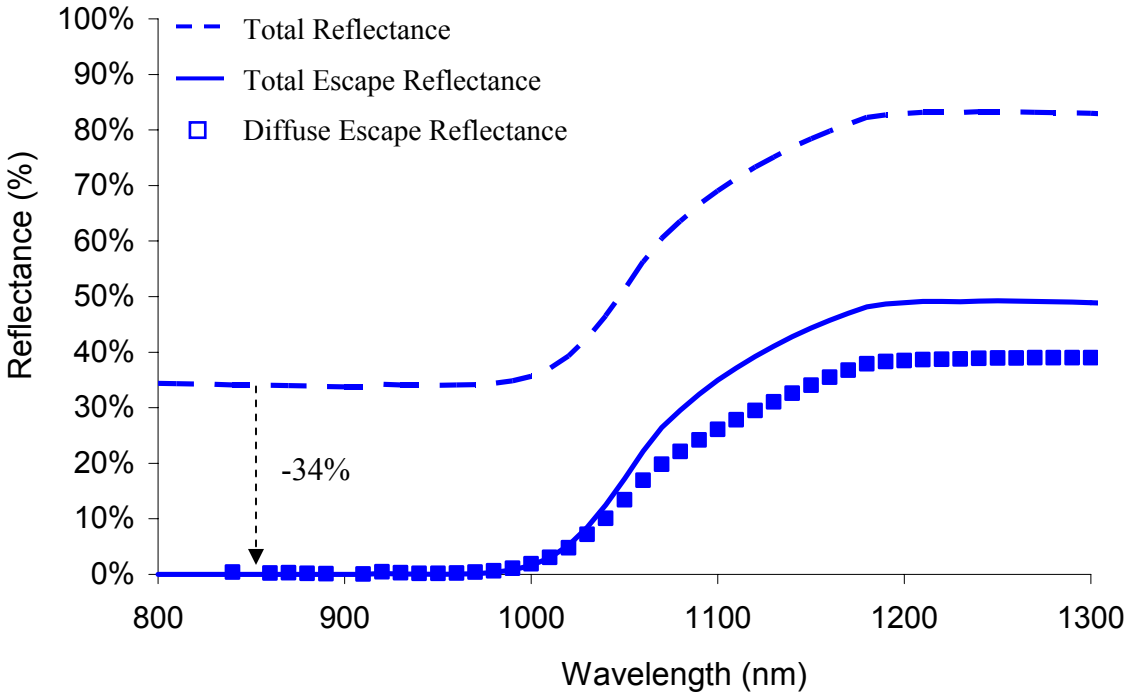

Figure 9.5 Reflectance curves of shiny-etched Si wafers with a sintered silver colloid reflector on the rear side.

colloid BSR is highly diffuse. Using each of the 5 metals, R_B and β values were extracted for both metal-only BSRs and Al-doped SOG/metal stack BSRs using the methods outlined in Section 9.2. The results summarized in Table 9.1 show that when applied directly onto the Si substrate:

1. The experimentally extracted R_B of 60% for the SP Al BSR is in close agreement with literature values that were determined via modeling [56, 60-62]. All of the other BSR materials have R_B close to or greater than the target of 95%.
2. All of highly reflective BSRs fail to match the 100% diffuse reflectance characteristic of the SP Al BSR. That said, the SP Ag paste and the Ag colloid BSR show appreciable scattering with the latter being ~90% diffuse. In contrast, the evaporated Ag and Al BSRs are nearly perfectly specular reflectors.

Table 9.1. Reflectance (R_B) and scattering fraction (β) of various BSRs.

BSR	*On Si*		*On Al-doped SOG*	
	R_B (%)	**β (%)**	**R_B (%)**	**β (%)**
Evaporated Al	91.6	5.0	95.1	4.1
Evaporated Ag	92.9	2.7	98.1	4.6
Ag Colloid (Room Temp. Dry)	96.0	85.6	95.7	77.1
Ag Colloid (sintered at 400 °C)	97.4	89.4	98.1	68.9
SP Ag Paste (sintered at 600 °C)	98.7	84.2	99.5	45.2
Al-BSF	60.0	100.0	-	-

When applied onto the Al-doped SOG to form a dielectric/metal stack BSR:

1. Reflectance increases for the BSR materials. The sintered Ag Colloid/SOG stack and SP Ag/SOG stacks are particularly promising with $R_B > 98\%$.
2. When the light-scattering metals are deposited on top of the SOG, the scattering fraction of the resulting stack is significantly reduced compared to the metal-only BSRs. The Ag colloid/SOG stacks achieves the highest diffusivities of ~70% which is far below the goal of 100%.

Introducing a dielectric between the Si substrate and the metal reflector reduces the scattering fraction because an additional reflective interface now exists – the Si/dielectric interface. Specular reflection at this interface reduces the amount of light reaching the light-scattering BSR thereby reducing the effective β of the stack. The specular nature of reflection at the Si/SOG interface was confirmed by measuring the total and diffuse reflectance of a sample with only an Al-doped SOG BSR as shown in Figure 9.6. The non-zero escape reflectance of this sample proves that reflectance does occur at the Si/SOG and the SOG/air interfaces (reflection also occurs at the latter interface since light will propagate through the ~800 Å thickness of the SiO_2 layer). The near zero diffuse reflectance (Figure 9.6) confirms that nearly all of the reflection at these interfaces is specular.

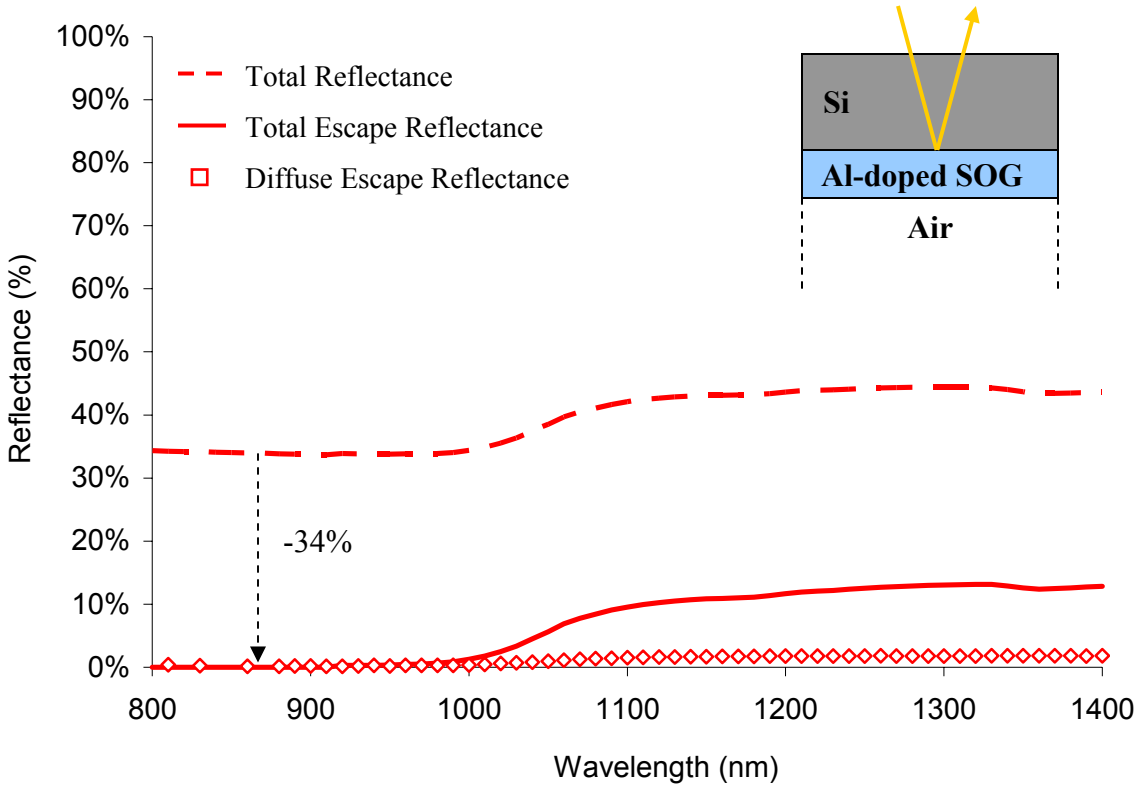

Figure 9.6 Reflectance curves of shiny-etched Si wafers with a layer of cured Al-doped SOG on the rear side. The inset shows the structure under test.

While none of the BSRs studied here achieve the desired optical characteristics (R_B = 95% **and** β = 100%), the Ag colloid BSR has the best combination of reflectance and scattering fraction (Table 9.1). Therefore, the Ag colloid will serve as the BSR for the cells fabricated in this study. The following sections examine the optical and electrical characteristics of this material in more detail.

9.3.1 Effect of Sintering on Reflectance and Adhesion Characteristics

The sintering of the diffuse BSRs – the SP Ag paste and the Ag colloid – was performed in order to simulate the cell processing sequence which includes an FGA step after contact firing in order to reduce the contact resistance of the front Ag contacts. Even though the FGA is performed at 400°C, the fritless silver paste was sintered at a higher temperature (600°C – see Table 9.1) as it had poor adhesion to the substrate after being sintered at 400°C and could easily be peeled off using tweezers. In contrast, the Ag colloid film cannot be easily removed after sintering at 400 °C and cannot be dissolved in deionized water, acetone, methanol, or isopropyl alcohol. To test the adhesion strength of the sintered Ag colloid film to bare Si and to the Al-doped SOG, a 'tape test' was performed in which adhesive tape was pressed onto the Ag colloid film and then ripped off. The adhesion between the substrate (both bare and SOG passivated) and the Ag colloid was strong enough that ripping the tape off often resulted in wafer breakage but resulted in zero to negligible removal of the colloid layer (as determined via visual inspection).

Although a temperature of 400°C can be easily tolerated by crystalline silicon, alternate materials such as amorphous silicon (a-Si) degrade at such high temperatures. As a-Si is a common absorber material in thin-film solar cells and is also a promising passivating layer for wafer-based Si solar cells (see Chapter 4 – Section 4.3) [123, 155], the reflectance characteristics of the Ag colloid BSR were also determined after drying it for ~5 minutes at room temperature (~ 23°C). Not sintering the colloid film results in R_B

and β values that are only slightly lower (Table 9.1). Though sintering has a fairly small impact on the reflectance characteristics of the Ag colloid BSR, the following section shows that the physical structure of the sintered and un-sintered Ag Colloid layers are very different and that this difference has a large effect on the electrical resistivity of the films. The robustness of the un-sintered film is similar to that of the sintered film in that it cannot be easily scraped off; however, it readily dissolves in acetone.

9.4 Detailed Characterization of the Ag Colloid Reflector

9.4.1 Light Scattering Mechanism

SEM images of the un-sintered Ag Colloid shows that it consists of discrete, microscopic Ag flakes randomly stacked on top of another (Figure 9.7). This creates an optically 'rough' interface and results in a high degree of diffuse reflectance as noted in Table 9.1. After sintering however, the structure of the colloid layer is significantly different. The cross section in Figures 9.8 and 9.9 show that, after sintering, the film is a continuous network of sintered silver particles that is filled with air voids. This void-filled structure extends through the entire thickness of the film. From SEM imaging of several samples, the average thickness of the Ag colloid films was found to be 6-8 μm. The porous nature of the film means that the film is held to the substrate by only a few anchor-points. As noted in the previous section (9.3.1) these are sufficient to firmly hold the film to either Si or the Al-doped SOG used in this thesis for rear surface passivation. However, cleaving wafers for preparing SEM samples sometimes resulted in these anchor-points separating from the substrate. Figure 9.10 shows that even the under-side of the anchor points has air-voids.

The dimensions of the voids vary significantly across the film (as seen in Figures 9.8 through 9.10) with the widths of the voids ranging from ~0.3-9 μm. As the sintered silver colloid film has no regular structure, it was not possible to estimate the void fraction

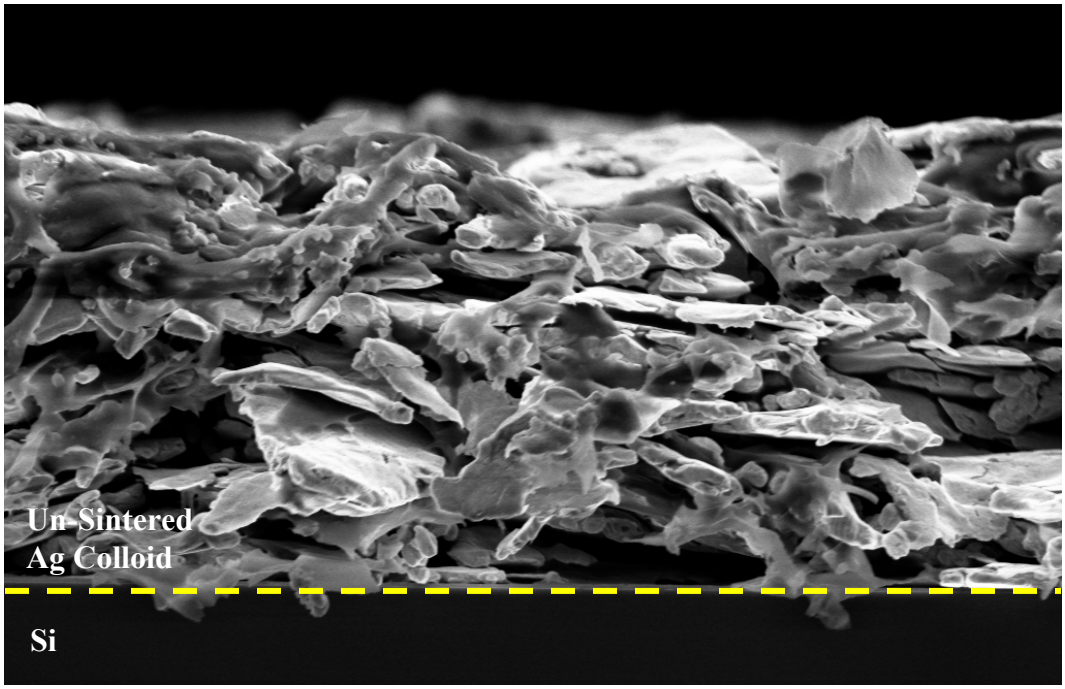

Figure 9.7. SEM image showing cross section of un-sintered Ag colloid film on silicon. Each particle is a discrete silver flake.

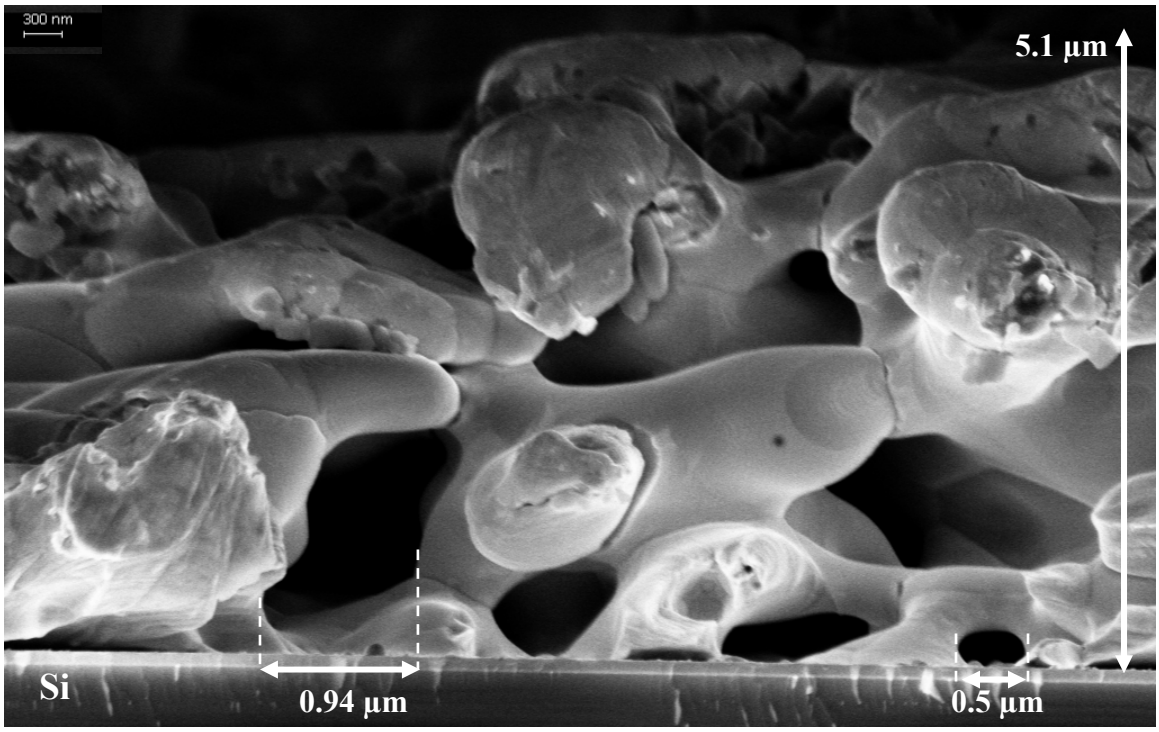

Figure 9.8 SEM image of the sintered Ag colloid showing the network of voids that extend through the film.

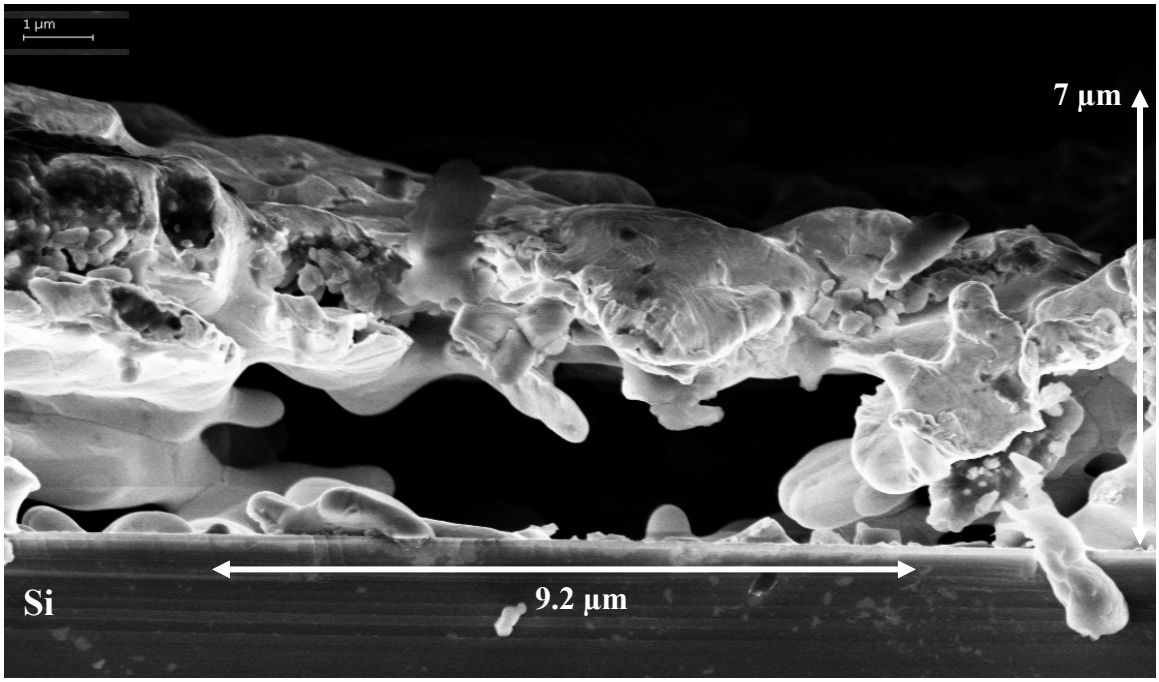

Figure 9.9 SEM image of the sintered Ag colloid showing a large single void in the film.

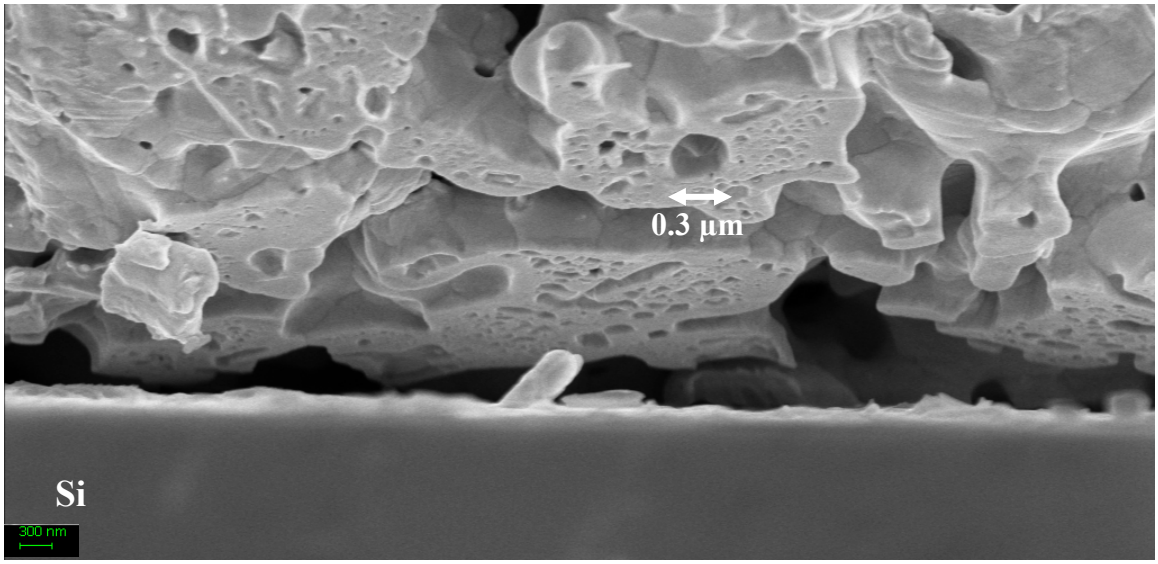

Figure 9.10 Close-up of the sintered Ag colloid showing voids in the under-side of the anchor-points which form the contact between the sintered colloid film and the substrate.

from the SEM images. This was instead calculated using

$$x\rho_{Air} + (1-x)\rho_{Ag} = \rho_{AgColloid} \tag{9.1}$$

where x is the void fraction, and ρ_{Air}, ρ_{Ag} are, respectively, the known densities of air (1.2 kg/m^3 at sea level) and silver (10.5 g/cm^3). $\rho_{AgColloid}$ is the density of the sintered silver colloid which was calculated from volume and weight measurements of sintered Ag colloid layers deposited on Si samples. From Eq. 9.1, the void fraction of the sintered colloid film was found to be 29-50 %. The spread in the calculated void fraction is primarily a result of uncertainty in the thickness of the deposited films (which as noted earlier is largely in the range of 6-8 μm) and variation in the void fraction from sample to sample.

The structure of the sintered Ag colloid film is very similar to that of packed/sintered polytetrafluroethylene (PTFE) materials, which are widely used for integrated sphere coatings (including the system used in this work), diffuse white standards, and laser cavities. These materials are amongst the most perfect diffuse reflectors known and their Lambertian reflectance characteristic is thought to be due to their porous structure which results in multiple reflections occurring within the first few micrometers from the surface [166, 167]. A commercially available version of sintered PTFE (sold under the brand name 'Spectralon') from Labsphere Inc. was reported to achieve optimum Lambertian reflectance properties at a void fraction of 30–50% [168].

The structural similarities between the sintered silver colloid film and the well-characterized PTFE reflectors suggest that the sintered silver colloid film should also be a highly diffuse reflector. This theory was tested using the reflectance setup previously described except that the reflectance sample was flipped so that light was incident directly on the Ag colloid BSR (as opposed to first passing through the Si substrate as in the prior measurements). Figure 9.11 shows the total (solid line) and the diffuse (points) reflectance curves for the silver colloid. From 300 to 1400 nm, the diffuse and total

reflectance curves almost perfectly overlap each other, confirming the hypothesis that the sintered silver colloid film is a highly diffuse reflector. Over the measured wavelength range, the average β value was 99.6%. For wavelengths less than 500 nm, the reflectance drops below 90%; this is a feature of silver and is not specific to the colloid used in this work and was also observed with evaporated Ag layers. It should be noted that Lambertian reflectance refers specifically to the case where the intensity of the reflected light is the same in all directions. The Lambertian nature of the Ag colloid's reflectance was not experimentally determined due to the measurement setup used in this work not being designed for angle-dependant measurements. However, the structural similarities between the sintered Ag colloid films and packed/sintered PTFE reflectors suggest that the former is also a Lambertian reflector.

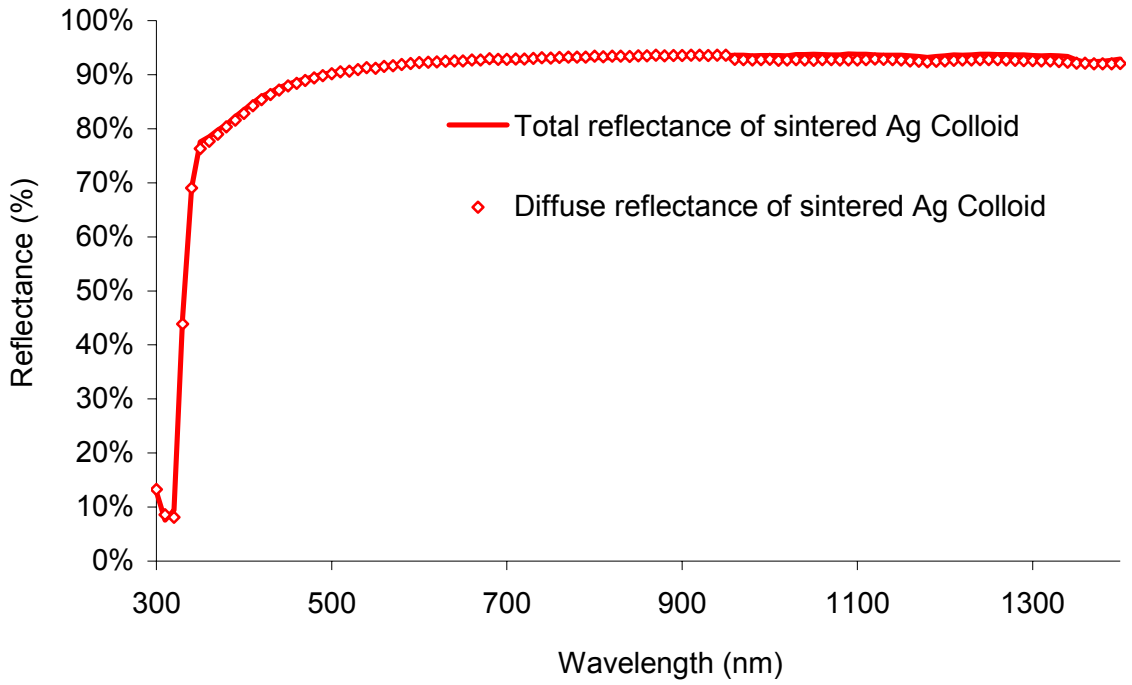

Figure 9.11 Total and diffuse reflectance curves of the sintered silver colloid reflector in air illustrating highly diffuse reflectance. The inset shows the structure under test.

Though the air-voids in the sintered Ag colloid film make it a close-to-ideal diffuse reflector in air, they are also responsible for the scattering fraction (β) of a sintered Ag colloid ***BSR*** being less than 99.6% (Table 9.1). This is a result of the fact that when a Lambertian BSR is applied to a Si substrate, the angular distribution of light inside the silicon layer will *not* be Lambertian if a refractive index step exists at the BSR/silicon interface. This is because the index step focuses the angular distribution of light according to Snell's law,

$$n_{BSR}.Sin(\theta_{BSR}) = n_{Si}.Sin(\theta_{Si}) \tag{9.2}$$

where n_{BSR} and n_{Si} (= 3.5 @ λ = 1300 nm) are the refractive indices of the BSR and Si, respectively, and θ_{BSR} and θ_{Si} are the angles of incidence and refraction, respectively [44]. Such focusing of scattered light does occur with the sintered Ag colloid BSR due to the large refractive index step at the air-void/Si interface as depicted in Figure 9.11. This focusing effect brings an increased fraction of the reflected light within the loss cone and is responsible for the β value for the Ag colloid BSR being < 99.6%.

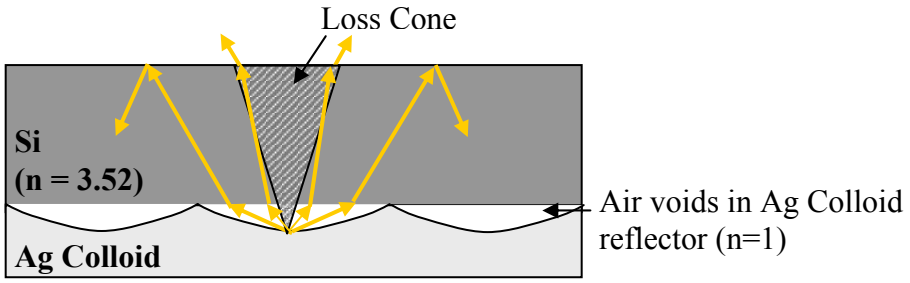

Figure 9.12 Ray-diagram illustrating the reduction in light-trapping caused by variation in refractive index at the Si/Ag Colloid rear interface.

9.4.2 Electrical Resistivity

Though the change in physical structure after sintering has only a modest impact on the reflectance characteristics of the Ag colloid, it has an acute effect on electrical

resistivity. The electrical resistivity of the BSR is an important parameter as the cell structure in Figure 9.1 calls for the BSR to be part of the rear electrical contact. To examine if the Ag colloid is suitable for this role, its electrical resistivity and those of various SP pastes were determined by measuring the resistance (R) across a thin strip of the materials. The resistivity (ρ) was then determined using the well known relation

$$R = \rho.\frac{L}{A} \tag{9.3}$$

where L and A are the length and cross-sectional area of the conductive strips, respectively. The Ag colloid strips were deposited on a SiN_X coated Si wafer; the insulating SiN_X layer prevents current flow through the Si substrate from affecting the measurement. The resistivity of two commercial SP Al pastes and two SP Ag pastes was also similarly determined.

All of the pastes were printed on Si substrates and fired at ~750°C to mimic the typical conditions that SP pastes are subjected to during solar cell manufacturing. Figure 9.13 shows that the collection of discrete flakes that characterizes the un-sintered film

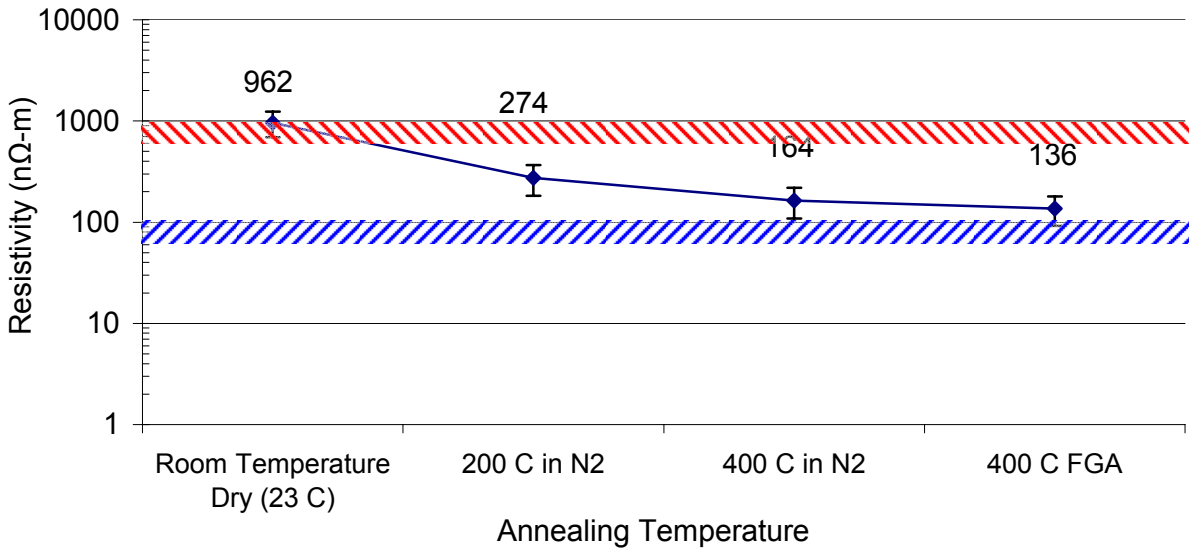

Figure 9.13 Resistivity of the Ag colloid film as a function of annealing temperature and ambient. The upper (red) and lower (blue) shaded bars show the resistivity range of several fired SP Al-BSF and Ag pastes, respectively.

results in a fairly high electrical resistivity. However, this resistivity is only marginally higher than that of a fired SP Al layer which suggests that even the un-sintered film may be a suitable interconnect material for the rear point contacts. The continuous network of Ag formed after sintering results in a large reduction in resistivity. After a 400°C anneal, the resistivity of the Ag colloid is similar to that of the fired SP pastes. The sintered Ag colloid is used for the cells fabricated in this work (Chapter 10) since a 400°C forming gas anneal (FGA) also reduces the contact resistance of the front SP Ag contacts.

9.5 Conclusions

Electrical and optical studies were undertaken in order to find an electrically conductive reflector which is 95% reflective and 100% diffuse. Though none of the materials examined here – evaporated Ag, evaporated Al, a SP Ag paste and an Ag colloid film – satisfy all the requirements, the Ag colloid film comes the closest. With room-temperature processing alone, the Ag colloid BSR provides a high diffuse reflectance as well as electrical resistivity that is similar to that of a fired SP Al layer. After sintering at 400°C, the physical structure of the colloid film changes in a way that lowers electrical resistivity while maintaining the superior reflectance characteristics. When deposited directly on Si, the sintered Ag colloid has a reflectance (R_B) of ~97% and scattering fraction (β) of ~89%. When used as part of a dielectric/metal stack, the Al-doped SOG/Ag colloid stack exhibits R_B and β of ~98% and 69% respectively.

Compared to a fritless SP Ag paste that was also studied, the Ag colloid exhibited superior adhesion to both Si and a passivating SiO_2-based dielectric with either room temperature drying or a 400°C sintering step. On the basis of these results, the Ag colloid film was chosen as the BSR/rear interconnect material for the 20% efficiency SP B-BSF solar cell that is the goal of this work. The wavelength-independent nature of the Ag

colloid's diffuse reflectance also makes it applicable to very thin cells which may not absorb a large fraction of the solar spectrum in one pass.

Chapter 10

FABRICATION AND CHARACTERIZATION OF 20% EFFICIENT BORON DIFFUSED SOLAR CELLS

The overall goal of this thesis was to fabricate 20% efficient screen-printed cells. The screen-printed cell results that are presented in this chapter are a culmination of the development work towards that goal as summarized below.

1. **Chapter 3**: The first step towards a 20% efficient screen-printed (SP) cell was the fabrication and analysis of a baseline 18.9% SP Al-BSF cell. PC1D modeling was then used to identify a set of improvements to the Al-BSF cell which could increase the efficiency from 18.9% to 20%. The modeling predicted that improving BSRV from 600 cm/s to 200 cm/s and R_B from 70% to 95% would result in 20% efficient cells with no changes made to the front-side of the baseline Al-BSF cell. A boron back surface field (B-BSF) cell structure was selected as the method for realizing these BSRV and R_B targets.

2. **Chapters 4 and 5**: In these chapters, it was experimentally demonstrated that water-based, spin-on solutions of boric acid are viable boron diffusion sources. Using boric acid solutions of different concentrations, BSFs/emitters of varying depths and surface concentrations were successfully formed by controlling the process time and temperature. Due to their promising performance, and their low-cost and non-toxic nature, the water-based, boric acid solutions were selected as the boron source for fabricating 20% efficient solar cells.

3. **Chapter 6**: The modeling work in Chapter 3 had set 200 cm/s as the BSRV target for achieving 20% efficient cells. In this chapter, a combination of experimental and modeling work showed that achieving this BSRV value with a diffused B-

BSF while maintaining the same throughput as the baseline full Al-BSF cell process (i.e. all process cycles must last ≤ 90 minutes) requires a passivated, shallow (electrically transparent) B-BSF. Based on the throughput requirement, the boron diffusion process used for cell fabrication was selected; this chosen process results in a shallow, ~1 μm deep B-BSF.

4. **Chapter 7**: Based on the findings in the previous chapters, various passivation methods – thermal SiO_2, PECVD SiN_X, a spin-on SiO_2, an Al-doped SOG, ALD Al_2O_3 and thermal SiO_2/PECVD SiN_X stacks – were investigated in this chapter on both planar and textured boron diffused Si surfaces. Two of these – the Al-doped SOG and a fired thermal SiO_2/PECVD SiN_X stack – were identified as the most promising candidates for passivating the shallow B-BSF selected in Chapter 6. The former was found to provide high quality passivation on only planar p^+ surfaces, while the latter provides passivation of similar quality on both planar and textured p^+ surfaces. In addition, area-average calculations showed that in order to meet the target BSRV of 200 cm/s with these passivating dielectrics *and* the shallow B-BSF profile, the rear SP contacts need to be point contacts with an area coverage of ~2.5%.

5. **Chapter 8**: A study into Fe contamination and gettering led to the selection of the Al-doped SOG as the rear passivating dielectric for the B-BSF cells fabricated in this thesis. This choice was a consequence of the finding that, of the various passivation methods explored in this work, only the Al-doped SOG can simultaneously passivate the p^+ surface and getter Fe from the wafer thereby ensuring that bulk lifetimes remain high enough (≥ 300 μs) to achieve 20% efficient cells. Since the passivation studies in Chapter 7 showed that the Al-doped SOG provides adequate passivation on planar, but not on textured, p^+

surfaces, the use of the Al-doped SOG for Fe gettering forces the rear B-BSF to be planar in order to maintain a low BSRV.

6. **Chapter 9**: This chapter focused on the development of the final piece needed for fabricating 20% efficient cells – an electrically conductive BSR material with 95% reflectance (R_B) and diffusivity (β) of 100%. While none of the BSR materials explored in this chapter met both the R_B and the β requirements simultaneously, a painted-on Ag colloid was chosen for cell fabrication because it came closest to meeting both targets. It was found that a 400°C sintered Al-doped SOG/Ag colloid stack has a R_B of ~98% and β of ~70%. The sintered Ag colloid also exhibited electrical resistivity similar to that of fired SP Ag pastes which allows it to be used as the electrical interconnect for the rear point contacts.

All of the above findings were then integrated into the process sequence shown in Figure 10.1. Since each step of the process in Figure 10.1 was designed to meet the target BSRV and R_B values of 200 cm/s and 95% (diffuse) respectively, successful integration of these steps should result in 20% efficient SP cells.

10.1 Process Sequence for 20% B-BSF Solar Cells

The process sequence begins with single-side texturing of 4" circular wafers followed by cleaning to remove organic and metallic residues. The cleaning involves an HF dip to remove the native oxide on the wafers, followed by cleaning in 2:1:1 H_2O:H_2O_2:H_2SO_4 and 2:1:1 H_2O:H_2O_2:HCl solutions to remove organics and trace metals respectively. An HF dip and DI water rinse is performed between the organic and metal cleans, followed by a final HF dip and DI water rinse. The wafers are then dipped once more in the H_2SO_4 solution to grow a thin chemical oxide layer which makes the surface hydrophilic, followed by a final DI water rinse.

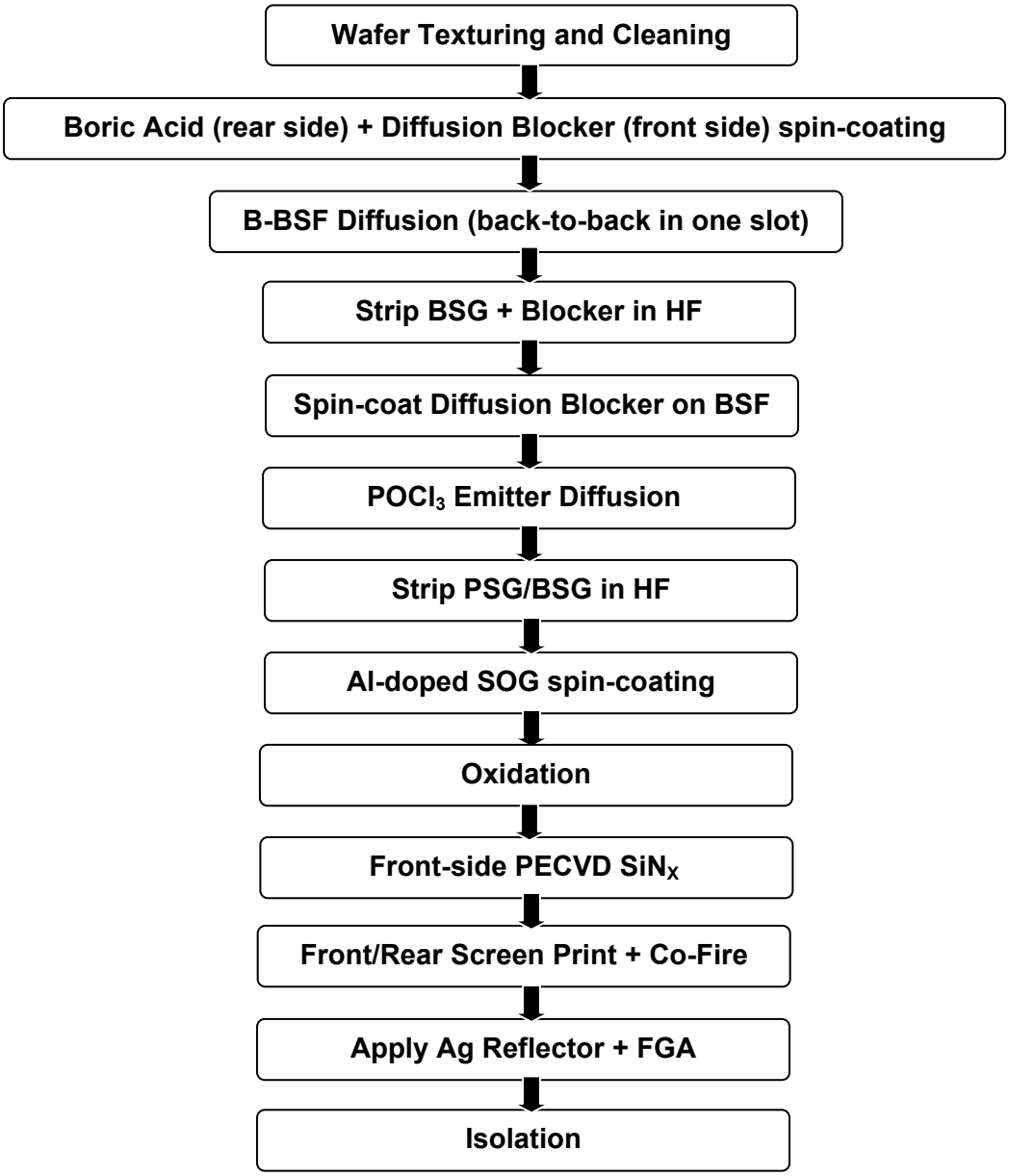

Figure 10.1 Process sequence for SP, passivated, B-BSF solar cell.

One out of every two wafers is then spin-coated on one side with a 1% boric acid/DI water source followed by spin-on coating of the Al-doped SOG on the opposite side to serve as a diffusion blocker. The coated wafers are directly loaded into a quartz furnace using the back-to-back two-wafers-in-one-slot method (one wafer coated with boric acid, the other un-coated) discussed in Chapter 4 and diffused at 1000°C for ~20 minutes.

At the end of the boron diffusion cycle, the wafers are removed from the furnace, separated and subjected to an HF dip to remove the borosilicate glass (BSG) and diffusion blocker. The B-BSF side of the wafer remains hydrophilic after the HF dip which suggests the presence of a boron rich layer (BRL) [92] which is not readily etched by HF. After a DI water rinse, the boron diffused side of the wafers is spin-coated with the Al-doped SOG which prevents counter-doping during the $POCl_3$ diffusion step that creates the front emitter. After spin-coating, the wafers are directly transferred to a $POCl_3$ diffusion furnace and diffused. Note that on a few samples, the pure spin-on SiO_2 examined in Chapter 7 was also used as the diffusion blocker both for the boron diffusion and the $POCl_3$ diffusion steps. Both spin-on dielectrics blocked cross-diffusion equally well and the choice of diffusion blocker made no difference in the cell results.

After $POCl_3$ diffusion, the wafers go through another HF dip to remove the phosphosilicate and borosilicate glasses. After this second HF dip, the B-BSF side becomes hydrophobic which suggests that BRL gets converted to a BSG during the $POCl_3$ cycle [75, 83]. The B-BSF side is then re-coated with the Al-doped SOG which will now serve as the rear passivating dielectric. The SOG is cured in a quartz furnace at 900°C for ~25 minutes (10 min. in O_2 ambient followed by a 15 min. N_2 anneal). The front emitter-side of the wafers are passivated with a thin (~150 Å) layer of thermal SiO_2 in the same step. After this step, the sheet resistance of the B-BSF is ~40-45 Ω/sq. and that of the emitter is ~70-80 Ω/sq. After capping the front oxide layer with a PECVD SiN_X layer, the wafers are ready for screen-printing.

A point-contact pattern with area coverage ~2% is printed on to the rear side of the wafers using an Ag/Al paste from Ferro Corp. (Ferro 3398). Printing on the front side is done using a screen that defines a set of nine $4cm^2$ cells on the 4" wafers. The front gridlines are printed using an Ag paste from from Heraeus (H8969). The wafers are then co-fired in an RTP furnace during which the Ag paste and the Ag/Al paste punch through the front SiO_2/SiN_X stack and the rear Al-doped SOG respectively and form a contact to

the underlying Si. Note that a belt furnace can also be used for firing – a few wafers were fired using a belt furnace and similar results were obtained with both belt and RTP firing. The rear point contacts are then interconnected by applying the Ag colloid with a brush followed by a ~15 min. forming gas anneal at 400°C. This step reduces the front contact resistance and sinters the Ag colloid. The width of the front contacts at this point is ~120 μm. The resulting cell structure is shown in Figure 10.2.

To electrically isolate the 9 cells on each wafer, the wafers are spin-coated on both sides with a protective layer of photoresist followed by dicing saw isolation of the 9 cells. The dicing saw isolation electrically separates the cells as it cuts through the p-n junction. The wafers are then immersed in a Si etching solution to remove the damage caused by the dicing saw. The photoresist protects the active cell area during the etch after which it is removed in acetone. Without this damage etch step, the cells exhibit a high ideality (n) factor which lowers the fill-factor (FF) and cell efficiency. All the cells in this thesis, including the baseline Al-BSF cell, went through this etch step.

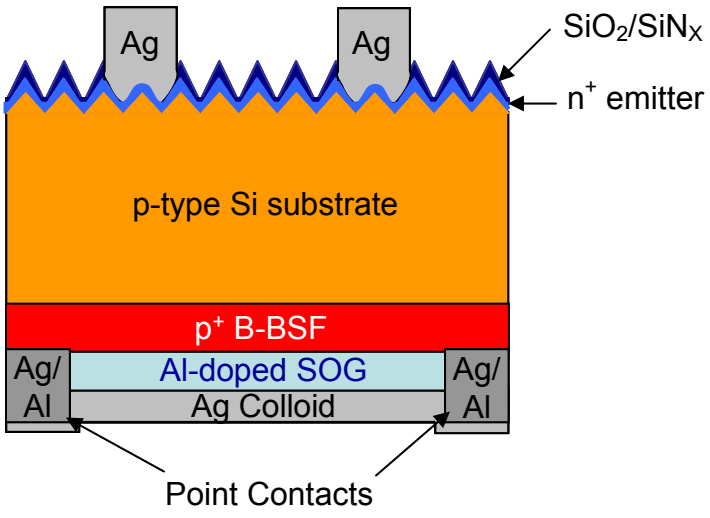

Figure 10.2 Schematic of the B-BSF cells fabricated in this study.

10.2 P-type Cell I-V Data: Results and Analysis

10.2.1 First Generation B-BSF cell

The cell fabrication process described above resulted in an independently confirmed cell efficiency of ~20% (Figure 10.3) with an open-circuit voltage (V_{OC}) of 647 mV, a short-circuit current density (J_{SC}) of 39.22 mA/cm^2 and a fill-factor (FF) of 78.6 % (Fig. 36). This achievement suggests that the various pieces of the cell developed in Chapters 4-9 (described in the previous section) were successfully integrated.

In order to confirm this, a PC1D fit was made to the measured IQE, reflectance and I-V characteristics of the 20% efficient B-BSF cell (Figure 10.4 and Table 10.1). As with the fit made to the baseline Al- BSF cell (Chapter 3), the measured series resistance, shunt resistance, front reflectance, J_{02} and n_2 (extracted from a two-diode fit to the dark I-V curve of the cell) were provided as inputs to PC1D. The measured bulk lifetime on cell wafers that went through the same processing steps was 400-1000 µs. This demonstrates, at the cell level, that the B-BSF process used here is able to maintain high lifetimes. At

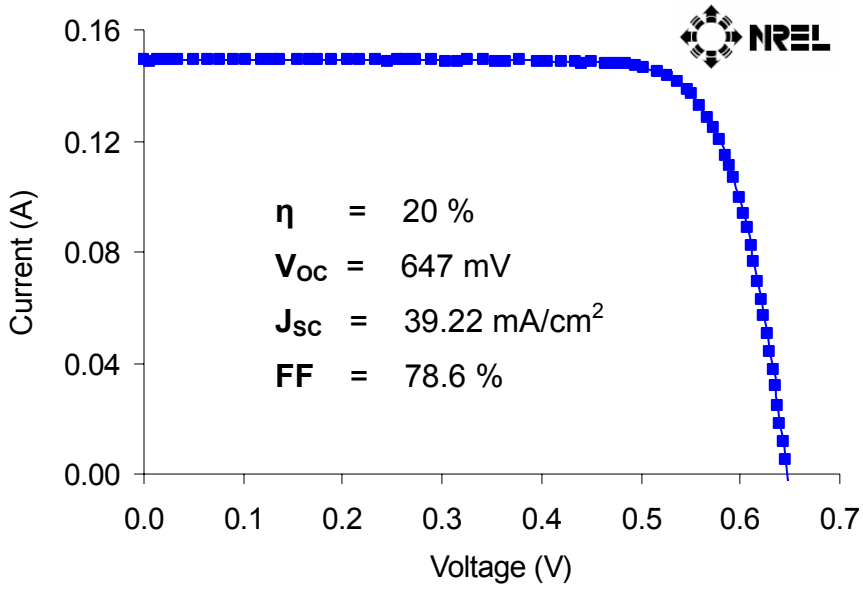

Figure 10.3 I-V characteristic of first generation dielectric passivated B-BSF solar cell.

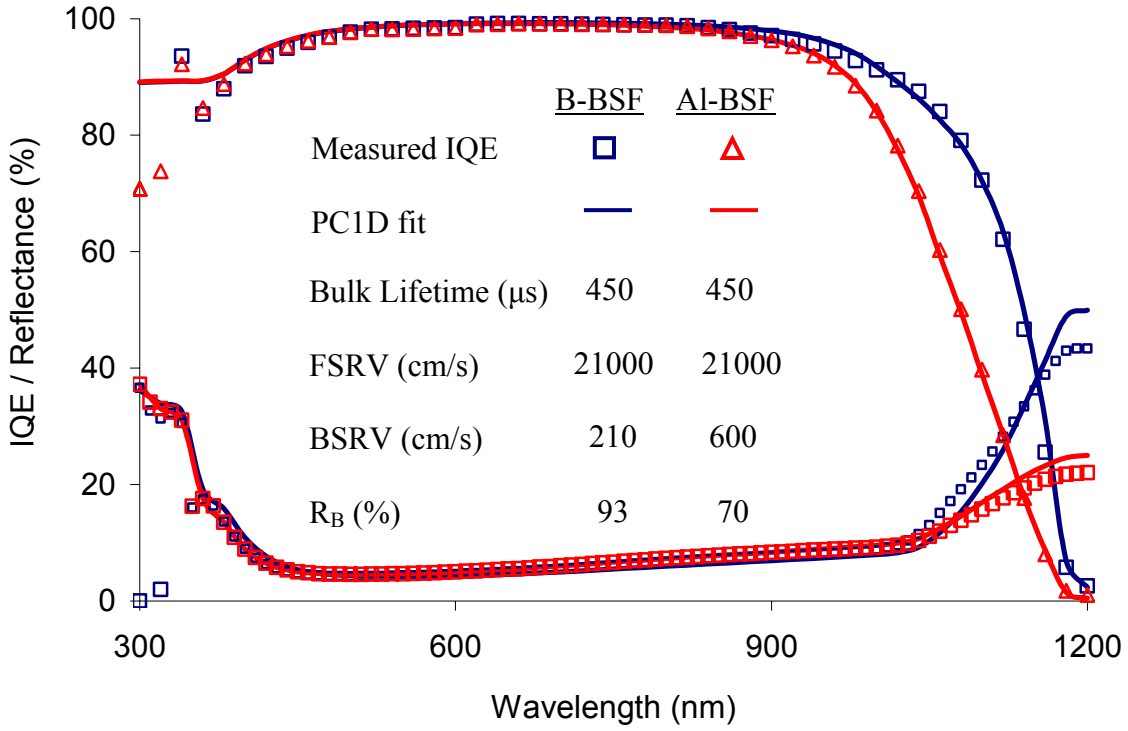

Figure 10.4 PC1D fits to the measured IQE and reflectance characteristics of a 20% efficient B-BSF cell and an 18.9% Al-BSF cell.

Table 10.1 NREL Verified I-V data of 20% efficient 4cm^2 B-BSF cell and simulated I-V data from a PC1D fit to the same cell. The cell was measured with an aperture mask of area 3.802 cm^2.

	η (%)	V_{OC} (mV)	J_{SC} (mA/cm^2)	FF (%)
Measured (NREL)	19.95	647.0	39.222	78.6
PC1D (simulated)	20.01	646.8	39.330	78.7

the low end of the measured lifetimes, the diffusion length is over 1000 μm or greater than three times the wafer thickness. The large spread in the cell lifetimes possibly comes from imperfect etching and surface preparation prior to passivation of the etched cell wafers with iodine/methanol. The PC1D fit in Figure 10.4 assumes a bulk lifetime of 450 μs as this is the value used for the baseline Al-BSF model and for the modeled 20% cell that was the target of this thesis (Chapter 3). The FSRV, BSRV and R_B parameters in PC1D were then varied till a 'best fit' to the cell was obtained. The simple optical model in PC1D supports just perfectly specular and Lambertian (i.e. perfectly diffuse) reflectance; the Lambertian option was selected for modeling even though the rear dielectric/Ag colloid reflector stack is just ~70% diffuse as discussed in Chapter 9. The quality of the resulting fit to the measured IQE and reflectance curves is shown in Figure 10.4 while the accuracy of the I-V fit is shown in Table 10.1

As clearly seen in Figure 10.4, the short-wavelength IQE response and the modeled FSRV of the B-BSF cell are unchanged from that of the 18.9% baseline Al-BSF cell due to the fact that the front sides of both cell structures are identically processed. In contrast, the long wavelength IQE response (which is affected by bulk lifetime and BSRV) and escape reflectance (which affects the IQE and reflectance curves at wavelengths > 1000 nm) are significantly higher due to the improved the BSRV and R_B of the passivated B-BSF cell.

Quantitatively, the values of BSRV (210 cm/s) and R_B (93% diffuse) extracted for this device are very close to the values of 200 cm/s and 95% diffuse that the PC1D modeling in Chapter 3 predicted were required to achieve 20% efficient cells. As noted earlier, the measured bulk lifetimes for B-BSF cells varied from 400-1000 μs; over this range of bulk lifetimes, the 'best fit' BSRV varies from 200-250 cm/s which is still in good agreement with the initial PC1D modeling in Chapter 3. The cell results validate the modeling and confirm that the various elements of this device that were developed in Chapters 4-9 were successfully integrated into a single process sequence.

The fact that the FF of this cell (0.786) is very similar to that of the 18.9% full Al-BSF cell that served as the baseline for this work confirms that the electrical conductivity of the Ag colloid BSR which interconnects the rear point-contacts is sufficient for high efficiency cells.

10.2.2 Second Generation B-BSF cell

In the first generation process, the boron diffusion step was performed with two wafers loaded back-to-back in each slot of the diffusion boat (Figure 10.1). After this step, the wafers were separated and sent through the subsequent $POCl_3$ diffusion and surface passivation steps with only one wafer per slot. In the second generation process however, the wafers were not separated immediately after boron diffusion. They were instead kept together through the post-diffusion HF dip as well as through the subsequent $POCl_3$ diffusion step (no diffusion blocker was used). The wafers were separated only after this step in order to etch the PSG/BSG in buffered HF. Unlike in the first generation process, the B-BSF side was found to remain hydrophilic after this HF dip which suggests that the BRL was not converted to a BSG by the $POCl_3$ step. After the HF dip and a DI water rinse, the B-BSF side was coated with the Al-doped SOG for surface passivation. Figure 10.5 shows abbreviated process sequences highlighting the differences between the first and second generation cell processes.

From four-point probe measurements, the B-BSF sheet resistance after the end of the second generation process was found to be lower – ~35-40 Ω/sq as opposed to ~40-45 Ω/sq. for the first generation process. The lower sheet resistance may be due to the BRL (which is known to act as a diffusion source [75]) providing additional boron doping during the $POCl_3$ diffusion process. In addition to achieving slightly heavier doping with no increase in process time, the back-to-back loading during $POCl_3$ diffusion also has the advantage of eliminating the diffusion blocker spin-coating step. With this tweaked process, an independently verified best cell efficiency of 20.2% was achieved with (V_{OC})

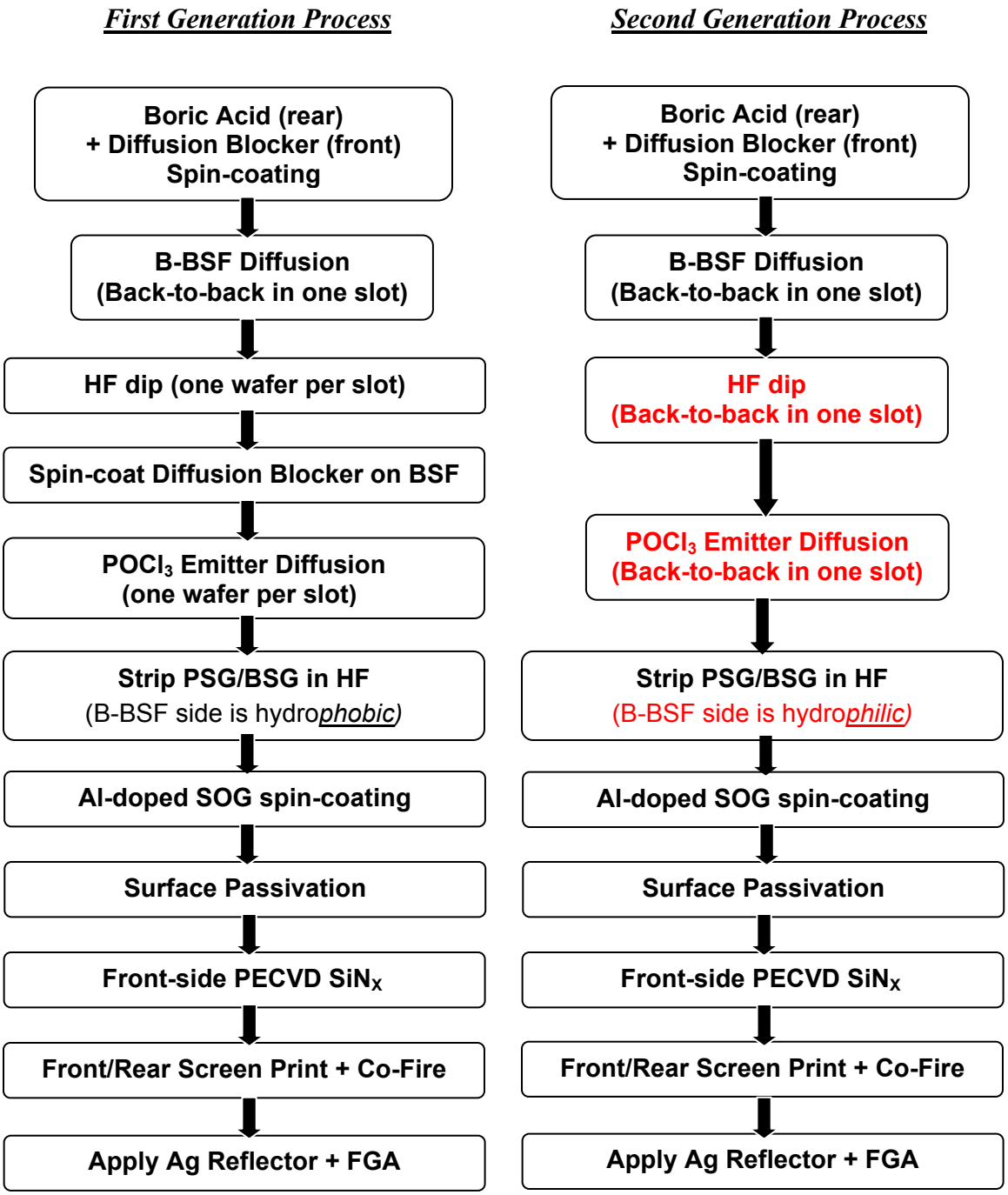

Figure 10.5 Abbreviated process sequences for the first and second generation B-BSF cells fabricated in this thesis. The differences are in red.

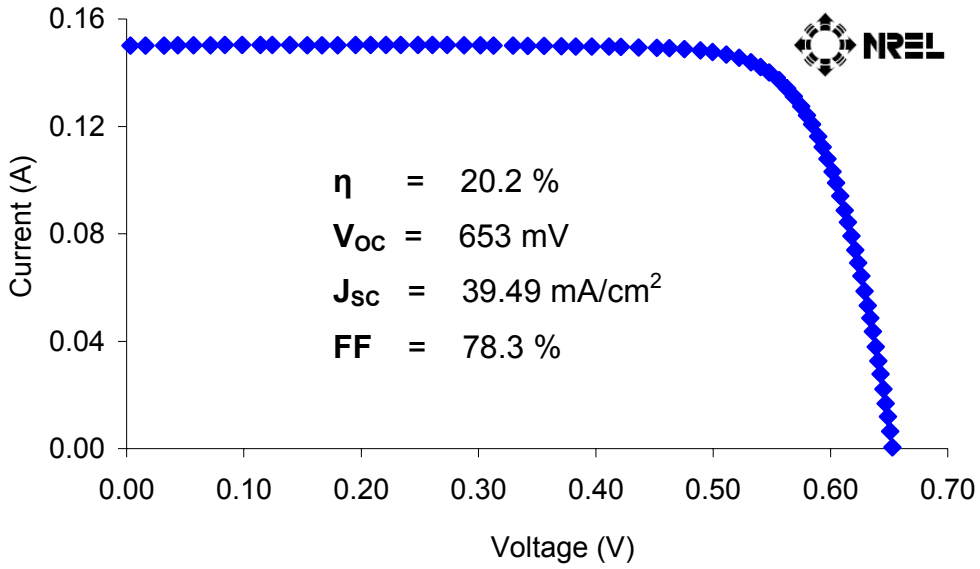

Figure 10.6 I-V characteristic of second generation, dielectric passivated B-BSF solar cell.

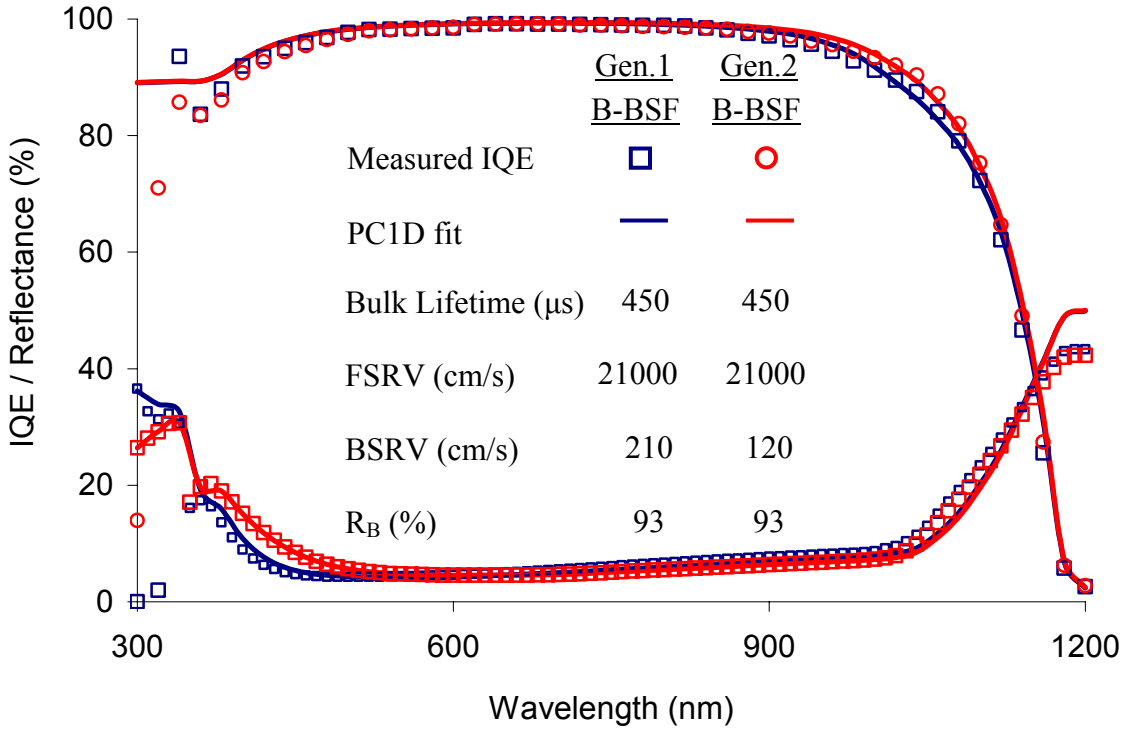

Figure 10.7 PC1D fits to the measured IQE and reflectance characteristics of the best Generation 1 and Generation 2 B-BSF cells.

Table 10.2 I-V data of a 20.2% efficient, 4cm^2 B-BSF cell, along with simulated I-V data from a PC1D fit to the same cell. Also shown is the average of GT measurements of 20 similarly processed cells. The NREL measurement used an aperture mask of area 3.802 cm^2 and the GT measurements used an aperture mask of area 3.893 cm^2.

		η (%)	V_{OC} (mV)	J_{SC} (mA/cm^2)	FF (%)
Best Cell	Measured (NREL)	20.20	653.2	39.485	78.3
	Measured (GT)	20.13	653.2	39.155	78.7
	PC1D (simulated)	20.23	651.4	39.500	78.7
Avg. of 20 cells	Measured (GT)	20.13	654.5	39.065	78.7

of 653 mV, a short-circuit current density (J_{SC}) of 39.5 mA/cm^2 and a fill-factor (FF) of 78.3 % (Figure 10.6). Comparing the IQE curves of the best B-BSF cells (Figure 10.7) shows that the boost in efficiency in the second generation process comes from an improved long-wavelength response. PC1D fitting reveals that this improvement corresponds to a lower BSRV of ~120 cm/s, while the rear reflectance is the same at 93%. The accuracy of the PC1D fit to the measured I-V data is shown in Table 10.3. Allowing the bulk lifetime to vary from 400-1000 μs (the uncertainty in the measured bulk lifetime), the 'best-fit' BSRV ranges from 110-160 cm/s.

Table 10.3 also shows the average of 20 cells fabricated using the same process and measured at Georgia Tech. Note that all cells measurements reported here used an aperture mask which shades all the other cells on the wafer (there were 9 cells per 4" wafer). This was necessary as the high bulk lifetimes of the wafers resulted in current collection from outside the active area of the cell (as defined by dicing saw isolation) which artificially inflated J_{SC} readings.

10.2.2.1 Double Side Textured B-BSF cell

The Al-doped SOG was used as the rear dielectric in all the 20%-type B-BSF cells fabricated in this thesis since it provides both high lifetime at the end of the cell process (due to Fe gettering) and good passivation on the *planar* p^+-Si surface of the B-BSF cells. However (as discussed in Chapter 7), it provides very poor passivation on a textured p^+-Si surface leading to ~20mV lower implied V_{OC}s on double-side textured B-BSF cell wafers. A comparison of the results in Tables 10.2 and 10.3 shows that this difference persists at the cell level – texturing the rear B-BSF reduced the best cell efficiency from 20.2% to 19.1%.

IQE analysis (Figure 10.8) confirms that the lower performance of the Al-doped SOG passivated, double-side textured B-BSF cell is due poor rear surface passivation. This is visible in the IQE curves as a lower response past 800 nm compared to the single-side textured, B-BSF cell (this is the same curve from Fig. 10.7 re-plotted for convenience). Note that while both bulk lifetime degradation and poor rear surface passivation can account for degradation in long-wavelength IQE, the former is not the cause of the observed IQE degradation as bulk lifetime measurements on double-side textured B-BSF cells showed lifetimes as high as 1.1 ms. As discussed in Chapter 7, non-uniformity in the BSF formed by the spin-on boric acid/DI H_2O sources is also not responsible for the poor passivation quality. This claim is supported by SEM imaging which shows that the BSF (seen as the bright strip in Figure 10.9) follows the contours of the pyramids fairly well.
PC1D fitting (Figure 10.8) to the IQE and I-V data reveals that the reduced IQE response is due to an increase in the BSRV from 120 cm/s (planar B-BSF) to 700 cm/s (textured B-BSF). This high BSRV happens to be close to that of the baseline Al-BSF cell (600 cm/s); as a result both devices have similar V_{OC} values (Table 10.3). However, compared to the baseline full Al-BSF cell, the textured B-BSF cell does have an enhanced IQE response past 1000 nm (Figure 10.8) due to the improved BSR with R_B = 91% (compared to 70% for the baseline Al-BSF cell). This is reflected in the higher J_{SC} of the textured B-BSF cell (Table 10.3).

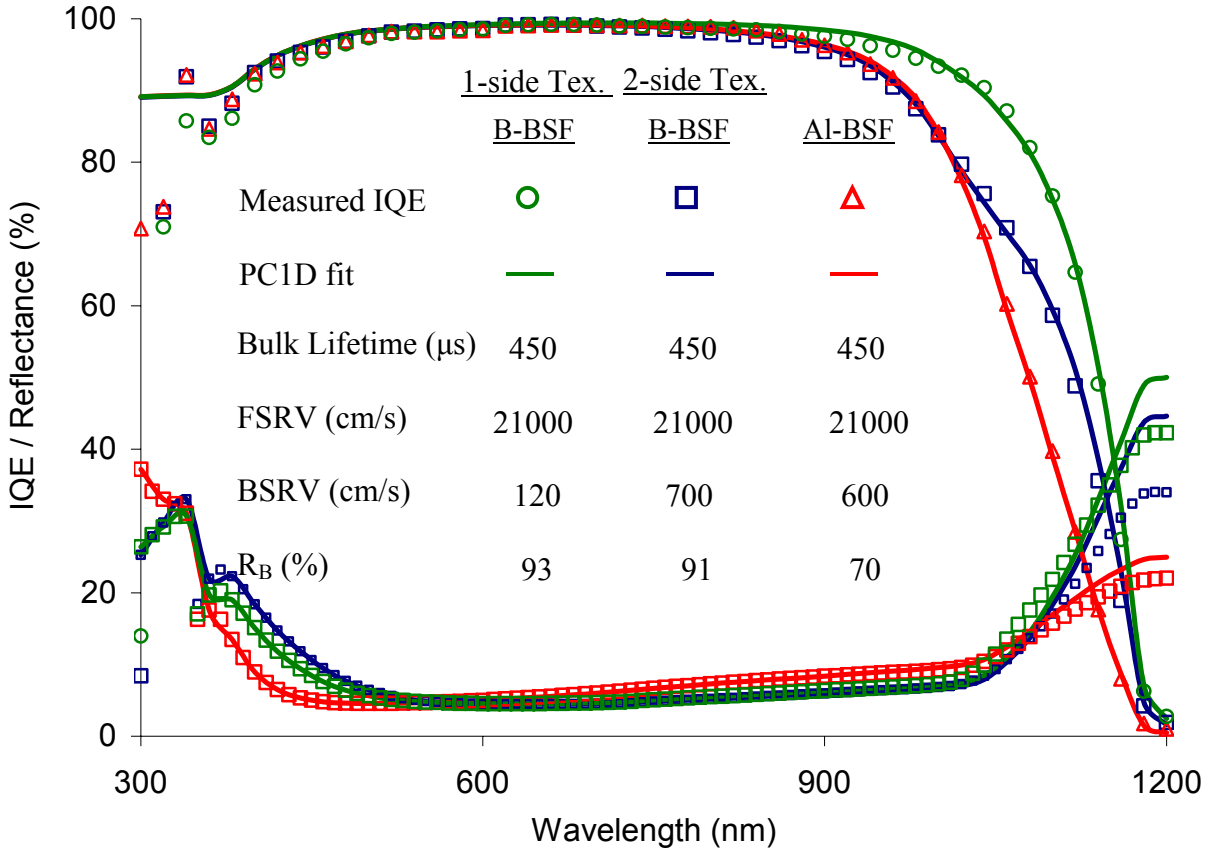

Figure 10.8. PC1D fits to the measured IQE and reflectance characteristics of the double-side textured B-BSF cell and the baseline Al-BSF cell.

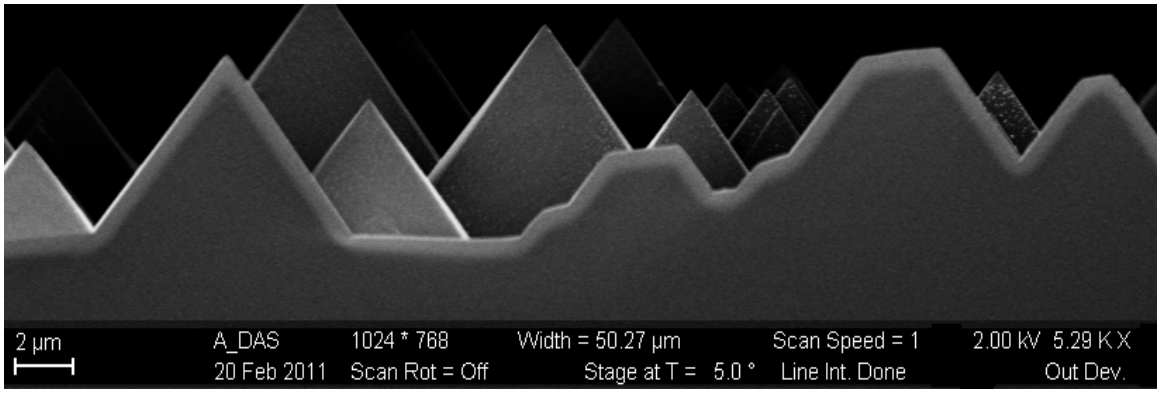

Figure 10.9. SEM image of a boron diffused layer formed on a textured surface using a boric acid/DI water spin-on source.

Table 10.3. I-V characteristics of a double-side textured B-BSF cell and the baseline Al-BSF cell (both 4cm^2) along with simulated I-V data from PC1D fits to the same cells. The NREL measurements used an aperture mask of area 3.802 cm^2. The GT measurements were with an aperture mask of area 3.893 cm^2.

		η (%)	V_{OC} (mV)	J_{SC} (mA/cm^2)	FF (%)
Double-side textured B-BSF	Measured (GT)	19.13	638.1	38.65	77.57
	PC1D (simulated)	18.92	635.7	38.37	77.57
Baseline Al-BSF	Measured (NREL)	18.87	639.5	37.67	78.33
	PC1D (simulated)	18.92	636.6	37.59	79.05

Note that the 700 cm/s BSRV value for the rear-side *textured* B-BSF cell was extracted while keeping the rear side of the PC1D model *planar*. If a rear surface texture is included in the PC1D model, the BSRV drops by a factor of ~1.7 to 400 cm/s due to the fact that PC1D automatically increases SRV to account for the increase in surface area due to texturing. The BSRV of 700 cm/s is an *effective* BSRV value which includes the effect of surface texturing. It is interesting to note that in the surface passivation studies of Chapter 7 it was found that due to the transparent nature of the shallow B-BSFs used for the cells in this thesis, using no passivation (i.e. air 'passivation') resulted in a BSRV of 689 cm/s (as determined on symmetrically diffused samples – see Fig. 7.6 in Section 7.3). The good agreement with the BSRV of 700 cm/s extracted from the finished double-side textured cells provides cell-level confirmation that the Al-doped SOG provides essentially no passivation on a textured p^+-Si surface.

10.3 Effect of Cell Design on Light Induced Degradation

While the cells in this thesis were fabricated on high-quality FZ Si, commercial monocrystalline Si solar cells are made on cheaper Cz material. A major difference between the two substrate types is that the bulk lifetime of boron-doped p-type Cz Si wafers is known to degrade under illumination [171, 172]. This light-induced degradation (LID) has been linked to the relatively large concentration of oxygen impurities in commercial Cz material which, under illumination, pair with boron to form electrically active B_sO_{2i} defects. The light-induced defect formation place a fundamental limit on the stabilized lifetime of such substrates and an empirical expression linking the stabilized lifetime (τ_{stable}) to the bulk boron and oxygen concentrations was proposed by Bothe et al. [173]:

$$\tau_{stable} = n \times 7.675 \times 10^{45} \times [B_s]^{-0.824} \times [O_i]^{-1.748} \quad (10.1)$$

where $[B_s]$ and $[O_i]$ are the boron and interstitial oxygen concentrations respectively. The multiplicative factor, n, was reported to range from 2 to 3 and was linked to a reduction in the concentration of B_sO_{2i} defects by high-temperature processing steps typical to solar cell processing [173]. As the boron concentration can easily be determined via four-point probe resistivity measurements, and the O_i concentration in most commercial p-type Cz material falls within a fairly narrow range of $6x10^{17}$ – $1x10^{18}$ cm^{-3} (12 – 20 ppm), Equation 10.1 provides a convenient way to estimate the stabilized lifetime for commercial boron-doped Cz Si material.

In order to see the effect that worst-case LID can have on the cells fabricated in this research, the bulk lifetime of the PC1D fits to the cells was changed to the value predicted by Equation 10.1 assuming n = 2 and $[O_i]$ of $1x10^{18}$ cm^{-3} (20 ppm). For the 1.3 Ω-cm resistivity wafers used in this work, the stabilized lifetime works out to be ~30 μs. The simulated LID results (Table 10.4) show that while both the baseline Al-BSF and the 20.2% efficient second generation B-BSF cell suffer large drops in efficiency due to LID,

Table 10.4. PC1D simulations showing the effect of LID on the efficiency of the baseline Al-BSF cell and the second generation B-BSF cells fabricated in this thesis.

	Bulk Lifetime (μs)	Baseline Al-BSF	Second Gen. B-BSF	Δη (abs.) [B-BSF – Al-BSF]
Initial	450 μs	18.9 %	20.2 %	1.3 %
Post-LID	31 μs	17.9 %	18.6%	0.7 %

its impact is much larger for the B-BSF cell. As a result, the efficiency gap between the two structures is almost halved after LID. In addition, the simulation results suggest that the main goal of this thesis, a screen-printed cell with *stable* 20% efficiency, cannot be achieved on commercial boron-doped Cz material with the 20% B-BSF cell structure developed in this thesis. This finding is examined in more detail in following sections which show quantitatively for the first time that the impact of LID is linked to cell design and that all well-passivated cells (i.e. not just the B-BSF cell designed here) will suffer a larger efficiency loss due to LID.

10.3.1 Modeling the Effect of Cell Design on LID

To better understand the result shown in Table 10.4, PC1D modeling was used to quantitatively examine how cell design influences the impact that LID has on cell efficiency. The starting point for this study was selected to be a PC1D model of a mediocre ~17% efficient Al-BSF cell whose parameters are listed in Table 10.5. Though all the cells in this thesis have been fabricated on 300 μm thick, 1.3 Ω-cm wafers, the LID modeling study discussed here uses 180 μm thick, 2 Ω-cm substrates instead as these are more representative of current Cz Si industrial cells. Many of the highest efficiency, large-area, screen-printed cells have been fabricated on Cz wafers of similar resistivity (2-3 Ω-cm) and thickness (~160-200 μm) [11, 62, 174, 175].

Table 10.5 List of PC1D parameters used to model a ~17% Al-BSF cell.

Cell Parameters	
Resistivity (Ω-cm)	2
Thickness (μm)	180
τ_{BULK} (μs)	250
Emitter (Ω/sq.)	60 (Spreading Resistance)
FSRV (cm/s)	100,000
BSRV (cm/s)	600
BSR (%)	60
R_{SERIES} (Ω-cm^2)	1
R_{SHUNT} (Ω-cm^2)	1000
J_{02} (nA/cm^2)	5
N_2	2
η (%)	17.2
V_{OC} (mV)	618
J_{SC} (mA/cm^2)	36.3
FF (%)	76.7

This baseline model was then gradually changed, one parameter at a time, to build a roadmap to 21% efficiency (Figure 10.10). While this piecemeal approach is not realistic, (for example, improvements in BSR are often tied to improvements in BSRV and reduction in the front grid shading can improve the FSRV) it is useful for determining which cell improvements affect the LID-induced efficiency loss. The worst-case impact of LID at each step of the roadmap was then simulated by reducing the bulk lifetime from 250 μs (Table 10.5) to the value predicted by Equation 10.1 assuming a high bulk oxygen concentration of $1x10^{18}$ (20 ppm) cm^{-3} and n = 2. For these values, the stabilized bulk

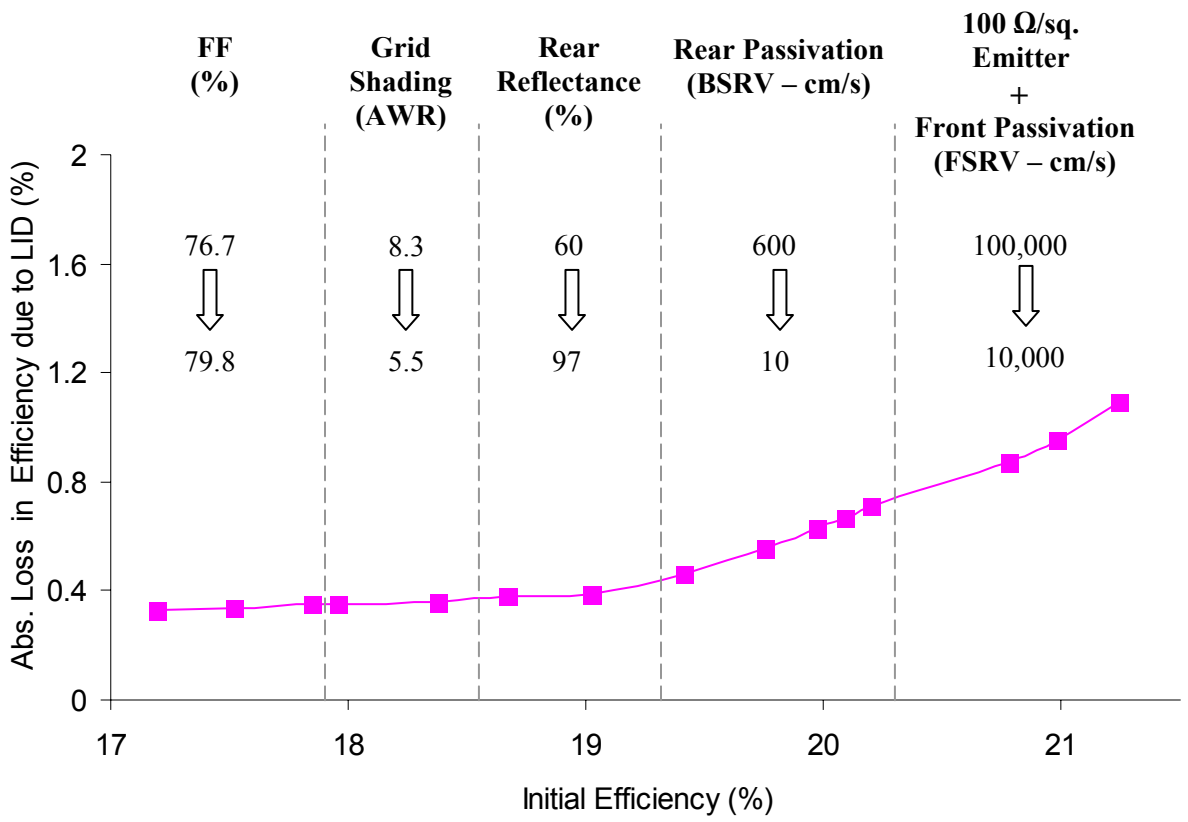

Figure 10.10. Technology roadmap from 17% to 21% efficient solar cells showing how improvements to various cell parameters influence the initial efficiency and the absolute loss in efficiency due to LID.

lifetime on 2 Ω-cm material works out to be 45 µs. Note that, in these simulations, the trap level of the B_SO_{2i} defect which is associated with LID was assumed to lie at mid-gap. This assumption is removed later in this chapter (see Section 10.3.3.2).

The results in Figure 10.10 show that so long as improvements to the cell do not result in improved carrier collection (i.e. the improvements are confined to FF, grid shading and rear reflectance) the efficiency loss due to LID remains approximately constant at ~0.35% (abs.). In this roadmap, the upper end of the FF values were limited to those achieved on the best screen-printed Al-BSF cells and the reduction in front-grid shading was limited to values that may be achievable with ~50 µm wide printed lines

using advanced metallization technologies such as extrusion printing and inkjet printing + plating [11, 176]. Given these restrictions, the modeling shows that improvements to FF and grid shading alone can improve the efficiency to 18.5% without paying an increased LID penalty. Raising the rear reflectance can further improve the cell efficiency to ~19%. But getting the initial (pre-LID) efficiency to ≥20% requires advanced front and rear surface passivation techniques. Unfortunately, Figure 10.9 clearly shows that improvements in surface passivation also result in a significant increase in the effect that LID has on cell efficiency. At the high-end of this roadmap, the LID loss is over 1% (abs.) or ~5% (rel.), i.e. a 21% cell (on 2 Ω-cm Cz) will drop to 20% after worst-case LID. The following section shows that a relationship between passivation quality and LID is predicted by device theory and is not specific to the roadmap in Figure 10.10.

10.3.2 Theoretical Understanding of the Effect of Cell Design on LID

Qualitatively, it is simple to understand why a relationship exists between BSRV and the magnitude of LID-induced efficiency loss. The purpose of improving the BSRV of a solar cell is to reduce the loss of photogenerated carriers at the rear surface of the cell. But after LID, the diffusion length is so low that the many carriers do not even 'see' the rear surface, i.e. they recombine in the bulk before reaching the rear surface. This concept is illustrated in Figure 10.11 for two extreme cases – a cell with very poor rear surface passivation (i.e. high BSRV) and a cell with perfect surface passivation (i.e. BSRV = 0 cm/s).

In the high BSRV example, a photogenerated electron moving towards the back surface is likely to be lost (i.e. is not collected by the front p-n junction) both before and after LID. Before LID, this loss is due to surface recombination, and post-LID, the loss is due to bulk recombination. Though the loss mechanism changes after LID, the net effect of LID in this case is zero. The situation changes for a cell with low BSRV. Given a high bulk lifetime (i.e. pre-LID), electrons diffusing towards the back of the device are now

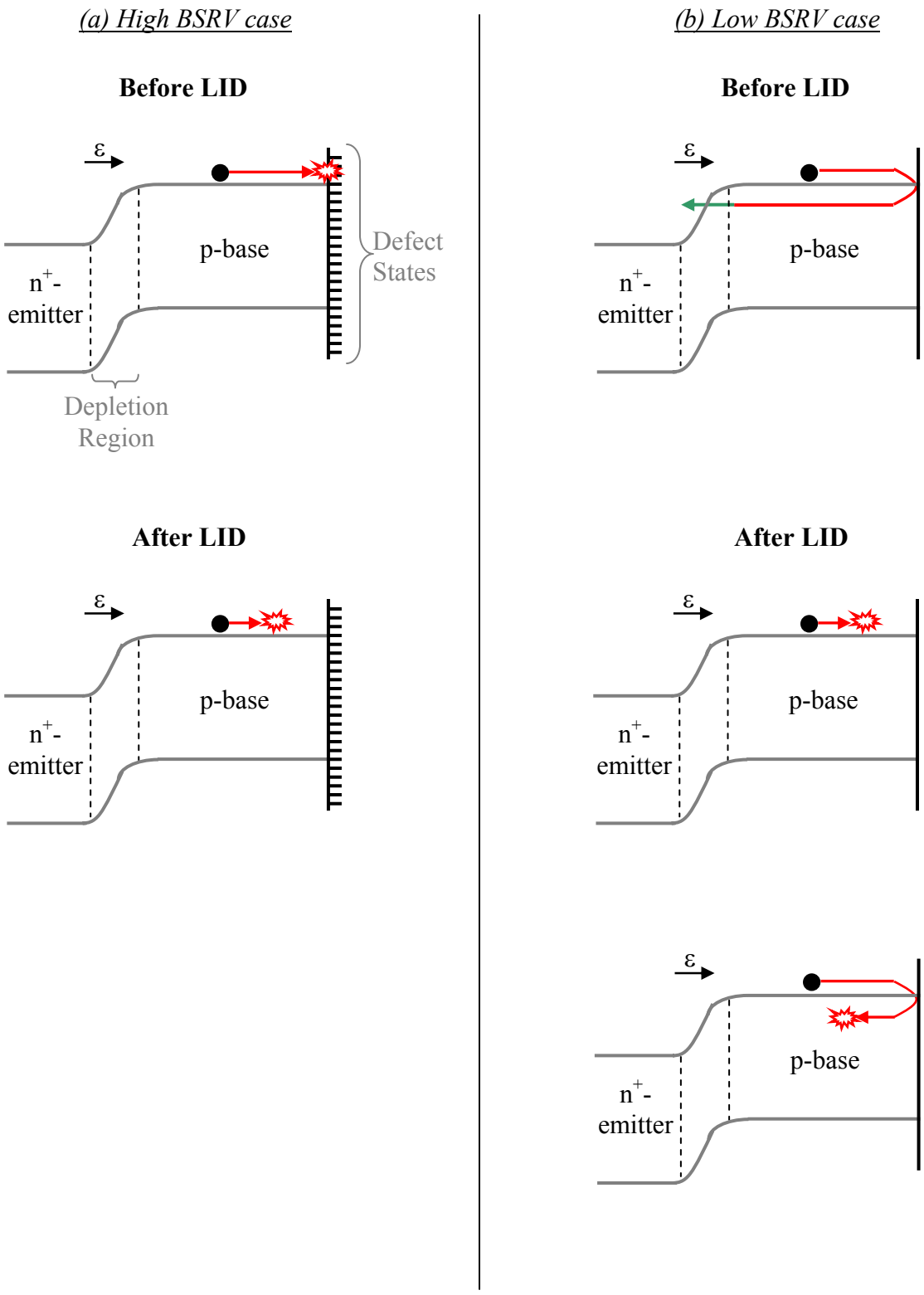

Figure 10.11 Energy band-diagrams illustrating how the effect of LID on carrier collection differs for (a) a high BSRV cell and (b) a low BSRV cell.

likely to be collected by the front junction and therefore contribute to the cell conversion efficiency. But after lifetime degradation due to LID, these electrons which were initially contributing to the cell conversion efficiency, no longer do so. Therefore, the full impact of improved rear passivation is lost after LID and the cell suffers a drop in efficiency.

Quantitatively, the existence of a relationship between BSRV and the LID-driven loss is also expected from semiconductor device equations. In the one-diode model of a solar cell, the open-circuit voltage (V_{OC}) is given by:

$$V_{OC} = \frac{kT}{q}\ln\left(\frac{J_{SC}}{J_{0\_total}} + 1\right) = \frac{kT}{q}\ln\left(\frac{J_{SC}}{J_{0e} + J_{0b}} + 1\right) \qquad (10.2)$$

where J_{0e} and J_{0b} are, respectively, the saturation current densities on the emitter and base sides of the depletion region. Figure 10.12 schematically shows the cell regions where these saturation currents are defined – J_{0b} is a measure of the recombination at the rear

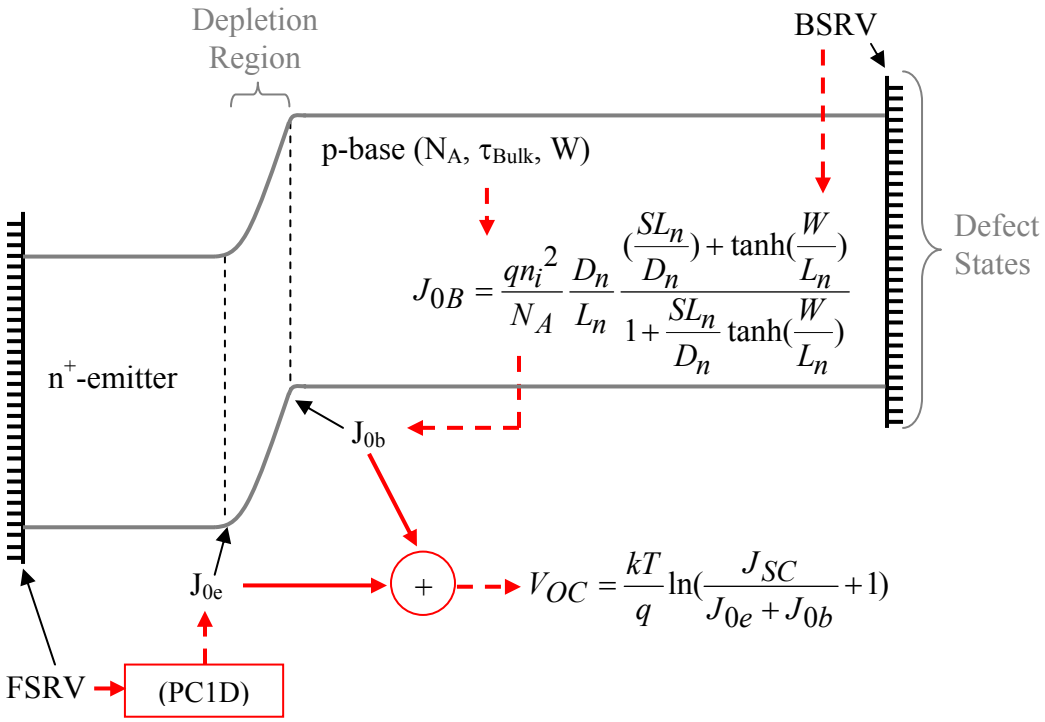

Figure 10.12 Energy band-diagram showing the interfaces at which J_{0e} and J_{0b} are defined as well as a summary of the method used to calculate V_{OC} from BSRV and FSRV.

surface and the base of the cell while J_{0e} is a measure of recombination at the emitter surface and within the emitter bulk. For p-type substrates, J_{0b} can be calculated using the relation:

$$J_{0b} = \frac{qn_i^2}{N_A}\frac{D_n}{L_n}\frac{(\frac{SL_n}{D_n}) + \tanh(\frac{W}{L_n})}{1 + \frac{SL_n}{D_n}\tanh(\frac{W}{L_n})} \tag{10.3}$$

where, D_n and L_n are the electron diffusivity and diffusion length respectively, n_i is the intrinsic carrier concentration, W is the thickness of the base region and N_A is the base dopant density. S is the back surface recombination velocity (BSRV) and the diffusion length, L_n, is proportional to the minority carrier bulk lifetime (τ_n):

$$L_n = \sqrt{D_n \tau_n} \tag{10.4}$$

Equations 10.2 through 10.4 can be used to calculate the effect of LID on V_{OC} as BSRV is varied. The workflow for these calculations is summarized in Figure 10.12 and detailed in the flowchart of Figure 10.13. The results (Figure 10.14 (a)) show that when bulk lifetimes are high, improvements in BSRV translate to large improvements in on J_{0b}. But at the LID-limited lifetime of 45 μs, the impact of BSRV on J_{0b} drops because the back surface is no longer as strongly coupled to the base of the device. Equation 10.2 was then used to re-formulate this J_{0b} data in terms of V_{OC} (assuming a fixed J_{0e} of 150 fA/cm^2). The results plotted in Figure 10.14 (b) clearly show that the lower the BSRV, the larger is the loss in V_{OC} after LID. Thus the V_{OC} trend derived from basic device equations verifies the trend observed in the PC1D simulations (Figure 10.10), i.e. the impact of LID on V_{OC} (and therefore cell efficiency) increases as BSRV improves.

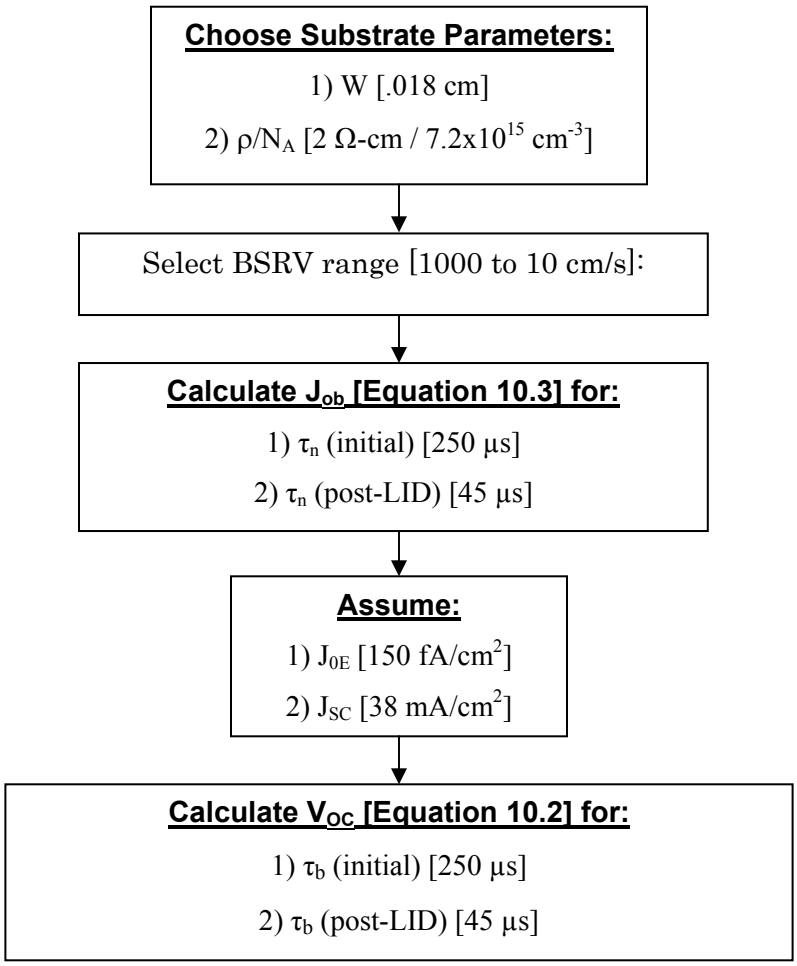

Figure 10.13. Workflow used to calculate the change in V_{OC} due to LID as a function of the back surface recombination velocity (BSRV). The numbers in square brackets are the values used for the calculations (Figure 10.14) in this work.

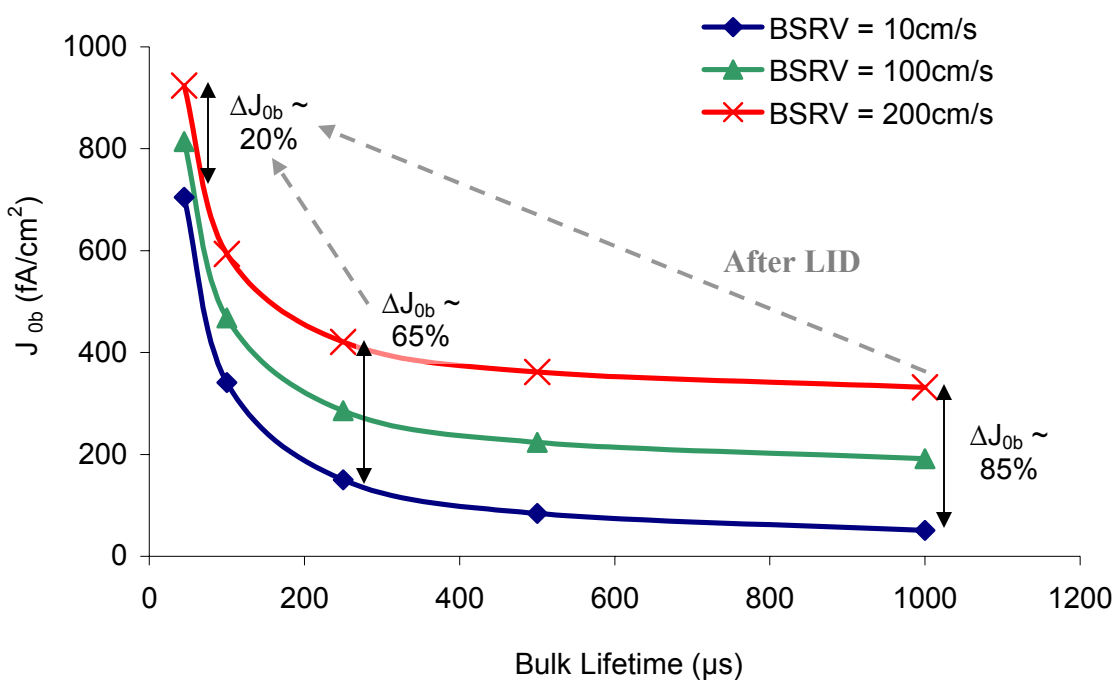

(a)

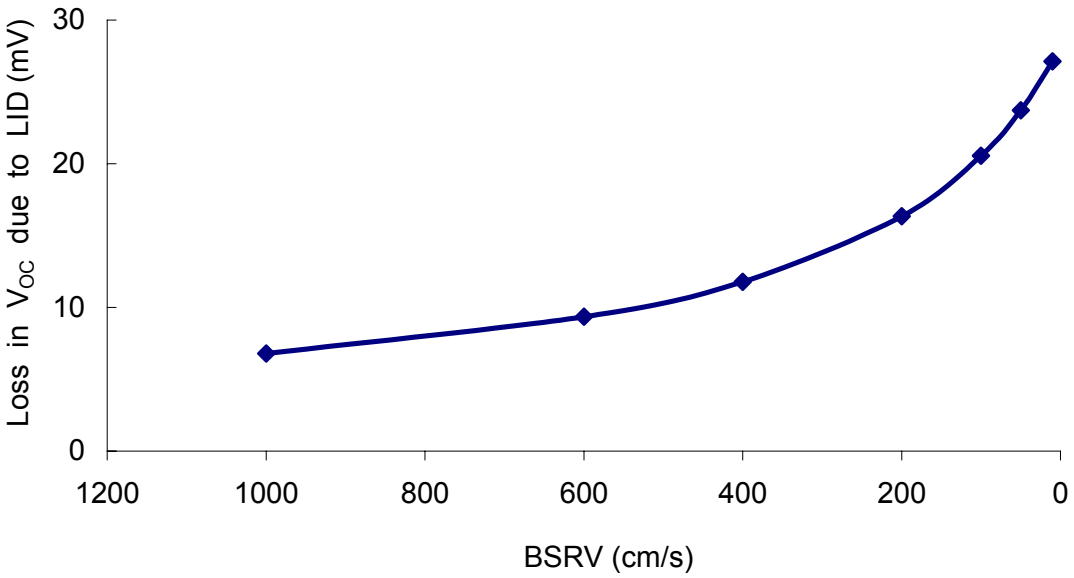

(b)

Figure 10.14 (a) Effect of bulk lifetime loss (due to LID) on the gain in J_{0b} from improved BSRV. The insets show the % reduction in J_{0b} from improvements in rear passivation at bulk lifetimes of 1000 µs, 250 µs and 45 µs. (b) The impact of carrier lifetime reduction from 250 µs (pre-LID) to 45 µs (post-LID) on V_{OC} as a function of BSRV.

Equations 10.2 to 10.4 can also be used to show that, theoretically, the impact of LID should also increase as FSRV improves. The workflow for these calculations is given in Figure 10.15. The calculations involve first converting a range of FSRV values to J_{0e} values using PC1D. Since FSRV and J_{0e} are defined at different planes of a cell (see Figure 10.12) an emitter profile is needed for this calculation. Here, the spreading resista-

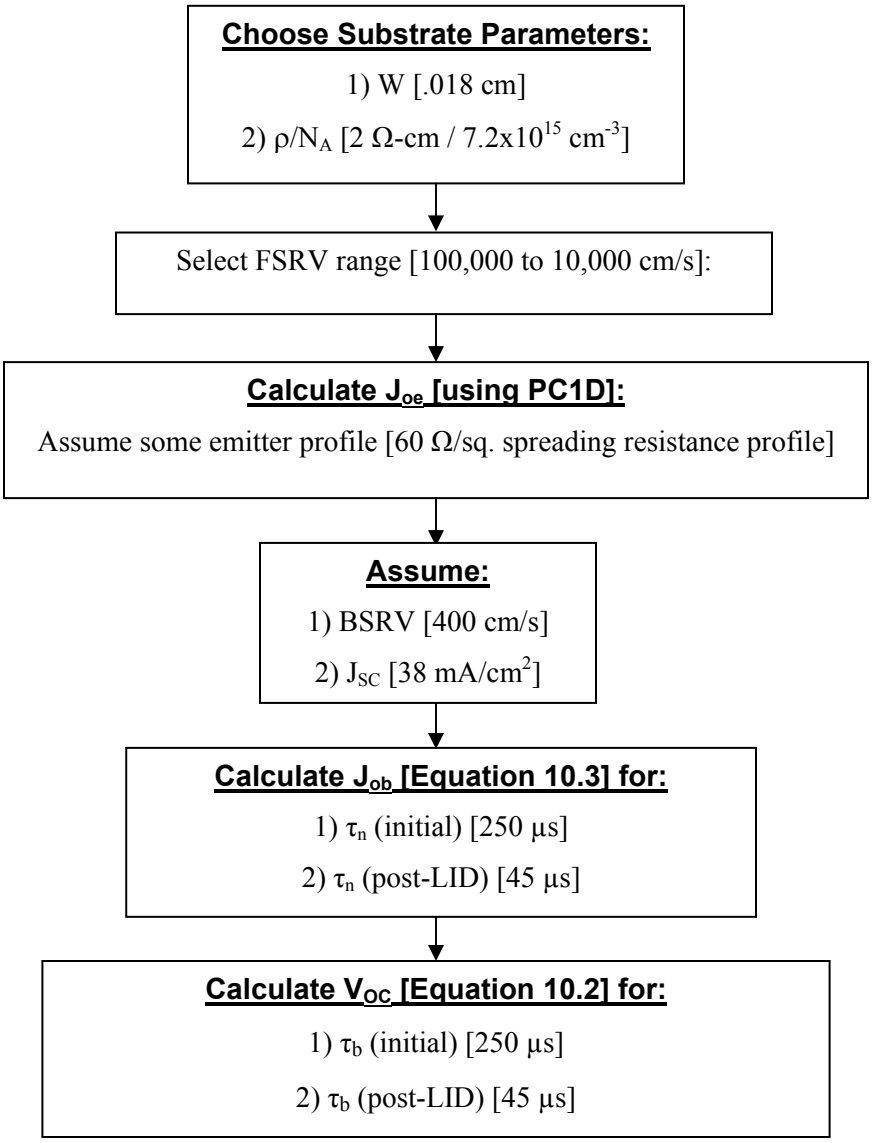

Figure 10.15 Workflow used to calculate the change in V_{OC} due to LID as a function of the front surface recombination velocity (FSRV). The numbers in square brackets are the values used for the calculations (Figure 10.16) in this work.

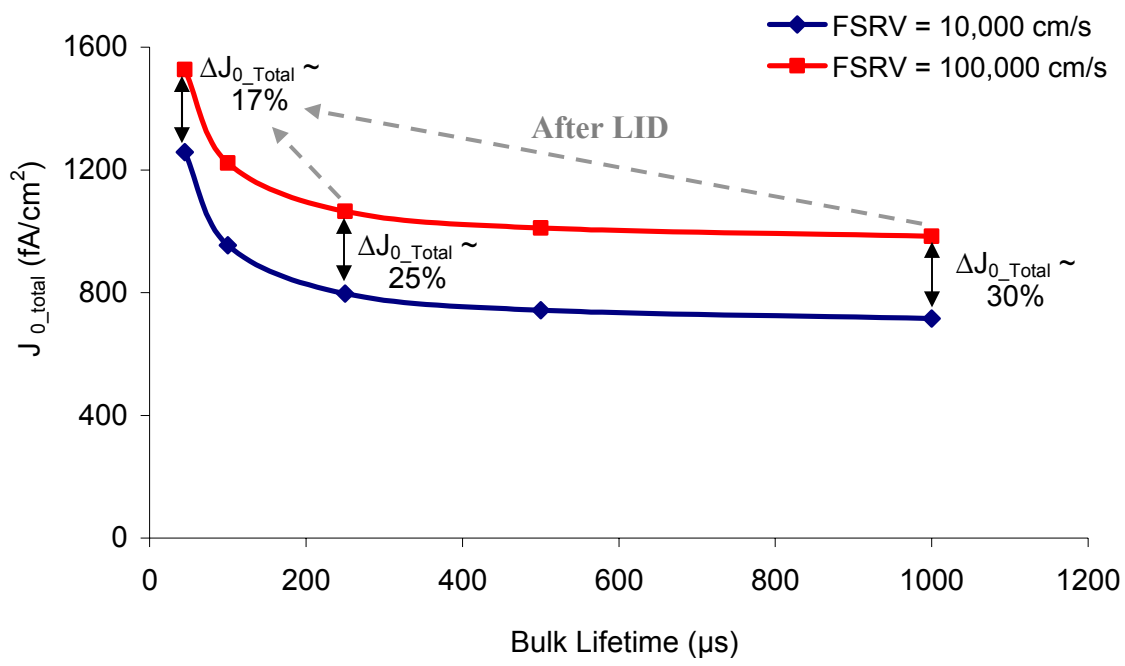

(a)

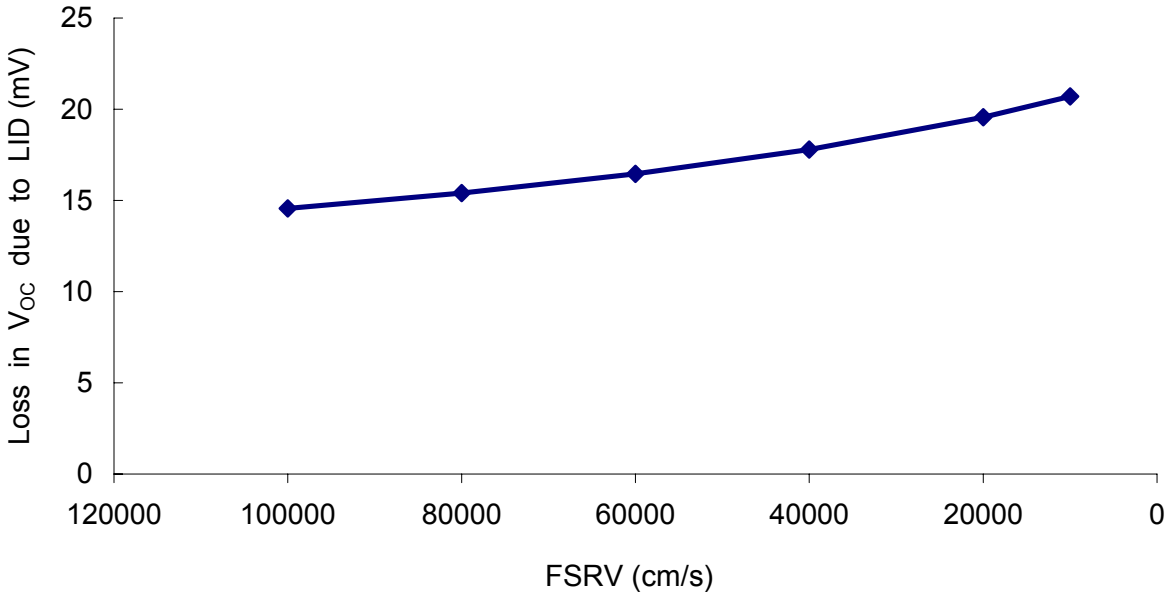

(b)

Figure 10.16 (a) Effect of bulk lifetime loss (due to LID) on the gain in J_{0_total} from improved FSRV. The insets show the % reduction in J_{0_Total} due to improving FSRV from 100,000 cm/s to 10,000 cm/s at bulk lifetimes of 1000 µs, 250 µs and 45 µs. (b) The impact that a drop in carrier lifetime from 250 µs to 45 µs (due to LID) has on V_{OC} as a function of FSRV.

ance profile of a ~60 Ω/sq. emitter (Figure 10.17) was used (details on extracting J_{0e} values using PC1D is given in Chapter 7). Next, pre- and post-LID J_{0b} values were calculated (Equation 10.3) assuming a fixed BSRV of 400 cm/s. Equation 10.2 was then used to calculate V_{OC} from the J_{0e} and J_{0b} values.

J_{0e} itself does not change after LID, since J_{0e} is determined by FSRV and bulk emitter recombination which are not affected by the bulk lifetime. However, as Figure 10.16 (a) shows, lifetime reduction to LID shrinks the impact that FSRV improvements have on the *total* cell J_0 ($J_{0\_total} = J_{0e} + J_{0b}$). This is similar to the trend observed in the J_{0b} calculations shown in Figure 10.14 (a). Expressed in terms of V_{OC}, this means that the better the front surface passivation quality, the larger is the penalty paid in V_{OC} (and cell efficiency) due to LID which again confirms the PC1D findings. That said, a comparison of Figures 10.14 (b) and 10.16 (b) shows that improvements to BSRV have a stronger impact on the LID-induced loss.

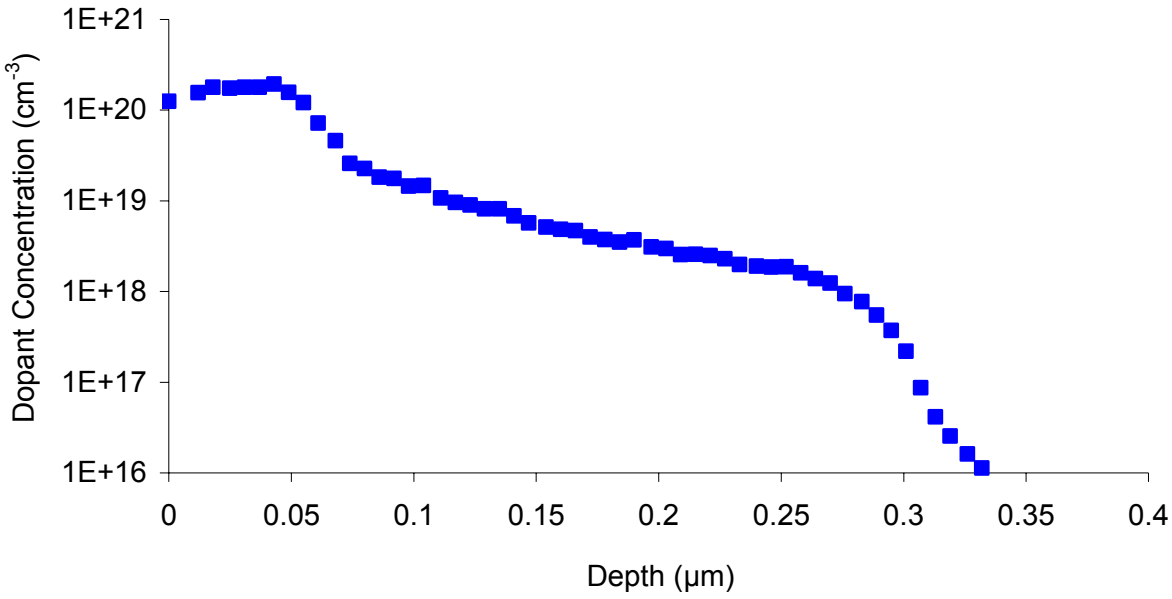

Figure 10.17 Spreading Resistance Profile of industrial-type phosphorous emitter used for calculations examining the effect of FSRV on LID (see text for details).

10.3.3 An Empirical Model for Predicting Stabilized Cell Efficiency

The discussion in the previous sections showed that both PC1D simulations and device theory agree on the point that the impact of LID on cell efficiency should increase as surface passivation is improved. Determining the stabilized, post-LID efficiency in practice requires either an experimental measurement which involves a time-consuming light-soaking step, or modeling the (pre-LID) device in a program such as PC1D and simulating the stabilized efficiency using a degraded (post-LID) lifetime (Equation 10.1). However, the LID simulations seem to indicate that, for a relatively wide range of cell designs, it may be possible to estimate the worst-case stabilized efficiency (i.e. $[O_i]$ = 20 ppm) given nothing other than the starting (pre-LID) cell efficiency.

The basis for this claim is most easily demonstrated by re-considering the roadmap presented earlier in Figure 10.10; it has been repeated in Figure 10.18 for the reader's

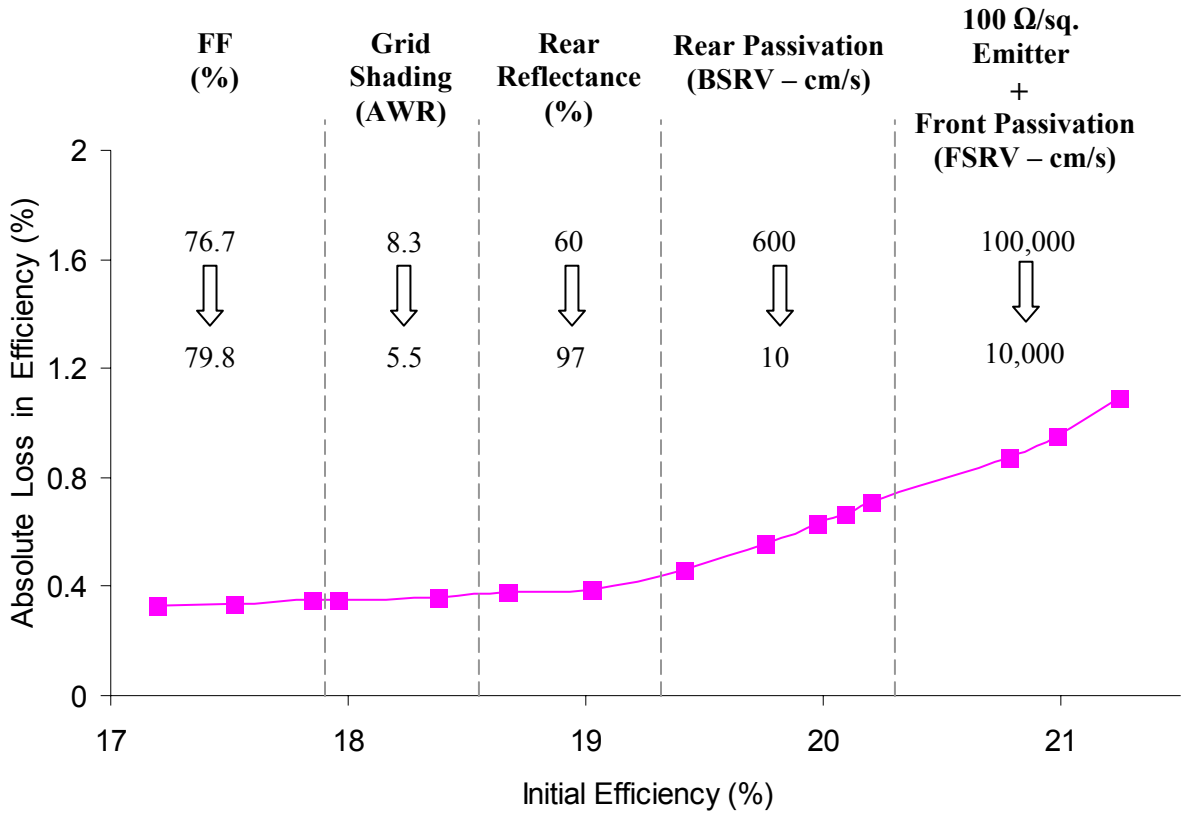

Figure 10.18 Technology roadmap from 17% to 21% efficient solar cells showing the dependence of LID on individual cell parameters.

convenience. When these data-points were re-plotted as shown in Figure 10.19, it was found that there is a strong linear relationship between the stabilized efficiencies and the initial efficiencies, with the least-squares linear fit having a $R^2 > 0.99$. Additional simulations showed that the strong linear correlation (i.e. $R^2 \geq 0.99$) between the initial and stabilized cell efficiencies held regardless of the order or combination in which the parameters were changed (i.e. the cell parameters did not need to be altered in exactly the order shown in Figure 10.18 for the linear correlation to appear).

The generality of this correlation was tested by repeating the LID simulations using different PC1D fits as the baseline – a fit to a ~18.3% efficient 239 cm^2 Al-BSF cell, a fit to a 19.6% efficient, 239 cm^2 rear dielectric passivated cell [62] and the two ~20% B-BSF fits presented earlier in this chapter. Each of these devices has different dark I-V (J_{02}

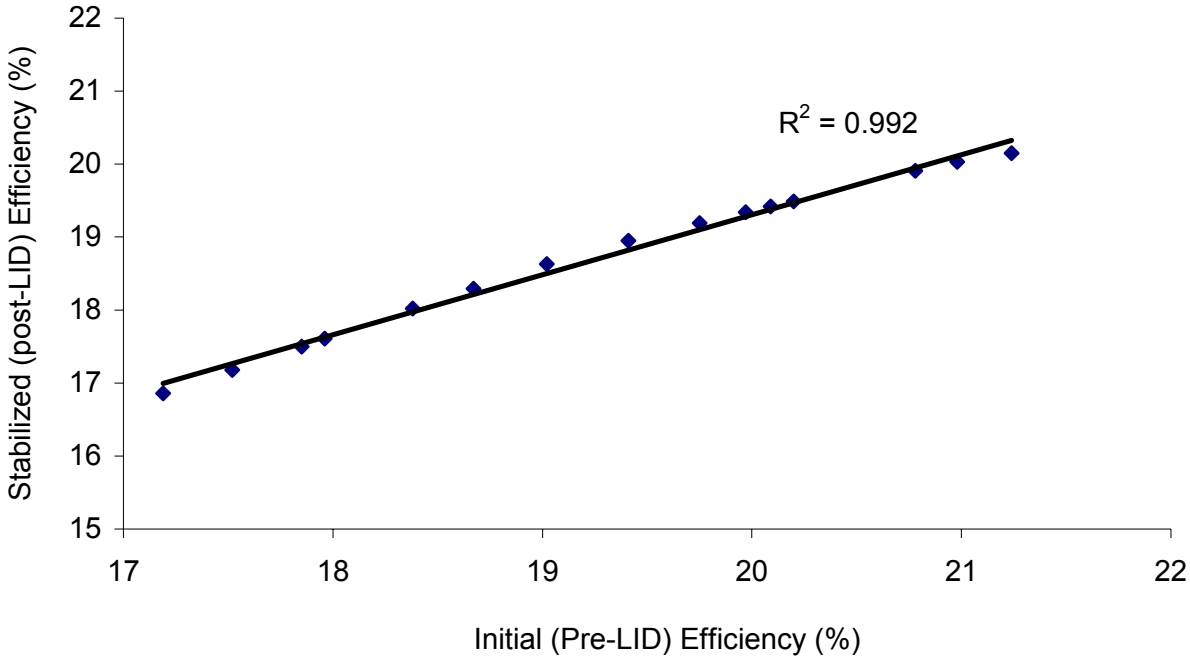

Figure 10.19 Plot of post- vs pre-LID efficiencies from the roadmap in Figure 10.18. The solid line is a linear fit to the data. The inset shows the coefficient of determination (R^2) for the fit.

and n_2) characteristics and different emitter sheet resistances/profiles. The FF, front shading, BSRV and FSRV for each baseline were then varied over the ranges shown in Figure 10.20. The additional 'roadmaps' generated in this way included cases where just one parameter was changed at each step as well as cases where multiple parameters were changed at each step. The resulting array of nearly 500 simulated cell designs (Figure 10.20) preserves the conclusion that a strong linear correlation exists between the initial and worst-case stabilized cell efficiencies. A linear fit to this larger dataset has the form

$$\eta_{Final} = (\eta_{Initial} * 0.805) + 3.15 \qquad (10.5)$$

The R^2 for this fit is 0.97 showing that a strong linear correlation exists between the stabilized and starting cell efficiencies for a wide range of cell designs. The fit has an

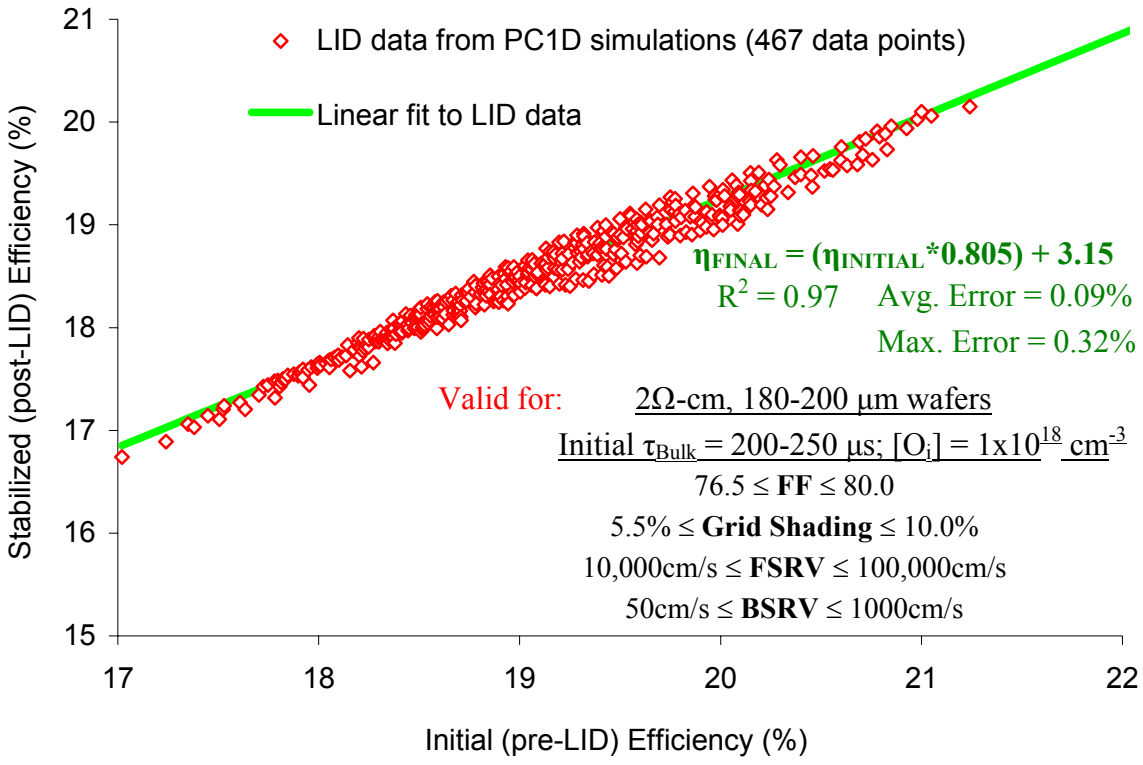

Figure 10.20 Plot of final (post-LID) efficiencies versus initial (pre-LID) efficiencies from multiple roadmap simulations. The insets quantify the accuracy of the linear fit and the range of cell parameters over which the fit is valid.

average error of 0.09% (abs.) and a maximum error of 0.32% (abs.). The error is defined as the difference between the stabilized efficiency predicted by PC1D and the stabilized efficiency predicted by the simple linear model. A histogram of the error is provided in Figure 10.21 showing that for most cell designs, the error is ≤ 0.2% (abs.).

The strong correlation between the initial and worst-case stabilized cell efficiencies is surprising as a given efficiency can be achieved by several different cell designs. For example, a 19% efficient cell can be achieved with a cell design featuring excellent surface passivation and mediocre FF or with a design featuring high FF and mediocre surface passivation. Since the impact of LID is tied to the surface passivation quality and not FF, the former, better passivated design should have a lower stabilized efficiency even though both have the same starting efficiency. This is reflected in the 'bulge' or

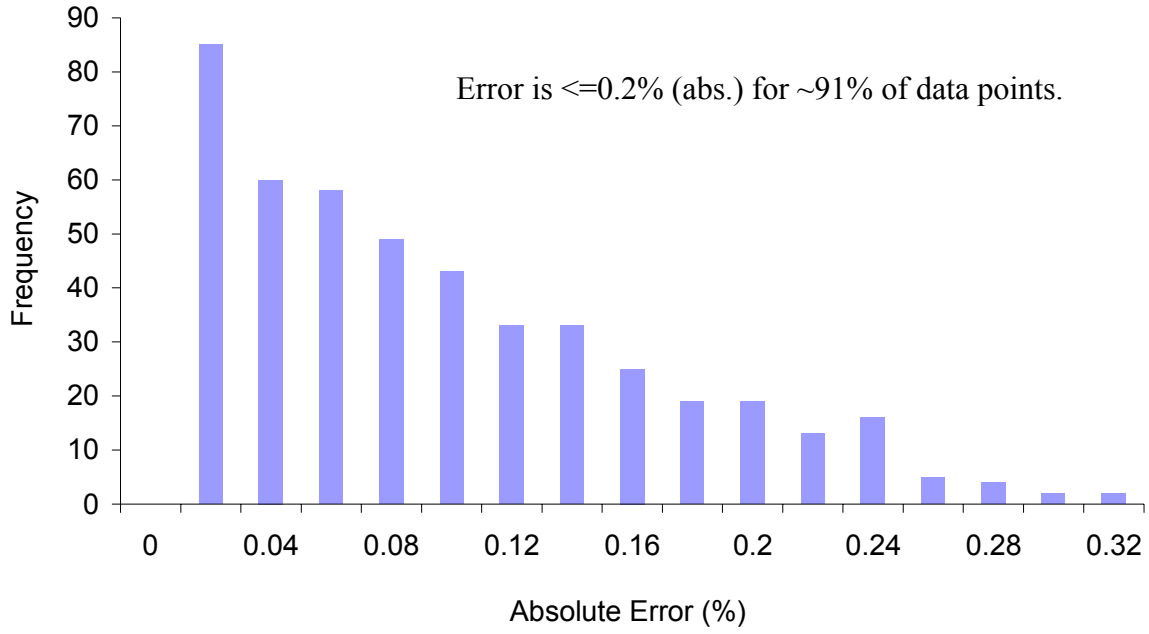

Figure 10.21 Histogram of error between the stabilized (post-LID) efficiencies as predicted by PC1D simulations (red points in Figure 10.17) and those predicted by a simple linear model (solid line in Figure 10.17).

scatter in the data points in Figure 10.20. However, *for the wide range of cell designs covered in these simulations* (see inset in Figure 10.20), the numbers work out such that this scatter is fairly small and so a strong linear correlation does exist between the initial and the worst-case stabilized efficiencies (i.e. for material with $[O_i] \sim 20$ ppm). Note that Equation 10.5 is a fit to simulations which used *only 2Ω-cm material and wafer thicknesses in the range of 180-200 μm*. It is not generally valid for other bulk resistivity/$[O_i]$/wafer thickness combinations as all three parameters affect the slope and intercept of the linear fit. Note also that Equation 10.5 cannot be extrapolated to any arbitrary starting efficiency (doing so increases the error of the fit) and that it is based only on front-junction structures. However the wide parameter space over which it *is* valid covers current industrial passivation and contacting technologies as well as values similar to or better than those that have only been demonstrated in lab-scale fabrication [11, 62, 174-176]. Over this wide range of cell designs, Equation 10.5 provides a simple way of estimating the worst-case stabilized efficiency.

10.3.3.1 Comparison to LID data from the Literature

In the literature, I-V data before and after LID is not routinely reported which makes it difficult to confirm the simulation findings. Table 10.6 lists pre- and post-LID data for two LFC PERC cells from *Fraunhofer ISE* which have substrate characteristics similar to those used for the simulations [178, 179]. The stabilized efficiencies of these cells as predicted by Equation 10.5 agrees well with the experimental stabilized efficiencies. Also included is a the data for an emitter-wrap-through (EWT) device from *ISFH* [180]; since the EWT structure does not have front metal shading, it falls outside the range of cell designs considered in the simulations and the prediction of the simple, linear model is slightly worse.

The fact that predictions of the linear model are in fairly good agreement with a few literature data points does not rule out the possibility that the accuracy of the predictions

Table 10.6 Comparison of experimental LID I-V data from Refs. [178-180] to the simple, linear model of Equation 10.5

Ref.	Structure	Wafer Thickness (μm)/Resistivity (Ω-cm)	Measured Initial η (%)	Measured Stabilized η (%)	Predicted (Eq. 10.5) Stabilized η (%)
[178]	LFC PERC (best)	180 μm / 1.6 Ω-cm	18.9	18.4	18.4
	LFC PERC (avg.)		18.8	18.2	18.3
[179]	LFC PERC	200 μm / 3 Ω-cm	18.1	17.8	17.7
[180]	EWT	NA / 1-2 Ω-cm	20.2	19.2	19.4

are due to chance. A systematic, *experimental* study of how the impact of LID changes with surface passivation quality is needed to confirm the fit to the simulation data presented here. Note however that the finding that a relationship exists between LID and surface passivation quality is theoretically sound.

10.3.3.2 Effect of B_sO_{2i} Defect Parameters on Simulated, Stabilized Cell Efficiencies

As noted earlier in Section 10.3.1, one simplifying assumption that was made in the LID simulations is that the B_sO_{2i} defect that is thought to be responsible for the LID effect was modeled as a mid-gap trap with symmetric capture cross-sections (i.e. $\tau_n = \tau_p$). However, literature data suggests that this may be an inaccurate assumption [177]. Therefore, several of the simulations were re-run using the defect model for B_sO_{2i} proposed by Rein and Glunz [177] which places the defect level at 0.15 eV above mid-

gap, with a capture-cross section asymmetry ($\sigma_n/\sigma_p = \tau_p/\tau_n$) of 9.3. When these defect parameters were used instead of the mid-gap assumption, the PC1D simulations (Tables 10.7 – 10.10) showed that LID causes a reduction in *all* the I-V parameters: V_{OC}, J_{SC} and FF. This is in keeping with experimental data in the literature which show significant losses in FF after LID [178, 179]. In contrast, assuming a mid-gap trap for the B_sO_{2i} defect doesn't cause any appreciable change in FF. The reduction in FF after LID when Rein and Glunz's defect model is used is likely due to the B_sO_{2i}-limited bulk lifetime being injection level dependent which arises from the capture cross-section asymmetry of the deep B_sO_{2i} level [181]. This is similar to the case with Fe_i (see Chapter 8) which is also a deep level recombination center with asymmetric capture cross-sections and produces a strongly injection level dependant lifetime. Note however, that using Rein and Glunz's defect model results in both a lower FF and a higher V_{OC} than the mid-gap defect model. These two effects cancel each other out so that both defect models predict the same stabilized efficiency after LID. Therefore, the simple linear fit of Equation 10.5 remains valid even when using Rein and Glunz's more realistic defect model.

Note that if any changes other than light-induced lifetime loss occur during experimental LID measurements – such as changes in contact/line resistance or degradation in surface passivation quality – they would count as additional loss mechanisms which are not included in the analysis here.

Table 10.7 PC1D simulation of stable, post-LID I-V parameters for a 17% efficient cell design.

~17% cell model	V_{OC} (mV)	J_{SC} (mA/cm^2)	FF (%)	η (%)
Initial	617.9	36.3	76.7	17.2
Post-LID (mid-gap defect model)	611.8	36.0	76.7	16.9
Post-LID (Rein/Glunz defect model)	612.8	36.0	76.6	16.9

Table 10.8 PC1D simulation of stable, post-LID I-V parameters for an 18% efficient cell design.

~18% cell model	V_{OC} (mV)	J_{SC} (mA/cm^2)	FF (%)	η (%)
Initial	625.5	37.2	78.7	18.3
Post-LID (mid-gap defect model)	617.3	36.9	78.6	17.9
Post-LID (Rein/Glunz defect model)	618.9	36.9	78.4	17.9

Table 10.9 PC1D simulation of stable, post-LID I-V parameters for a 20% efficient cell design.

~20% cell model	V_{OC} (mV)	J_{SC} (mA/cm^2)	FF (%)	η (%)
Initial	641.4	38.9	78.5	19.6
Post-LID (mid-gap defect model)	626.2	38.5	78.4	18.9
Post-LID (Rein/Glunz defect model)	630.6	38.5	77.8	18.9

Table 10.10 PC1D simulation of stable, post-LID I-V parameters for a ~21% efficient cell design.

~21% cell model	V_{OC} (mV)	J_{SC} (mA/cm^2)	FF (%)	η (%)
Initial	658.6	40.5	79.6	21.2
Post-LID (mid-gap defect model)	635.9	39.9	79.6	20.2
Post-LID (Rein/Glunz defect model)	643.8	39.9	78.6	20.2

10.3.4 Reducing the Impact of Light Induced Degradation

The conclusion from the prior section that LID has a bigger impact on higher-efficiency cells poses a challenge for the goal of achieving grid-parity with c-Si PV. As noted back in Chapter 1, cost calculations call for cell efficiencies around 20%. The LID simulations suggest that getting to *stable* 20% efficiencies with the current substrate of choice for high-efficiency c-Si cells (i.e. traditionally pulled, boron-doped Cz of 2-3 Ω-cm resistivity and ~180-200 μm thickness) requires that manufacturers overshoot the target and achieve initial cell efficiencies of ~21% (Figure 10.20) before suffering a worst-case loss of ~1% (abs.) due to LID. As higher efficiency designs typically come with a higher manufacturing cost, avoiding such a large degradation is important from a cost perspective.

10.3.4.1 Thin Wafers

One method for reducing the impact of LID is to move to thinner wafers as they require lower bulk lifetimes for complete carrier collection. This was reflected in additional LID simulations which showed (Figure 10.22) that while the effect of an LID-induced lifetime drop from ~250 μs to 45 μs does reduce efficiencies even on 50 μm thick substrates, the magnitude of this loss is much reduced compared to the ~180-200 μm thick substrates currently used in industry.

However, thinner wafers may not be an easier route to stable 20% efficient cells, despite their reduced sensitivity to LID. This is due to the fact that thinning the wafer down reduces the starting efficiency of the cell. For example (Figure 10.22), a cell design that achieves efficiencies ~21% on 180-200 μm achieves efficiencies ~0.5% (abs.) lower on 50 μm thick wafers. So even though the thinner wafer suffers a smaller loss after LID, both wafer types end up at approximately the same stabilized efficiency. The solid line in Figure 10.22 is a fit to 130 data points from PC1D simulations on 50 μm thick wafers and has the form

$$\eta_{Final} = (\eta_{Initial} * 0.914) + 1.41 \quad (10.5)$$

The R^2 for this fit is > 0.99, with an average error of 0.06% (abs.) and a maximum error of 0.23% (abs.). Note that this fit is to cell designs that cover the same parameter ranges as those used in the simulations for 180-200 µm thick wafers (see Figure 10.20).

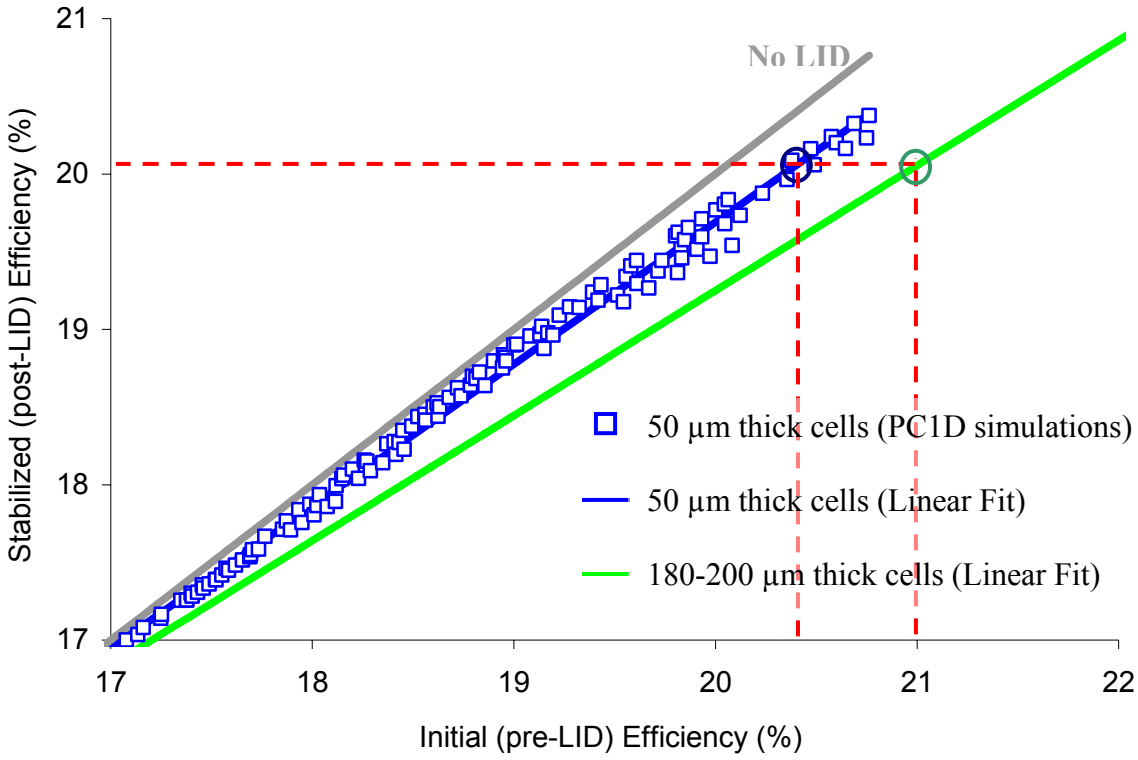

Figure 10.22 Plot of final (post-LID) efficiencies versus initial (pre-LID) efficiencies for 50 µm and 180-200 µm thick wafers.

10.3.4.2 N-type Wafers

An alternate approach towards low-cost, stable, high-efficiency cells is to shift to n-type substrates which are free of boron dopants [182]. As the LID effect results from the simultaneous presence of boron and oxygen in Si wafers [171-173], removing boron from

the substrate eliminates LID. With that in mind, Equation 10.5 (re-plotted in Figure 10.23) can be interpreted as defining the 'efficiency parity' points between n-type and p-type (2 Ω-cm, 180-200 µm thick) cells. For example, an n-type cell with a starting efficiency of ~20% will be at parity with a p-type cell with a starting efficiency of ~21% as the latter can suffer a loss of up to 1% (abs.) due to LID. Similarly, a 19.3% n-type cell is at parity with a 20% efficient p- type cell. Since lower efficiency cells are generally cheaper to manufacture, n-type cells may be an easier route to achieving grid-parity.

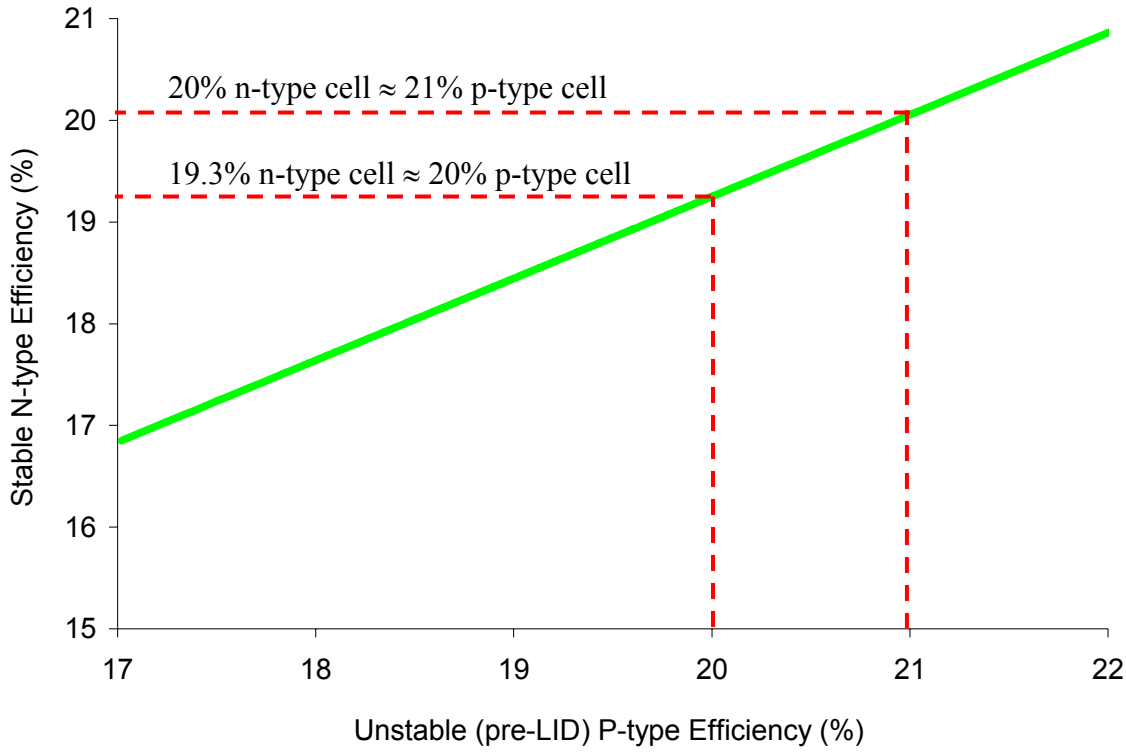

Figure 10.23 Plot defining the points at which the starting efficiencies of n-type and p-type cells (2 Ω-cm, 180-200 µm thick) are at parity after the effect of LID is taken into consideration.

10.4 Development of N-type Cells

As n-type cells do not suffer from boron-oxygen complex related LID, the cell fabrication process developed for p-type B-BSF cells was applied to 2.5 – 3 Ω-cm, 190 μm thick n-type Fz Si substrates. Figure 10.24 shows the schematic for these cells. Since the process sequence for the n-type cells is nearly identical to that of the second generation p-type B-BSF (see Sections 10.1 and 10.2), it is not repeated here in full. The only differences between that process and the n-type process are:

1) The boron diffusion time was cut from 20 minutes to 12 minutes resulting in an emitter sheet resistance of ~50 Ω/sq.
2) Both sides of the wafers are symmetrically passivated using thermal SiO_2/SiN_X stacks (the p-type devices use an Al-doped SOG for B-BSF passivation for reasons re-iterated below).
3) The front screen-printed contacts are achieved with an Ag/Al paste (H9383M) from Heraeus and the rear Ag point contacts are printed using H9237 Ag paste also from Heraeus.

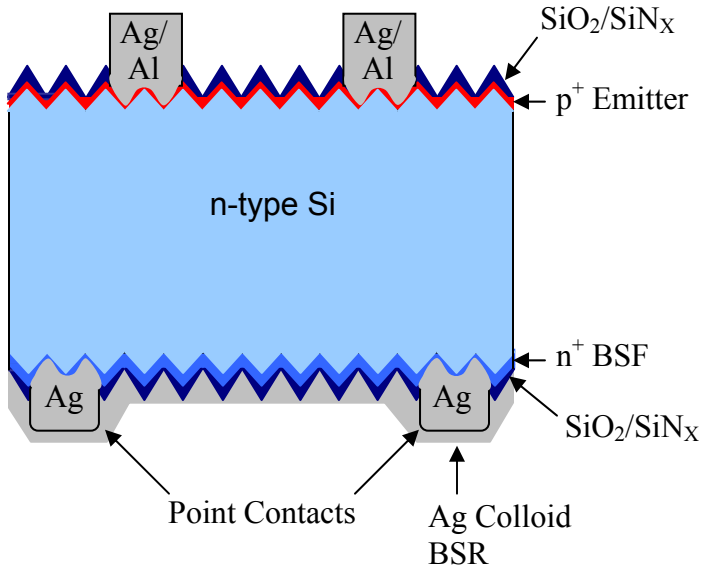

Figure 10.24 Schematic of the screen-printed n-type cells fabricated in this study.

As with the p-type cells, boric acid/DI water spin-on and $POCl_3$ sources are used for the boron and phosphorous diffusions respectively.

Back in Chapter 7, fired thermal oxide/SiN_X stacks and an Al-doped SOG were identified as promising materials for passivating p^+-Si surfaces. For the p-type B-BSF cells presented earlier in Section 10.2, the Al-doped SOG is used to passivate the B-BSF as it provides good passivation on planar p^+-surfaces and simultaneously getters lifetime-killing Fe which gets incorporate into the wafer during boron diffusion (See Chapter 8). However, the Al-doped SOG provides poor passivation on textured p^+ surfaces; this was demonstrated in both passivation studies (Chapter 7) and at the cell level (Section 10.2.2.1). In contrast, a fired oxide/SiN_X stack was found to provide passivation of similar quality on both planar and textured p^+ surfaces. Since the emitter on front-junction n-type cells needs to be textured to reduce reflectance, the oxide/SiN_X stack was used for passivating the boron emitter of the n-type cells. Both the p-type and n-type cells used oxide/SiN_X passivation of the phosphorous emitter/BSF.

The downside of the oxide/SiN_X passivation scheme is that Fe measurements on p-type substrates (Chapter 8) showed that the oxidation step results in significant Fe contamination of the wafer bulk. Fortunately Fe contamination is less of a concern for n-type cells, since the hole capture-cross section for interstitial Fe (Fe_i) is much smaller than its electron capture cross-section ($\sigma_p \ll \sigma_n$) [142, 145]. As holes are the minority carriers in n-type solar cells, Fe contamination has a much smaller impact on the lifetime of n-type wafers than it does on p-type wafers where electrons are the minority carriers. This was confirmed by lifetime experiments where bulk lifetimes of ~600-1500 μs were measured after boron diffusion and oxidation of the same type of wafers (~3 Ω-cm Fz Si) used for cell fabrication. Based on measurements on companion p-type wafers, the wafers are believed to have bulk Fe concentrations of $2\text{-}5\text{x}10^{11}$ cm^{-3} (see Chapter 8 for details on how Fe concentrations were measured in this study). Even at the low-end of the n-type

lifetime distribution, the corresponding diffusion length of ~770 µm is more than 4x the thickness (~190 µm) of the wafers.

10.4.1 Results and Analysis of ≥ 20% Efficient N-type Cells

Figure 10.25 shows the NREL-verified I-V characteristics of the best n-type cell (4 cm^2) fabricated in this study which has an efficiency of ~20.3%, with V_{OC} of 647 mV, J_{SC} of 40.1 mA/cm^2 and FF of 78%.

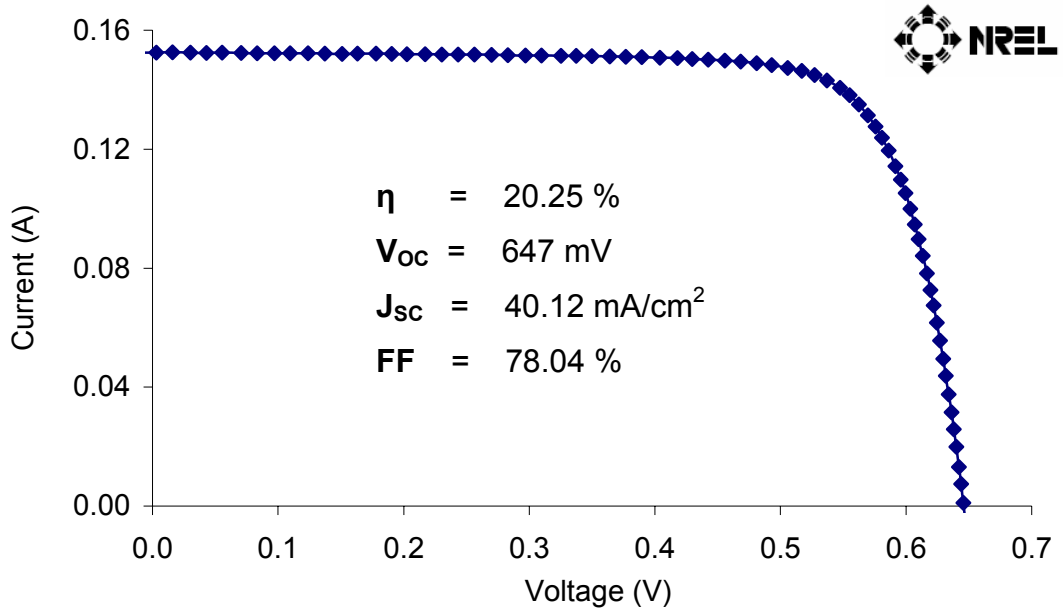

Figure 10.25 I-V characteristics of screen-printed n-type cell fabricated in this study.

The 'best fit' to the IQE, reflectance and I-V data (Figure 10.26) indicates that the device has a BSRV of 40 cm/s (assuming a bulk lifetime of 600 µs), and an FSRV of ~4000 cm/s. Note that this BSRV is an *effective* SRV value which includes the effect of rear surface texturing (i.e. rear-side texturing was turned off in PC1D). If the model includes a rear surface texture, then the BSRV drops by a factor of 1.7 to ~25 cm/s. This is due to the fact that if a surface texture is included in PC1D, the simulator automatically increases the BSRV to account for the increase in surface area due to texturing. If the

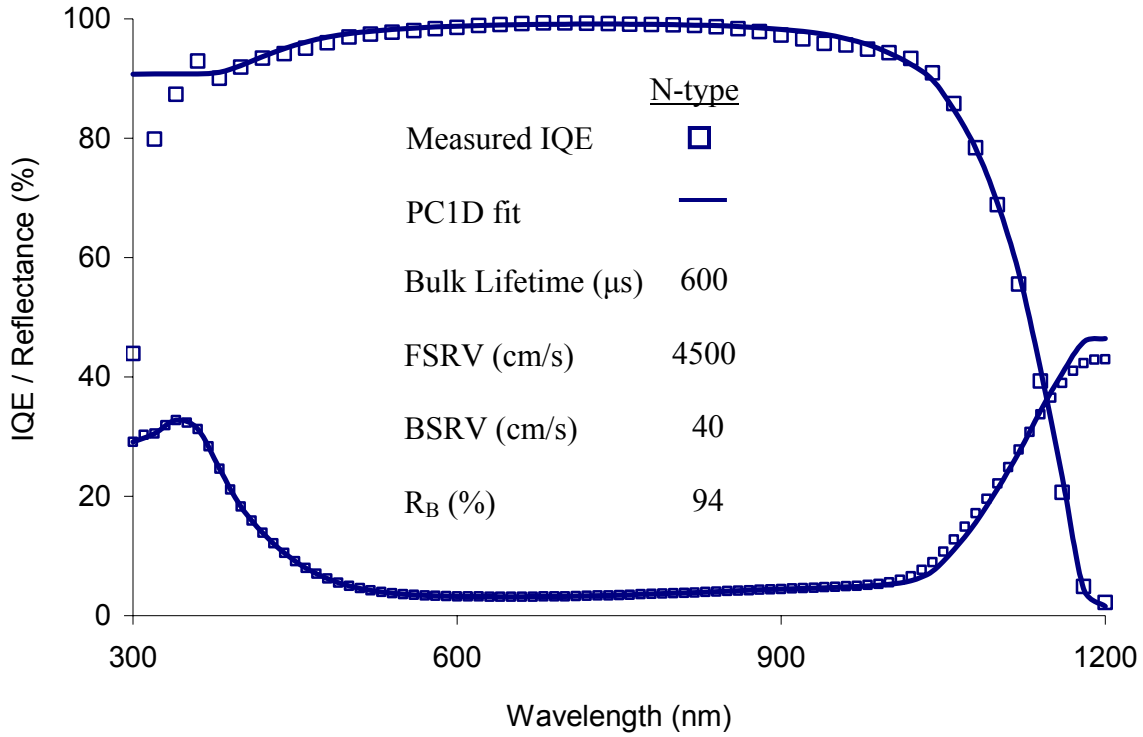

Figure 10.26 PC1D fits to the measured IQE and reflectance characteristics of the best n-type cell fabricated in this study.

Table 10.11 Verified I-V data of ~20.3% efficient n-type cell and simulated I-V data from a PC1D fit to the same cell. The NREL measurement was performed with an aperture mask of area 3.802 cm^2. The GT measurements were performed with an aperture mask of area 3.893 cm^2.

		η (%)	V_{OC} (mV)	J_{SC} (mA/cm^2)	FF (%)
Best Cell	Measured (NREL)	20.25	646.9	40.12	78.04
	Measured (GT)	20.40	649.9	39.83	78.83
	PC1D (simulated)	20.19	647.8	39.55	78.80
Avg. of 15 cells	Measured (GT)	19.90	648.3	39.03	78.58

high-end of the measured n-type bulk lifetimes (1500 μs) is used, the 'best fit' effective BSRV is ~60 cm/s.

Table 10.11 compares the simulated I-V characteristics from the PC1D fit to the measured I-V data. Also shown is the average I-V characteristics of 15 cells fabricated using the same process and measured at Georgia Tech. Note that all cells were measured with an aperture mask to prevent carrier collection from outside the periphery of the cell.

10.5 Conclusions

By integrating into a cell process sequence, the boron diffusion, surface passivation, iron gettering and rear reflector studies performed in Chapter 3-8, a 20.2% efficient screen-printed B-BSF field cell (4 cm^2; 300 μm thick Fz Si) was successfully achieved. This represents a 1.3% (abs.) efficiency enhancement over the 18.9% efficient baseline Al-BSF cell in this work which has the same front (emitter) side as the B-BSF cell. Through detailed analysis, the B-BSF cell was found to have a BSRV of 120 cm/s and R_B of 93%. In comparison the Al-BSF cell has a BSRV of 600 cm/s and R_B of 70%.

The effect that light-induced degradation (LID) would have if this B-BSF device were fabricated on oxygen-containing p-type Cz substrates was examined via simulations and device theory. This study showed that a direct correlation exists between the surface passivation quality of a p-type cell and the efficiency loss that cell will suffer due to LID, i.e. better passivated cells will suffer a greater loss due to LID. These simulations showed that while an ~18% efficient cell (fabricated on 180-200 μm thick, ~2 Ω-cm substrates) can lose ~0.4% (abs.) in efficiency due to LID, a well-passivated ~21% efficient cell would lose ~1.0% (abs.). The ~20% efficient B-BSF cells fabricated in this study would lose ~0.7% (abs.). From a collection of nearly 500 simulated cell designs which cover a wide range of cell parameters, an approximately linear relationship was found to exist between the starting efficiency of a cell design and its stabilized efficiency after worst-

case LID (i.e. material with a high bulk oxygen concentration of 20 ppm). As n-type cells do not suffer from light-induced degradation, this empirical relationship also provides a method for estimating the 'efficiency parity' threshold between n- and p-type cells. For example, an n-type cell with an efficiency of ~20% can be at parity with (i.e. is equivalent to) a ~21% p-type Cz cell as the latter can suffer an efficiency loss of up to 1% (abs.) due to LID.

Due to the realization that LID can have a very large impact on the stabilized efficiency of well-passivated p-type cells (such as the B-BSF cell developed in this thesis), the B-BSF process was slightly modified and applied to n-type substrates. Using symmetric thermal SiO_2/SiN_X stack passivation, a ~20.3% efficient screen-printed n-type cell (4 cm^2; ~3 Ω-cm; 190 μm thick Fz Si) was achieved.

Chapter 11

GUIDELINES FOR FUTURE WORK

The work presented in this thesis resulted in two high-efficiency, screen-printed boron-diffused cell designs. On p-type Si, efficiencies as high as 20.2% (p-type) were achieved with a passivated boron back-surface-field structure compared to 18.9% on an Al-BSF cell with an identical front (emitter) side. On n-type wafers, efficiency of ~20.3% was achieved using only commercially-friendly, thermal oxide/SiN_X stacks for surface passivation. Both the p-type and n-type process sequences were designed with the goal of keeping the process throughput similar to that of the baseline Al-BSF process; though both processes involve three high temperature steps, each step is shorter than the ~90 minute $POCl_3$ diffusion used in the baseline Al-BSF process. In addition, a low-cost and non-toxic boric acid source was developed as an alternative to conventional boron dopant sources such as boron tribromide (BBr_3) and a novel Al-doped spin-on dielectric was introduced which can simultaneously getter Fe and passivate the Si surface in a short thermal cycle. This chapter suggests research avenues which can improve the commercial manufacturability of the cell designs and fabrication sequences developed here, and lead to a deeper understanding of the physical processes involved in the cell technology.

11.1 Thin, Large Area Substrates

All the cells fabricated in this work were small-area (4 cm^2) cells, while commercial cells are typically 239 cm^2 or larger. While most of the technology used here, namely, atmospheric pressure tubes for thermal processing, screen-printed contacts, thermal oxide and silicon nitride for surface passivation, are suitable for large-area substrates, process tweaks may be required to achieve uniform application of the spin-on boric-acid/DI

sources and the Al-doped spin-on glass on large-area wafers. As the boric acid sources are water based, they are suitable for spray-on tools which may provide a higher throughput than spin-coating. Alternate high-throughput sources such as screen-printed pastes which have historically provided very low bulk lifetimes may also be able to provide high-efficiency cells when used with the process developed in this thesis which includes strong process-induced Fe gettering.

While the 20%+ p- and n-type cells fabricated in this work are on ~200-300 μm thick substrates, PC1D modeling (using the fits presented in Chapter 10) shows that 20% efficiency can be maintained on substrates as thin as 100 μm. Since the cost of the wafer, which is typically ~180-200 μm thick for commercial cells, comprises ~60% of the cost of a Si PV module, the cell designs developed here offer a way to maintain high-efficiencies while reducing the wafer thickness and thus wafer cost in half.

11.2 Alternate Substrate Types

The second change required to improve the commercial viability of the cells developed in this thesis is to use Cz Si substrates, instead of the more expensive FZ Si substrates. For the p-type B-BSF cells, this means moving to commercial boron-doped Cz Si wafers. A downside associated with using such substrates is that they suffer from light-induced degradation (LID) of the bulk lifetime and cell efficiency. Simulation and theory work presented in this thesis has shown that well-passivated cells (like the B-BSF cells designed here) suffer a larger drop in efficiency due to LID than the conventional Al-BSF structure. Therefore, alternate substrates such Ga-doped Cz and low-oxygen, boron-doped material such as magnetically-stabilized Cz (MCz) and monocast wafers should be investigated. As the LID effect results from the simultaneous presence of boron and oxygen in Si, these alternate substrates may provide higher stabilized cell efficiencies.

Since n-type wafers are not thought to suffer from LID, transferring the n-type FZ Si cell process that was developed here to n-type *Cz* Si substrates may be more attractive for manufacturing especially as it uses simple thermal oxide/SiN_X stacks for surface passivation. However, it should be noted that compensated n-type Si wafers (i.e. n-type wafers that are doped with both boron and phosphorous) do suffer from LID [182]. Care should also be taken to ensure that the quality of the wafer and the lifetime after processing are high enough for high-efficiencies. This is emphasized in the Figure 11.1 which shows that n-type cells are more sensitive to drops in bulk lifetimes than p-type cells. The data points in the figure were obtained using the PC1D fits to the 20%+ p-type and n-type cells that were presented in Chapter 10 and varying the bulk lifetime from 10-2000 µs. For both the n-type and p-type simulations, 200 µm thick wafers were assumed.

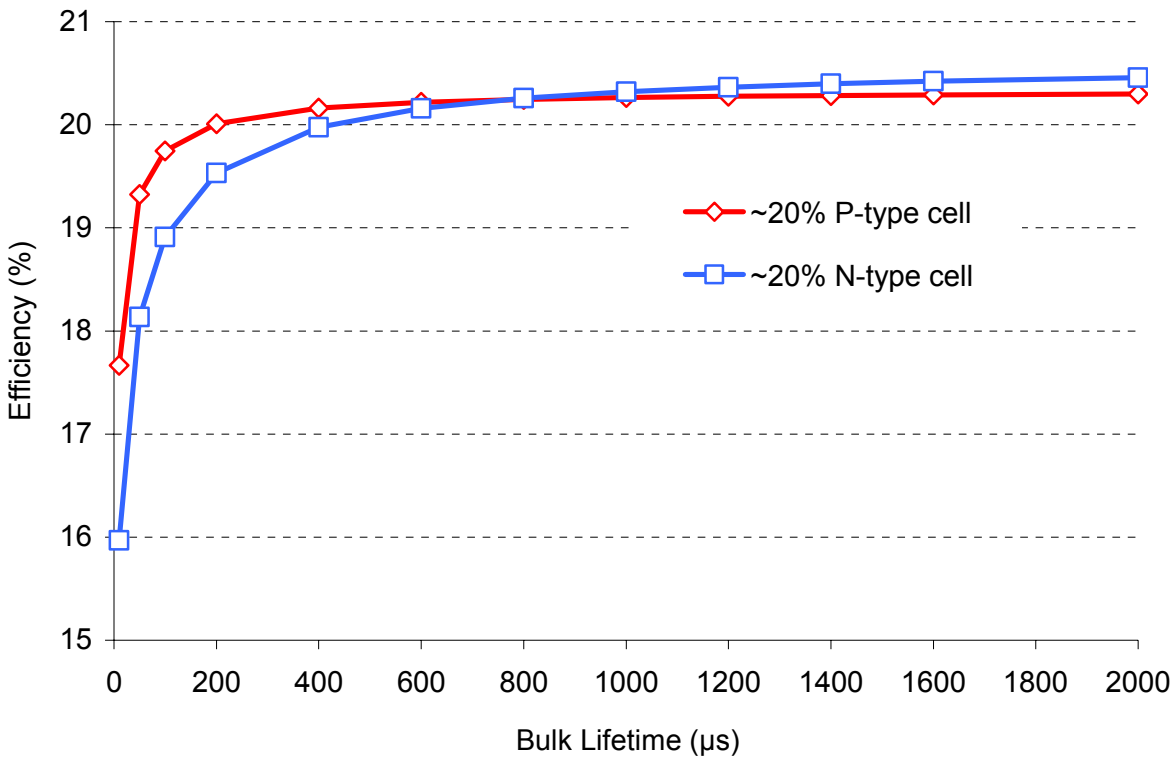

Figure 11.1 Effect of bulk-lifetime variation on the ~20% efficient p-type and n-type cells developed in this work assuming 200 µm thick wafers.

11.3 Improved Understanding of the Gettering Mechanism of the Al-doped SOG

The novel negatively charged Al-doped SOG that was used in this thesis to passivate p^+-Si surfaces, was found to strongly getter Fe from silicon. The data obtained thus far suggests that the negative charge is responsible for the gettering and that the gettered Fe may end up in the SOG, instead of remaining inside the Si substrate at the Si/SOG interface. However, further work is needed to clarify this proposed gettering mechanism. The species responsible for the negative charge in the dielectric, and its location are also currently not known. Monitoring the charge density in the dielectric via C-V measurements while gradually thinning down the SOG could be used to identify whether the charge is distributed in the bulk of the SOG or lies close to the Si/SOG interface. The effect of time/temperature/ambient on the effectiveness of the gettering effect should also be studied; if strong gettering can be obtained at lower temperatures and shorter process times that those used in this work, it would improve the commercial viability of the Al-doped glass.

11.4 Examine Alternate Methods for Boron Doping

At the start of this thesis, two B-BSF structures were considered – these are shown again in Figure 11.2. The structure with the fully metallized rear is clearly simpler to fabricate. However, this simpler structure was not developed in this thesis since obtaining a 20% efficient B-BSF cell with full-area rear metallization requires a very deep (~3 μm) BSF. Obtaining such heavy doping via boron diffusion requires prolonged processing at very high temperatures (see Chapter 6) which is incompatible with high-throughput commercial manufacturing. Alternate BSF formation methods such as epitaxial Si deposition or ion implantation may be able to provide such heavily doped B-BSFs using shorter process times and temperatures, thereby making the simpler B-BSF structure more commercially viable.

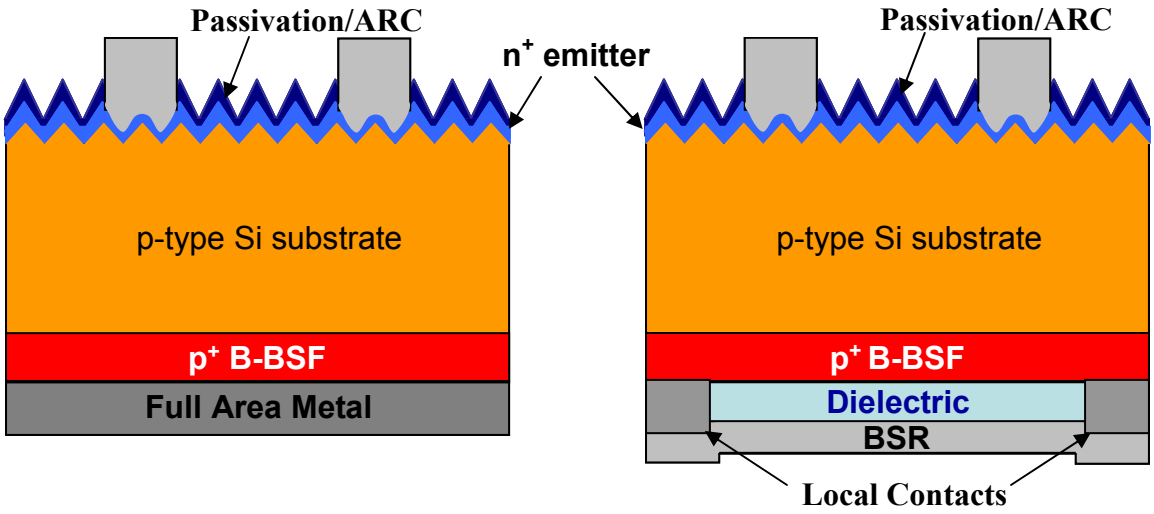

Figure 11.2 The two B-BSF structures that were considered for 20% efficient cells in this thesis (taken from Chapter 6).

It should be noted that since dielectric/metal stacks typically offer higher reflectance than a metal BSR alone (as seen in Chapter 9), light-trapping may be less effective in the simpler, fully metallized structure. The effect of this on the efficiency of thin cells should be considered when choosing between the two cell structures.

CONCLUSIONS

In this thesis, > 20% efficient, screen-printed, boron diffused solar cells were achieved on both p-type and n-type Fz Si. This was accomplished via extensive device characterization and computer modeling, and development of relevant technology. The road to 20% efficient cells started with the fabrication and characterization of an 18.9% efficient screen-printed Al-BSF cell (4cm^2 on 300 μm thick, 1.3 Ω-cm FZ Si). Computer modeling of this 'baseline' device showed that the efficiency could be increased to 20% if the BSRV (600 cm/s) and back surface reflectance (70%) could be improved to 200 cm/s and 95% respectively, while maintaining a bulk lifetime of ≥ 300 μs.

Conceptually, an improved BSRV can be achieved by doping the BSF more heavily (leading to improved field-effect passivation) and by passivating the BSF (leading to a lower density of defect states at the BSF surface). Since boron doping can provide a more heavily-doped BSF (as it has higher solubility in Si than aluminum) and the surface of a B-BSF can be more easily passivated with a dielectric, this thesis focused on achieving 20% efficient cells using a passivated B-BSF cell structure.

While several ≥ 20% efficient B-BSF cells that have been reported in the literature, their processing involved photolithography and prolonged thermal cycles at very high temperatures (> 1000°C). Such processing methods are too high-cost and low-throughput to be commercially viable. This thesis examined whether efficiencies ≥ 20% can be achieved with a full-area B-BSF cell structure using short (≤ 90 minute) process steps and low-cost, screen-printing technology for contact formation. The 90 minute time limit was based on the fact that the longest step in the simple, Al-BSF cell process is a 90 minute long $POCl_3$-diffusion step (note this figure includes the time taken to ramp to/from the peak process temperature).

The first task in the development of a 20% efficient B-BSF cell involved selecting a boron diffusion source. Though the highest bulk lifetimes and the highest cell efficiencies

reported in the literature have been achieved using the boron tribromide (BBr_3) source, BBr_3 is also pyrophoric and toxic. Therefore, a boric-acid based spin-on source was developed in this thesis as a low-cost, non-pyrophoric and non-toxic alternative to BBr_3. It was found that boron emitters with a wide range sheet resistances (~20-200 Ω/sq.), surface concentrations (~$1x10^{19}$-$1x10^{20}$ cm^{-3}) and junction depths (~0.2-1.5 μm) can be achieved with very dilute boric acid solutions (~0.5-2 wt.% boric acid in DI water) by controlling the diffusion time and temperature.

Once is was determined that a wide range of boron profiles can be achieved with boric acid/DI water sources, PC1D modeling was used to select a B-BSF profile that can achieve the target BSRV of 200 cm/s and thereby deliver a 20% efficient B-BSF cell. The modeling showed that even with no surface passivation (i.e. full-area rear metallization) the BSRV target could be achieved using a ~3 μm deep, electrically 'opaque' B-BSF with a high surface concentration of ~$1x10^{20}$ cm^{-3}. However, the literature indicates that even with very high processing temperatures of ~1100°C, fabricating such a heavily doped BSF requires a ~5.5 hr. deposition + drive-in process. This is much longer than the 90 minute time limit that this thesis imposes on all cell process steps due to throughput considerations. Experimentation using boric-acid/DI water sources showed that a 90 minute diffusion cycle at a relatively moderate temperature of 1000°C results in a shallow, electrically 'transparent' ~0.8 μm deep B-BSF. Modeling showed that such a shallow B-BSF has a BSRV of ~550 cm/s without any surface passivation (i.e. full-area metallization). This means that if the throughput of the baseline Al-BSF process is to be maintained, increased process complexity in the form of an additional passivation step and local contacts is unavoidable. Specifically, the PC1D modeling suggested that achieving the target BSRV or S_{p/p^+} of 200 cm/s with the transparent B-BSF requires a S_{p^+} of ~40,000 cm/s.

Several dielectrics were therefore examined in this thesis, with the aim of finding one that provides the required passivation quality (S_{p^+} ~ 40,000 cm/s) and is stable through a

high-temperature firing step. On planar p^+ surfaces, an annealed Al-doped spin-on glass (SOG) and a fired thermal SiO_2/SiN_X stack were found to provide the best passivation. However, only the fired thermal oxide/SiN_X stack was able to provide similar passivation on a textured p^+ surface. The thermal oxidation/SOG annealing step used in these passivation studies was < 90 minute long in accordance with the time limit imposed on all cell process steps in this thesis. Area-average calculations showed that achieving the cell-level S_p^+ of 40,000 cm/s with either passivation method requires a metal fraction of ≤ 2.5%. Since achieving such a low metal fraction with current screen-printing technology requires a point-contact pattern, the passivation studies also helped to determine the rear contact structure of the cells fabricated in this thesis.

In summary, the results of the passivation studies provided two options for achieving a 20% efficient, passivated B-BSF cell: 1) a point-contacted, transparent, *planar* B-BSF with either Al-doped SOG or thermal oxide/SiN_X passivation and 2) a point-contacted, transparent, *textured* B-BSF with thermal oxide/SiN_X stack passivation. Since planarizing one side of a wafer can add up to two steps to the cell fabrication process, the latter appeared to be the more commercially-friendly option. However, bulk lifetime studies showed that the thermal oxide/SiN_X passivation scheme resulted in severe degradation in the bulk lifetime due to Fe contamination of the wafer during oxidation. In contrast, the Al-doped SOG was found to both strongly getter Fe *and* passivate the B-BSF in the same thermal cycle. Since high lifetimes are required for achieving 20% efficient cells, these findings forced the use of the more complex rear-side structure – a *planar* B-BSF with Al-doped SOG passivation. From experimental studies, the strong Fe gettering ability of the Al-doped SOG was attributed to its negative charge density, i.e. the gettering is driven by electrostatic attraction between negatively-charged complexes in the SOG and positively charge interstitial Fe.

The final piece of the 20% efficient cell designed using PC1D modeling, i.e. an electrically conductive back surface reflector (BSR) material with R_B = 95% and high

diffusivity (β) was met using a Ag colloid. From reflectance measurements, the Al-doped SOG/Ag Colloid stack was found to have $R_B \sim 98\%$ and $\beta \sim 70\%$. Electrical resistivity measurements showed that after a short sintering step at 400°C, the resistivity of the Ag colloid is similar to that of screen-printed Ag pastes fired at ~700-800°C.

These technology developments, i.e. boric-acid diffusion, passivation and Fe gettering with an Al-doped SOG and BSR formation with the Al colloid, were integrated into a cell process leading to a 20.2% efficient passivated, screen-printed, full-area B-BSF cell (4 cm^2 on 300 μm thick, 1.3 Ω-cm FZ Si). This result was verified by the National Renewable Energy Laboratory (NREL). However, device modeling showed that if this cell structure and process were transferred to commercial p-type Cz Si material, light-induced degradation (LID) could reduce the efficiency to ~19%. This large drop in cell efficiency was shown, via device modeling and device theory, to be linked to the well-passivated surfaces of the B-BSF cell. Specifically, it was found that as the quality of surface passivation improves, the impact of LID on cell efficiency becomes larger. Since n-type substrates do not suffer from the same LID effect, the B-BSF cell process was applied to n-type FZ wafers. The Al-doped SOG used that was used for passivating the B-BSF of the 20.2% p-type cell was replaced with a thermal oxide/SiN_X stack, as the Al-doped SOG provides poor passivation on textured boron-diffused Si surfaces. The p-type B-BSF and the n-type boron emitter cell processes were otherwise nearly identical. With this tweaked process, a cell efficiency of ~20.3% was achieved (4cm^2 on 190 μm thick, 3 Ω-cm n-type Fz Si) and confirmed by NREL.

In summary, > 20% efficient p-type *and* n-type cells (4cm^2) were achieved through a combination of modeling-driven cell and process design, technology development and process integration. These small-area cells are proofs-of-concept for the technologies and cell processes developed in this thesis and further work is required to scale them up to the large (≥ 239 cm^2) substrates used for commercial Si solar cells.

REFERENCES

[1] Annual Energy Review 2010, U.S. Energy Information Administration, Report number DOE/EIA-0384, 2011, http://www.eia.gov/aer/contents.html.

[2] State of the Climate in 2009, National Oceanic and Atmospheric Administration, National Climatic Data Center, http://www.ncdc.noaa.gov/bams-state-of-the-climate/2009.php.

[3] Energy Technology Perspectives 2010- Scenarios & Strategies to 2050, International Energy Agency, 2010, ISBN: ISBN: 978-92-64-08597-8.

[4] CO_2 Emissions from Fuel Combustion: Highlights (2010 edition), International Energy Agency, 2010.

[5] Hugo Ahlenius, United Nations Environment Programme (UNEP), NASA Surface meteorology and Solar Energy (SSE) Release 6.0 Data Set, 2008. http://maps.grida.no/go/graphic/natural-resource-solar-power-potential

[6] Levelized Cost of New Generation Resources in the Annual Energy Outlook 2011, U.S. Energy Information Administration, Nov. 2010. http://www.eia.gov/oiaf/aeo/electricity_generation.html

[7] A. Rohatgi, A. Ristow, A. Das, and S. Ramanathan, "Road to cost-effective Si PV," in *Tech. Digest of the 18th I-PVSEC*, Indian Association for the Cultivation of Science, Kolkata, India, 2009.

[8] PV News, Paul Maycock, 1997.

[9] Market Report 2011, European Photovoltaic Industry Association, 2010.

[10] P. Lolgen, C. Leguijt, J. A. Eikelboom, R. A. Steeman, W. C. Sinke, L. A. Verhoef, P. F. A. Alkemade, and E. Algra, "Aluminum back-surface field doping profiles with surface recombination velocities below 200 cm/s," in *Proc. 23rd IEEE PVSC*, pp. 236-242, 1993.

[11] A. Rohatgi and D. Meier, “Developing novel low-cost, high-throughput processing techniques for 20%-efficient monocrystalline silicon solar cells,” *Photovoltaics International* **10**, pp. 87-93, 2010.

[12] A. Schneider, C. Gerhards, P. Fath, E. Bucher, R. J. S. Young, J. A. Raby, and A. F. Carroll, "Bow reducing factors for thin screenprinted mc-Si solar cells with Al BSF," in *Proc.29th IEEE PVSC*, pp. 336-339, 2002.

[13] Analyst Reaction - Solar Price Surveys, Bloomberg New Energy Finance, Nov. 2010.

[14] N. Merchant, A. Shaikh, C. Khadilkar, S. Sridharan and E. Graddy, “SEM Microstructure, Composition, Property Correlation-Ships in Aluminum Conductors, in *Proc. 33rd IEEE PVSC*, 2008.

[15] A. Ebong, K. Nakayashiki, V. Upadhyaya, A. Rohatgi, B. R. Bathey, M. D. Rosenblum, J. Salami, and A. Shaikh, “Screen-printed solar cells on less than 200-µm thick EFG sheet silicon,” in *Proc. 22nd EU-PVSEC*, pp. 1442-1445, 2007.

[16] P. A. Basore, “Numerical modeling of textured silicon solar cells using PC-1D,” *IEEE Trans. Electron Devices* **37**, pp. 337-343, 1990.

[17] O. Breitenstein, P. Altermatt, K. Ramspeck, M.A. Green, J. Zhao, and A. Schenk, “Interpretation of the commonly observed I-V characterisitics of c-Si cells having ideality factor larger than two,” in *Proc. 4th WCPEC*, pp. 879-884, 2006.

[18] D. Macdonald and A. Cuevas, “Reduced fill factors in multicrystalline silicon solar cells due to injection level dependent bulk recombination lifetimes,” *Prog. Photovolt: Res. Appl.* **8**, pp. 363-375, 2000.

[19] V. Meemongkolkiat, “Development of high efficiency monocrystalline Si solar cells through improved optical and electrical confinement,” Ph.D. Thesis, Georgia Institute of Technology, 2008.

[20] K. R. McIntosh, “Lumps, Humps and Bumps: Three Detrimental Effects in the Current-Voltage Curve of Silicon Solar Cells,” Ph.D. Thesis, Australian National University, 2001.

[21] M.A Green, “Solar Cells: Operating Principles, Technology and System Applications”, University of New South Wales, 1998.

[22] H. Schlangenotto, H. Maeder, and W. Gerlach, "Temperature dependence of the radiative recombination coefficient in silicon," *Physica Status Solidi A* **21a**, pp. 357-367, 1974.

[23] J. Dziewior and W. Schmid, “Auger coefficients for highly doped and highly excited silicon,” *Appl. Phys. Lett.* **31**, pp. 346-348, 1977.

[24] M. Kerr and A. Cuevas, "General parameterization of Auger recombination in crystalline silicon," *J. Appl. Phys.* **91**, pp. 2473-2480, 2002.

[25] W. Shockley and W. T. Read, "Statistics of the recombinations of holes and electrons," *Physical Review* **87**, pp. 835-842, 1952.

[26] R. N. Hall, "Electron-hole recombination in germanium," *Physical Review* **87**, pp. 387-387, 1952.

[27] F. Montillo and P. Balk, “High temperature annealing of oxidized silicon surfaces,” *J. Electrochem. Soc*, **118**, pp. 1463-1468, 1971.

[28] M.A. Green, “The path to 25% silicon solar cell efficiency: History of silicon cell evolution,” *Prog. Photovolt: Res. Appl.* **17**, pp. 183-189, 2009.

[29] D.E. Kane and R.M. Swanson, “Measurement of the emitter saturation current using a contactless photoconductivity decay method,” in *Proc. 18th IEEE PVSC*, pp. 578-583, 1985.

[30] A. B. Sproul and M. A. Green, “Improved value for the silicon intrinsic carrier concentration from 275 to 375 K,” *J. Appl. Phys.* **70**, pp. 846-854, 1991.

[31] J.A. Del Alamo and R.M. Swanson, “The physics and modeling of heavily doped emitters,” *IEEE Trans. Electron Devices* **31**, pp.1878-1888, 1984.

[32] A Cuevas and M.A. Balbuena, “Review of analytical models for the study of highly doped regions of silicon devices,” *IEEE Trans. Electron Devices* **36**, pp. 553-560, 1989.

[33] R. R. King and R. M. Swanson, "Studies of diffused boron emitters: saturation current, bandgap narrowing, and surface recombination velocity", *IEEE Trans. Electron Devices* **38**, pp. 1399-1409, June 1991.

[34] P. P. Altermatt, J. O. Schumacher, A. Cuevas et al., "Numerical modeling of highly doped Si:P emitters based on Fermi-Dirac statistics and self-consistent material parameters," *J. Appl. Phys.* **92**, pp. 3187-3197, 2002.

[35] F. L. Pedrotti and L. S. Pedrotti, "Introduction to Optics", 2nd ed., Prentice Hall, Englewood Cliffs, New Jersey, 1993.

[36] E.D. Palik (editor), "Handbook of Optical Constants of Solids", Academic Press, Elsevier, 1985.

[37] S. Laux *et al.*, "Room-temperature deposition of indium tin oxide thin with plasma ion-assisted evaporation," *Thin Solid Films* **335**, pp. 1-5, 1998.

[38] M. Balestrieri, D.Pysch, J.-P.Becker, M.Hermlea, W.Warta, S.W.Glunz, "Characterization and optimization of indium tin oxide films for heterojunction solar cells," Solar Energy Mater. Sol. Cells **95**, pp. 2390-2399, 2011.

[39] H. Yoshikawa and S. Adachi, "Optical constants of ZnO," *Jpn. J. Appl. Phys.* **36**, pp. 6237-6243, 1997.

[40] M.H. Kang, D.S. Kim, A. Ebong *et al.*, "The study of silane-free SiC_xN_y film for crystalline silicon solar cells," *J. Electrochem. Soc.* **156**, pp. H495-H499, 2009.

[41] D.K. Schroder, R.N. Thomas, and J.C. Swartz, "Free Carrier Absorption in Silicon", *IEEE Trans. Electron Devices* **25**, pp. 254-261, 1978.

[42] D. Kray, M. Hermle, S. Glunz, "Theory and experiments on the back side reflectance of silicon wafer solar sells," *Prog. Photovolt: Res. Appl.* **16**, 2008, pp. 1-15.

[43] M.M. Koltun, "Solar Cells: Their Optics and Metrology," Allerton Press Inc., New York, 51 (1988).

[44] M.A. Green and M. Keevers, "Optical properties of intrinsic silicon at 300 K," *Prog. Photovolt.: Res. Appl.* **3**, p.189-192, 1995.

[45] Reference Solar Spectral Irradiance: ASTM G-173, http://rredc.nrel.gov/solar/spectra/am1.5/ASTMG173/ASTMG173.html

[46] Keith Emery, National Renewable Energy Laboratory, *Private Communications*, 2011.

[47] M. Bass, E.W. van Stryland, D.R. Williams, W.L. Wolfe, "Handbook of Optics vol. II (2nd Ed.): Devices, Measurements and Properties," McGraw Hill, 1995.

[48] E. Yablonovitch, "Statistical Ray Optics," *J. Opt. Soc. Am.* **72**, pp. 899-907, 1982.

[49] E. Yablonovitch and G.D. Cody, "Intensity enhancement in textured optical sheets for solar cells," *IEEE Trans. Electron Devices* **29**, pp. 300-305, 1982.

[50] A. Goetzberger, "Optical confinement in thin-Si solar cells by diffuse back reflectors," in *Proc. 15th IEEE PVSC*, pp. 867-870, 1981.

[51] R. Sinton and A. Cuevas, "Contactless determination of current–voltage characteristics and minority carrier lifetimes in semiconductors from quasi-steady-state photoconductance data," *Appl. Phys. Lett.* **69**, pp. 2510-2512, 1996.

[52] T. W. Krygowski, "A novel simultaneous diffusion technology for low-cost, high-efficiency silicon solar cells," Ph.D. Thesis, Georgia Institute of Technology, 1998.

[53] K. R. McIntosh and L. P. Johnson, Recombination at textured silicon surfaces passivated with silicon dioxide, *J. Appl. Phys.* **105**, 124520, 2009.

[54] M. Kerr, "Surface, Emitter and Bulk Recombination in Silicon and Development of Silicon Nitride Passivated Solar Cells," PhD thesis, Australian National University, 2002.

[55] A. Cuevas, P. A. Basore, G. Giroult-Matlakowski, C. Dubois, "Surface recombination velocity of highly doped n-type silicon," *J. Appl. Phys.* **80**, pp. 3370-3375, 1996.

[56] M. Hilali, “Understanding and development of manufacturable screen-printed contacts on high sheet-resistance emitters for low-cost silicon soloar cells,” PhD thesis, Georgia Institute of Technology, 2005.

[57] J. L. Murray and A. J. McAlister, "The Al-Si (Aluminum-Silicon) system," *Bull. Alloy Phase Diagrams* **5**, pp.77-84, 1984.

[58] P. Lolgen, W. C Sinke, C. Leguijt, A. W. Weeber, P. F. A. Alkemade, L. A. Verhoef, “Boron doping of silicon using coalloying with aluminum,” *Appl. Phys. Lett.* **65**, pp. 2792-2794, 1994.

[59] T. Fellmeth, S. Mack, J. Bartsch, D. Erath, U. Jager, R. Preu, , F. Clement, D. Biro, “20.1% efficient silicon solar cell with aluminum back surface field,” *IEEE Electron Dev. Lett.* **32**, pp. 1101-1103, 2011.

[60] S. Ramanathan, V. Meemongkolkiat, A. Das, A. Rohatgi, I. Koehler, “Understanding and fabrication of 20% efficient cells using spin-on based simultaneous diffusion and dielectric passivation,” *IEEE J. Photovoltaics* **2**, pp. 22-26, 2012.

[61] S. Ramanathan, A. Das, A. Rohatgi, “Optimization of phosphoric acid based limited-source-diffusion to obtain high quality emitter for screen printed contacts, *Proc.37th IEEE PVSC*, 2011.

[62] J.-H Lai, A. Upadhyaya, S. Ramanathan, A. Das, K. Tate, V. Upadhyaya, A. Kapoor, C.-W. Chen, and A. Rohatgi, “High-efficiency large-area rear passivated silicon solar cells with local Al-BSF and screen-printed contacts,” *IEEE J. Photovoltaics* **1**, pp. 16-21, 2011.

[63] F. Huster, “Investigation of the alloying process of screen printed aluminum pastes for the BSF formation on silicon solar cells,” in *Proc.20th EU PVSEC*, pp. 1466-1469, 2005.

[64] J. Zhao, A. Wang and M. A. Green, “24.5% Efficiency Silicon PERT Cells on MCZ Substrates and 24.7% Efficiency PERL Cells on FZ Substrates,” *Prog. Photovolt: Res. Appl.* **7**, pp. 471-474, 1999.

[65] J. Zhao, A. Wang and M. A. Green, “24.5% Efficiency PERT silicon solar cells on SEH MCZ substrates and cell performance on other SEH Cz and FZ substrates,” Solar Energy Mater. Sol. Cells **66**, pp. 27-36, 2001.

[66] M. A. Green, A. W. Blakers, J. Zhao, A. M. Milne A. Wang, and X.. Dai, "Characterization of 23-percent efficient silicon solar cells," *IEEE Trans. Electron Devices* **37**, pp. 331-336, 1990.

[67] G. L. Vick and K. M. Whittle, "Solid solubility and diffusion coefficients of boron in silicon," *J. Electrochem. Soc.* **116**, pp. 1142-1144, 1969.

[68] S. F. Guo and W.F. Chen, "A model for boron deposition in silicon using BBr_3," *J. Electrochem. Soc.* **129**, pp. 1592-1596, 1982.

[69] K.A. Münzer, A. Froitzheim, R.E. Schlosser, R. Tölle, M.G. Winstel, "Over 18% industrial screen printed silicon solar cells, " in *Proc. 21st EU-PVSEC*, pp. 538-543, 2006.

[70] A. Wang, J. Zhao, and M.A. Green "24% efficient silicon solar cells," *App. Phys. Lett.* **57**, pp. 602-604, 1990.

[71] R. Meyer, P. Engelhart, B. Terheiden, and R. Brendel, "A process sequence for silicon solar cells with local boron diffused back surface field," in *Proc. 21st EU-PVSEC*, pp. 713-716, 2006.

[72] J. Y. Lee and S. W. Glunz, "Boron-back surface field with spin-on dopants by rapid thermal processing," in *Proc. 19th EU-PVSEC*, pp. 998-1001, 2004.

[73] G. Bueno, I. Freire, K. Varner, L. Pérez, R. Lago, J.C. Jimeno, J. Salami, H. Kerp, K. Albertsen, and A. Shaikh, "Simultaneous Diffusion of Screen Printed Boron and Phosphorous Paste for Bifacial Silicon Solar Cells," in *Proc. 20th EU-PVSEC*, pp. 1458-1461, 2005.

[74] A. Kränzl, R. Kopecek, K. Peter, P. Fath, "Bifacial solar cells on multi-crystalline silicon with boron BSF and open rear contact," in *Proc. 4th WCPEC*, pp. 968-971, 2006.

[75] G. Pignatel and G. Queirolo, "AES study of boron diffusion in silicon from a boron nitride source with hydrogen injection," *J. Electrochem. Soc.* **126**, pp. 1805-1810, 1979.

[76] R.R. King, E.W. Thomas, W.B. Carter, and A. Rohatgi, "The effect of aluminum and boron solid-source doping on recombination in silicon solar cells", in *Proc. 22nd IEEE PVSC*, pp. 229-234, 1991.

[77] A. Kränzl, R. Kopecek, K. Peter, A. Schneider, P. Fath, "Industrial η=15.5% mc-Si solar cells with boron BSF and open rear contact", in *Proc. 20th EU-PVSEC*, pp. 781-784, 2005.

[78] Y.Komatsu, V.D.Mihailetchi, L.J.Geerligs, B.vanDijk, J.B.Rem, M.Harris, "Homogeneous p+ emitter diffused using boron tribromide for record 16.4% screen-printed large area n-type mc-Si solar cell," *Solar Energy Mater. Sol. Cell*s **93**, pp. 750-752, 2009.

[79] B.S. Murthy, K.R. Wadhera, P.R.S. Rao, "Boron diffusion into silicon using boron tribromide (BBr3) as source," *J. Institution of Telecommunication Engineers* **14**, pp. 301-306, 1968.

[80] R.C. Thomas, "Boron Tribromide as a Diffusion Source," *Solid State Technology* **17**, pp. 44-46, 1974.

[81] E. Arai, H. Nakamura, and Y. Terunuma, "Interface Reactions of B_2O_3-Si System and Boron Diffusion into Silicon", *J. Electrochem. Soc.* **120**, pp. 980-987, 1973.

[82] E. Dominguez, E. Lora-Tamayo, and B. Blanchard , "Analytic Study of the Si-B Phase When B_2O_3 Is Diffused in Si," *J. Electrochem. Soc.* **125**, pp. 1521-1524, 1978.

[83] P. Negrini, A. Ravaalia, and S. Solmi, "Boron predeposition in silicon using BBr_3," *J. Electrochem. Soc.* **125**, pp. 609-613, 1978.

[84] Makoto Miyoshi, Naohiro Shimizu, Yuichiro Imanishi, Osamu Oda, and Junichi Nishizawa, "Investigation of Boron Diffusion into Silicon Using a Liquid Boron Tribromide Source and Its Application to Buried-Gate-Type Static-Induction Thyristors," *J. Electrochem. Soc.* **152**, pp. G601-G607, 2005.

[85] N. Ohe, K. Tsutsui, T. Warabisako, and T. Saitoh, "Effect of boron gettering on minority-carrier quality for FZ and CZ Si substrates," *Solar Energy Mater. Sol. Cells* **48**, pp. 145-150, 1997.

[86] P. J. Cousins and J. E. Cotter, "The Influence of Diffusion-Induced Dislocations on High Efficiency Silicon Solar Cells," *IEEE Trans. Electron Devices* **53**, pp. 457-464, 2006.

[87] A. A. Istratov, H. Hieslmair, and E. R.Weber, "Iron contamination in silicon technology", *Appl. Phys. A* **70**, pp. 489-534, 2000.

[88] S. Prussin, "Generation and distribution of dislocations by solute diffusion," *J. Appl. Phys.* **32**, pp. 1876-1881, 1961.

[89] H. J. Queisser, "Slip patterns on boron-doped silicon surfaces," *J. Appl. Phys.* **32**, pp. 1776-1780, 1961.

[90] X. J. Ning, "Distribution of residual stresses in boron doped p+ silicon films," *J. Electrochem. Soc.* **143**, pp. 3389-3393, 1996.

[91] F. Gaiseanu, G. Kissigner, D. Kruger, and H. Richter, "Analysis of the Generation of the Misfit Dislocations during the Boron Prediffusion in Silicon," in *Proc. SPIE* **3507**, pp. 281-289, 1998.

[92] M. A. Kessler, T. Ohrdes, B. Wolpensinger, and N.-P. Harder, "Charge carrier lifetime degradation in Cz silicon through the formation of a boron-rich layer during BBr_3 diffusion processes," *Semicond. Sci. Technol.* **25**, 055001, 2010.

[93] S. K. Ghandhi, "VLSI fabrication principles : silicon and gallium arsenide," 2nd Edition, New York, J. Wiley, 1994.

[94] A. Cuevas, M. Stuckings, J. Lau, and M. Petravic et al., "The recombination velocity of boron diffused silicon surfaces," in *Proc. 14th EU-PVSEC*, pp. 2416-2419, 1997.

[95] Boron Tribromide Material Safety Data Sheet, Air Products, v.1.21, Rev. Date 03/12/2010.

[96] Boron Trichloride Material Safety Data Sheet, Air Products, v.1.6, Rev. Date 07/27/2009.

[97] Boron Trichloride Material Safety Data Sheet, Trona, v.1, Rev. Date 09/29/2009.

[98] Diborane Material Safety Data Sheet, Praxair, Rev. Date May 2009.

[99] Silane Material Safety Data Sheet, Praxair, Rev. Date 10/15/2007.

[100] D. Rupprecht, J. Stach, "Oxidized Boron Nitride Wafers as an In-situ Boron Dopant for Silicon Diffusions", *J. Electrochem. Soc.* **120**, pp. 1266-1271, 1973.

[101] K. Ryu, A. Upadhyaya, A. Das, S. Ramanathan, Y-W Ok, H. Xu, L. Metin, A. Bhanap, and A. Rohatgi, "High efficiency N-type silicon solar cell with a novel inkjet-printed boron emitter," in *Proc. 37th IEEE PVSC*, 2011 (*in press*).

[102] J. Benick, A. Leimenstoll, O. Schultzm "Comprehensive studies of passivation quality on boron diffused silicon surfaces," in *Proc. 22nd EU-PVSEC*, pp. 1244-1247, 2007.

[103] J. Snel, "The doped Si/SiO_2 interface," *Solid State Electron.* **24**, pp. 135-139, 1981.

[104] P.P. Altermatt, H. Plagwitz, R. Bock, J. Schmidt, R. Brendel, M.J. Kerr, A. Cuevas, "The surface recombination velocity at boron-doped emitters: Comparison between various passivation techniques," in *Proc. 21st EU-PVSEC*, pp. 647-650, Sept. 2006.

[105] A. Aberle, S. Glunz, W. Warta, "The impact of illumination level and oxide parameters on Shockley-Read-Hall recombination at the Si-SiO_2 interface," *J. Appl. Phys.* **71**, pp. 4422-4431, 1992.

[106] R. R. King, P. E. Gruenbaum, R. A. Sinton, R. M. Swanson, "Passivated emitters in silicon solar cells," in *Proc. 21st IEEE PVSC*, pp.227-232, 1990.

[107] J. Zhao et al., "Performance instability in n-type PERT silicon solar cells," in *Proc. 3rd WCPEC*, pp. 923-926, 2003.

[108] A. G. Aberle and R. Hezel, "Progress in low-temperature surface passivation of silicon solar cells using remote-plasma silicon nitride," *Prog. Photovolt: Res. Appl.* **5**, pp. 29-50, 1997.

[109] F. W. Chen, T. A. Li, and J. E. Cotter, "Passivation of boron emitters on n-type silicon by plasma-enhanced chemical vapor deposited silicon nitride," *Appl. Phys. Lett.* **88**, 263514, 2008.

[110] J. Benick, B. Hoex, O. Schultz, S. W. Glunz, "Surface passivation of boron diffused emitters for high efficiency solar cells," in *Proc. 33rd IEEE PVSC*, 2008.

[111] Y. Veschetti, R. Cabal, P. Brand, V. Sanzone, G. Raymond, and A. Bettinelli , "High Efficiency on Boron Emitter n-Type Cz Silicon Solar Cells With Industrial Process," *IEEE J. Photovoltaics* **1**, pp. 118-122, 2011.

[112] V. D. Mihailetchi, Y Komatsu, L. J. Geerligs, "Nitric acid pretreatment for the passivation of boron emitters for n-type base silicon solar cells," *Appl. Phys. Lett.* **92**, 063519, 2008.

[113] K. J. Weber and H. Jin, "Improved silicon surface passivation achieved by negatively charged silicon nitride films," *Appl. Phys. Lett*. **94**, 063509, 2009.

[114] Y. Ren, N. M. Nursam, D. Wang and K. J. Weber, "Charge stability in LPCVD silicon nitride for surface passivation of silicon solar cells," in *Proc. 35th IEEE PVSC*, pp. 897-901, 2010.

[115] H. Jin, K.J. Weber, C. Zhang and Y. Ren, "Low Si surface recombination through negatively charged Si_3N_4 films," in *Proc. 24th EU-PVSEC*, pp. 72-76, 2009.

[116] B. Hoex, J. Schmidt, R. Bock, P. P. Altermatt, M. C. M. van de Sanden and W. M. M. Kessels, "Excellent passivation of highly doped p-type Si surfaces by the negative-charge-dielectric Al_2O_3," *Appl. Phys. Lett.* **91**, 112107, 2007.

[117] G. Agostinelli, A. Delabie, P. Vitanov, Z. Alexieva, H.F.W. Dekkers, S. De Wolf, G. Beaucarne, "Very low surface recombination velocities on p-type silicon wafers passivatved with a dielectric with fixed negative charge," *Sol. Energy Mater. Sol. Cells* **90**, pp. 3438-3443, 2006.

[118] J. Benick, A. Richter, T.-T. A. Li, N. E. Grant, K. R. McIntosh, Y. Ren, K. J. Weber, M. Hermle, S. W. Glunz, "Effect of a post-deposition anneal on Al_2O_3/Si interface properties," in *Proc. 35th IEEE PVSC*, pp. 891-896, 2010.

[119] J. Benick, B. Hoex, M. C. M. van de Sanden, W. M. M. Kessels, O. Schultz, and S. W. Glunz, "High efficiency n-type Si solar cells on Al_2O_3-passivated boron emitters," *Appl. Phys. Lett.* **92**, 253504, 2008.

[120] Jan Benick, Armin Richter, Martin Hermle, and Stefan W. Glunz, "Thermal stability of the Al_2O_3 passivation on p-type silicon surfaces for solar cell applications," *Phys. Status Solidi RRL* **3**, pp. 233-235, 2009.

[121] A. Richter, M. Hörteis, J. Benick, S. Henneck, M. Hermle, S. W. Glunz, "Towards industrially feasible high-efficiency n-type solar cells with boron-diffused front side emitter – Combining firing stable Al_2O_3 passivation and fine-line printing," in *Proc. 35th IEEE PVSC*, pp. 3587-3592, 2010.

[122] A. Richter, S. Henneck, J. Benick, M. Hörteis, M. Hermle and S.W. Glunz, "Firing stable Al_2O_3/SiN stack passivation for the front side boron emitter of n-type solar cells," in *Proc. 5th WCPEC*, pp. 1453-1459, 2010.

[123] J. Schmidt, A. Merkle, R. Bock, P. P. Altermatt, A. Cuevas, N-P. Harder, B. Hoex, R. van de Sanden, E. Kessels, and Rolf Brendel, "Progress in the surface passivation of silicon solar cells," in *Proc. 23rd EU-PVSEC*, pp. 974-981, 2008.

[124] Boric acid 99.999% (trace metals basis), Sigma-Aldrich Corp., Product Number: 202878.

[125] Boric acid Puratronic 99.9995% (metals basis), Alfa Aesar, Product Number: 10659.

[126] The Merck index : An encyclopedia of chemicals, drugs, and biologicals (14th ed.), M.J. O'Neil, Editor, Merck, Whitehouse Station, New Jersey, 2006.

[127] Boron, Its Compounds and Alloys, Academy of Sciences of the Ukranian S.R.R, Kiev, 1960 (Translation by the United States Atomic Energy Commission).

[128] The chemistry of boron and its compounds, E.L. Muetterties, Editor, John Wiley & Sons, Inc., New York, 1967.

[129] Filmtronics Spin On Diffusants Guide, Rev. 6, 2004.

[130] S. L. Elliot, R. F. Broom, and C. J. Humphreys, "Dopant profiling with the scanning electron microscope – A study of Si," *J. Appl. Phys.* **91**, pp. 9116-9122, 2002.

[131] A. A. Istratov, H. Hieslmair, and E. R. Weber, "Iron and its complexes in silicon," *Appl. Phys. A* **69**, pp. 13-44, 1999.

[132] H. M'saad, J. Michel, A. Reddy, and L. C. Kimerling, "Monitoring and Optimization of Silicon Surface Quality," *J. Electrochem. Soc.* **142**, pp. 2833-2835, 1995.

[133] G. Dingemans, M. C. M. van de Sanden, and W. M. M. Kessels, "Excellent Si surface passivation by low temperature SiO2 using an ultrathin Al_2O_3 capping film," *Phys. Status Solidi RRL* **5**, pp. 22–24, 2011.

[134] B. Sopori, R. Reedy, K. Jones, L. Gedvilas, B. Keyes, Y. Yan, M. Al-Jassim, V. Yelundur, and Ajeet Rohatgi, "Damage-layer-mediated H diffusion during SiN:H processing: A comprehensive model," in *Proc. 4th WCPEC*, pp. 1028–1031, 2006.

[135] M. Sheoran, D. S. Kim, and A. Rohatgi, "Hydrogen diffusion in silicon from PECVD silicon nitride," in *Proc. 33rd IEEE PVSC*, 2008.

[136] R. R. King, R. A. Sinton, and R. M. Swanson, "Studies of diffused phosphorus emitters: Saturation current, surface recombination velocity, and quantum efficiency," *IEEE Trans. Electron. Devices* **37**, pp. 365-371, 1990.

[137] D. Macdonald, A. Cuevas, and F. Ferrazza, "Response to phosphorus gettering of different regions of cast multicrystalline silicon ingots," *Solid-State Electron.* **43**, pp. 571-581, 1999.

[138] M. Sheoran, "Development of high-efficiency solar cells on then silicon through design optimization and defect passivation," PhD Thesis, 2009.

[139] H. M'saad, J. Michel, A. Reddy, and L. C. Kimerling, "Monitoring and Optimization of Silicon Surface Quality," *J. Electrochem. Soc.* **142**, pp. 2833-2835, 1995

[140] Zoth and Bergholz, "A fast, preparation free method to detect iron in silicon," *J. Appl. Phys.* **67**, pp. 6764-6771, 1990.

[141] D. H. Macdonald, L. J. Geerligs, and A. Azzizi, "Iron detection in crystalline silicon by carrier lifetime measurements for arbitrary injection and doping," *J. Appl. Phys.* **95**, pp. 1021-1028, 2004.

[142] A. A. Istratov, H. Hieslmair, and E. R. Weber, "Iron and its complexes in silicon," *Appl. Phys. A* **69**, 13-44, 1999.

[143] D. Macdonald, A. Cuevas, and J. Wong-Leung, "Capture cross sections of the acceptor level of iron–boron pairs in p-type silicon by injection-level dependent lifetime measurements," *J. Appl. Phys.* **89**, pp. 7932-7939, 2001.

[144] M. A. Green, "Intrinsic concentration, effective densities of states, and effective mass in silicon," *J. Appl. Phys.* **67**, pp. 2944-2954, 1990.

[145] S. Rein and S.W. Glunz, "Electronic properties of interstitial iron and iron-boron pairs determined by means of advanced lifetime spectroscopy," *J. Appl. Phys.* **98**, 113711, 2005.

[146] J. E. Birkholz, K. Bothe, D. Macdonald and J. Schmidt, "Electronic properties of iron-boron pairs in crystalline silicon by temperature- and injection-level-dependent lifetime measurements," *J. Appl. Phys.* **97**, 103708, 2005.

[147] D. Macdonald, T. Roth, P. N. K. Deenapanray, T. Trupke, and R. A. Bardos, "Doping dependence of the carrier lifetime crossover point upon dissociation of iron-boron pairs in crystalline silicon," *Appl. Phys. Lett.* **89**, 142107, 2006.

[148] D. Macdonald, H. Mäckel and A. Cuevas, "Recombination in n- and p-type silicon emitters contaminated with iron," in *Proc. 4th WCPEC,* pp. 952-955, 2006.

[149] T. Joge, I. Araki, T. Uemastsu, T. Warabisako, H. Nakashima, and K. Matsukuma, "Low-Temperature boron gettering for improving the carrier lifetime in Fe-contaminated bifacial silicon solar cells with n^+pp^+ back-surface-field structure," *Jpn. J. Appl. Phys*. **42**, pp. 5397–5404, 2003.

[150] T. Terakawa, D. Wang, H. Nakashima, "Role of heavily B-doped layer on low-temperature Fe gettering in bifacial Si solar cell fabrication," *Jpn. J. Appl. Phys*. **45**, pp. 2643–2647, 2006.

[151] D. Macdonald, A. Cheung and A. Cuevas, "Gettering and poisoning of silicon wafers by phosphorus diffused layers," in *Proc. 3rd WCPEC*, pp. 1336-1339, 2003.

[152] H. Shimizu and C. Munakata, "Effect of surface photovoltages in thermally oxidized n-type silicon wafers," *Jpn. J. Appl. Phys.* **31**, pp.729-731, 1991.

[153] H. Shimizu, "Behavior of metal-induced oxide charge during thermal oxidation in silicon wafers," *J. Electrochem. Soc.* **144**, pp.4335-4330, 1997.

[154] R. S. Johnson, G. Lucovskya and I. Baumv, "Physical and electrical properties of noncrystalline Al2O3 prepared by remote plasma enhanced chemical vapor deposition," *J. Vac. Sci. Technol. A* **19**, pp.1353-1360, 2001.

[155] J. K. Rath, "Low temperature polycrystalline silicon: a review on deposition, physical properties and solar cell applications," *Sol. Energy Mater. Sol. Cells* **76**, pp. 431-487, 2003.

[156] V. T. Daudrix, J. Guillet, F. Freitas, A. Shah, C. Baliff, P. Winkler, M. Ferreloc, S. Bengali, X. Niquille, D. Fischer, and R. Morf, "Characterisation of rough reflecting substrates incorporated into thin-film slicon solar cells," *Prog. Photovoltaics* **14**, pp. 485-198, 2006.

[157] N. Taneda, T. Oyama, and K. Sato, "Light scattering effects effect of highly textured trabsparent comductive [*sic*] oxides films," in *Tech. Digest 17th I-PVSEC*, Toyota Technological Institute, Fukuoka, Japan, pp. 309-310, 2007.

[158] H. Sai, H. Fujiwara, and M. Kondo, "Back surface reflector with periodic textures fabricated by self-ordering process for light trapping in microcrystalline silicon solar cells," in *Tech. Digest 17th I-PVSEC*, Toyota Technological Institute, Fukuoka, Japan, pp. 315-136, 2007.

[159] O. Berger, D. Inns, and A. G. Aberle, "Commercial white paint as back surface reflector for thin-film solar cells," *Sol. Energy Mater. Sol. Cells* **91**, pp. 1215-1221, 2007.

[160] J. E. Cotter, "Optical intensity of light in layers of silicon with rear diffuse reflectors," *J. Appl. Phys.* **84**, pp. 618-624, 1998.

[161] K. Katsuma, S. Hayakawa, A. Masuda, T. Matsui, and M. Kondo, "Fabrication of superstrate-type thin-film silicon solar cells on textured plastic substrates," in *Proc. of the 22nd EU-PVSEC*, pp. 1831-1834, 2007.

[162] M. L. Addonizio, R. Manoj, and I. Usatii, "Optimizations of low pressure-chemical vapor deposited ZnO thin films as front electrode of thin film silicon based solar cells," in *Proc. of the 22nd EU-PVSEC*, pp. 2129-2133, 2007.

[163] K. Winz, CM. Fortmann, Th. Eickhoff, C. Beneking, B. Fiech, O. Kluth, H. Wagner, "Smooth TCO/glass substrates and diffuse rear reflectors for efficient low cost amorphous silicon-based solar cells," in *Proc. 25th IEEE PVSC*, pp. 1149-1152, 1996.

[164] A. Ristow, M. Hilali, A. Ebong, and A. Rohatgi, "Screen-printed back surface reflector for light trapping in crystalline silicon solar cells," in *Proc. 17th EU-PVSEC*, p. 1335, 2001.

[165] J.M. Gee, "The effect of parasitic absorption losses on light trapping in thin silicon solar cells," in *Proc. 20th EU-PVSEC*, pp. 549-554, 2001.

[166] V. R. Weidner and J. J. Hsia, "Reflection properties of pressed polytetrafluoroethylene powder," *J. Opt. Soc. Am.* **71**, pp. 856-861, 1981.

[167] A. W. Springstreen, "A novel class of Lambertian reflectance metaerials for remote sensing application," *SPIE Optical Radiation Measurements II* **1109**, 1989.

[168] A. W. Springstreen, "Laser Cavity Material," U.S. Patent 4,912,720, 1990.

[169] A.R. Burgers, R.C.G. Naber, A.J. Carr, P.C. Barton, L.J. Geerligs, X. Jingfeng, L. Gaofei, S. Weipeng, A. Haijiao, H. Zhiyan, P.R. Venema, A.H.G. Vlooswijk, "19% Efficient N-type solar cells made in pilot production", in *Proc. 5th WCPEC*, pp. 1144-1147, 2010.

[170] D. D. Smith, M. J. Cudzinovic, K. R. McIntosh, B. G. Mehta, "Use of doped silicon dioxide in the fabrication of solar cells," U.S. Patent 7,135,350 B1, Nov. 16, 2006.

[171] H. Fischer and W. Pschunder, "Investigation of photon and thermal induced changes in silicon solar cells", in *Proc. 10th IEEE PVSC*, pp. 404-411, 1973.

[172] J. Schmidt and K. Bothe, "Structure and transformation of the metastable boron- and oxygen-related defect center in crystalline silicon", *Physical Review B (Condensed Matter)* **69**, pp. 241071-241078, 2004.

[173] K. Bothe, R. Sinton, and J. Schmidt, "Fundamental boron-oxygen-related carrier lifetime limit in mono- and multicrystalline silicon", *Prog. Photovolt.: Res. and Appl.* **13**, pp. 287-296, 2005.

[174] S. Gatz, H. Hannebauer, R. Hesse1, F. Werner, A. Schmidt, Thorsten Dullweber, J. Schmidt, K. Bothe, and R. Brendel, "19.4%-efficient large-area fully screen-printed silicon solar cells," *Phys. Status Solidi RRL* **5**, pp. 147-149, 2011.

[175] A. Wolf, E.A. Wotke, A. Walczak, S. Mack, B. Bitnar, C. Koch, R. Preu, and D. Biro, "Pilot line processing of 18.6% efficient rear surface passivated large area solar cells," in *Proc. 35th IEEE PVSC*, pp. 1014-1018, 2010.

[176] M. Horteis and S. W. Glunz, "Fine line printed silicon solar cells exceeding 20% efficiency," *Prog. Photovolt.: Res. & Appl.* **16**, pp. 555-560, 2008.

[177] S. Rein and S.W. Glunz, "Electronic properties of the metastable defect in boron-doped Czochralski silicon: Unambiguous determination by advanced lifetime spectroscopy," *Appl. Phys. Lett.* **82**, pp. 1054-1056, 2003.

[178] S. Mack, U. Jager, G. Kastner, E.A. Wotke, U. Belledin, A. Wolf, R. Preu, and D. Biro, "Towards 19% efficient industrial PERC devices using simultaneous front emitter and rear surface passivation by thermal oxidation," in *Proc. 35th IEEE PVSC*, pp. 34-38, 2010.

[179] A. Wolf, A. Walczak, S. Mack, E.A. Wotke, A. Lemke, C. Bertram, U. Belledin, D. Biro, and R. Preu, "The SiNTO process: Utilizing a SiNx anti-reflection layer for emitter masking during thermal oxidation," in *Proc. 34th IEEE PVSC*, pp. 534-539, 2009.

[180] B. Lim, S. Hermann, K. Bothe, J. Schmidt, and R. Brendel, "Solar cells on low-resistivity boron-doped Czochralski-grown silicon with stabilized efficiencies of 20%," *Appl. Phys. Lett.* **93**, 162102, 2008.

[181] J. Schmidt, A. Cuevas, S. Rein, and S. W. Glunz, "Impact of light-induced recombination centers on the current-voltage characteristic of Czochralski silicon solar cells," *Prog. Photovolt: Res. Appl.* **9**, pp. 249-255, 2001.

[182] B. Lim, K. Bothe, V. Voronkov, R. Falster, and Jan Schmidt, “Light-induced degradation of the carrier lifetime in n-type Czochralski-grown silicon doped with boron and phosphorous,” in *Proc. 26th EU-PVSEC*, pp. 944-948, 2011.

LIST OF PUBLICATIONS

[1] D. S. Kim , V. Meemongkolkiat, A. Ebong, B. Rounsaville, V. Upadhyaya, **A. Das** and A. Rohatgi, "2D-Modeling and development of interdigitated back contact solar cells on low-cost substrates," in *Proc. 4th WCPEC,* pp. 1417-1420, 2006.

[2] **A. Das**, V. Meemongkolkiat, A. Ristow, and A. Rohatgi, "Conductive silver colloids for light trapping in crystalline silicon solar cells with rear local contacts," in *Tech. Digest 17th I-PVSEC*, Toyota Technological Institute, Fukuoka, Japan, pp. 428-429, 2007.

[3] **A. Das**, D. S. Kim, and Ajeet Rohatgi, "Impact of Intrinsic Buffer Layer Thickness on the Open-Circuit Voltage in aSi/p-cSi Heterojunction Solar Cells," in *Tech. Digest 17th Workshop on Crystalline Silicon Solar Cell Materials and Processes*, pp. 275-280, 2007.

[4] D.S Kim, **A. Das**, K. Nakayashiki, B. Rounsaville, V. Meemongkolkiat, A. Rohatgi, "Silicon Solar Cells with Back Surface Field Formed by Using Boric Acid", in *Proc. 22nd EU-PVSEC*, pp. 1730-1733, 2007.

[5] **A. Das**, D. S. Kim, V. Meemongkolkiat and A. Rohatgi, "19% efficient screen-printed cells using a passivated transparent boron back surface field," in *Proc. 33rd IEEE PVSC*, 2008.

[6] A. Rohatgi, A. Ristow, **A. Das**, and S. Ramanathan, "Road to Cost Effective Silicon PV," in *Tech. Digest 8th I-PVSEC*, IACS, Kolkata, India, 2009. (Invited paper and presentation)

[7] S. Ramanathan, V. Meemongkolkiat, **A.Das**, A. Rohatgi, I.Koehler, "Fabrication of 20 % efficient cells using spin-on based simultaneous diffusion and dielectric anneal," in *Proc. 34th IEEE Photovoltaics Specialists Conference*, pp. 2150-2153, 2009.

[8] **A. Das**, V. Meemongkolkiat, D.S. Kim, S. Ramanathan and A. Rohatgi, "20% Efficient Screen Printed Boron BSF Cells Using Spin-on Dielectric Passivation," in *Proc. 34th IEEE Photovoltaics Specialists Conference*, pp. 477-481, 2009. (Invited paper and presentation)

[9] **A. Das** and A. Rohatgi, "Optical and electrical characterization of silver microflake colloid films," *J. Electrochem. Soc.* **157**, pp. H301–303, 2010.

[10] **A. Das**, S. Ramanathan, A. Upadhyaya, V. Meemongkolkiat and A. Rohatgi, "Practical Challenges of Achieving High-Efficiency Boron Back Solar Cells," in *Proc. 35th IEEE PVSC*, pp. 906-912, 2010.

[11] S. Ramanathan, **A. Das**, I.B. Cooper, A. Rohatgi, A. Payne, I. Koehler, "20% efficient screen printed LBSF cell fabricated using UV laser for rear dielectric removal," in *Proc. 35th IEEE PVSC*, pp. 678-682, 2010.

[12] **A. Das**, D. S. Kim, K. Nakayashiki, B. Rounsaville, V. Meemongkolkiat, and A. Rohatgi, "Boron Diffusion with boric acid for high efficiency silicon solar cells," *J. Electrochem. Soc.* **157**, pp. H684–H687, 2010.

[13] **A. Das**, V. Meemongkolkiat, D.S. Kim, S. Ramanathan, and A. Rohatgi, "20% Efficient Screen Printed Boron BSF Cells Using Spin-on Dielectric Passivation," *IEEE Trans. Elec. Devices* **57**, pp. 2462-2469, 2010. (Invited paper)

[14] S. Ramanathan, **A. Das**, and A. Rohatgi, "Optimization of Phosphoric Acid Based Limited-source-diffusion to Obtain High Quality Emitter for Screen Printed Contacts," in *Proc. 37th IEEE PVSC*, 2011.

[15] **A. Das** and A. Rohatgi, "The Impact of Cell Design on Light Induced Degradation in P-type Silicon Solar Cells," in *Proc. 37th IEEE PVSC*, 2011.

[16] **A. Das**, K. Ryu, Y-W Ok, and A. Rohatgi, "20% Efficient Screen-Printed N-type Solar Cells using a Spin-On Source and Thermal Oxide/Silicon Nitride Passivation," *IEEE J. Photovoltaics* **1**, pp. 146-152, 2011. (Invited paper)

[17] K. Ryu, A. Upadhyaya, **A. Das**, S. Ramanathan, Y-W Ok, H. Xu, L. Metin, A. Bhanap, and A. Rohatgi, "High efficiency N-type silicon solar cell with a novel inkjet-printed boron emitter," in *Proc. 37th IEEE PVSC*, 2011.

[18] J-H Lai, A. Upadhyaya, R. Ramanathan, **A. Das**, K. Tate, V. Upadhyaya, A. Kapoor, C-W Chen, and A. Rohatgi, "High-Efficiency Large-Area Rear

Passivated Silicon Solar Cells With Local Al-BSF and Screen-Printed Contacts," *IEEE J. Photovoltaics* **1**, pp. 16-21, 2011. (Invited paper)

[19] M-H Kang, A. Rohatgi, J. Hong, B. Rounsaville, V. Upadhyaya, A. Ebong and **A. Das**, "Effect of carbon containing SiN_x antireflection coating on the screen-printed contact and low illumination performance of silicon solar cell," *Prog. Photovolt.: Res. Appl.*, doi: 10.1002/pip.1184, 2011.

[20] S. Ramanathan, V. Meemongkolkiat, **A. Das**, A. Rohatgi, and I. Koehler, "Understanding and Fabrication of 20% Efficient Cells Using Spin-on-Based Simultaneous Diffusion and Dielectric Passivation", *IEEE J. Photovoltaics* **2**, pp. 22-26, 2012.

[21] Y. Liu, **A. Das**, S. Xu, Z. Lin, C. Xu, Z. L. Wang, A. Rohatgi, and C. P. Wong, "Hybridizing ZnO Nanowires with Micropyramid Silicon Wafers as Superhydrophobic High-Efficiency Solar Cells," *Advanced Energy Materials* **2**, 2012.

[22] B. C. Rounsaville, I. Cooper, J. K. Tate, M. Kadish, **A. Das**, Ajeet Rohatgi, "Analysis of Cast Monocrystalline Ingot Characteristics with Applications to Solar Cells," in *Proc. 38th IEEE PVSC*, 2012.

VITA

Arnab Das received the Bachelor's of Science degree in Electrical and Computer Engineering in 2004 from the Georgia Institute of Technology, Atlanta. He then joined the University Center of Excellence for Photovoltaics at the Georgia Institute of Technology, where he is currently pursuing the Doctor of Philosophy degree in Electrical Engineering under the supervision of Dr. Ajeet Rohatgi. His graduate research has focused on the fabrication and characterization of high-efficiency, boron diffused, monocrystalline silicon solar cells. This work has resulted in over 20 publications in peer-reviewed journals, international refereed conferences and workshop proceedings.